Development of Additively Manufactured Titanium Based (Ti6Al4V) Implants with Different Inclination Angle and its Implications on Bio-interface for Orthopaedic Applications

A thesis submitted in fulfilment of the requirements for the degree of Doctor of Philosophy

Avik Sarker

M. Sc. (Medical Science), Soonchunhyang University

B. Sc. (Electrical & Electronic Engg.), Khulna University of Engineering & Technology

School of Engineering

College of Science, Engineering and Health

RMIT University

Melbourne, Australia

December, 2019

Declaration

I certify that except where due acknowledgement has been made, the work is that of the author alone; the work has not been submitted previously, in whole or in part, to qualify for any other academic award; the content of the thesis is the result of work which has been carried out since the official commencement date of the approved research program; any editorial work, paid or unpaid, carried out by a third party is acknowledged; and, ethics procedures and guidelines have been followed. I acknowledge the support I have received for my research through the provision of an Australian Government Research Training Program (RTP) Scholarship.

Avik Sarker

18 December,2019

Dedication

To my parents

Who taught me how to survive and stay cool even in the most adverse condition

Acknowledgements

At first, I would like to express my heartfelt gratitude to Almighty for giving me the strength, confidence, courage to accomplish this thesis on time. First and foremost, I would like to express my sincere gratitude to my senior supervisor, Assoc Prof. Kate Fox, for accepting me as a PhD student. Her constant inspiration, suggestions, and support throughout this PhD period helped me to finish thesis in due time. It was a great privilege to work with her and helped me to learn the one of the most important skills in academia to work in a collaborative environment. I would also like to express my genuine appreciation to my second associate supervisor, Prof. Martin Leary, for his helpful input, supportive advice, his patience, and contribution during this research project. His expertise and scholastic comments in additive manufacturing field helped me greatly to integrate my biomaterials knowledge with additive manufacturing. Because of his day to day guidance smoothed my PhD journey and made me passionate about my topic. I would also like to express my sincere gratitude to my third supervisor, Dr. Richard Williams, for his expertise in biomaterials and tissue engineering field. I am also grateful to Dr. Nhiem Tran from RMIT and Dr. Phong Tran from QUT for their great collaboration to complete my research goal in due time by their biological expertise. My special appreciation goes to my colleague Aaqil Rifai, for being so helpful during experiments and data analyses throughout my PhD period. I am grateful to my other colleagues Matthew McMillan, Rance Tino, Tobias Maconachie, Bill Lozanovski, Carmelo Todaro, Nabi Chowdhury. I was so lucky to start my PhD project receiving prestigious RTP scholarship funded by commonwealth government under Advanced Manufacturing Precinct (AMP) at RMIT which is quite exceptional not only in Australia but also among the world in terms of metallic 3D printing. I would like to acknowledge the facilities within the Advanced Manufacturing Precinct (AMP) for the SLM manufacture process and highly grateful to Prof. Milan Brandt (Director, Centre of Additive Manufacturing) for giving me the opportunity to manufacture titanium- based implants. I

hereby acknowledge the stuff members from RMIT Microscopy and Microanalysis Facility (RMMF) staff members Dr Matthew Field, Dr Edwin Mayes for providing me training and support in solving technical issues that arose in this research. I am also grateful to Micro Nano Research Facility (MNRF) staff member Dr Zeyad Nasa for his technical support. I want to thank my friends Mirza Muhit, Prodip Mistry, Kallyanashis Paul, Subrata Saha for their support during this journey. I would like to take the opportunity to express my deepest gratitude to my parents for whom I am here today. I also want to extend my sincere gratitude to my father-in-law for inspiring me during PhD thesis submission time. Last but not the least, I am indebted to my wife, Permita Mazumder, who suddenly entered into my life like a comet and inspired me and provided me encouragement during the thesis submission time by her level of super patience and understanding.

Abstract

Musculoskeletal injuries and defects are considered globally as some of the most critical types of injury in orthopaedic field and it often requires surgical intervention to deal with these problems. These injuries may occur in different way such as tumor resection, traumatic bone injury, and osteitis. Bone trauma or defect can significantly deteriorate on the status of human's life. The design of tissue engineering materials for both orthopaedic and dental implants is a great challenge in terms of desirable mechanical properties, biocompatibility, and improved osseo-integration. Titanium has been an effective implant material due to its excellent strength to weight ratio, corrosion resistance, toughness, and bio-inert oxide surface. Due to the recent progress of additive manufacturing technique it is possible to make patient-specific implants. Therefore, additive manufacturing has the huge potentiality to disrupt traditional orthopaedic implants to met up the demand of increasing population.

Selective laser melting (SLM) is an additive manufacturing process that fabricates constructs based on CAD design by scanning powdered materials using the thermal energy supplied by a focused and computer-controlled laser beam. SLM allows the generation of complex 3D parts by a layer-wise material addition technique that selectively melts successive layers of metal powder on top of each other.

There have been several reports existed in the current literature which showed the relationship between different process parameters of additive manufacturing with its different surface properties, mechanical properties and microstructure. There have been also reported that there are several ways to improve the interface of additively manufactured by different surface treatments such as anodization, alkali treatment, surface modifications by coating, grafting and polishing. There has been only limited research has been carried out that how the build inclination angle can be used to improve the bio-interface of additively manufactured titanium

implant surface for better osseo-integration without changing any process parameter of additive manufacturing.

Therefore, understanding and investigating the relationship between as manufactured parts and its different surface profile properties (surface texture both 2D and 3D), surface roughness (Ra, Rq), surface morphology, and surface wettability are so essential prior to successful clinical application. At the initial stage, we have manufactured Ti6Al4V parts by selective laser melting process (SLM) with different inclination angle with respect to the build plane from 5 to 90 degrees with 5 degrees interval. The upward and downward faces of as-manufactured parts have been investigated profoundly using optical microscopy (OM), profilometer scanning electron microscopy (SEM). Herein, we demonstrated how the surface roughness, surface morphology, and surface wettability are changed with the alteration of inclination angle of SLM parts. There is much more percentage of correlation of arithmetic average of roughness (Ra) value for 5 average data points is found on lower surface on the linear, exponential and logarithmic regression line than the upper surface of SLM plates in the change of inclination angle. This study provides us a deep insight in terms of understanding how the surface properties are influenced by the design angle of additive manufacture when the processing parameters are constant.

In the next stage, we have manufactured Ti6Al4V implants with three inclination angles (0 degree, 45 degrees and 90 degrees) and tried to establish a relationship between mammalian cell attachment with the surface properties of different inclination angle. It has been found that during the SLM process there is an increasing trend of partially melted particles with the increase of inclination angle which greatly influence the surface topography, surface chemistry and surface roughness. It has been found from the mammalian cell (CHO-GHP) attachment on different inclined surface that higher inclination angle induces the better cell attachment on

implant surface with higher amount of spindle like shape with higher spindle dimension than lower inclination angle.

Implant associated infection is also a major concern among orthopaedic research community. Different coating, grafting, surface modification approaches have been carried out on metallic implant surface in order to prevent against biofilm formation. In this study, we have printed three different inclination angle 10, 45, and 90 degrees and *Staphylococcus aureus* (*S.aureus*) were grown on all these samples. After 48 hours of incubation, it has been found that lower inclination angle 10 degrees surface can inhibit biofilm formation due to its lower hydrophobicity, lower roughness, higher surface energy, and fewer partially melted metal particles than 45, and 90 degrees surface. In addition, the bulk chemistry was not altered in both lower and higher inclination angle and mammalian cell growth was not compromised in any of the inclination angle. This work demonstrates us a novel one step method at additive manufacturing that without using any surface modification approach we can develop additively manufactured surface which can shield against implant associated infection with superior surface functionality.

In final stage, we have manufactured Ti6Al4V cylindrical single at three different inclination angles (30 degrees, 60 degrees and 90 degrees) with 0.2 mm, 0.6 mm, 1.0 mm diameter struts by selective laser melting process as a proof of concept of orthopaedic lattice implants. The surface properties (surface roughness) of individual cylindrical strut is dependent both with the inclination angle and diameter. In detailed porosity analysis of individual cylindrical strut has been conducted to understand how the pore size and pore orientation are changed with the inclination angle and strut diameter along the build height. The stress analysis and buckling behaviour have also been analysed for individual single strut. After that, rat primary osteoblast cells were grown on individual struts to understand how the bone cells are attached on strut surface after 3 & 7 days of incubation by scanning electron microscope. This work gives us the

deep understanding of utilising SLM technology for the development of customized metallic implants for orthopaedic application specially where lattice geometry is required for healing the bone trauma.

Keywords: additive manufacturing, surface roughness, surface morphology, surface wettability, build inclination angle, selective laser melting, partially melted particles, Ti-6Al-4V alloy, mammalian cell (Chinese Hamster Ovarian), *Staphylococcus aureus***,** biofilm formation, cell attachment, rat primary bone cell, cylindrical strut, strut diameter, strut inclination angle.

Author's Publications

Published

[1] **A. Sarker**, N. Tran, A. Rifai, M. Brandt, P.A. Tran, M. Leary, K. Fox, R. Williams, Rational design of additively manufactured Ti6Al4V implants to control Staphylococcus aureus biofilm formation, **Materialia** 5 (2019) 100250.

[2] A. Rifai, N. Tran, P. Reineck, A. Elbourne, E.L.H. Mayes, **A. Sarker**, C. Dekiwadia, E.P. Ivanova, R.J. Crawford, T. Ohshima, B.C. Gibson, A.D. Greentree, E. Pirogova, K. Fox, Engineering the Interface: Nano-diamond Coating on 3D-Printed Titanium Promotes Mammalian Cell Growth and Inhibits Staphylococcus aureus Colonization, **ACS Applied Materials & Interfaces** (2019).

[3] E. Yang, M. Leary, D. Downing, B. Lozanovski, M. Mazur, **A. Sarker**, A. Khorasani, A. Jones, T. Maconachie, S. Bateman, M. Easton, M. Qian, P. Choong, M. Brandt, Effect of Geometry on the Mechanical Properties of Ti-6Al-4V Gyroid Structures Fabricated via SLM: A Numerical Study, **Materials & Design** 184 (2019) 108165.

[4] M.Leary, T. Maconachie, **A. Sarker**, O. Faruque, M. Brandt, Mechanical and Thermal Characterisation of AlSi10Mg SLM Block Support structures, **Materials & Design** 183 (2019) 108138.

[5] **A. Sarker**, N. Tran, A. Rifai, J. Elambasseril, M. Brandt, R. Williams, M. Leary, K. Fox, Angle defines attachment: Switching the biological response to titanium interfaces by modifying the inclination angle during selective laser melting, **Materials & Design** 154 (2018) 326-339.

[6] A. Rifai, N. Tran, D.W. Lau, A. Elbourne, H. Zhan, A.D. Stacey, E.L.H. Mayes, **A. Sarker**, E.P. Ivanova, R.J. Crawford, P.A. Tran, B.C. Gibson, A.D. Greentree, E. Pirogova, K. Fox, Polycrystalline Diamond Coating of Additively Manufactured Titanium for Biomedical Applications, **ACS Applied Materials & Interfaces** 10(10) (2018) 8474-8484.

Under Submission

[1] P. A. Tran, **A. Sarker**, N. Tran, C. Jeffery, A. Rifai, K. Fox, Book Chapter: Coatings for metallic biomaterials, in the book Metallic Biomaterials Processing and Medical Device Manufacturing, **Elsevier** 2019(Submitted).

[2] S. Houshyar, **A. Sarker**, A. Jadhav; G.S. Kumar, A. Bhattacharyya, R. Nayak, R. A Shanks, T. Saha, R.Padhye, K. Fox, Next Generation of Surgical Mesh; Polypropylene-Nanodiamond Composite, **Materials Science and Engineering C** , 2019 (Under review).

[3] T. Maconachie, M. Leary; J. Zhang; A.Medvedev; **A Sarker**; D. Ruan; G. Lu; O. Faruque; M. Brandt, Effect of build orientation on the quasi-static and dynamic response of SLM AlSi10Mg, **Materials & Design**(under review).

Under Preparation

[1] **A. Sarker**, M. Mcmillan, A. Rifai, M. Brandt, R. Williams, M. Leary, K. Fox, Understanding the Relationship between Additively Manufactured Different Inclined Support Free as- Manufactured Ti6Al4V parts and their Surface Properties for Biomedical Applications, **The International Journal of Advanced Manufacturing Technology**, in preparation for submission by December (2019).

[2] **A. Sarker**, D. Downing, R. Tino, A. Rifai, T. Maconachie, M. Brandt, R. Williams, K. Fox, M. Leary, Fabrication of Additively Manufactured Single Cylindrical Struts with Different Inclination Angle, Diameter for Orthopaedic Application, **Materials Science and Engineering: C**, in preparation for submission by January (2019).

[3] A. Rifai, C. Todaro, **A. Sarker**, N. Tran, B. C. Gibson, A. D. Greentree, E. Pirogova, K. Fox, Annealing 3D-printed titanium coated nano-diamond for enhanced mammalian cell activity and adhesion, JOM, in preparation for submission in December (2019).

[4] A. Rifai, A. D. Stacey, N. Tran, **A. Sarker**, A.D. Greentree, E. Pirogova, K. Fox Polycrystalline Diamond Coating of Curved 3D-Printed Scaffolds for Bone Implants, Materials Science and Engineering: C, in preparation for submission by December (2019).

List of Conferences

1. 1st Asia-Pacific International Conference on Additive Manufacturing, RMIT University, Melbourne, Australia on June 30- July 03,2019 2. Oral Presenter titled "**Effect of build inclination angle on additively manufactured titanium implants and their implications on mammalian cell attachment and staphylococcus aureus biofilm formation".**

2. 2018 MRS Spring Meeting & Exhibit, Phoenix, Arizona, USA on April 2-6, 2018. Oral Presenter titled **"Selective Laser Melted (SLM) Ti6Al4V Alloy for Biomedical Implants".**

3. 1st Asia-Pacific International Conference on Additive Manufacturing, RMIT University, Melbourne, Australia on 4-6 December 2017. Poster Presenter titled "**Surface Profile Properties of Ti6Al4V Selective Laser Melted (SLM) Plates of Different Build Inclinations".**

4. The 25th Annual ASBTE Conference in conjunction with the7th Indo-Australian Conference on Biomaterials, Implants, Tissue Engineering and Regenerative Medicine, Canberra, Australia on 18- 20 April 2017. Oral presenter titled "**Poly-L-lysine Surface Coating on Selective Laser Melted (SLM)Titanium Plate for Improved Biocompatibility**".

5. 10th Australasian biomechanics conference, December 4th -6th 2016 Melbourne, Australia. Poster Presenter titled "**Detailed Investigation of Surface Roughness and Surface Morphology of Different Inclinations of Ti6Al4V SLM Plates**".

This page is left intentionally blank

Table of Contents

This page is left intentionally blank

List of Figures

The page is intentionally left blank

List of Tables

Chapter One: Introduction

1.1 Problem Statement

Musculoskeletal injuries are regarded as some of the most critical types of injury known and can lead to severe long-term effects without surgical intervention[1]. These injuries may occur via traumatic bone injury, osteitis, and tumor resection. Trauma or degenerative diseases incurred to bone can significantly impact the condition of life of individuals. Cost of treatment in the US alone exceeded $17 billion in 2005 and is predicted to rise to $25 billion per year by 2025[2]. Importantly, it is quite prominent from the demographic data that the bone defect or trauma will increase over the coming years among the population due to the ageing population and modern lifestyle[3]. Therefore, it is quite inevitable to introduce the latest technologies to address the patient-specific implants by the orthopaedic surgeons to assist bone repair. The global orthopaedic market was valued at $29.2 billion in 2012 and expected to reach $41.2 billion by 2019[4].The market is expected to grow at a compound annual growth rate of 4.9 per cent over the next five years, according to the Transparency Market Research report[5]. In 2012-13, 2.5 million hospital admissions involved surgery in Australia[5]. 1 in 7 of hospital patients was admitted for orthopaedic surgery on bones, joints, ligaments and tendons, including knee and hip replacements[4]. From a statistics, it has been found that by the year 2030 the total number of hip replacements would rise to 572,000 procedures[6]. Also, the number of total knee replacement procedures is expected to rise to 3.48 million[7]. Therefore, it is quite expected that there will be a huge demand to develop novel metallic implants with superior functionality. In case of large bone defect, the tissue's endogenous regeneration is very much limited, so bone tissue engineering is essential for healing the defect zone[8]. Recently additive manufacturing technology has been introduced in orthopaedic regenerative medicine field to develop customized bone implants. In Belgium Dr. Jules Poukens and his

team implanted the world's first additively manufactured mandible in a patient by in 2012[9]. SLM technology has established a reliable approach for fabricating different types of solid titanium alloys in comparison with other additive manufacturing technologies because of their superior mechanical properties than the conventional technique.

1.2 Motivation and Scope

In 2014, Prof. Peter Choong, an Australian surgeon from St Vincent's Hospital, together with scientists from the Commonwealth Scientific and Industrial Research Organization (CSIRO) and Anatomics, successfully implanted the world's first 3Dprinted titanium heel bone into a patient. In 2015 Prof. Milan Brandt and his team from RMIT led research on Australia's first locally- made additively manufactured spinal implant which was successfully delivered to Amanda Gorvin in a local hospital named Saint Vincent hospital[10]. After few weeks later, she was reported to be completely pain free.

Figure 1. 1: 3D-printed titanium cage to fit perfectly into the spine[10].

AM facilitates the manufacture of metallic bone implant that mimics patient specific geometries and associated mechanical response[11]. In addition, AM enables indirect control of biologically relevant parameters such as porosity, pore size, shape and permeability, on the

biological performance of metallic bone grafts. AM enables economic production of small production volumes and medical alloys (notably Ti64) are widely used for orthopaedic are compatible with AM.

Being inspired from the RMIT project that led the research to develop additively manufactured lattice spinal implant, I started my PhD research to improve the interface of 3D printed titanium implant. There have been several reports which show the relationship between additive manufacturing processing parameters with the manufactured part's surface properties, microstructure and mechanical properties. There have been also existing literature which show that there are several ways we can improve the interface of additively manufactured implants by applying different surface treatments such as hot isostatic pressure treatment[12], anodization[13, 14], surface modification by nano-diamond coating[15], polymer grafting[16], nano-particle immobilising[17]. But there has been limited research carried out that if the design angle of additive manufacturing process is altered how the implant surface can exhibit different surface properties and how the biological properties are associated with the change of build inclination angle. It opens up a huge opportunity for us to improve the interface of additively manufactured implants from the additive manufacturing processing stage for better osseo-integration without applying any surface modification approach. In addition, improving interface from the manufacturing stage would provide a deep insight for biomedical manufacturers to commercialise metallic implants because of the reduced cost and easy FDA approval process as there is no secondary material is being applied.

1.3 Research Objectives

The main aim of this research is to develop the relationship between the surface properties such as surface roughness, surface wettability, surface chemistry with different inclined SLM implants with respect to the building plane. Afterwards, to understand how these surface properties influence the behaviour of cell-material interaction and biofilm formation. This aim can be accomplished by accumulating the following objectives.

1. To manufacture different inclined SLM Ti6Al4V implants with respect to the build plane.

2. To establish a relationship between the surface properties, such as surface topography, surface roughness, and surface wettability with different inclined SLM Ti6Al4V implant for both upward and downward surface.

3. To observe how the mammalian cell attachment behaviour can be altered with the inclination angle of SLM Ti6Al4V implants.

4. To control the ***Staphylococcus aureus*** biofilm formation on SLM implants from the additive manufacturing processing stage without applying any surface modification approach.

5. To establish a relationship between bone cell attachment with the alteration of strut inclination angle along with strut diameter of cylindrical struts as a proof concept in lattice implant for better osseointegration for successful orthopaedic applications.

1.4 Research Questions and Rationale

At the very first stage of our project, we focused on the evaluation of the surface texture of 3D SLM plates of different inclination angles varying 5 degrees to 90 degrees with 5 degrees interval for both upward and downward surface. The upward and downward faces of as-fabricated Ti6Al4V samples have been investigated profoundly using profilometer, optical microscopy (OM), scanning electron microscopy (SEM). As the growing demand for patient specific implants are increasing day by day, understanding and investigating the relationship between the implants design with its different properties such as surface profile properties (surface texture both 2D and 3D), surface roughness (Ra, Rq), surface morphology and surface wettability are so essential prior to successful clinical application because those properties have direct link with the osseo-integration.

1. How the surface morphology and surface texture of different inclination angle of Ti6Al4V SLM plates for both upper and lower surface is changed with the increase of the inclination angle?
2. How the surface roughness and surface wettability of different inclination angle of Ti6Al4V SLM plates for both upper and lower surface is changed with the increase of the inclination angle and establish a correlation between roughness and build inclination angle?

Among these inclination angles, we will choose 0, 10, 45, & 90 degrees growth angles in order to make the relationship between the mammalian cell attachment (by Chinese hamster ovarian) and biofilm formation (*Staphylococcus aureus*).

1. How does surface topography of different build inclined SLM specimens influence mammalian cells morphology and spindle dimension?
2. Is there any relationship between the biofilm formation and different inclination angle of SLM plates and how biofilm formation is controlled by altering the build inclination angle of SLM plates?

At the 3rd stage of our work, different cylindrical specimens varying two variables (strut inclination angle and strut diameter) (30 degrees, 60 degrees, 90 degrees with 0.2 mm, 0.6 mm, 1.0 mm) were manufactured mimicking the actual sturts located into lattice structure. This time we have seeded the rat primary osteoblasts cells on different cylindrical samples to observe the osteoblast cells proliferation over 3, and 7 days.

1. How cylindrical specimens with different strut inclination angle and diameter of Ti6Al4V samples will be printed by SLM?
2. How rat primary osteoblasts cells attachment and proliferation happened with the alteration of inclination angle along with strut diameter?

1.5 Thesis Outlines

The research work presented in this thesis is divided into eight chapters. The thesis chapter has been outlined as follows:

Chapter one highlights the significance of the development of additively manufactured metallic implant for orthopaedic applications. In this chapter the overall background, problem statement, motivation and scope, the rationale of this project, research questions and research objectives have been presented in this chapter.

Chapter two investigates the available metallic powder bed additive manufacturing technologies with their basic principles and their capabilities in terms of developing orthopaedic implants. Detailed description of commonly used metallic and titanium-based

alloys employed in additive manufacturing technologies for orthopaedic applications using different geometric topography has also been presented. This chapter provides a comprehensive review of different surface properties of metallic implants and their relationship with cellular attachment and bacterial colonies formation. This chapter also shows how different surface modification techniques have been applied to improve the bio-interface of metallic implants for better osseo-integration and control biofilm formation to protect against implant associated infection. This review helps to engineer and design the surface of metallic implants by additive manufacturing process for improved cellular attachment and control the biofilm formation for next generation patient-specific orthopaedic implants.

Chapter three presents all experimental procedures and the details of the materials used for this project. This chapter briefly describes the fabrication of different build inclined SLM Ti6Al4V implants and their characterization techniques. The details process of cell and bacterial study has also been presented.

Chapter four shows the manufacture of different build inclined AM TI6Al4V implants. This chapter investigates the relationship between different build inclination angle of Ti6Al4V SLM plates and their different surface properties such as surface roughness, surface topography, surface wettability. This chapter also compares the change of surface roughness, surface topography and surface wettability between upward and downward surface of Ti6Al4V SLM plates.

Chapter five shows how the alteration of build inclination angle of SLM Ti6Al4V implant can switch the interface between titanium and mammalian cell attachment. The detailed surface roughness, surface topography, surface wettability and surface chemistry of three different inclined implant surface have been investigated. The higher inclination angle with increased surface roughness adhering higher amount of partially melted particles triggered the mammalian cells to be more elongated than lower inclination angle. The cell viability of each

inclination angle has also been evaluated. The morphology of mammalian cells adhered on different inclined surface of SLM plates have also been observed and semi-automated matlab script has been applied to quantity the spherical and spindle shaped cells on implant surface.

Chapter six shows the relationship between different inclined SLM implant surface with biofilm formation. The detailed surface roughness, surface topography, surface wettability, surface energy has been investigated and how the build inclination angle can be used for controlling implant associated infection without using any surface modification from the additive manufacturing processing stage has been clearly stated.

Chapter seven shows the design and manufacturability of different inclined cylindrical struts with different strut diameter and the detailed surface profile properties were analysed for individual strut with specific strut diameter. How the bone cell attachment happens on individual strut surface has also been observed by in-vitro experiment.

Chapter eight summarises the major findings of this PhD research project and indicates the major contribution of this project to the body of knowledge in orthopaedic field to improve the interface of additively manufactured titanium-based implants. Finally, the perspective of further investigations in this area is outlined.

Chapter Two: Literature Review

2.1 Chapter overview

This chapter investigates the available metallic powder bed additive manufacturing technologies with their basic principles and their capabilities in terms of developing orthopaedic implants. Detailed description of commonly used metallic and titanium-based alloys employed in additive manufacturing technologies for orthopaedic applications using different geometric topography has also been presented. This chapter provides a comprehensive review of different surface properties of metallic implants and their relationship with cellular attachment and bacterial colonies formation. This chapter also shows how different surface modification techniques have been applied to improve the bio-interface of metallic implants for better osseo-integration and control biofilm formation to protect against implant associated infection. To address these problems in addition to structural modifications many surface engineering approaches are explored such as surface chemistry, hydrophobicity/hydrophilicity, charge have been discussed. This review helps to engineer and design the surface of metallic implants by additive manufacturing process for improved cellular attachment and control the biofilm formation for next generation patient-specific orthopaedic implants.

2.2 Additive Manufacturing

Additive manufacturing (AM) enables manufacturers to build up any complex structure or part by depositing material layer by layer using computer-aided design (CAD) with excellent engineering properties [18-20]. The term “3D printing” is also used as a synonym for Additive Manufacturing. The addition of material is occurred in additive manufacturing by adding the successive layer of deposition which makes it fundamentally different than traditional

manufacturing technologies [21]. Additive manufacturing (AM) field has gained a lot of traction and popularity among different industries in recent years because of its capability to present innovative application opportunities for the technology to expand beyond a prototyping tool. Different alloy compositions are being used for making additively manufactured final parts or component for applying in aerospace[22, 23], automotive[24], medical[4, 5], and military industries[6].

In recent time, AM has received huge interest from industry's perspective not only for prototyping, but also for serial production because of the improvement of production rate and raw materials used for additive manufacturing process. AM can set new standard of economic and technical production tool for automotive, aerospace and biomedical industries with excellent level of precision and enhanced technical performance [25-28]. Both stereo-lithography (STL) or Additive Manufacturing Format (AMF) is used as the digital representation of desired geometry for AM. This digital representation of AM opens huge level of opportunities and challenges for design engineers to create generative design for ensuring the compatibility with manufacturability[29].Generative design enables high complexity outcomes and low-cost fabrication at small production volumes, such as for example in the case of cost-effective design and fabrication of orthopaedic implants that mimic patient-specific geometry and mechanical properties.Additive manufacturing (AM) enables different type of engineering design structure with highly geometric complexity which offers us huge opportunities and challenges to optimize the design and processing parameter for the desired superior technical outcome than traditional manufacturing process[30].Additive manufacturing is an important production tool that facilitates the investigation of individual parameters such as porosity, pore size, shape and permeability, on the biological performance of synthetic bone grafts[31].

In comparison with conventional production techniques, AM offers combined technologies for building components in an additive and layer-by-layer design. These technologies can broadly be grouped into one of seven major classes based on the mechanism in which each layer is formed: photo-polymerization, extrusion, sheet lamination, beam deposition, direct write and printing, powder bed binder jet printing, and powder bed fusion [32]. Figure 2.1 shows the classification of different additive manufacturing techniques. It has been found from Fig 2.1 that additive manufacturing is broadly categorised as two parts, i.e. laser based additive manufacturing and non-laser based additive manufacturing. SLS, SLM, EBM are classified as powder bed fusion technology. LMD, LENS have been categorised under directed energy deposition category.

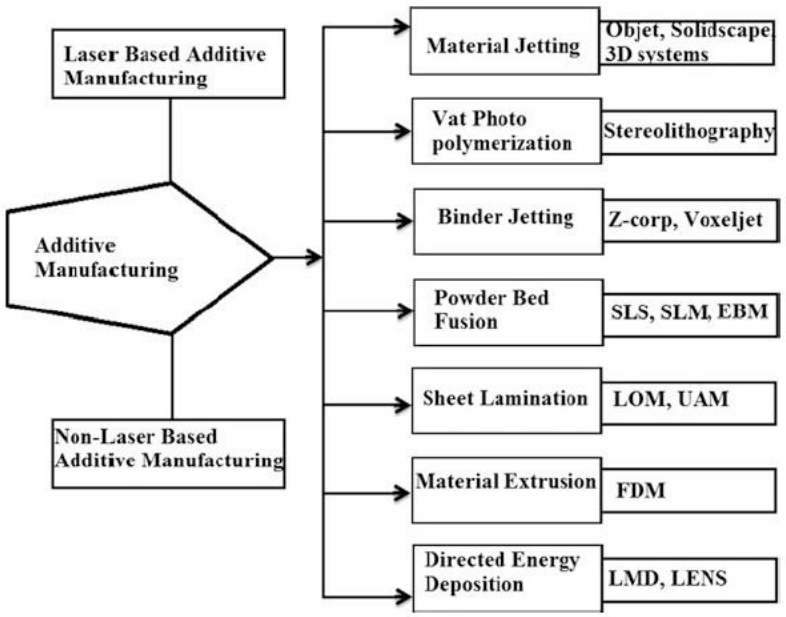

Figure 2. 1: Classification of additive manufacturing [33]

AM offers the unique capability to control the microstructure of a material to design mechanical properties for a specific application while building a complex part layer-by-layer. Therefore, real life application for AM requires the integrated knowledge between specific material, process optimization and design topology. Topology optimization plays crucial role in AM of

reducing cost with minimal mass allowing maximum stress under different load conditions [34-36]. Topology optimization is an applied technique which ensures the efficient designs with minimal a priori decisions. Because of the complexity and intricacy of the solutions obtained, topology optimization was often constrained to research and theoretical studies. Additive manufacturing, a rapidly evolving field, fills the gap between topology optimization and application. Additive manufacturing has minimal limitations on the shape and complexity of the design, and is currently evolving towards new materials, higher precision and larger build sizes. Simulation process is required for optimizing the processing parameters for required mechanical properties showing great structural efficacy.

2.3. Metal additive manufacture (MAM)

Metal additive manufacturing comprises of electron beam melting (EBM), selective laser sintering (SLS), selective laser melting (SLM), laser engineered net shaping (LENS), direct metal laser sintering (DMLS) and laser aided additive manufacturing (LAAM) process. With the advent of electron beam melting (EBM), selective laser sintering (SLS), selective laser melting (SLM), laser engineered net shaping (LENS), direct metal laser sintering (DMLS) and laser aided additive manufacturing (LAAM) process direct replication of metallic structures has become a reality. SLM and EBM both used different source of energy beam to fuse powder particles together on a layer-by-layer basis. SLM used the laser beam with tunable wavelength and EBM used electron beam. The main advantage of SLM/SLS process over EBM is that SLM/SLS can process polymers, ceramics and metal whereas EBM can process only conductive metals and limited feature size [37]. In recent time, metallic AM has received huge interest from industry's perspective not only for prototyping, but also for serial production because of the improvement of production rate and raw materials used for additive manufacturing process. In comparison with conventional production techniques, metallic

powder-bed AM technology offers a wide diversified freedom for its design space so that it enables the production of different parts with innovative design.

2.3.1. Selective Laser Melting (SLM)

Selective laser melting (SLM) is an additive manufacturing process that creates parts by scanning powdered materials using the thermal energy supplied by a focused and computer-controlled laser beam based on CAD Files[20, 26]. SLM is a complex multi-physics system of layer-wise material addition technique that allows the generation of complex 3D parts by selectively melting successive layers of metal powder on top of each other. Among different MAM technologies, selective laser melting (SLM) is a powder bed fusion technology which is capable of fabricating high complex geometric parts with enough robust mechanical properties. With reference to commercial MAM technologies, SLM is characterized by good repeatability, medium productivity and medium to [21].Despite the associated commercial opportunities, SLM is a highly dimensional process[38] that is subjective to complex geometries[39],complex multi-physics interactions[40], transient heat transfer paths[41],and material properties that are stochastic in nature and poorly documented [42].

SLM system often requires process optimization due to its inherent complexity and uncertainty. For laser based MAM, process optimisation is typically made with reference to the laser energy density, E; defined according to the laser power, *P*, scanning speed, *v*, hatch spacing, *h*, and layer thickness, *t* (Eq. (1)).

$$E = \frac{P}{v} * h * t \quad \text{.....(1)}$$

where, E: energy density (J/mm^3), P: laser power (W), v: laser scanning speed (mm/s), h: hatching distance (mm), t: layer thickness (mm).

Fig. 2.2 shows the schematic diagram of SLM process. The SLM system comprises of a fibre laser, galvanometer, F-theta lens, protective lens, powder re-coater, build specimen and build platform. A typical fibre laser which can operate up to 1 kW depending on the laser module

installed in the system. Galvanometer is used for controlling the beam focus and the movement of the beam is controlled by the F-theta lens. Normally a part is built by SLM process using a layer of powder with 20–100 μm thickness. The powder is carried and spread by the powder re-coater across the build table. The preheating temperature can be up to 200°C on build table. CAD file is used for defining the geometry of build parts and based on that the layer of powder is selectively melted. In SLM process, each layer of a part is built in two steps. At first the outer boundary of the part is built which is known as contouring and the powder within the contour is melted subsequently to complete one layer. This entire process is only completed once the desired three-dimensional part is entirely built based on the provided CAD geometry.

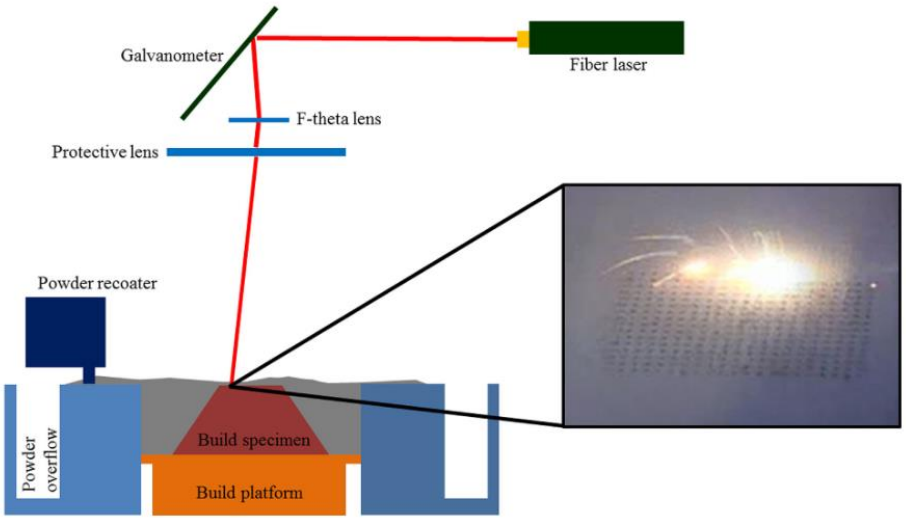

Figure 2.2: Schematic diagram of SLM-process [43, 44]

SLM process is also suitable for applying in orthopaedic and dental applications because of patient specific design, complex geometry and high aggregate price. Moreover, the manufacturing of multiple unique parts in a single production run enables mass customization. The SLM process was reported to be capable of fabricating implants of several pure titanium and titanium based alloys for implants such as Ti6Al7Nb[45], Ti-24Nb-4Zr-8Sn[44],Ni-Ti[46], Ti-13Nb-13Zr[47] other β titanium alloys[48] and most importantly Ti6Al4V[49, 50]. Recently, it was reported that SLM has the ability to fabricate porous bio-inert Ti6Al4V

structures with high control and reproducibility in terms of their morphological and mechanical properties[51] and showed excellent biocompatibility [52]. A group of Japanese researchers showed that SLM can be a great method of manufacturing porous titanium metal with a structure analogous to human cancellous bone using the optimum operating conditions[53]. Fig. 2.3 (a) represents a CT image which shows the trabecular bone structure of a man aged 53 years. In Fig. 2.3 (i) shows a porous titanium body manufactured by the assembly of multiple unit cells from Fig. 2.3 (a). Fig. 2.3 (b) shows a CT image of the cancellous bone of a 48-year-old female, and the porous structure of titanium mimicking the cancellous bone structure has been shown in Fig. 2.3(ii). Fig.2.3 (c) shows a hollow cubic unit cell and its stacking, while (iii) is a porous body produced from (c).

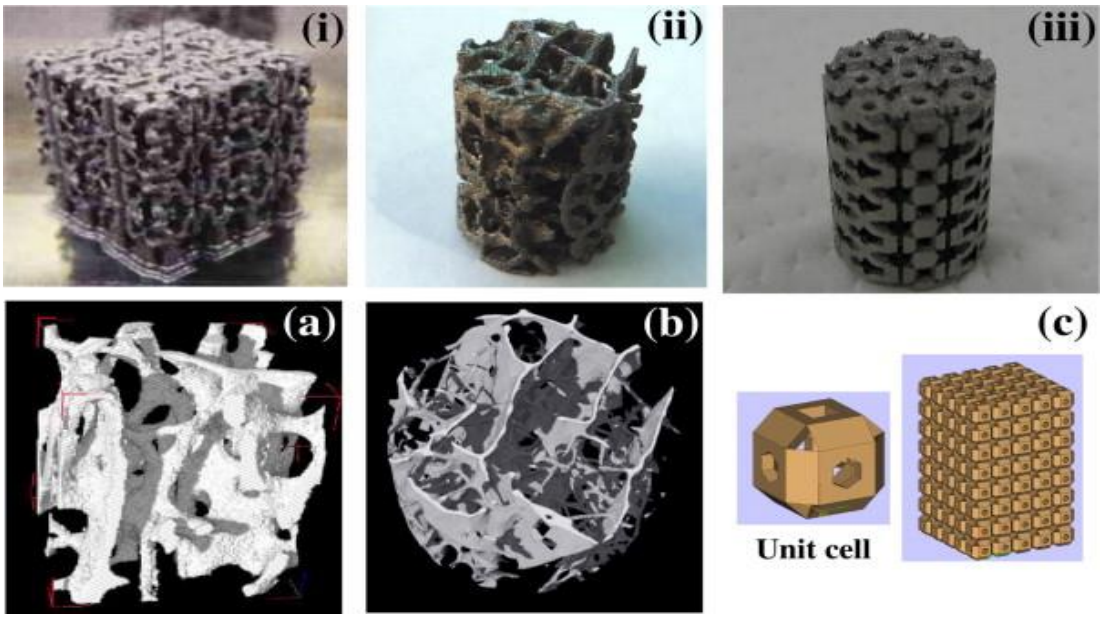

Figure 2.3: Titanium porous structure fabricated by SLM (i–iii) based on micro-CT images of human cancellous bones (a, b) and stacked hollow cubes (c). Specimen size: (a) 15 × 15 × 15 mm; (b, c) 6 mm diameter, 10 mm length. Notation: (ii) CBS; (iii) IPS[53].

2.3.2. Laser Metal Deposition (LMD)

Laser Metal Deposition (LMD) also formerly called laser cladding is a promising additive manufacturing(AM) technique which utilises laser heat source to melt a stream of powder feedstock[43, 54, 55] to build any complex near-net shape component. The technology was

advanced by the group of researchers from Sandia National Laboratories in US in nineties and the process was names Laser Engineered Net Shaping (LENS)[56]. This advanced laser metal deposition technology called LENS is now the most widely used LMD technology in the academia and in the industries. A unique feature of LMD is the inherent anisotropy in microstructure and resultant mechanical properties. Various studies have been conducted to evaluate the factors responsible for this anisotropy [57]. LMD can provide the modifications of chemical composition and produce a large number of small-scale samples [58, 59]. Fig. 2.4 shows the experimental set up of LMD process. In LMD, centre of coaxial nozzle is used to deliver high energy laser beam and then it is focused by a lens which is then applied to a substrate to repair it or build a new part based on the computer aided design (CAD). This laser energy beam generates a melt pool formation into which the powder feedstock is deposited. These complex phenomena of melt pool formation by LMD depends on powder attributes (composition, size distribution, shape, flow rate, etc.) and processing parameters like laser properties (power, type, spot size scan speed, etc.). In order to achieve desired microstructure and mechanical properties these parameters need to be effectively controlled. These parameters need to be effectively controlled to achieve powder consolidation and the desired microstructure and mechanical properties[60, 61] .

Argon/nitrogen/helium inert gas is normally flowed through the nozzle shown in Fig.2.4 not only delivers powder but also provides the shield from oxygen deposition. Three-dimensional component is produced by depositing consecutive layers additively one above the other. This is achieved by either moving the deposition head with respect to a stationary work piece, or moving the work piece with respect to a stationary head[62].

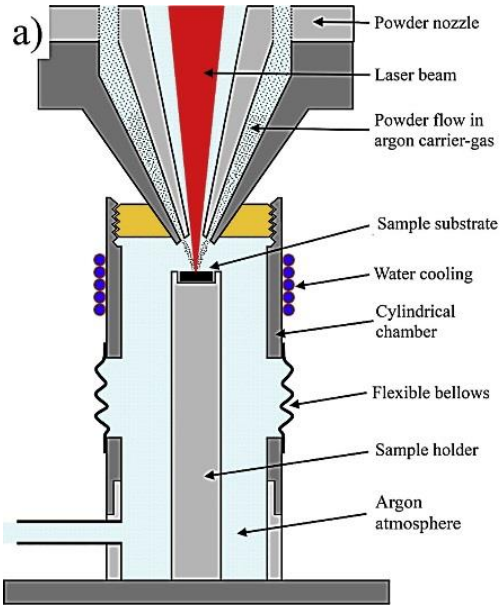

Figure 2.4: Experimental set up of LMD process[63]

LMD can manufacture a wide range of metallic alloys. Laser direct metal deposition (LDMD) is one of the few available AM techniques which is capable of producing a structure with graded porosity and/or composition from different biomaterials including, Ti–6Al–4V, titanium, and shape memory alloys and stainless steel[64]. It can generate implants with more flexible geometric verities than other AM techniques, however it is quite cumbersome process to predict the desired outcome from a combination of LDMD input parameters because of the complex nature of the process which involves with a lot of 'trial-and-error' method.

2.3.3. Electron Beam Melting (EBM)

Electron beam melting (EBM) is another metallic powder bed technology which uses high energy electron beam to induce fusion between metal powders[65-68]. This AM process shows its exceptional potentiality to make medical devices and industrial components via great shape control and strength to weight ratio[69]. Electron beam melting (EBM) is originally technology developed by Arcam AB in Sweden which is now commercially available with 60 systems globally. The minimum resolution, feature size and surface finish of an EBM process is

typically larger than for a SLM process. Fig. 2.5 shows the typical EBM system consists of an electron gun which is similar to an electron beam welding machine or an electron gun in a scanning electron microscope and the operating power is 60 KW to generate a focused beam of energy density above 100kW/cm^2. The beam focus is controlled by the electromagnetic lenses and the movement of the beam on the build table is controlled by deflection coils shown in Fig. 2.5[44]. A powder layer consisting of 100 µm thickness is spread over the table for building the part. The powder is supplied from two hoppers kept inside the build chamber. A moving rake fetches powder from both sides and spread over the table. The electron beams first pre-heats the powder layer with a higher scan speed, followed by melting the powder layer based on the geometry defined by the CAD file. In EBM, every layer of a part is built in two steps. The outer boundary of the part is built first which is referred as contouring and the powder within the contour is melted subsequently to complete one layer.

Figure 2.5:Schematic of EBM system. The system includes an electron beam system (electron gun assembly, electron beam focusing lens and deflection coils used to control the electron

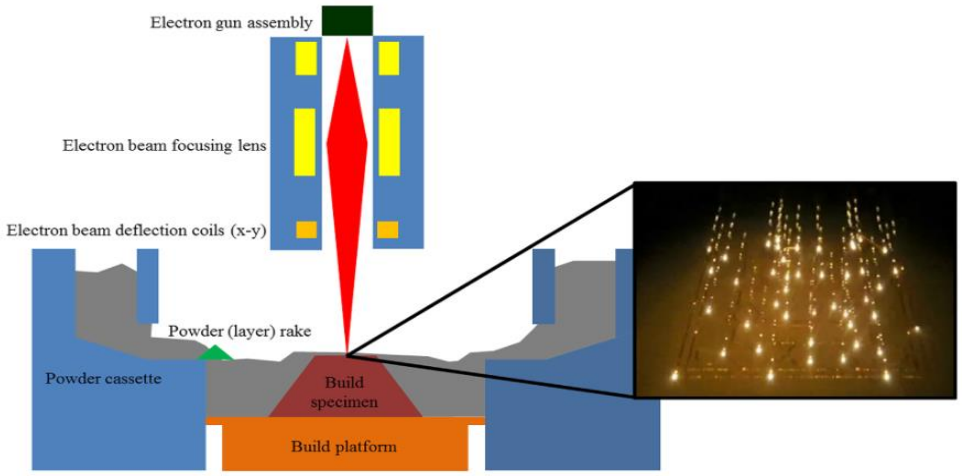

beam) and the mechanical system (movable powder rake and fixed powder cassettes). A view of electron beam scanning the powder bed is also shown[44].

EBM has been applied for producing different orthopaedic implants such as hip[70], knee, jaw[71], spinal fusion cages [72], and maxillofacial plates[70, 73]. EBM has widely been used for producing Ti-6Al-4V based implants with different lattice topology[50, 70]. A great variety of metallic alloys has been introduced in EBM technology because of the high energy density which can melt different alloy powders. Fig 2.6 demonstrates the feature of complex, patient-specific, functional orthopaedic implants manufactured by EBM which is not only mechanically compatible but also it can allow normal bone ingrowth and regrowth, vascularization and nutrient delivery. It has also been found from Fig.2.6 that EBM structure shows interconnected porous structure which is generally required for cellular penetration and vascular tissue growth.

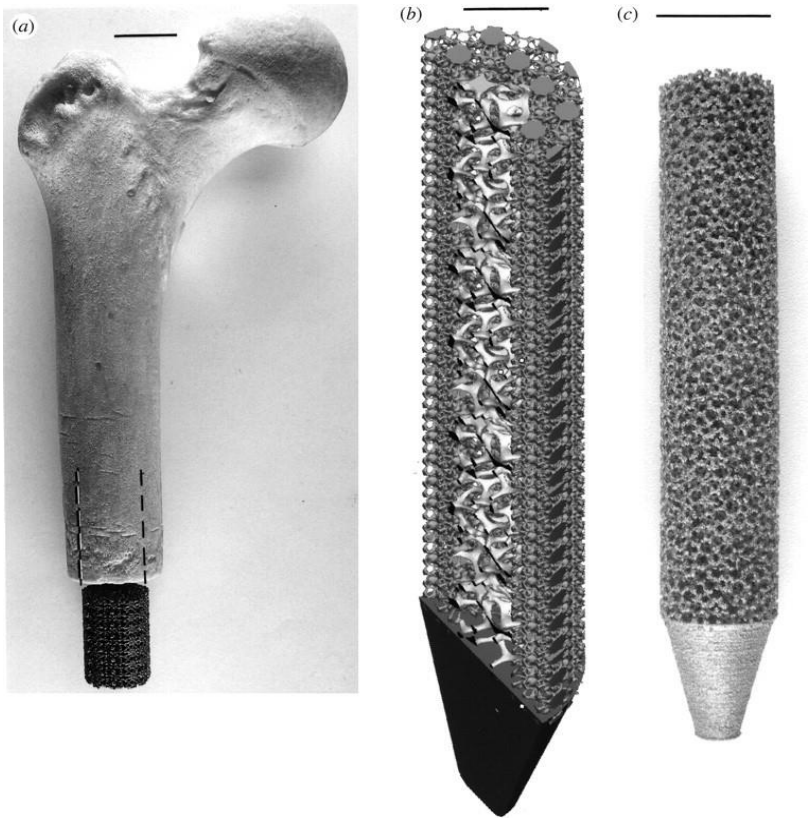

Figure 2.6: Functional mesh/mesh and mesh/foam bone shaft stem or rod device prototypes manufactured by EBM.(a) Femoral component with mesh/mesh rod section inset.(b) Femoral rod software model half-section (mesh/foam). (c) EBM-built prototype[74]

2.4. Titanium Based Alloy for Tissue Engineering and Orthopaedic Applications

Tissue engineering is a vast field which aims to develop biological substitutes for restoring, improving, maintaining tissue or organ functions utilizing the combined principles of engineering and life sciences[75]. It is clearly understood from its definition that it is a comprehensive multidisciplinary research. Therefore, integrating biology, biochemistry and clinical medicine with materials science, physics and engineering disciplines is imperative to achieve clinical applications[76].Among the vast field of tissue engineering, bone tissue engineering is a promising therapeutic technique to regenerate the bone tissue for faster healing in case of bone defects caused by traumatic bone injury, tumor resection, and osteitis[8]. In case of large bone defect, the tissue's endogenous regeneration is very much limited[77], so bone tissue engineering is essential for healing the defect zone. Bone tissue engineering is a complex and dynamic process which has the ability of proliferating, differentiating, forming matrix of osteo-progenitor cells along with the remodelling of the bone[78]. Implanting scaffolds into the defect zone in order to guide and stimulate bone formation is the most popular approach in the bone tissue engineering field. Scaffolds play a crucial role in bone tissue engineering, facilitating ingrowth of mineralized tissue into the porous network and mechanical support[79]. These scaffolds require the optimum pore size, shape and interconnected networks for facilitating nutrient and oxygen diffusion ensuring the desired bone growth into the defect zone[80]. Porous scaffolds made with biopolymers and bio-ceramics are very popular approach in the recent time in order to promote bone or tissue ingrowth into pores in the bone tissue engineering field[81]. Despite having good biocompatibility and relative faster degradation properties of these polymers and ceramics, they have the limitation in case of load bearing application in hard tissue engineering [82, 83]. This limits their application as a potential bone graft because of their soft and weak mechanical properties.

Figure 2.7 shows the representation of additively manufactured Porous scaffolds were used for compression tests and in vivo experiments and exhibited a height and diameter of 30 and 10mm, respectively (Fig. 3a). The microstructure, pore size and pore morphology of the fabricated porous Ti6Al4V alloy scaffolds were visualized using SEM (SU8220, HITACHI, Japan; imaging mode of low magnification; accelerating voltage of 3.0 kV; working distance of 8.7mm or 10.6mm) and analyzed by Image J 1.48 (National Institutes of Health; USA). The porosity of the samples was determined using the gravimetric method30

Figure 2.7: Additively manufactured Ti6Al4V scaffolds used for in-vivo experiment with a height and diameter of 30 and 10 mm (a) gross specimens at different time points (3 months, 6 months and 12 months) (b)[84].

Metals and alloys have a long history of application as bone implants [73, 85, 86]. Metal and metal alloys including titanium, tantalum, titanium-nickel, stainless steels, cobalt (Co) based alloys (CoCrMo) have been applied as potential bone graft because of their good mechanical properties [87-90]. However, implants made from some of these materials despite having good biocompatibility usually exhibit higher modulus of elasticity than the host bone which lead to stress shielding effect. Stress shielding effect is the primary reason for bone resorption and eventual failure of such implants [5]. Cortical bone (compact bone) has elastic moduli ranging from 3 to 30 GPa, while trabecular or cancellous bone has significantly lower elastic moduli of 0.02e2 GPa. Titanium alloys, particularly Ti-6Al-4V, are widely used as orthopaedic and dental implants because of their excellent biocompatibility, corrosion resistance, high strength to weight ratio, and modulus of elasticity relatively lower modulus of elasticity than cobalt(Co) based alloy(CoCrMo) and stainless steel.[91-94] Several techniques have been developed in order to introduce a degree of porosity in titanium and titanium based alloy scaffolds including combustion synthesis, solid state foaming by expansion of argon-filled pores, electron beam melting, polymeric sponge replication, selective laser melting process [95-97]. Fig.2.7 represents the repair of trabecular bone using porous Ti scaffold[98]. It has been found from this figure that the void in the trabecular region was created during the surgery with the drill which has been unable to regenerate without bone graft and the areas of incomplete bone regeneration observed below the scaffold. Bone histomorphometry was applied on to quantify the amount of bone ingrowth in scaffold and control groups. It has been found from Fig. 2.8 that the BV/TV was significantly higher (p = 0.01) in the scaffold group compared to the control group.

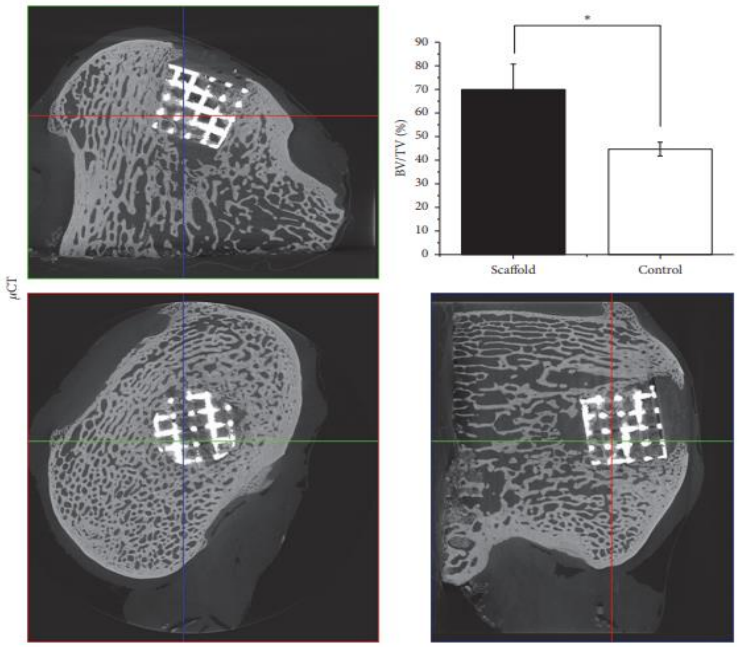

Figure 2.8: Bone ingrowth into Ti matrix. μCT images show bone formation within the Ti scaffold; $*$ shows significantly higher bone volume formation in the scaffold compared to control (p = 0.01)[98]

2.4.1. Power Bed Additive Manufacture of Titanium Based Implants

Powder bed additive manufacturing enables to manufacture any complex shaped titanium-based implants based on CAD design. SLM, EBM and LMD are the most popular metallic powder bed additive manufacturing technologies for generating complex design topology of titanium-based implant. In our research among different powder bed fusion technology SLM has been used because of fabricating porous, bio-inert Ti6Al4V structures with complex and reproducible morphological and mechanical properties [51, 99] yet retained their excellent biocompatibility[52]. In addition, SLM can create smaller feature size compared to competing AM technologies and its mechanical response is quite well understood[100]. Several reports show that porous Ti6Al4V structures can be very effective in terms of supporting cell growth and new bone formation due to the cytocompatibility of Ti6Al4V structures[53, 101-103]. Figure 2.9 shows addiitvely manufactured lattice structure of Ti6Al4V spinal implants consisting different topology for optimum bone growth. Fig. 2.9(a) shows the different spinal interbody case strucure manufactured by K2M, USA. Fig.2.9(b) and Fig.2.9(c) respectively

shows the spinal structure manufactured by 4WEB Medical, USA and EIT, Germany [104]. Fig. 2.10 shows the world's first additively manufactured mandible implanted by a group of surgeons in Belgium in 2012[9].

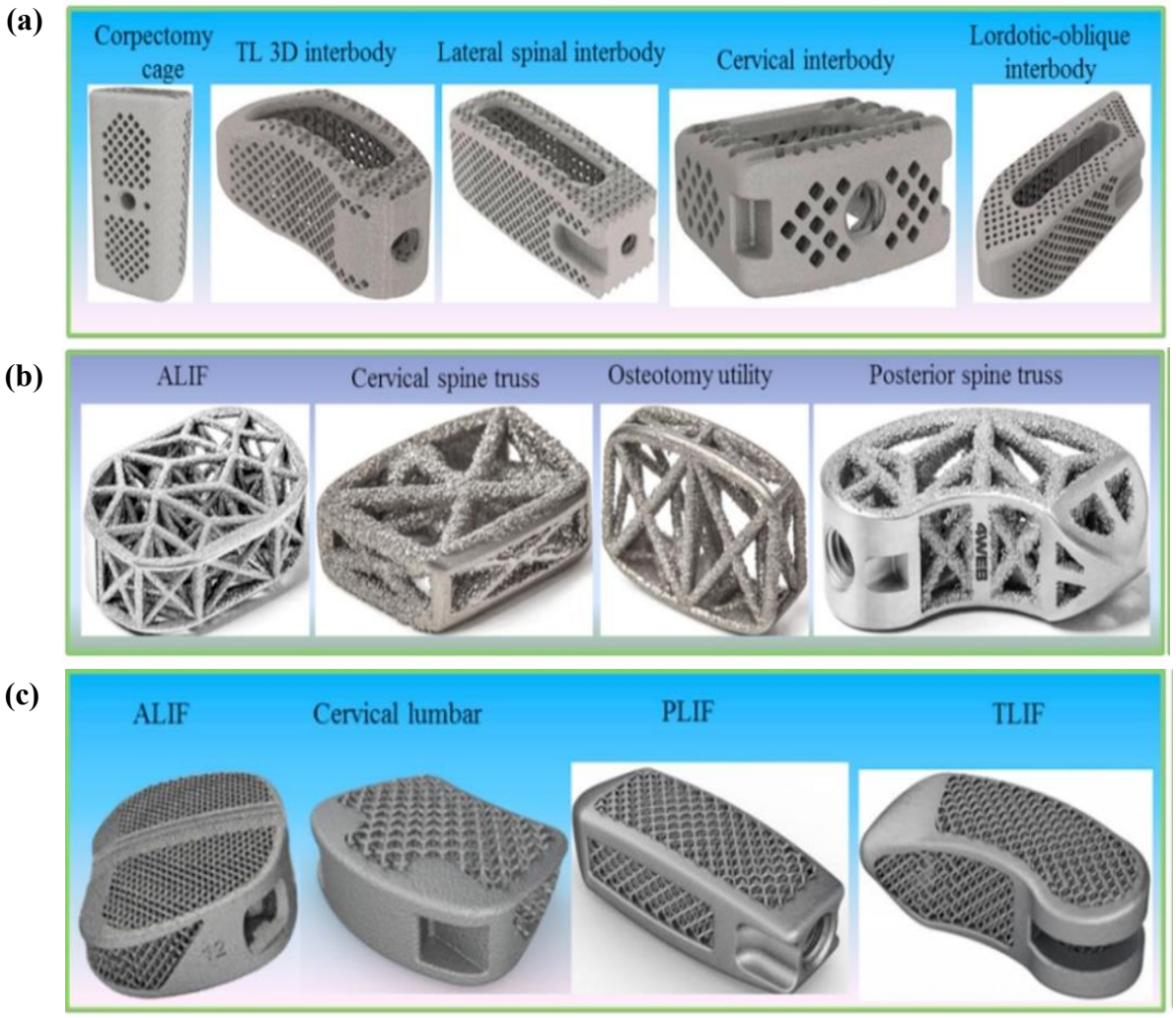

Figure 2.9: Examples of FDA-approved additively manufactured Ti-6Al-4V lattice implants, (a) By K2M, USA[105], (b) By 4WEB Medical, USA[104], (c) By EIT, Germany [104]

Figure 2.10: In Belgium Dr.Jules Poukens and his team implanted the world's 1st additively manufactured mandible in a patient in 2012[9].

2.5. The implant Interface

One of the biggest health related concerns across the world among the population is due to musculoskeletal disorders. From a statistics, it has been found that around 310,800 hip replacements were performed in US alone in 2010 at age between 45 and up[106]. Patients under 40 years have been also found receiving hip implants are anticipated to increase which indicates that shorter implant life is expected due to their higher activity lifestyle. There are several factors which are directly responsible for limiting life of metallic load-bearing implants such as poor osseointegration, stress shielding, or implant loosening. The term 'implant interface' is defined as the surface of the implant which gets direct contact with the host bone. When an implant is placed into the defect site, within nanoseconds there is formation of water molecule layer around it where implant surface is reported to play the most crucial role[107]. The term 'Osseointegration' is often used to explain about implant interface which is an ongoing process of formation and adaptation to function and repair, which takes place due to osteoblastic and osteoclastic activity of bone, also known as coupling[108, 109]. Several factors of implant surface are directly related to osseointegration. Among different factors surface roughness and surface topography are the key parameter which directly influence osseointegration[110, 111]. The size and number of gap between implant with the host tissue can be effectively reduced by increasing bone-implant contact. Small micromotion over the

time with implant use can help to progress implant failure. Aseptic loosening which is one of the primary reasons of implant failure can be occurred due to creating polymeric and metallic wear particles into bone-implant interface. In addition, cells in bone-implant interface can experience inflammatory state due wear particles which are easily phagocytosed by macrophages, in which they secrete a series of cytokines[112]. These cytokines, such as tumor necrosis factor a (TNF-a), can lead to the generation of osteoclasts and the local resorption of bone tissue, effectively forming and enlarging gaps at the prosthetic tissue interface [23].

2.6. Effect of Surface Properties on Titanium Based implants for Bone Growth and Biofilm Formation

Several studies show that bone growth and osseo-integration are highly dependent on implant surface topography, surface roughness, surface chemistry[113-115]. The final implant surface properties manufactured by additive manufacturing can be greatly influenced by different process parameters such as laser power, scanning speed, hatch spacing, layer thickness, powder bed temperature [116].

Even though rough surfaces have been reported as beneficiary for bone integration [117, 118] but there is also existing controversy in the literature based on optimal roughness for cell attachment. For example, some studies suggest that smooth surfaces favour cell attachment (Ra<1 μm)[119, 120]; whereas some other studies show that higher roughness values (Ra=3-5μm) even more favours cell attachment. It has also been reported that implant surface with hierachical surfaces with nano/submicron roughness are more favourable for cell growth and fraction. There are several features which can be introduced simultaneously by increased surface roughness such as surface area, improved cell attachment and migration. Extensive studies have been carried out in order to understand the role of implant surface roughness with cellular attachment, proliferation and differentiation [119]. Most of the literature investigated the traditionally manufactured titanium implant surface properties and their relationship with

cell attachment and biofilm formation. However, implants manufactured by additive manufacturing and their relationship with the change of their design parameter has not been explored thoroughly. In addition, the relationship between the cell attachment and biofilm formation with these additively manufactured surface properties is fairly unknown. Therefore, thoroughly investigating the surface profile properties, surface morphology, and surface wettability of additively manufactured part is highly essential to design the clinically desired successful implant.

Staphylococcus aureus (*S. aureus*) is a very common grown bacteria on implant surface; these bacteria are capable of forming polysaccharide on implant surface which is quite difficult to control with conventional antibiotics[121, 122]. Implant associated infections are directly corelated with loosening which often requires revision surgery. As a result, it causes longer hospital-stay for patients. It also brings significant cost to the patients and higher mortality rates.[123]

There has been extensive research effort has been carried out in terms of developing anti-biofilm implant surface by several means such as adding antimicrobial agent to the implant surface by grafting, coating, or immobilising. Much research effort has therefore been focused on developing anti-biofilm implant surfaces, which are typically achieved by adding an antimicrobial agent, such as silver compounds, to the surfaces through secondary processes such as coating, immobilising, or grafting [124-129]. Even though some of these techniques are suitable for both additively manufactured titanium and traditionally manufactured titanium implants but there are some limitations of these approaches which is a great concern among orthopaedic research community. Delamination of antibacterial coating from metallic surface can cause off target arising from the toxicity or carcinogenicity of the antimicrobial agents[130, 131], associated high cost, and often slow and cumbersome processing [132]. In addition, the

concern for bacterial resistance against traditional antibacterial agents is rising globally which poses a great medical threat.

To address this problem being motivated by the need for a simple approach, we show for the first time to control biofilm formation on additively manufactured titanium implant surface without applying any antibacterial agent or surface modification approach. Instead, the surface topographies of selective laser melted Ti6Al4V parts were controlled by adjusting the build inclination angle which is the design parameter of SLM where no other process parameter was altered. It has been shown that both chemical and surface topographical modification can inhibit biofilm formation[133, 134]. However, the control of biofilm formation just from the inherent processing stage from topographical feature changing without using secondary chemical agent receiving huge interest[135, 136]. Mechanisms of manipulating the surface topography have been achieved; both bio-inspired[132, 137], nature inspired[136], or by introducing both micro and nano-scale surface features[138]. Here, we showed that single one step method changing the design build angle of Ti6Al4V parts, in-situ SLM manufacturing process retain the desirable surface chemistry and mechanical strength without affecting mammalian cell viability and attachment. Further analysis however, revealed the inclination angle allowed markedly significant control over the surface topography, area, roughness, wettability, and surface energy; these differences enable significant control over the level of *Staphylococcus aureus* (*S.aureus*) biofilm formation.

2.7. Conclusions

A literature review of different powder bed metallic additive manufacturing techniques has been applied in terms of developing next generation customized orthopaedic implants. Substantial developments have been made in last one-decade in terms of developing metallic implants including its design, manufacture and surface modifications for successful clinical outcome.

The literature concludes the following:

1. Additive manufacturing (AM) enables to design any complex structure with extreme geometric fidelity and superior mechanical properties than traditional manufacturing process.

2. Metallic powder bed additive manufacturing technique enables to manufacture patient-specific orthopaedic implants with superior mechanical properties and complex geometric topology.

3. In comparison with other metallic additive manufacturing techniques SLM is characterized by good repeatability, high surface quality and medium productivity. The main advantage of SLM process over other additive manufacturing(EBM) technique is that SLM has the ability to process polymers, ceramics and metal whereas EBM can process only conductive metals[37].

4. Titanium based alloy is the most popular metallic alloy for orthopaedic application because of its some exceptional properties than other metallic alloy.

5.Additive manufacturing techniques enable to develop Ti6Al4V implant with highly complex geometry for orthopaedic application with great clinical success. However, the surface properties of additively manufactured titanium implants can be altered based on its design parameters. Implants surface properties highly influence the cellular attachment and biofilm formation.

6. Several studies came up with different outcomes in terms of the relationship between surface roughness and cellular attachment. Some studies suggest that lower surface roughness creates favourable environment for cell attachment (Ra<1 μm)[119, 120]; whereas some other studies show that higher roughness values (Ra=3-5μm) even more favours cell attachment. Some literature also showed that nano/submicron rough implant surface showing hierarchical structure are more favourable for cell growth and fraction.

7. Extensive research has been carried out to develop anti-biofilm implant surface by different approaches such as coating, grafting, immobilising antibacterial agent. Some research groups showed that the manipulation of surface topography by nature inspired[136] bio-inspired[132, 137], or by introducing both micro and nano-scale surface features[138] can be effective way to prevent biofilm. However, limited research has been carried out in terms of manipulating additively manufactured titanium implants for prevent against implant associated infection.

Chapter Three: Materials and Methods

3.1 Chapter Overview

This chapter describes the materials and methods section that have been used to characterize different build inclined Ti6Al4V implants manufactured by selective melting process and observe the biological response on these Ti6Al4V implants. This chapter has been divided into eight key sections. Section 3.1 outlines the chapter overview, introduction. Section 3.2 discusses the details of the material that has been used in this PhD project. Section 3.3 illustrates the details of the fabrication of different inclined Ti6Al4V samples by SLM. Section 3.4 explains the overall experimental techniques used for characterization of Ti6Al4V implant surfaces. Section 3.5 highlights the in-vitro response of Ti6Al4V samples by Chinese Hamster Ovarian and Rat Primary Bone cell. Section 3.6 describes about *Staphylococcus aureus* biofilm formation behaviour on different build inclined Ti6Al4V samples.

3.2 Materials

3.2.1. Ti6Al4V powder

Ti6Al4V powder with 25-45 µm size (ASTM Grade 23, ELI, TLS Technik GmbH & Co., BitterfeldWolfen, Germany), size, was used to manufacture different build inclined SLM implants. The composition of Ti6Al4V powder is presented in Table 3.1.

Chemical composition (wt.%)							
Ti	Al	V	Fe	C	N	O	H
balanced	6.47	4.08	0.17	0.008	0.009	0.1	0.002

Table 3.1: The chemical composition of ELI Ti6Al4V powder.

3.3. Sample Preparation for Different Inclined Support Free Ti6Al4V Implants from 5 to 90 degrees with 5 Degrees Interval

Inclination samples (thickness =0.5 mm, length=5 mm, depth=2.5 mm) were fabricated by selective laser melting (SLM) with a SLM250HL machine (SLM Solutions, Germany) with a variable power 400 W fibre laser. The SLM powder was titanium alloy Ti-6Al-4V, with average particle size of approximately 40 μm. Test specimens were manufactured with the following process parameters: laser power, P=100W, scanning speed, v=375mm/s, layer thickness, t=30 μm, hatch spacing, h=0.12 mm and focal offset, f=0 mm. These parameters correspond to: volumetric energy density, E_v= 68.5 J/ mm^3 where $E_v = P/vht$ and provide high geometric quality with fully dense structure. These parameters were used in the manufacture of implants with inclination angles of 0 to 90 degrees. The support structures were removed from the struts using plyer and struts were cleaned using standard cleaning methodology of sequential sonication in acetone, methanol and isopropanol and dried under a steady flow of nitrogen gas.

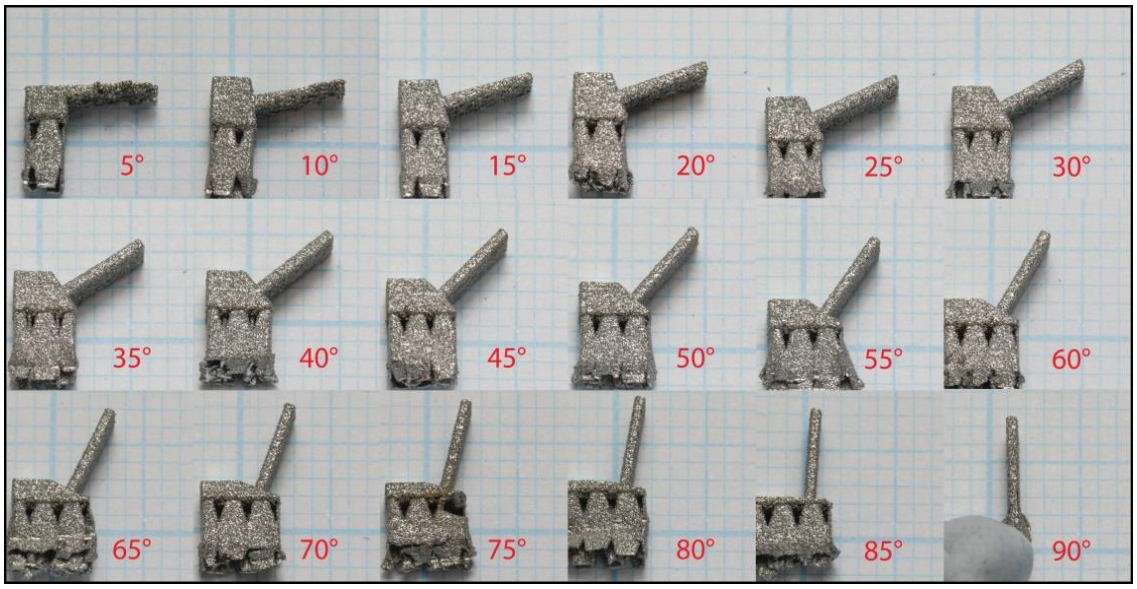

Figure 3.1: Optical view of different inclined support-free Ti6Al4V SLM parts varying from 0 to 90 degrees

3.3.1. Sample preparation for Different Inclined (0, 10, 45, & 90 degrees) Ti6Al4V Samples with Support Structure

Inclination samples (10 x 10 x 2 mm^3) were fabricated by selective laser melting (SLM) with a SLM250HL machine (SLM Solutions, Germany) shown in Figure 3.2 based on CAD geometry (Fig. 3.3) with a variable power 400 W fibre laser. The SLM powder was titanium alloy Ti-6Al-4V, with average particle size of approximately 40 μm. Test specimens were manufactured with the following process parameters: laser power, P=100 W, scanning speed, v=375 mm/s, layer thickness, t=30 μm, hatch spacing, h=0.12 mm and focal offset, f=0 mm.

Figure 3.2: SLM250HL machine (SLM Solutions, Germany)

These parameters correspond to: volumetric energy density, E_v= 68.5 J/ mm^3 where $E_v = P/vht$ and provide high geometric quality with fully dense structure. These parameters were used in the manufacture of implants with inclination angles of 0, 45, and 90 degrees. Support structures were removed from the struts and struts were cleaned using standard cleaning methodology of sequential sonication in acetone, methanol and isopropanol and dried under a steady flow of nitrogen gas.

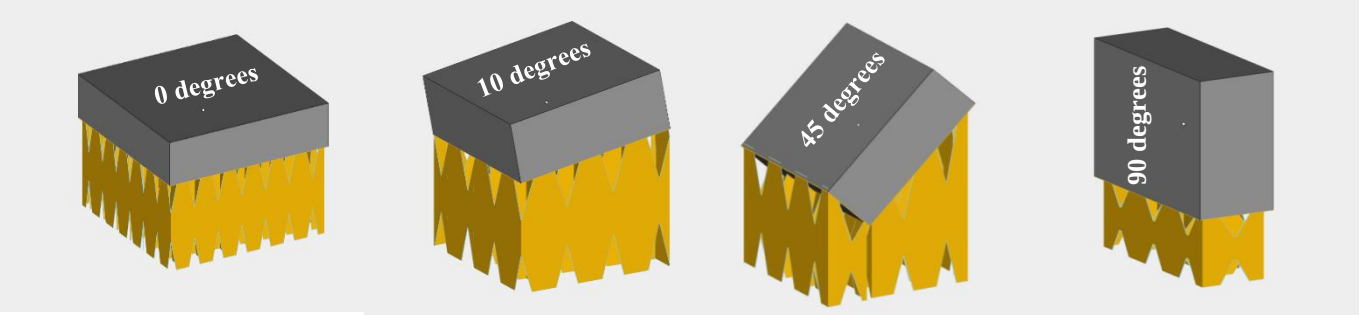

Figure 3.3:CAD design of inclined support-free Ti6Al4V SLM parts varying from 0 to 90 degrees

3.3.2. Cylindrical Strut Inclined (30, 45, & 90 degrees) Ti6Al4V Samples with Support Structure

Struts are cylindrical in shape with 10 mm length with 30, 60, & 90 degrees inclination angle with 0.2, 0.6, and 1.0 mm diameter manufactured by selective laser melting (SLM) with a SLM250HL machine (SLM Solutions, Germany) with a variable power 400 W fibre laser. The SLM powder was titanium alloy Ti-6Al-4V, with average particle size of approximately 40 µm. Test specimens were manufactured with the following process parameters: laser power, P=100W, scanning speed, v=375mm/s, layer thickness, t=30 µm, hatch spacing, h=0.12 mm and focal offset, f=0 mm. These parameters correspond to: volumetric energy density, E_V= 68.5 J/mm^3, where $= P/vht$ and provide high geometric quality with fully dense structure. These parameters were used in the manufacture of implants with inclination angles of 0, 45 and 90 degrees. Support structures were removed from the struts and struts were cleaned using standard cleaning methodology of sequential sonication in acetone, methanol and isopropanol and dried under a steady flow of nitrogen gas.

3.4. Characterization

3.4.1. CT scan

The SLM built inclined surfaces at different angles were analysed using General Electric Phoenix v|tome|x s 240 X-ray Computed Tomography (CT). Key feature of interest is the surface finish of the parts. The CT scanned parts were of 10 x10 x2.0 mm³ and the CT scans

were performed using 190 KV and 50 μA for X-ray generation, including beam filters of 1 mm tin and 0.1mm copper, at a resolution of 9 μm. To reduce the beam hardening effect, two copper filters of 0.1 mm in thickness were used which block the low energy beams. The projected X-ray images were acquired at 333ms per image, with 2000 images in stepwise rotation of the sample.

3.4.2. Micro-CT

High-resolution micro-CT (Bruker Skyscan 1275 Micro CT) uses multiple angular views and provides information on how much X-ray absorption occurs within each cubic voxel element of the scanned volume. Image data are acquired, reconstructed, and analysed using the Skyscan software (Skyscan 1076, Antwerp, Belgium) which displays the data as 3D reconstructed SLM samples images.

Micro-CT scanning was repeated 5 times. Data was analysed using Gwyddion image processing software(Department of Nanometrology, Czech Metrology Institute).Internal pore defects from SLM built inclined struts at different angles were examined using Micro-Computed Tomography (μCT) (Bruker 1275) shown in Fig. 3.4 where a voltage source of 100 kV and a current source of 100 μA were used. A 1 mm Aluminium (Al) filter was used to minimize beam hardening effects whilst conserving optimal attenuations. Furthermore, scanning results were improved utilizing a pixel size of 7 μm covering most of the strut specimen's length of 10 mm. For μCT reconstruction, post-processing procedures were used to further minimize imaging noises such as ring artefacts and beam hardening effects. Scanning parameters are listed in Table 3.2.

Figure 3.4: Micro-Computed Tomography (μCT) (Bruker 1275)

For preparing reconstructed models for analysis, a lower grey threshold (95) and an upper grey threshold (255) were used to define regions of air and solid material, respectively. A despeckling method was further implemented to exclude unnecessary white speckles surrounding the strut specimens. For consistency, margins of 0.5 mm were removed from bottom and top section of each strut specimens to allow strut porosity comparison.

Parameter	Value
Voltage source (kV)	100
Current source (μA)	100
Filter	1 mm Al
Pixel size (μm)	7
Rotation step (deg)	0.2
Frame averaging	2

Table 3.2: μCT scanning and reconstruction parameters

3.4.3. Surface Profile Analysis

Digital Microscope VHX-500 (Keyence, Japan) was used for optical photos, 2D profile and 3D profile analysis.

3.4.4. Surface Roughness Analysis

Roughness was assessed using a XP-2 Stylus Profiler (Ambios Technology, Inc,USA) shown in Fig. 3.5 of 3D scanning at a force 1.0 mg, scan speed of 50 µm/s with X scan size 1000 µm, Y scan size 200 µm with 5 traces having 50 µm Y spacing. Each sample was repeated 5 times. Data was analysed using Gwyddion image processing software. Tencor profilometer was also used to measure the average surface roughness of the sample.

Figure 3. 5: XP-2 Stylus Profiler (Ambios Technology, Inc, USA)

3.4.5. Surface Wettability Analysis

Contact angle instrument (Data Physics OCA20) was used to measure the contact angle on different inclined Ti6Al4V samples [177]. The 2µL drop was used for each measurement. A droplet of 2µL was deposited by a syringe which was positioned above the sample surface. The measurement was done once the stable value was achieved. A high-resolution camera was used to capture the image from the side view. The image was then analysed using image analysis

software SCA software, USA). Measurements were done on various areas of the samples to confirm the uniformity of the surface.

3.4.6. Surface Morphology by SEM

SEM micrographs were acquired using a scanning electron microscope (Philips XL30 SEM, Japan) shown in Fig.3.6(a). Topographical imaging of samples was performed at an acceleration voltage of 30 KV with spot size 5. FEI Quanta 200 ESEM (2002) shown in Fig.3.6(b) was also used to compare the morphology of different inclined Ti6Al4V samples manufactured by selective laser melting. Samples were mounted on an aluminium stub using carbon tape to attach firmly during imaging so that it cannot move during SEM scanning. Constant acceleration voltage, spot size and magnification were maintained before collecting the images.

(a) (b)

Figure 3.6: (a) Philips XL30 SEM, Japan and FEI Quanta 200 ESEM (2002)

3.4.7. EDX Analysis

EDX analysis was performed with 30 KV accelerating voltage applying primary X-max type detector model 66868-X020 for 2048 channels. FEI Quanta 200 ESEM (2002) with Oxford X-MaxN 20 EDXS detector (2014) was used to analyse the elemental analysis of SLM Ti6Al4V surfaces. 5 KV to 15 KV was applied to determine the EDX spectra. The scanning was continued until a stable value was achieved. Each EDX mapping procedure was performed up

to 30 minutes on each sample to identify the elemental composition of the micro-level thickness of the surface. The line mapping continued until a stable value was achieved. Each sample was repeated 5 times at different scanning areas for better accuracy in results. The Aztec software (Oxford Instruments,UK) was used to analyse the EDX data.

3.4.8. Surface free energy determination

The total apparent surface free energy values were calculated applying Owens-Wendt (O-W) and Neumann Equation of State (Eq.State) using appropriate equations[139, 140]. The surface free energy components were obtained using a contact angle instrument (Data Physics OCA20).

3.4.9. Phase identification – X-ray diffraction (XRD)

Phase identification by X-ray diffraction (XRD) shown in Fig.3.7 was performed on the cross section at the height of 5 mm (middle) of each selected Ti–6Al–4V cube using a X-ray diffractometer (Cu K_{α}; Bruker D4 ENDEAVOR with Lynx-Eye PSD), operated at 30 kV and 35 mA with a step size of 0.02° and a dwelling time of 1 s per step.

Figure 3.7: Cu K_{α}; Bruker D4 ENDEAVOR with Lynx-Eye PSD

3.4.10. Chemical Composition – X-ray Photon Spectroscopy

Analysis of the samples was performed by XPS (Thermo- Fisher K-Alpha, USA) shown in Fig.3.8, using an Mg Kα radiation source at a power of 300 W. The spot size of analysis was 400 µm. Sample scanning was performed using the flood gun to compensate for charging and auto height to determine optimal distance between the X-ray beam and the sample. In a constant analyser energy mode, survey spectra were collected at a pass energy of 50 eV.

Figure 3.8: XPS (Thermo- Fisher K-Alpha, USA)

The XPS binding energy (BE) values from high-resolution scans of elemental signals (pass energy 50 eV) were not charge-corrected with respect to that of adventitious carbon at 284. eV due to scanning being undertaken using the flood gun. In particularly, high-resolution XPS spectra were collected for the key elements carbon, oxygen and titanium identified from the survey spectra. High resolution scanning was undertaken with a step size of 0.1 eV and a dwell time of 50 ms. Depth profiles were obtained by sputtering the specimen at a rate of 1.35 Å/s using a 3 K eV argon ion gun. The relative intensity of the detected elements was plotted against binding energy and the chemical composition of the surface was characterised. Peak deconvolution was performed using Gaussian-Lorentzian curves to obtain the chemical states

of the elements present in the surface. Avantage 5.52 Chemical Profile data system (Thermo Fisher Scientific, USA) was used for data acquisition and processing. Statistical analysis of the XPS results was performed by analysing three areas of each 0, 45, and 90 degrees sample.

3.5. Cellular Response

3.5.1. Chinese Ovarian Hamster Cells expressing GFP Cell Viability Assay

For MTS assay, approximately $4*10^4$ cell/cm^2 CHO cells were seeded on SLM fabricated Ti6Al4V plates of 10*10 mm^2 size in a 24-well plate. Chinese Ovarian Hamster Cells expressing GFP (CHO: ATCC CCL-061, kindly provided by T.Himton, CSRIO) were grown in MEMα modification. The media was supplemented with 10% Fetal Bovine Serum, and 1% penicillin and streptomycin. Cells were grown at 37^0 C with 5% CO_2.The plate was incubated for 24, 72, and 96 hrs at 37^0 C. Then, 200 µL of [3-(4, 5-dimethylthiazol-2-yl)-5-(3-carboxymethoxyphenyl)-2-(4-sulfophenyl)-2H-tetrazolium, inner salt; MTS(a)] (Promega, Cell Tilter96) aqueous solution was added to the wells and the plate was incubated for additional 3 hours. 100µL medium of each well was transferred to a 96-well plate, and absorbance at 490nm was recorded using a plate reader (Spectramax paradism-molecular device, USA).

3.5.2. Cell Morphology Analysis

CHO-GHP cells were seeded onto the Ti6Al4V SLM plates at a concentration of $4*10^4$cells/cm^2. After 24 and 72 hours of incubation at 37^0C, the samples were rinsed with PBS twice and fixed in 4% paraformaldehyde (Sigma-Aldrich) for 15 min at room temperature. The samples were then rinsed with PBS twice. The cells were visualized with a confocal fluorescent microscope (N-Storm SuperResolution, Nikon) using GFP filter.

Cell morphology and attachment was also studied using FEI Quanta 200 ESEM (2002), USA. The cells were seeded on Ti6Al4V struts similar to aforementioned methods. After 24 hrs of

incubation, the samples were fixed with 2.5% v/v glutaraldehyde, pH 7.3, for 30 mins at room temperature and were then rinsed three times with PBS. Fixed specimens were then dehydrated through a series of 50%, 70%, 90%, 95% and 100% ethanol and were incubated for 10 min between each change. The specimens were then critical point-dried (Denton Vacuum, Moorestown, NJ, USA) and gold-coated in a SC500 Bio-Rad sputter coater (Bio-Rad) with 20 nm thickness before examination using an FEI Quanta 200 scanning electron microscope (FEI, Hillsboro, OR, USA).

3.5.3. Visualization of F-actin

F-actin was stained by rhodamine phalloidin to assess the cytoskeletal organization of CHO-GHP cells on the Ti6Al4V struts of all three inclination angles (0, 45 and 90 degrees). The cells were seeded at the same density as in MTS assay experiments. After 72 hrs of incubation, the samples were rinsed twice using PBS and then fixed by 4% formaldehyde solution for 15 min at room temperature and after that washed with PBS three times. The fixed cells were further permeabilized in 1% Triton X-100 for 15 mins before rinsed with PBS three times. 5µL rhodamine phalloidin working solution (Cytoskeleton Inc., USA), 100uL DAPI, 100 µL PBS were added to the samples at room temperature in dark for 15 min. After a thorough washing with PBS, cells on samples were visualized with a confocal fluorescent microscope (N-Storm SuperResolution, Nikon) using Cy5 and DAPI filters.

Matlab Simulation for Cell Type Counting and Dimension Measurement

The code was developed on Matlab R2014b software (Mathworks, USA) and applied for counting the cell type and dimension measurement.

3.5.4. *In-vitro* assay by Rat Calvariae Primary Osteoblasts

The cell densities of rat calvariae primary osteoblasts (OBs) (ROst-583, Lonza, Walkersville) grown on the surface of cylindrical strut with 30, 60, 90 degree inclined with 0.2, 0.6, and 1.0

mm diameter were determined using fluorescence microscopy and an MTS assay (CellTiter 96 Aqueous One Solution (Promega) according to the manufacturer's suggested protocol). OB cells were selected as they are bone-forming cells. These cells are particularly important to determine the osseointegration with the samples for orthopaedic applications. Prior to cell seeding, all of the samples were autoclaved to ensure that surfaces were sterile. For fluorescence microscopy, the samples were placed into a 24-well plate and seeded with OB cells in DMEM with 4.5 g/L glucose (Lonza No. 12-604F) supplemented with the rat MSCGM SingleQuots kit (Lonza No. 00192820). The rat MSCGMTM SingleQuots kit contains 50 mL of FBS (10% final concentration in media), Lglutamine, and GA-1000. The rMSC osteogenic SingleQuots kit contains 20 mL of FBS (10% final concentration in media), Lglutamine, GA-1000, ascorbate, dexamethasone, and β-glycerophosphate (all obtained from Lonza) at a density of 5000 cells/cm^2. The well plate was incubated for 3 days at a temperature of 37 °C under 5% CO2. After incubation, cells were rinsed with phosphate-buffered saline (PBS). Then, paraformaldehyde was applied for 30 min to fix the cells. The cells were permeabilized and blocked with 0.3% Triton X-100 and 1% BSA, respectively, and were washed three times with PBS. The actin filaments were then stained with Alexa Fluor 594 Phalloidin (1:40 dilution, Thermo Fisher Scientific, Scoresby, VIC, Australia) and incubated for 2 h at room temperature. Then, 1 μL of 300 nM 4′,6-diamidino-2-phenylindole (DAPI, dihydrochloride) (Thermo Fisher Scientific) was added to the cells for 5 min to stain the nucleus. The samples were washed with PBS and stored with 1 mL of PBS at 4 °C for fluorescent microscopy imaging (Olympus confocal microscope FV1200).

3.5.5. *In vitro* Hemocompatibility Evaluation

The whole human blood in hemocompatibility tests was obtained from Australian Red Cross Blood Service in agreement with Queensland University of Technology (approval NO. 18-03QLD-04).

3.6. *Staphylococcus aureus* biofilm formation

Staphylococcus aureus (*S. aureus*) ATCC 25923 was purchased from In Vitro Technologies (Noble Park, VIC, Australia). *S. aureus* was streaked on tryptone soya agar (TSA) plates and incubated at 37°C overnight. A single colony was selected using a disposable loop and mixed into 10 mL of tryptone soya broth (TSB) in a centrifuge tube. The tube was placed in a shaking incubator at 200 rpm and 37°C overnight. The bacteria solution was diluted to 10^6 cfu/mL with TSB for seeding on titanium substrates. The 3D printed titanium substrates (10, 45, and 90 degrees build inclination) were placed in each well of a 24-well plate. 1 mL of bacterial solution was added to each well and the plate was incubated at 37°C. After 24 hr, the samples were removed and placed into another 24-well plate with 1 mL of fresh TSB in each well. This bacterial growth on inclined samples were done by our collaborator from RMIT named Dr. Nhiem Tran. The samples were incubated for another 24 hr before they were prepared for SEM analysis, fluorescent confocal microscopy imaging, and a crystal violet assay.

For SEM analysis, the substrates were washed with PBS three times to remove non-adherent bacteria. 500 µL of a 4% formaldehyde solution was then added to each well to fix the bacteria. The plate was left for 15 min at room temperature before formaldehyde was removed and the samples were rinsed with PBS twice. The samples were then dehydrated by submerged in a series of ethanol solutions with increasing alcohol content (50%, 70%, 90%, 100%, 100%, 100%). The samples were then dried and coated with gold by gold sputter for SEM (FEI Quanta 200 ESEM) observation.

For fluorescent confocal microscopy analysis, the biofilm samples were also rinsed with PBS three times to remove non-adherent bacteria and were fixed with 4% formaldehyde solution for 15 min. The samples were rinsed with PBS and added with 500 µL of Triton X-100 solution to enhance the permeability of the cell membrane for subsequent fluorescent staining. Triton X-100 solution was removed after 15 min and the samples were rinsed with PBS twice before

500 µL of blocking solution containing 1% bovine serum albumin (BSA) was added to each sample to prevent non-specific binding of the dye. After 30 minutes, BSA was removed and the samples were rinsed with PBS. 300 µL of nucleus dye Hoechst 33258 (10 µg/mL) was added to each sample. The substrates were covered at room temperature for 15 min before finally rinsed with PBS twice to remove the excess dye. The samples were kept in PBS and at 4^{o}C until examined by using a confocal fluorescent microscope (Olympus IX83). For this, at least three random fields on each sample were captured using a Hoechst 33258 filter (352nm/461nm). *S. aureus* biofilm surface coverage was analysed using Fiji software (ImageJ, NIH).

For measuring the biomass of the biofilms, a crystal violet assay established by George O'Toole was modified and used[141]. Briefly, the *S. aureus* biofilm samples that were grown for 48 hr were rinsed with PBS twice to remove non-adherent bacteria. The samples were then transferred to a new 24-well plate and 250 µL of 0.1% crystal violet solution was added to each sample. The samples were incubated for 15 min and then were rinsed with water three times to remove excess dye. The samples were then dried in the air at room temperature before photographs were taken to show the visual difference of crystal violet stained biofilm sample. For quantifying the amount of crystal violet on each sample, 250 µL of 30% acetic acid was added to each well to solubilise the dye. 125 µL of the solubilised crystal violet was transferred to a well of a 96-well plate and the absorbance at 550 nm was measured using a spectrophotometer.

Chapter Four: Understanding the Relationship between Additively Manufactured Different Inclined Support Free as-Manufactured Ti6Al4V parts and their Surface Properties for Biomedical Applications

4.1. Chapter Overview

Support free structures design are the recent most interest in metallic additive manufacturing for both aerospace and medical industries because of its capacity to reduce cost, manufacture time and minimise hassle for removing the support part which could damage the original part. The demand for manufacturing metallic part by additive manufacturing with customized design, tuneable geometry and desired mechanical properties for aerospace industries and patient specific implants with required porosity and pore size for medical industries is increasing day by day. Therefore, understanding and investigating the relationship between as manufactured parts and its different surface profile properties (surface texture both 2D and 3D), surface roughness (Ra, Rq), surface morphology, and surface wettability are so essential prior to successful practical application. In this work, we have manufactured Ti6Al4V parts by selective laser melting process (SLM) with different inclination angle with respect to the build plane from 5 to 90 degrees with 5 degrees interval. The upward and downward faces of as-manufactured parts have been investigated profoundly using profilometer, optical microscopy (OM), scanning electron microscopy (SEM). Herein, we demonstrated how the surface roughness, surface morphology, and surface wettability are changed with the alteration of inclination angle of SLM parts. There is much more percentage of correlation of arithmetic average of roughness (Ra) value for 5 average data points is found on lower surface on the linear, exponential and logarithmic regression line than the upper surface of SLM plates in the change of inclination angle. It is also clearly observed from the surface morphology that there is a corresponding increase in the number of partially melted particles on the upward SLM support-free part from 5 to 90 degrees whereas there is no regular trend was observed in terms

of partially melted particles on downward surface. Highest contact angle value 130.150^0 is found in 75 degrees inclination and lowest contact angle value 80.81^0 is found in 35 degrees inclination for upper surface. In case of lower surface, the contact angle value observed for all inclined SLM plates > 90 degrees which means the lower surface of SLM plates reveal the hydrophobic surface. This work demonstrates a deep insight in terms of understanding the relationship between different inclined additively manufactured titanium parts with their surface properties for aerospace and medical applications.

4.2. Introduction

Fabrication of support-free part by additive manufacturing are the recent most interest to get rid of increasing surface roughness, longer manufacture time, and damaging part when the support is required to be removed [142-144]. For the SLM/SLS process, there are over 50 different SLM/SLS process parameters that impact the ultimate quality of the finished part, creating a significant challenge in understanding process physics and developing an effective process and control strategy. Laser power, scanning rate, scanning direction, hatch distance, exposure time, building plate temperature, power size and shape, point distance are the most critical processing parameters for SLM process and all those parameters have the influence on the parts' quality [145-147]. But there is limited research has been carried on how the design parameter such as inclination angle can influence the surface properties of additively manufactured titanium implants.

In biomedical industries, there is a direct link between the additively manufactured implants' final surface topography (roughness, surface profile properties), surface morphology, and surface wettability with the host tissue [148-151]. The success or failure of an implant has the direct link with the surface roughness reported by different research groups [157-159]. Usually the parts fabricated by additive manufacturing process come with the higher surface roughness value because of the inherent stair-step and ball milling effect. In this work we have profoundly

analysed the surface roughness for both upper and lower surface of SLM plates with the change of inclination angle maintaining the same powder size, layer thickness, hatch spacing, scanning strategy even though all those parameters have direct effect on roughness.

Generally, rough surfaces have been reported as beneficial for bone integration [117, 118] but the literature lacks agreement on optimal roughness for cell attachment. For example, some studies suggest higher roughness values (Ra=3-5μm); while others favour more smooth surfaces (Ra<1 μm)[119, 120]; and, other studies suggest that surfaces with nano roughness or a hierachical nano/submicron roughness are more favourable for cell growth and fraction. Increased roughness can simultaneously increase the surface area of the implant, improve cell migration and attachment to the implant [26, 152, 153]. Extensive studies have been carried out so far to understand the relationship between roughness and cell attachment, proliferation and differentiation[119]. Previously, we have reported that build orientation of additively manufactured titanium implants can influence the surface topography and roughness of the surface and plays crucial role in terms of mammalian cell attachment[26] and biofilm formation[153]. Therefore, thoroughly investigating the surface profile properties, surface morphology, and surface wettability of additively manufactured part is highly essential to design the clinically desired successful implant. We have previously shown that the mechanical properties of SLM manufactured Ti-6Al-4V & AlSi12Mg lattice structures can be effectively manipulated to match tissue specific parameters [154, 155].

In this work, we fabricated support free Ti6Al4V SLM part varying the inclination angle from 5 degrees to 90 degrees with 5 degrees interval. As there are lot of controversies about the surface roughness of the implant with the osseo-integration in the existing literature, a profound roughness analysis is essential prior to the implantation. Because of the stair effect due to the layer wise production, surface roughness of a sloping plane depends on the sloping angle. In addition, roughness of top surfaces differs strongly from roughness of bottom surfaces. This

paper discusses the relationship of the surface profile properties (surface texture, surface roughness), surface morphology, and surface wettability of SLM part with the change of the build inclination angle for the both upward and downward surface. This work will, we believe, have significant impact on the design and fabrication of these materials for both aerospace and biomedical applications.

4.3. Experimental Set up

The samples were fabricated according to chapter-3 – Materials and Methods section outlined in 3.2, fabrication according to 3.3 and characterized according to section 3.4.

4.4. Results & Discussion

4.4.1. Surface Texture Analysis of Different Inclined SLM parts

The 2D and 3D surface texture of support-free Ti6Al4V parts inclined from 0 to 90 degrees with 5 degrees interval are shown in Figure. 4.1.1- 4.1.4 and Fig. 4.2.1- 4.2.4 by optical microscope using focus variation measurement false colour height map. The partially melted particles are observed for all inclination angles for both upward and downward surface on SLM plates. It is clearly observed that the number of partially melted titanium particles increases with the increase of the inclination angle from 5 degrees to 90 degrees for the upward surface of the Ti6Al4V parts but there is no common trend found in terms of partially melted particles for downward surfaces. In case of lower inclination angle from 5 to 15 degrees on downward surface partially melted particles are observed to be stuck in an agglomerate fashion. It is observed that the step edge border from both 2D and 3D surface profile from 5 degrees to 45 degrees and there are no step edge borders are observed in case of 50 degrees to 90 degrees for upward surface. In case of downward surface, there is no step edge border is observed from any of the inclination angle of SLM parts. The bullet-shaped like appearance is also noticed on the surface of 5 degrees inclined upward surface. In case of the surface texture from the upper

face of SLM part, the step edge border is also observed to prominent in case of 5 and 10 degrees and the sharpness of step edge border is observed to be dim gradually from 15 degrees to 45 degrees. The distance between step edges of the 5 degrees inclination angle is higher than the 45 degrees angle. In case of the higher inclination angle starting from 50 degrees to 90 degree inclination angle, the step edge border is due to the discontinuities along step edges and higher concentration of partially melted particles stuck at edge[156].

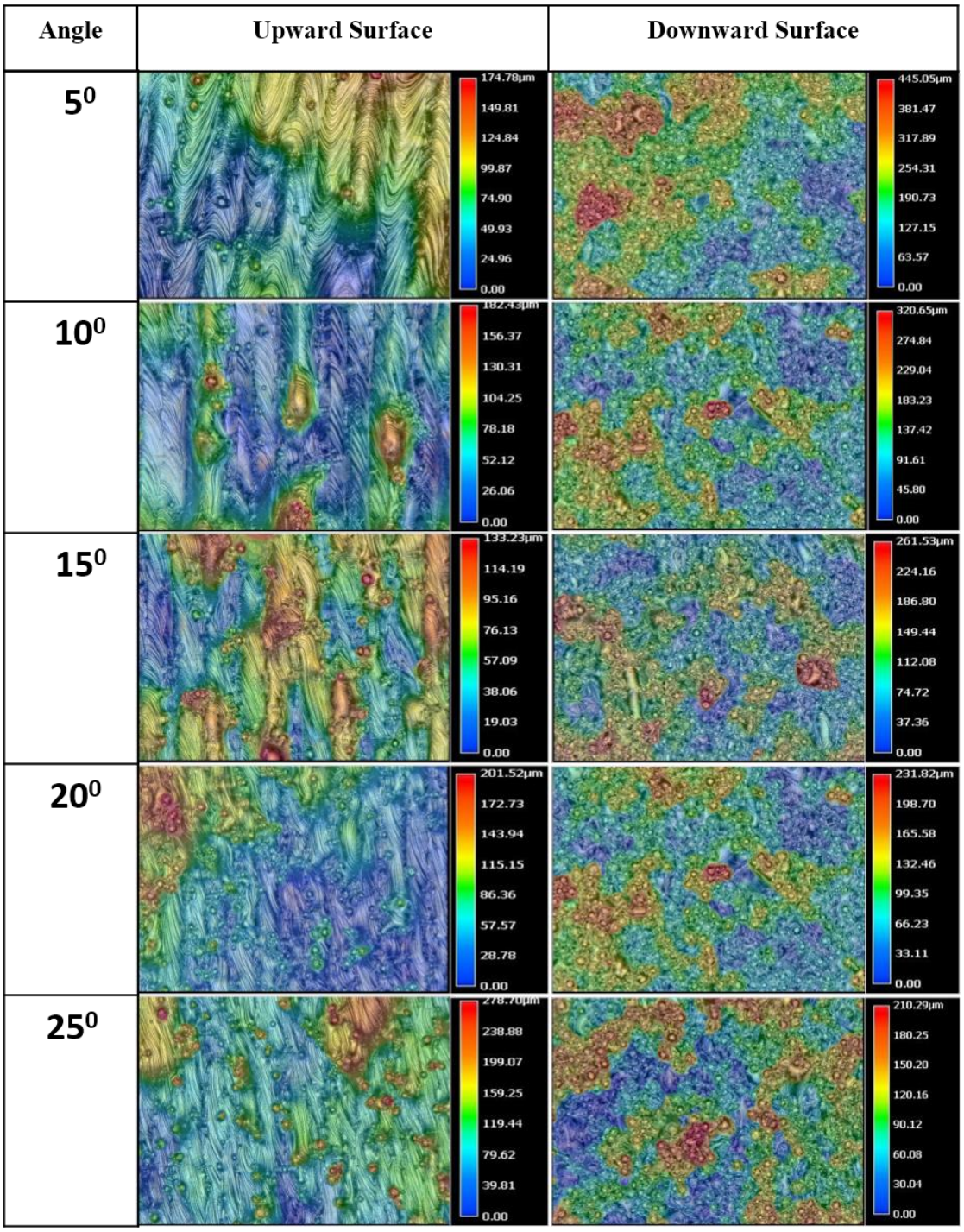

Figure 4.1.1**:** 2D surface profile of different inclined support-free SLM parts of both upward and downward surface from 30 to 50 degrees obtained by the digital microscope showing topographical changes as the angle increases

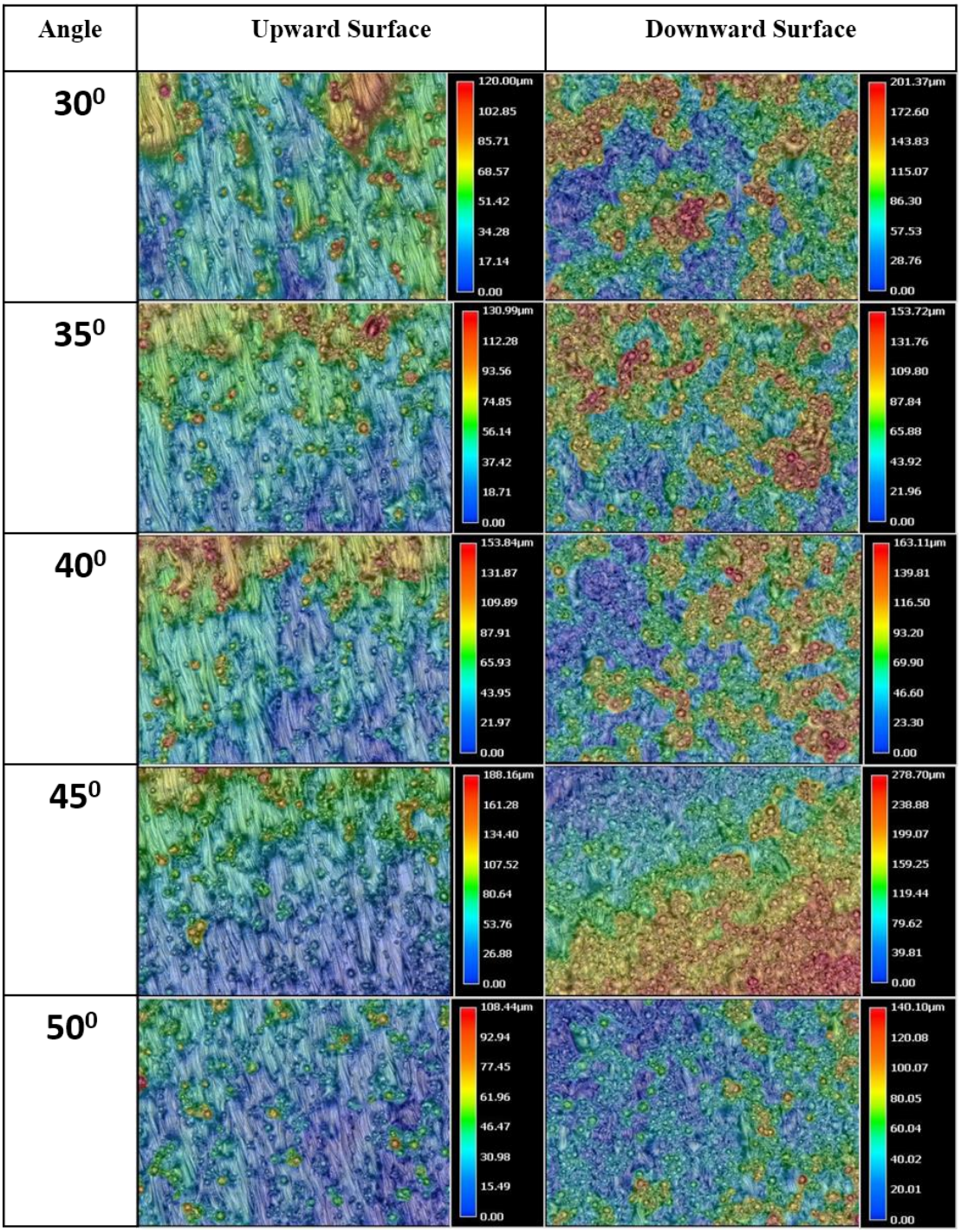

Figure 4.1.2: 2D surface profile of different inclined support-free SLM parts of both upward and downward surface from 55 to 75 degrees obtained by the digital microscope showing topographical changes as the angle increases.

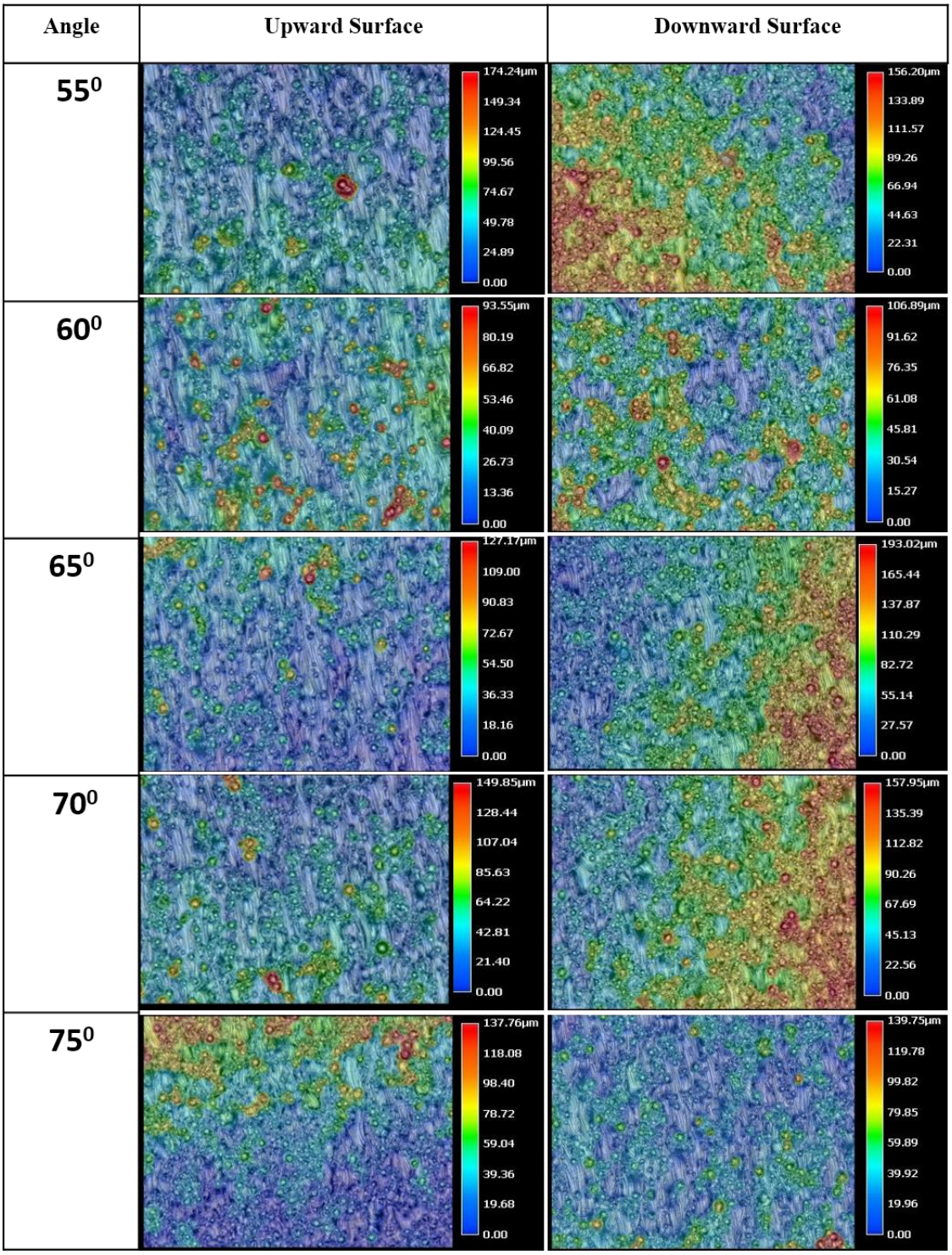

Figure 4.1.3: 2D surface profile of different inclined support-free SLM parts of both upward and downward surface from 55 to 75 degrees obtained by the digital microscope showing topographical changes as the angle increases.

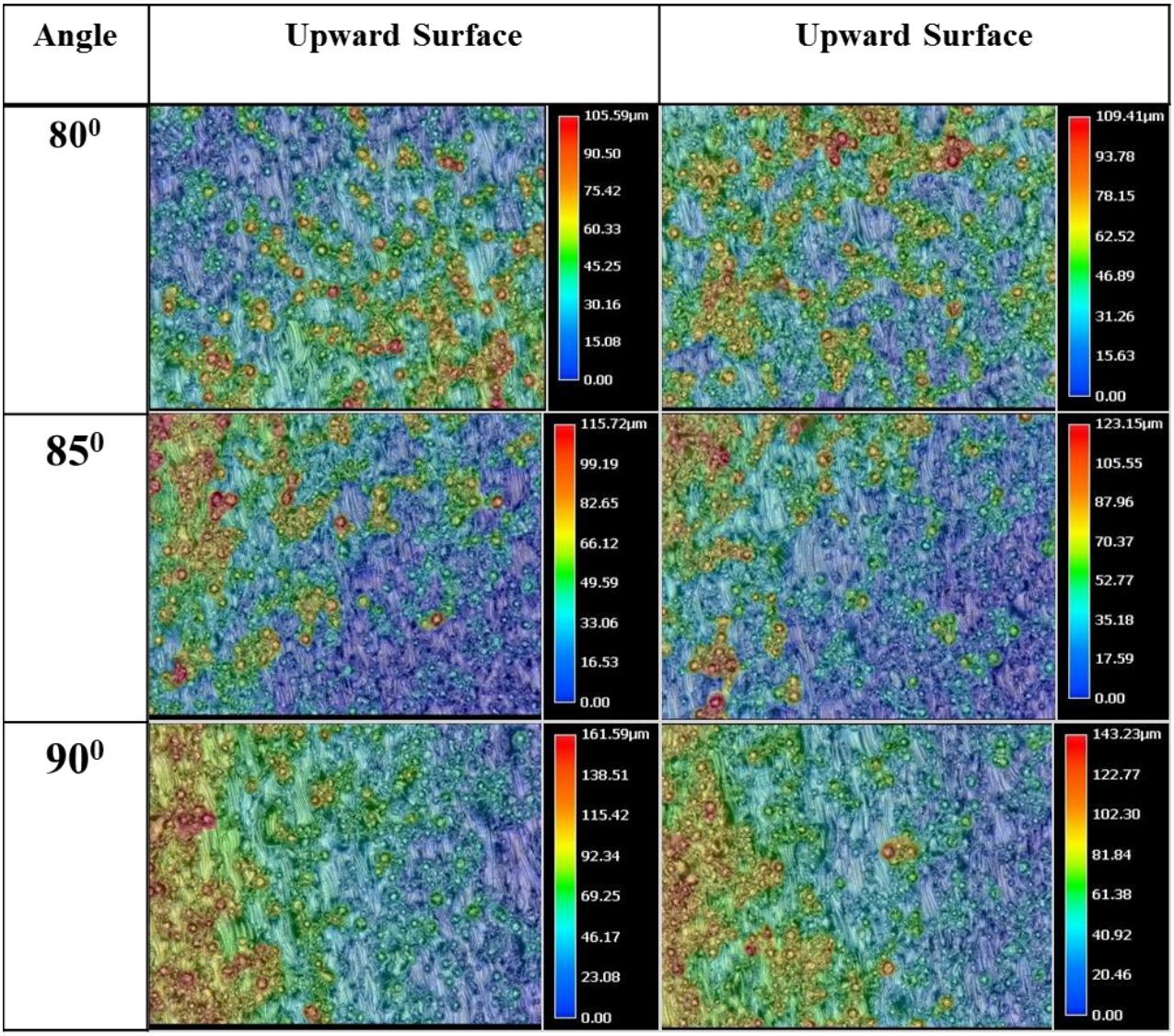

Figure 4.1.4: 2D surface profile of different inclined support-free SLM parts of both upward and downward surface from 80 to 90 degrees obtained by the digital microscope showing topographical changes as the angle increases.

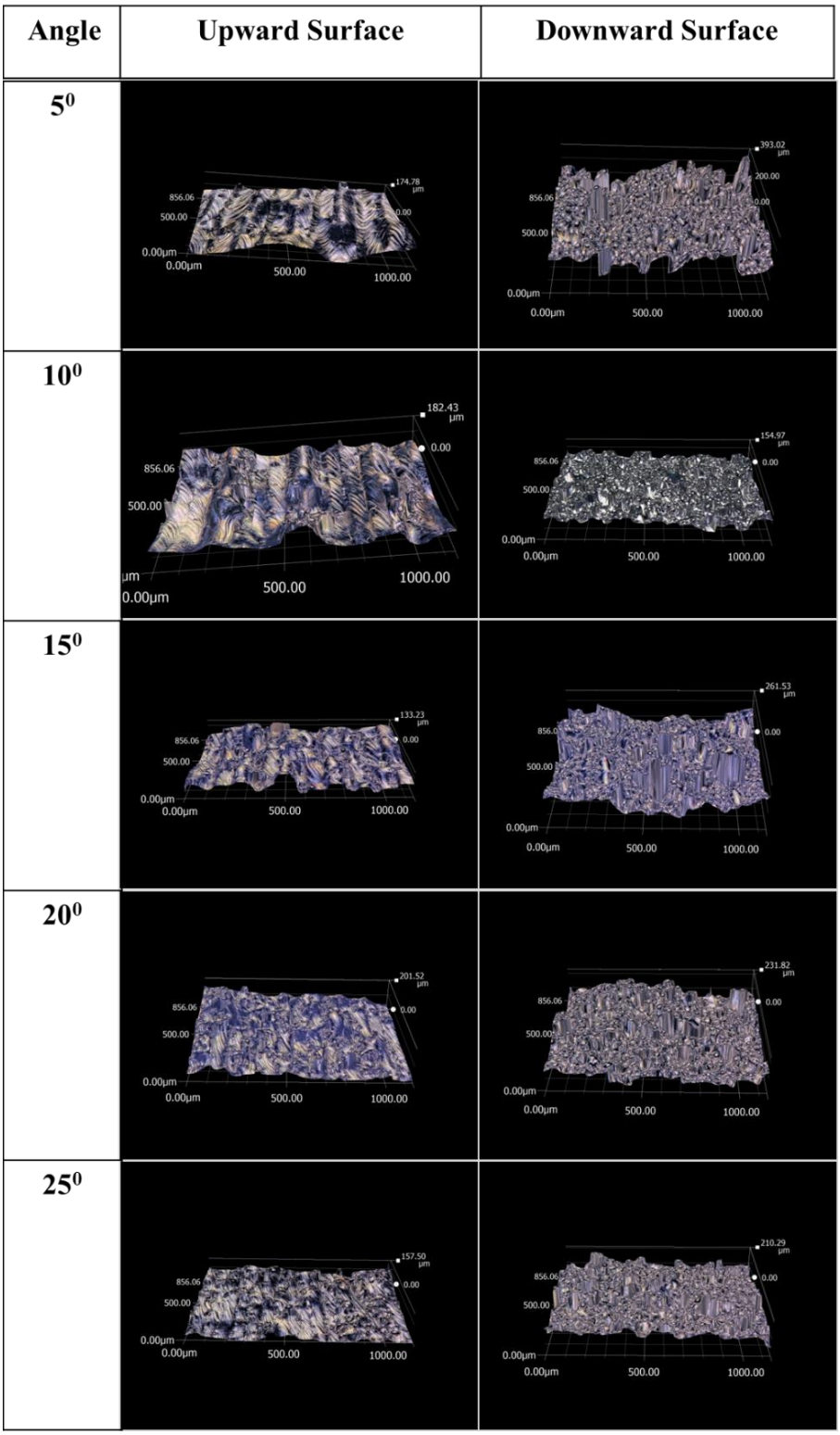

Figure 4.2.1**:** 3D surface profile of different inclined support-free SLM parts of both upward and downward surface from 5 to 25 degrees obtained by the digital microscope showing topographical changes as the angle increases.

Angle	Upward Surface	Downward Surface
30^0	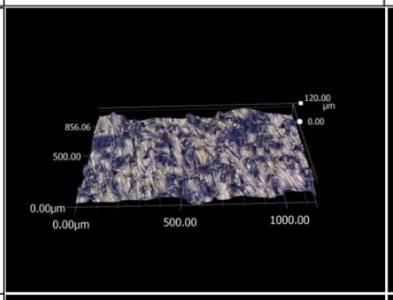	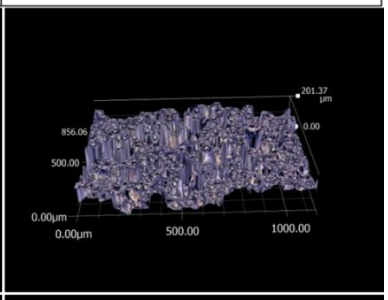
35^0	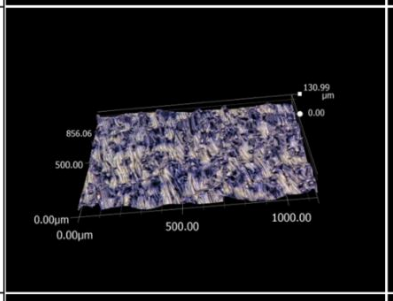	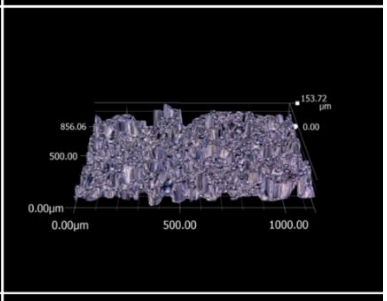
40^0	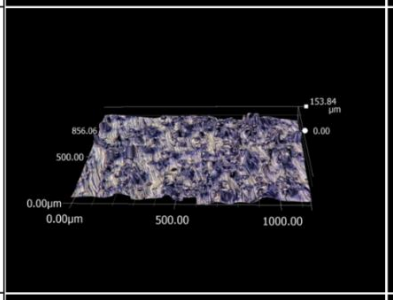	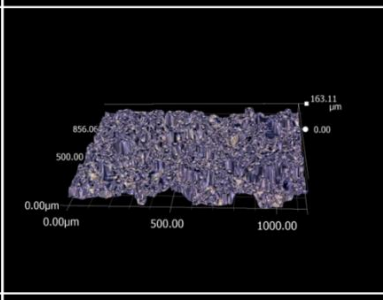
45^0	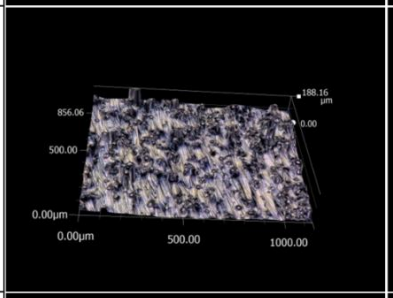	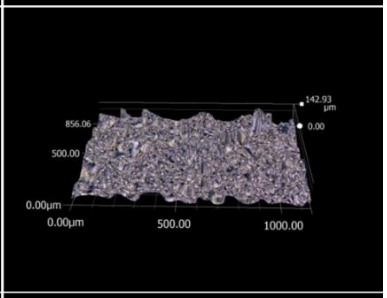
50^0	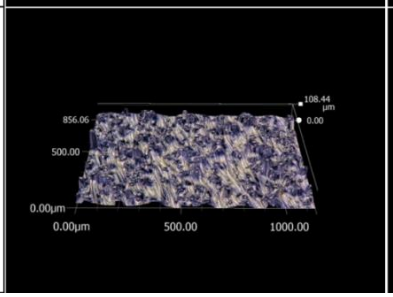	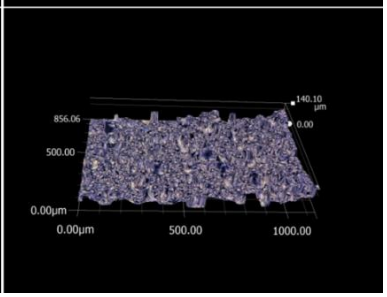

Figure 4.2.2: 3D surface profile of different inclined support-free SLM parts of both upward and downward surface from 30 to 50 degrees obtained by the digital microscope showing topographical changes as the angle increases.

Angle	Upward Surface	Downward Surface
55^0	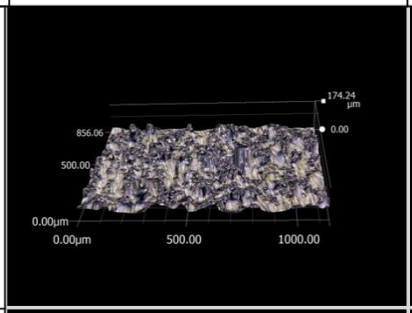	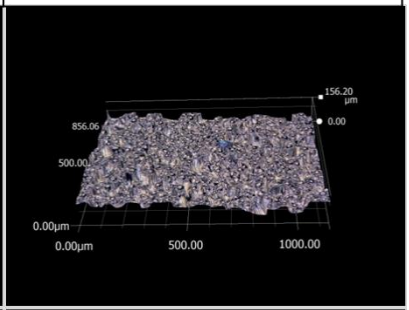
60^0	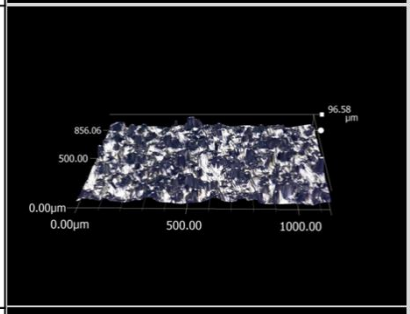	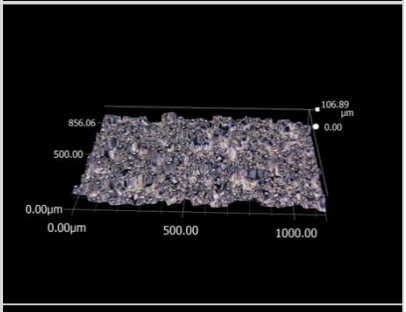
65^0		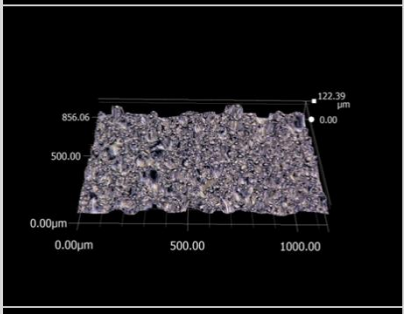
70^0	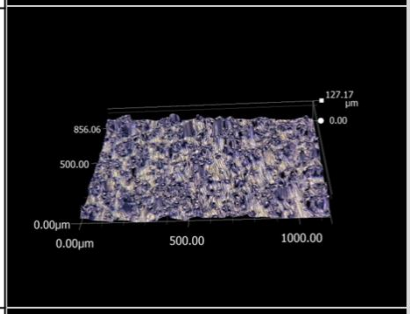	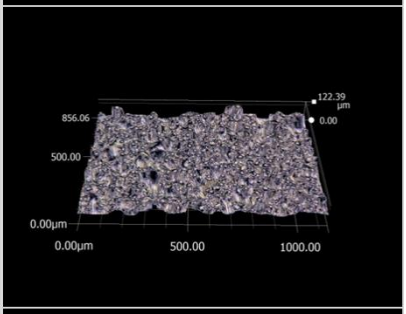
75^0	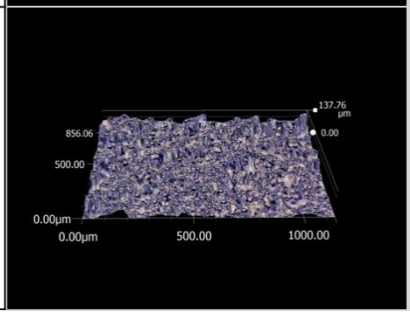	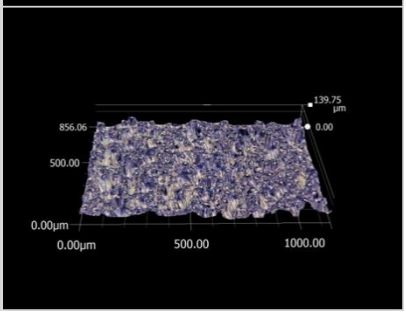

Figure 4.2.3: 3D surface profile of different inclined support-free SLM parts of both upward and downward surface from 55 to 75 degrees obtained by the digital microscope showing topographical changes as the angle increases.

Angle	Upward Surface	Downward Surface
80^0	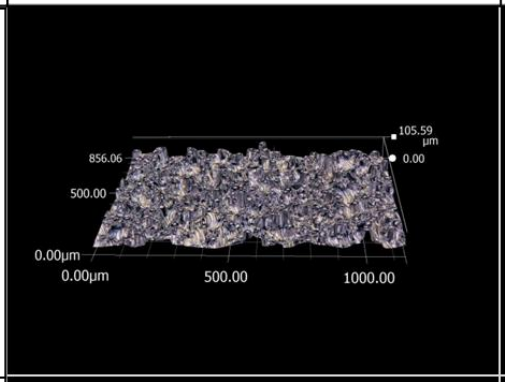	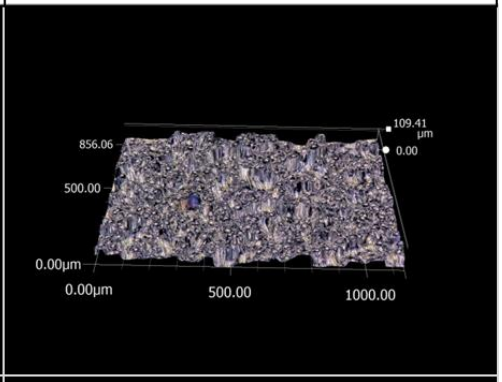
85^0	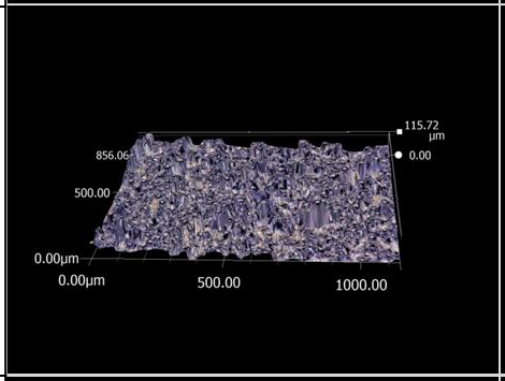	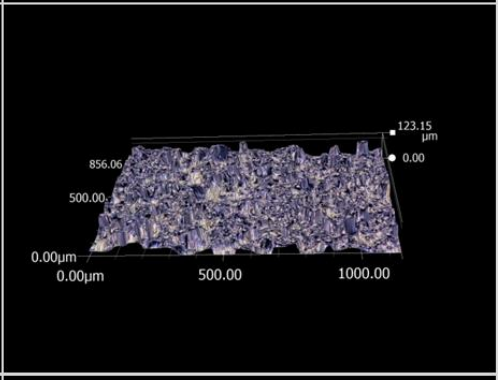
90^0	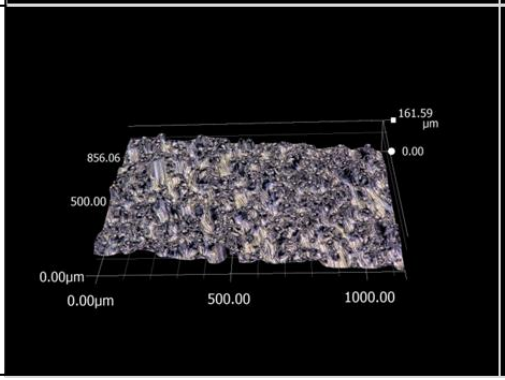	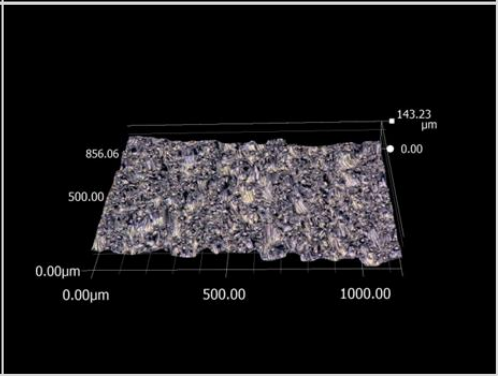

Figure 4.2.4:3D surface profile of different inclined support-free SLM parts of both upward and downward surface from 80 to 90 degrees obtained by the digital microscope showing topographical changes as the angle increases

4.4.2. Surface Roughness Analysis of Different Inclined SLM parts

Titanium based implants used currently in clinical purpose for both orthopaedic and dental implant vary with its roughness and composition. In dentistry, commercially pure titanium (Ti) has become one of the most commonly used implant materials whereas in orthopaedics Ti alloys have virtually replaced Ti because of strength requirements [18, 19]. Implant surface topography is normally characterized by two most common roughness parameters: surface arithmetic average of roughness profile (R_a), root mean square deviation of the roughness profile (R_q). Arithmetic average of roughness profile (R_a) which is regarded as the most universally used parameter is as the average absolute deviation of the roughness irregularities from the mean line over one sampling length [156, 160, 161]. To be compatible with other contributions in this field, the arithmetic average roughness, R_a, is used; where R_a measures the arithmetic average deviation of the measured profile from the centreline of the measured profile (Equation 1). Where y_i is the vertical distance from the mean line to the i^{th} data point, and i refers to the facet of interest and R_q measures the root mean square average of the roughness profile ordinates (Equation 2).

$$R_a = \frac{1}{n}\sum_{i=1}^{n}|y_i| \quad \ldots\ldots(1)$$

$$R_q = \sqrt{\frac{1}{n}\sum_{i=1}^{n} y_i^2} \quad \ldots\ldots(2)$$

$R_{a,i}$	[µm]	Average roughness of facet i
Rq	[µm]	Root mean square average of the roughness profile ordinates.
t	[m]	Layer thickness
l	[m]	Overhang distance
Y_j	[m]	Vertical distance from the mean line to the data point
N_{orient}	-	Number of assessed orientations
p	-	Unit vector oriented vertically downward to the plate

Fig.4.3.1 and Fig.4.3.2 shows the surface arithmetic average of roughness profile (R_a) of SLM plates for upward and downward surface respectively with the change of the inclination angle from 5 degrees to 90 degrees obtained by stylus profilometer. In both figures (a) linear regression analysis, (b) exponential regression analysis, (c) logarithmic regression analysis were shown by plotting into graph for both upward and downward surface of SLM plates from 10 degrees to 90 degrees with 5 degrees interval. We can observe the highest surface arithmetic average of roughness profile (R_a) for 10 degrees in all occasions 1 data point (R_a=10.7μm), mean value of 3 data points (R_a=10.06μm) and mean value of 5 data points (R_a=10.32μm). The relative higher surface roughness of SLM plates up to 45 degrees could be explained by the narrowing of the step edges, and the associated concentration of partially melted particles at step edges. Lowest surface arithmetic average of roughness profile is found for 5 degrees in case of 1 data point (R_a=5.44μm), 3 average data points (R_a=5.18 μm) and 5 average data points (R_a=4.90 μm) respectively. The coefficient of determination (R^2) was determined for all linear regression, exponential regression, and logarithmic regression analysis plot for both upper and lower surface for 1, 3 and 5 average data points respectively. The coefficient of determination (R^2) shows the percentage variation in surface arithmetic average of roughness profile (R_a) by inclination angles. The R^2 coefficient of determination is a statistical measure of how well the regression line approximates the real data points. We can see from the linear regression analysis plot in Fig.4.3.1(a) that the value of R^2 is 0.0015, 0.0497 and 0.0267 respectively where red linear regression line is denoted for accounting 1 data point, blue is for 3 average data points and black is for 5 average data points. That means only 0.15 %, 4.97 % and 2.67 % R_a data points fall within the red (1 data point), blue (3 average data points), and black (5 data points) linear regression line. Fig. 4.3.1(b) shows the plot for exponential regression analysis where the value of R^2 is 0.0002, 0.0695 and 0.0495 for 1, 3 average and 5 average data points of R_a. That means only 0.02 %, 6.95 % and 4.95 % data points fit within the red (1 data point), blue

(3 average data points), and black (5 average data points) exponential regression line. In case of logarithmic regression analysis shown in Fig. 4.3.1(c) for 0.27%, 3.46% and 5.46 % R_a value fits on the logarithmic regression line consisting the red (1 data point), blue (3 average data points), and black (5 average data points) respectively. That means much more data points fit on exponential regression line than linear and exponential line for upper R_a.

We can observe the highest surface arithmetic average of roughness profile (R_a) for lower surface for 5 degrees in 1 data point (R_a=12.8μm), 15 degrees in case of 3 average data points (R_a=12.8μm) and 85 degrees in case of 5 average data points (R_a=12.7μm). Lowest surface arithmetic average of roughness profile is found for 50 degrees in case of 1 data point (R_a=6.1μm), 70 degrees in case of 3 average data points (R_a=7.47μm) and 70 degrees in case of 5 average data points (R_a=7.79μm) respectively. From the plot for linear regression analysis of arithmetic average of roughness (R_a) shown in Fig. 4.3.2(a) for lower surface of SLM plates that 0.15%, 4.97%, 2.67% R_a data points fall within the red (1 data point), blue (3 average data points), and black (5 average data points) linear regression line 3.31%, 13.14% and 39.6% data points fit within the red (1 data point), blue (3 average data points), and black(5 average data points) exponential regression line. In case of logarithmic regression analysis shown in Fig.4.3.2(c) for 10.38%, 15.19% and 40.06% R_a value fits on the logarithmic regression line consisting the red (1 data point), blue (3 average data points), and black (5 average data points) respectively. We can see in case of lower surface of arithmetic average of roughness (R_a) value for 5 average data points there is much more percentage of data points exist on the linear, exponential and logarithmic regression line than the upper surface of SLM plates in the change of inclination angle. In case of lower surface of SLM plates from the plots for 5 average data points highest R_a value is found for 15 degrees (R_a=12.34μm) inclination angle whereas highest R_a value is found for 10 degrees (R_a=10.32μm) for the upward surface. Lowest R_a value exists (5 degrees) for upward (R_a=4.906μm) and 70 degrees (R_a=7.79μm) for downward surface.

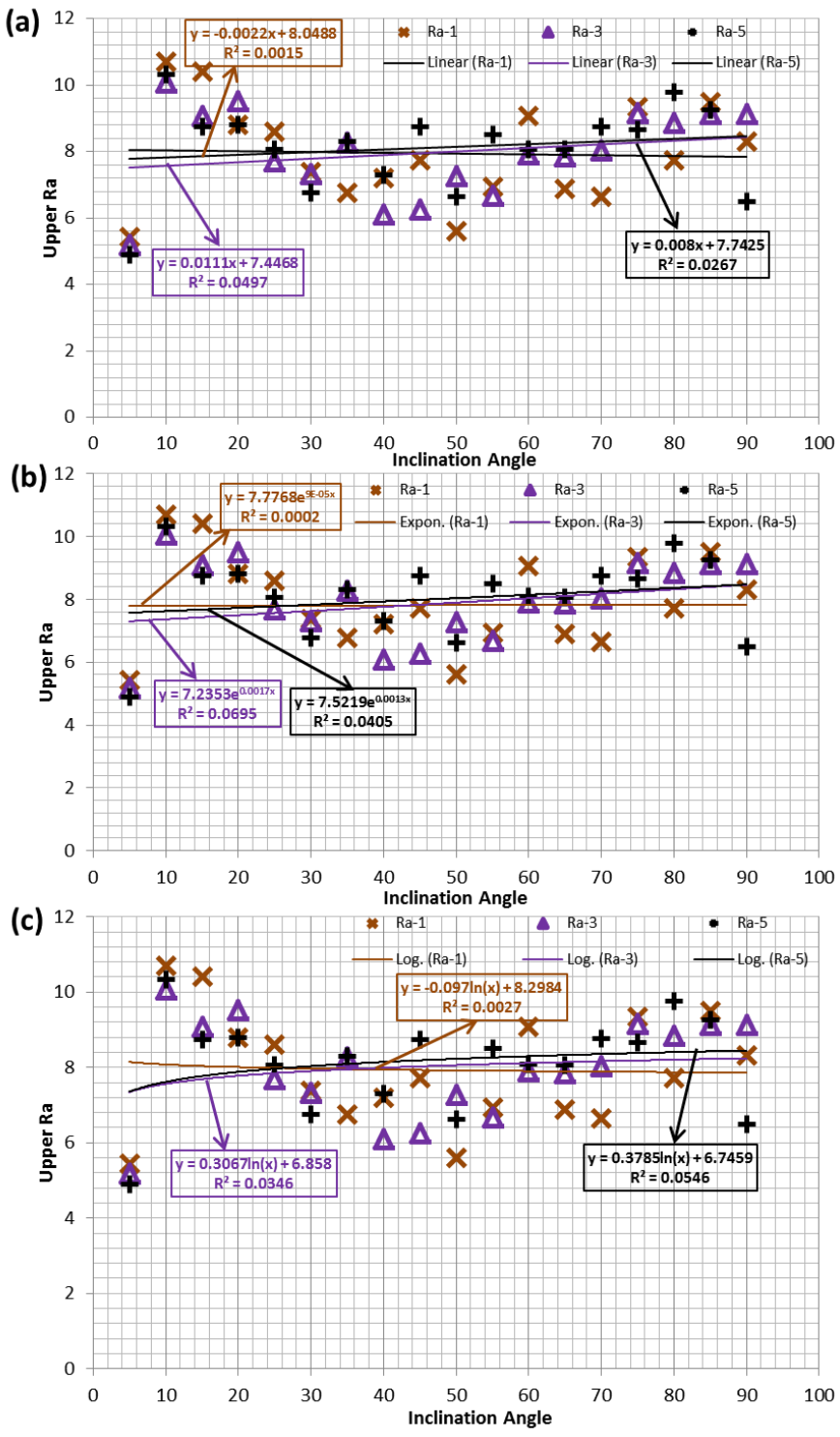

Figure 4.3.1:Surface arithmetic average of roughness profile (R_a) analysis by stylus profilometer for the upward surface with the function of inclination angle varying from 5 degrees to 90 degrees with 5 degrees interval for 1, 3 average and 5 average data points (a) showing the linear regression analysis, (b) showing the exponential regression analysis, (c)showing the logarithmic regression analysis.

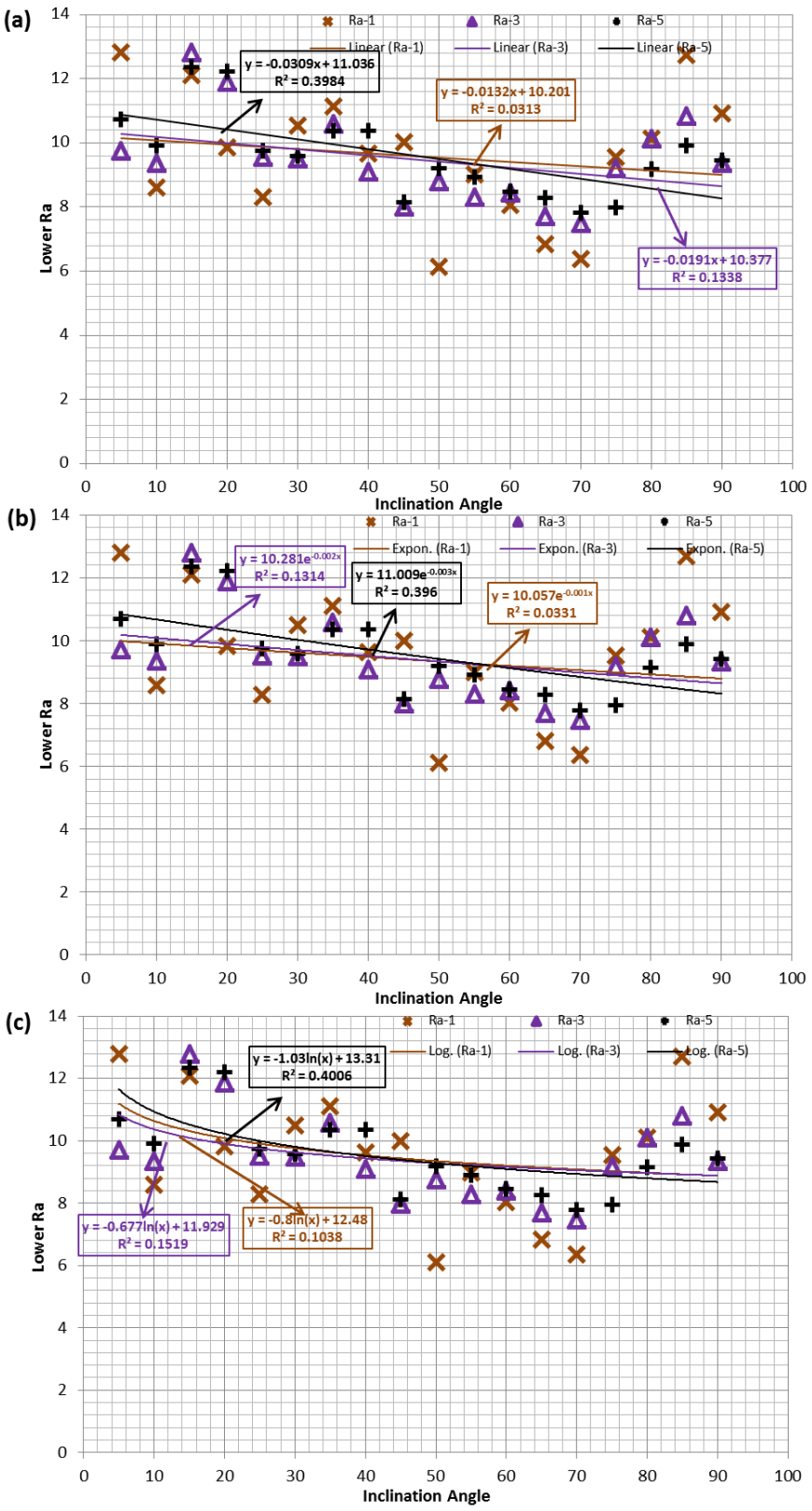

Figure 4.3.2:Surface arithmetic average of roughness profile (R_a) analysis by stylus profilometer for the downward surface with the function of inclination angle varying from 5 degrees to 90 degrees with 5 degrees interval for 1, 3 and 5 data points (a) showing the linear

regression analysis, (b) showing the exponential regression analysis, (c) showing the logarithmic regression analysis.

Fig.4.3.3 and Fig.4.3.4 shows the root mean square deviation of the roughness profile (R_q) for (a) linear regression analysis, (b) exponential regression analysis, (c) logarithmic regression analysis of SLM plates for upward and downward surface respectively with the change of the inclination angle from 5 degrees to 90 degrees with 5 degrees interval obtained by stylus profilometer. We can observe the highest root mean square deviation of the roughness profile (R_q) for 10 degrees 1 data point (R_q=13.5μm), mean value of 3 data points for 15 degrees (R_q=12.4μm) and mean value of 5 data points (R_q=12.7μm) for 15 degrees for the upward surface. Lowest root mean square deviation of the roughness profile is found for 50 degrees in case of 1 data point (R_q=6.91μm), 10 degrees in case of 3 average data points (R_q=7.07μm) and 5 average data points (R_q=6.938μm) respectively. The coefficient of determination (R^2) was determined for all linear regression, exponential regression, and logarithmic regression analysis plot for both upper and lower surface for 1, 3 and 5 average data points respectively. We can see from the linear regression analysis plot in Fig.4.3.3(a) that the value of R^2 is 0.0008, 0.029 and 0.0097 respectively. That means only 0.08 %, 2.9 % and 0.97% R_q data points fall within the red (1 data point), blue (3 average data points), and black (5 average data points) linear regression line. Fig. 4.3.3(b) shows the plot for exponential regression analysis where the value of R^2 is 0.0002, 0.0414 and 0.0173 for 1, 3 average and 5 average data points of R_q. That means only 0.02%, 4.14% and 1.7 % data points fit within the red (1 data point), blue (3 average data points), and black (5 average data points) exponential regression line. In case of logarithmic regression analysis shown in Fig. 4.3.3(c) for 0.42%, 1.41% and 2% R_q value fits on the logarithmic regression line consisting the red (1 data point), blue (3 average data points), and black (5 average data points) respectively.

We can observe the highest root mean square deviation of the roughness profile (R_q) for lower surface for 5 degrees in 1 data point (R_q=15.5μm), 15 degrees in case of 3 average data points (R_q=15.3μm) and 15 degrees in case of 5 average data points (R_q=14.66μm). Lowest surface arithmetic average of roughness profile is found for 50 degrees in case of 1 data point (R_q=7.75 μm), 70 degrees in case of 3 average data points (R_q=8.89μm) and 70 degrees in case of 5 average data points (R_q=9.49μm) respectively. From the plot for linear regression analysis of root mean square deviation of the roughness profile (R_q) shown in Fig. 4.3.4(a) for lower surface of SLM plates that 6.64%, 21.01%, 42.77% data points data points fall within the red (1 data point), blue (3 average data points), and black (5 average data points) linear regression line. 0.62%, 20.49% and 42.1% data points fit within the red (1 data point), blue (3 average data points), and black (5 average data points) exponential regression line. In case of logarithmic regression analysis shown in Fig. 4.3.4 (c) for 15.63%, 24.86% and 41.16% R_q value fits on the logarithmic regression line consisting the red (1 data point), blue (3 average data points), and black (5 average data points) respectively. We can see in case of lower surface of arithmetic average of roughness (R_q) value for 5 average data points there is much more percentage of data points exist on the linear, exponential and logarithmic regression line than the upper surface of SLM plates in the change of inclination angle. In case of lower surface of SLM plates from the plots for 5 average data points highest R_q value is found for 15 degrees(R_q=14.66 μm) inclination angle whereas highest R_q value is found for 10 degrees(R_q=12.7μm) for the upward surface e. Lowest R_q value exists in 5 degrees inclination angle of upward (R_q=6.93 μm) and 70 degrees of downward (R_q=9.49μm) surface.

Surface profile properties such as maximum peak height (R_p), maximum valley depth (R_v), skewness of the roughness profile (R_{sk}), kurtosis of the roughness profile (R_{ku}) are also obtained using a profilometer (shown in supplementary figures).

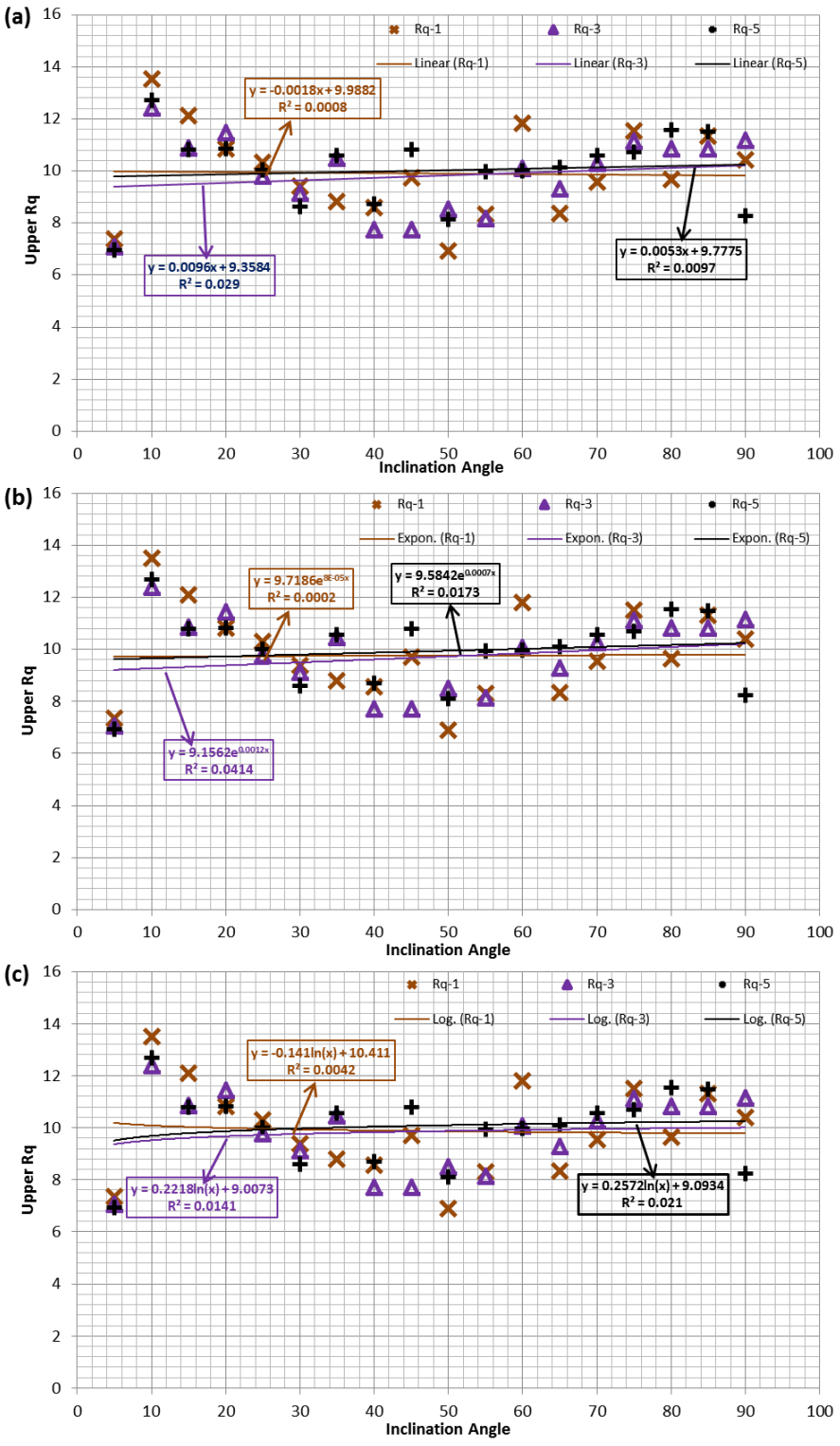

Figure 4.3.3:Root mean square deviation of the roughness profile (R_q) analysis by stylus profilometer for the upward surface with the function of inclination angle varying from 5 degrees to 90 degrees with 5 degrees' interval for 1, 3 and 5 data points (a) showing the linear regression analysis, (b) showing the exponential regression analysis, (c) showing the logarithmic regression analysis.

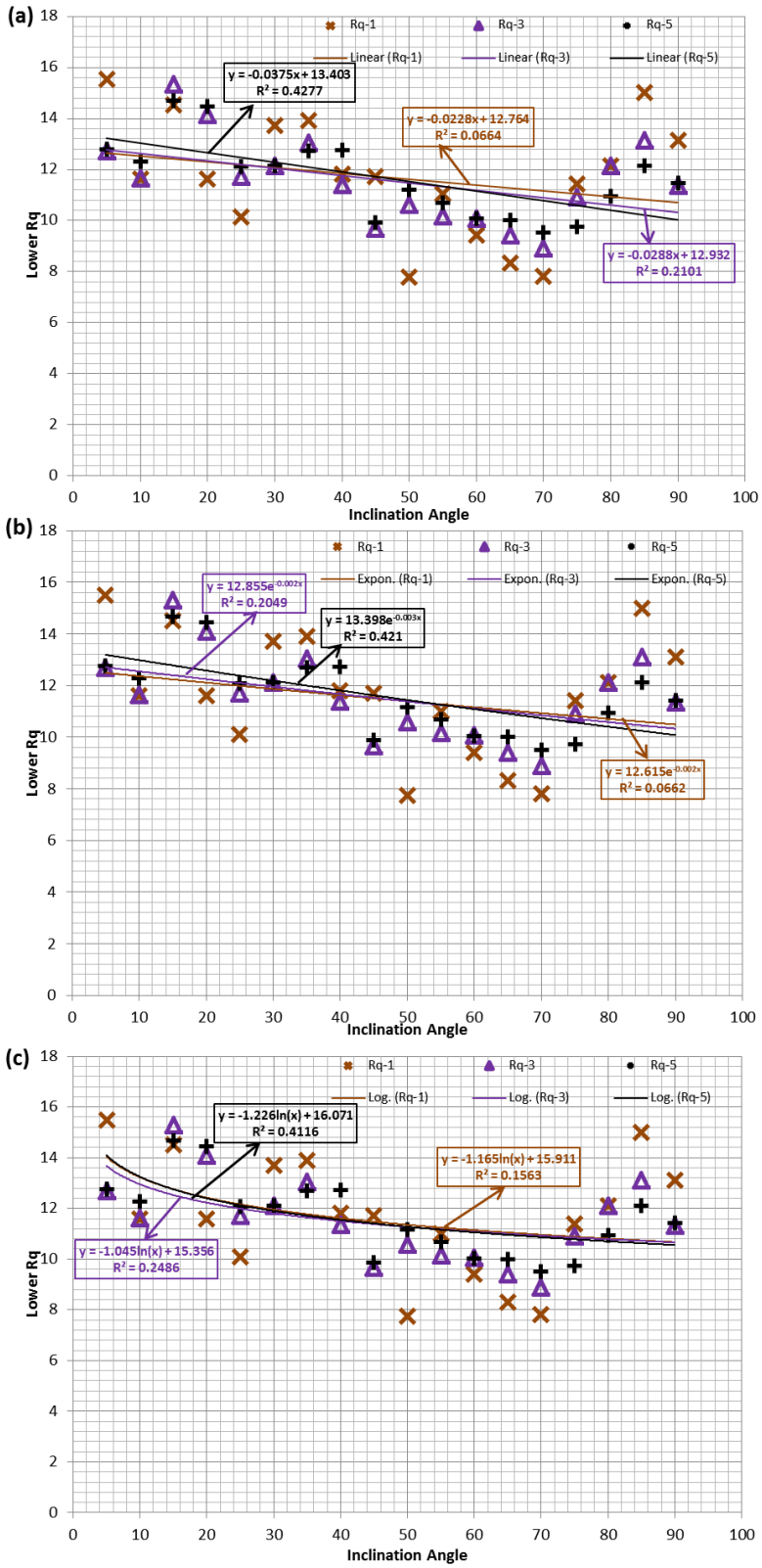

Figure 4.3.4: Root mean square deviation of the roughness profile (R_q) analysis by stylus profilometer for the downward surface with the function of inclination angle varying from 5 degrees to 90 degrees with 5 degrees' interval for 1, 3 and 5 data points (a) showing the linear

regression analysis, (b) showing the exponential regression analysis, (c) showing the logarithmic regression analysis.

4.4.3. Surface Morphology Analysis of Different Inclined SLM parts

Surface morphology plays a critical role for the bone cells growth [162, 163]. Extensive level of researches has been carried out so far to understand the role of surface morphology for bone regeneration for titanium implants mostly on traditional titanium implants manufactured by casting process[164-167]. Even though some different research groups they have investigated the additively manufactured titanium implants pore geometry's effect on in-vitro[168], changing the surface morphology by chemical treatment[169, 170], but still it is not so much explored for additively manufactured titanium surface morphology role without doing post-processing treatment and getting rid of partially melted particles for orthopaedic implants as the surface topography can be manipulated easily by changing the build inclination angle. Therefore prior to clinical application, it is so essential to observe the surface morphology of different inclined SLM plates for both upward and downward surface.

Fig.4.4.1 and Fig.4.4.2 represent the surface morphology of Ti6Al4V SLM plates of upper and lower surface from 5 degrees to 90 degrees incliantion angle varying 5 degrees by SEM images for lower and higher magnification respectively. In all occasions for both upward and downward surface we can observe the partially melted particles stuck on the SLM plates.The phenomena of partially melted particles occurs by three mechanisms:(1) thermal diffusion occurs due to the significant temperature difference between loose powder and solidified material, leading to local fusion of powder to the edge of the scan track of the SLM surface[171, 172]; (2) balling phenomenon in SLM process which is responsible for forming particles on the laser melted surface[144]; (3)the stair-stepping effect of the implant of varying inclination angles are partially built on the loose powder; and thus some metal particles below each layer will be totally or partially melted and then bonded on the bottom of the layer[173].

The phenomena for balling is defined as its ability of breaking up the melt pool into smaller entities when the total surface of a molten pool becomes larger than that of a sphere with the same volume which causes several impediments on interlayer connection[174]. Marangoni convection theory supports the balling phenomena by explaining the thermal gradient which occurs due to balling and create a thermos-capillary flow of fluid within the melt pool from low surface tension region to high surface tension region[175]. Balling is the breakup of the melt pool into small spheres. It occurs when molten material does not wet well to the underlying substrate or material due to high surface tension differences generated as a result of variations in thermal properties within the melt pool [176-178].Balling is a severe impediment on interlayer connection, it decreases part density and increases top surface roughness and side roughness. However, the balling effect more dominantly affects the side roughness of parts due to the direction of balling scattering to either side of the melt pool rather than settling on the top surface.

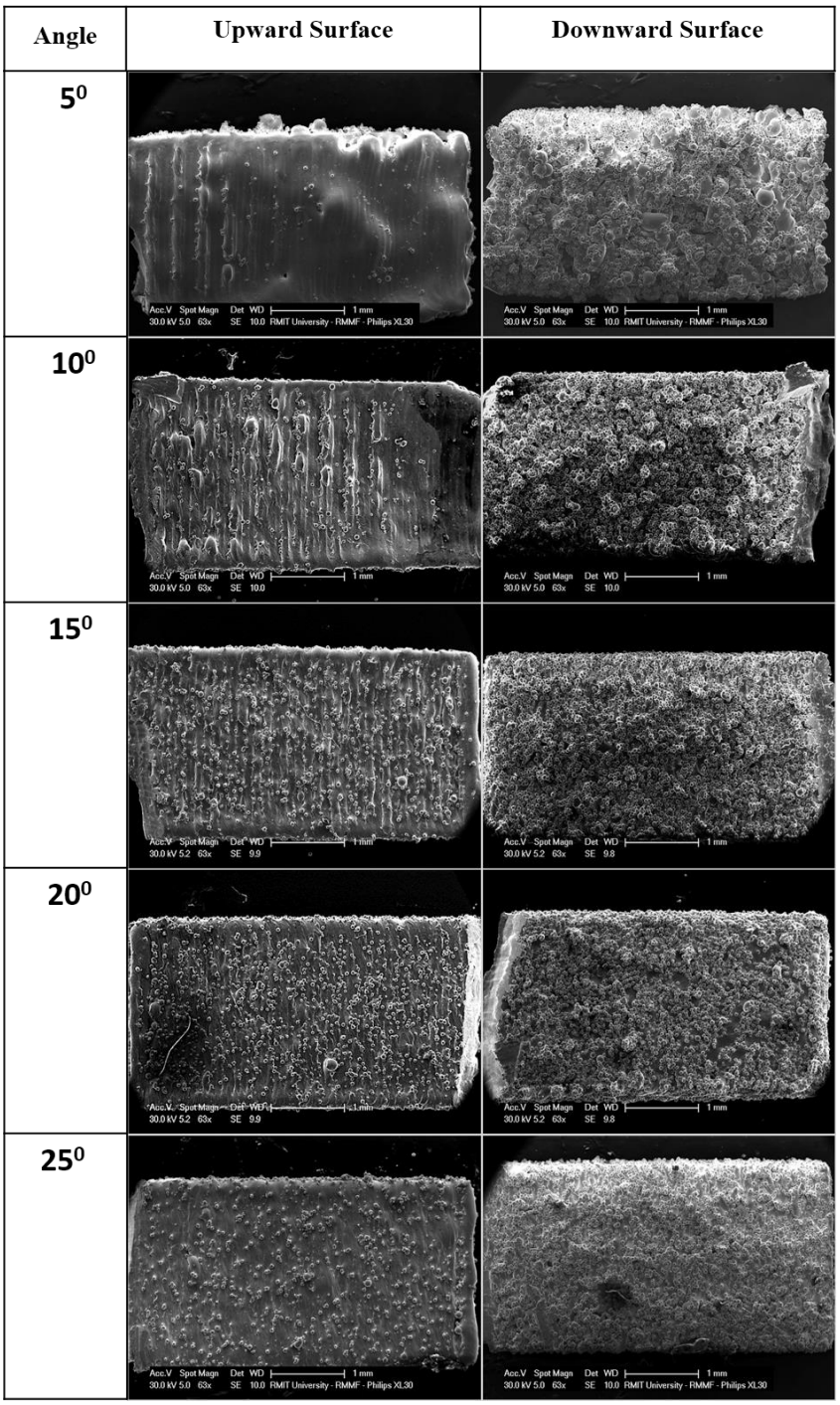

Figure 4.4.1: SEM micrograph shows the surface morphology of Ti6Al4V SLM plates of both upper and lower surface 5 to 25 degrees inclination angle with 5 degrees interval for lower (63X) magnitude.

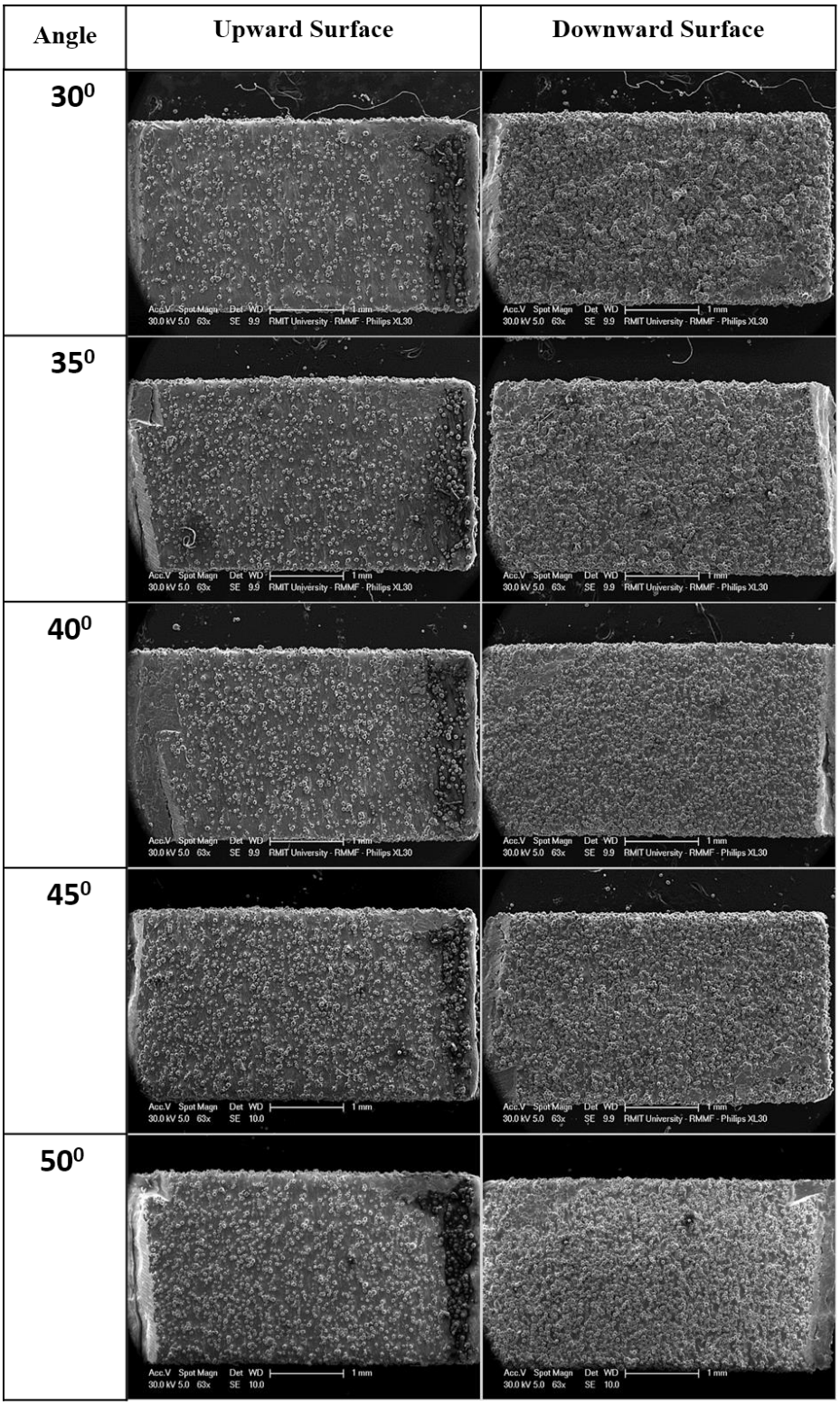

Figure 4.4.2: SEM micrograph shows the surface morphology of Ti6Al4V SLM plates of both upper and lower surface 30 to 50 degrees inclination angle with 5 degrees interval for lower (63X) magnitude.

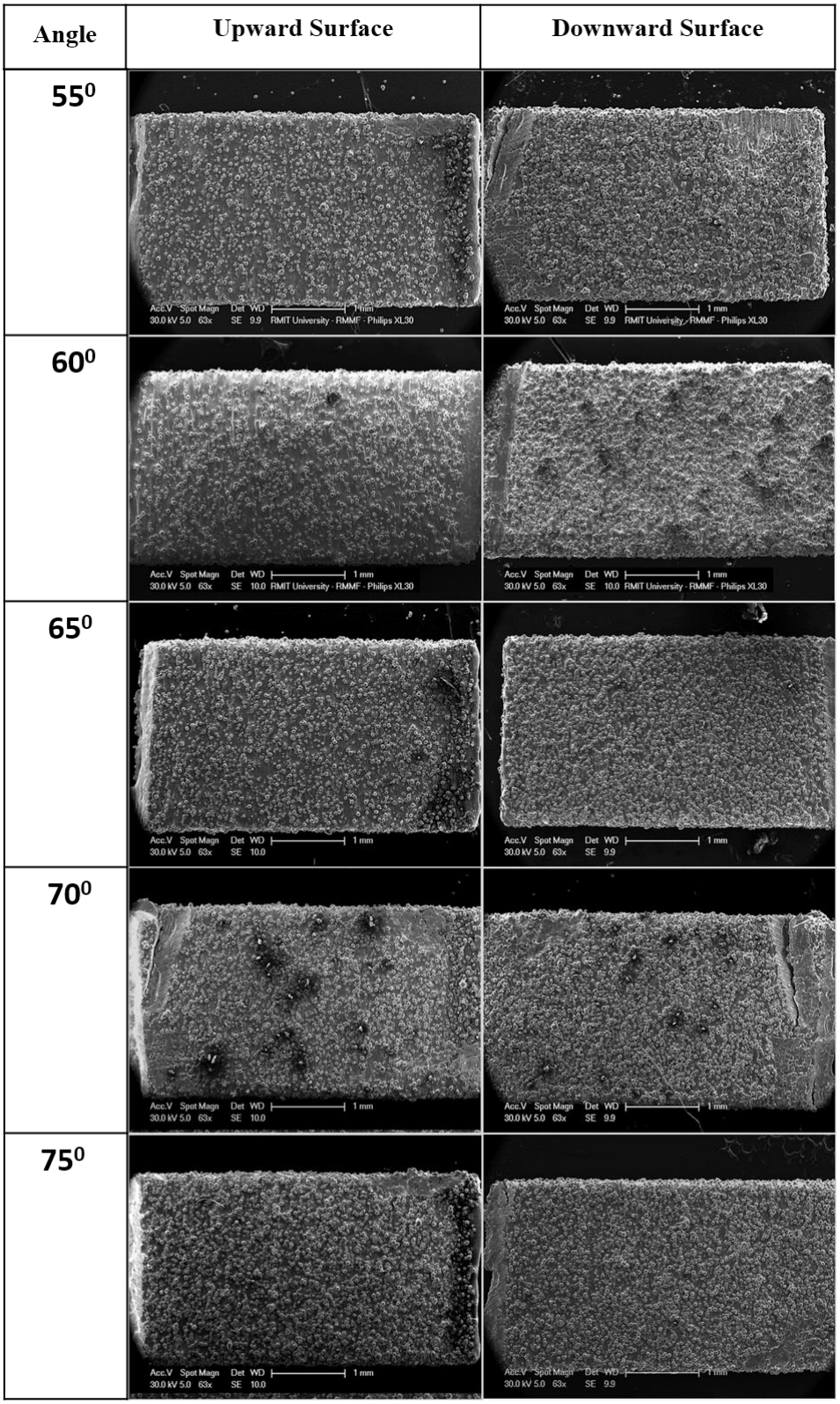

Figure 4.4.3: SEM micrograph shows the surface morphology of Ti6Al4V SLM plates of both upper and lower surface 55 to 75 degrees inclination angle with 5 degrees interval for lower (63X) magnitude.

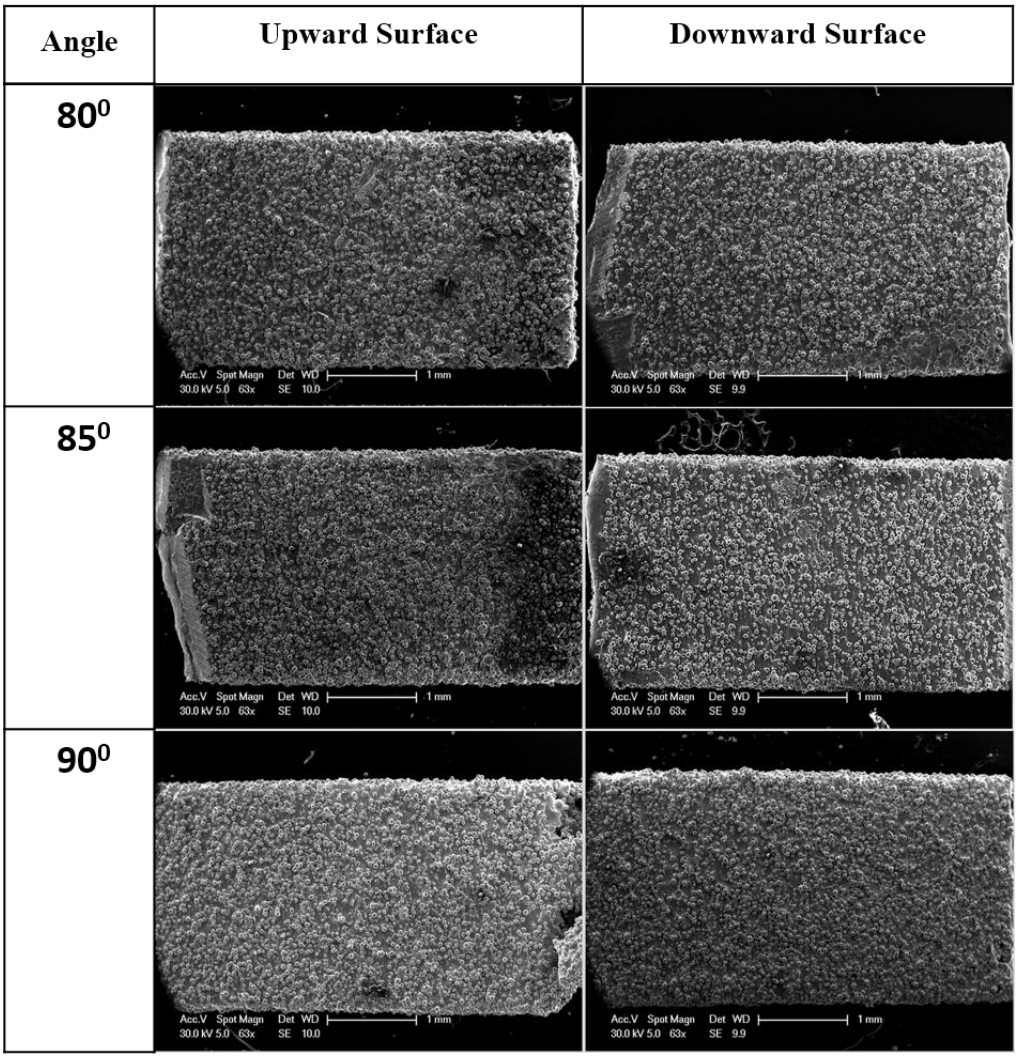

Figure 4.4.4: SEM micrograph shows the surface morphology of Ti6Al4V SLM plates of both upper and lower surface 80 to 90 degrees inclination angle with 5 degrees interval for lower (63X) magnitude.

It is observed from Fig.4.4.1 that with the increase of the inclination angle, there is a corresponding increase in the number of partially melted particles on the upward SLM support-free part from 5 to 90 degrees, and there is no regular trend was observed in terms of partially melted particles on downward surface. It is apparently seen from Fig.8 that there are some distinguishable spaces between particles melted particles from 5 degrees to 70 degrees whereas 75 to 90 degrees the partially melted particles are in dense fashion on the upper surface. We can clearly see that in case of 10 degrees inclination, powders are less densely located on the

SLM plate but in case of 90 degree inclination, powders are quite densely located on the SLM plate. In case of lower surface, it observed that the particially melted particles are located in agglomerate fashion from 5 degrees to 35 degrees where 5 to 15 degrees are particularly highly agglomerated. From 40 to 90 degrees it can be observed that the partially melted particles located densly on SLM plates but there the aglomeration of particles are almost negligible.

It is also observed from Fig.4.4.2 that the sharpness of step edge border is dimmed with the increase of the inclination angle for upper surface of SLM plates from 5 to 45 degrees and no step edge border was found from 50 to 90 degrees. From 5 to 20 degrees the step edge border is completely prominent. In case of lower surface of SLM plates no step- edge border is found in any of the inclination angle. We can also observe that the distance between two step edge borders are also shrinking from 10 degrees to 30 degrees for the upper SLM parts shown by red line in SEM images. The distance between two step edge borders is 335 µm, 235 µm, 219.28 µm, 191.21 µm, 136.84 µm for 10,15, 20,25,30 degrees inclination angle respectively.

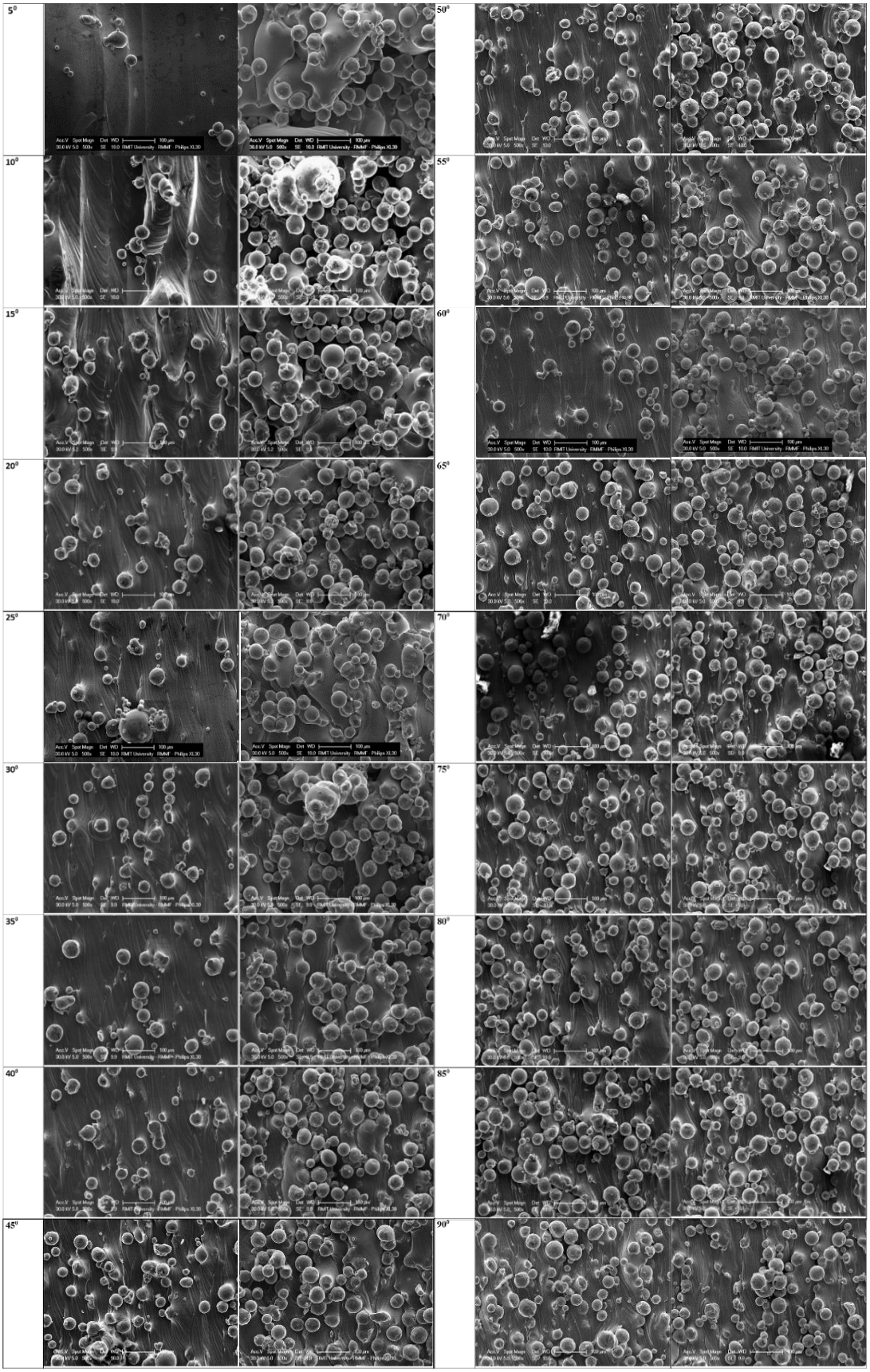

Figure 4.4.5: SEM micrograph shows the surface morphology of Ti6Al4V SLM plates of both upper and lower surface 5to 90 degrees inclination angle with 5 degrees interval for higher

(500X) magnitude.

4.5. Surface Wettability Analysis of Different Inclined SLM parts

Surface wettability has been reported to play a crucial role in terms of biological interaction between implant surface and surrounding host tissue including blood[179]. For example, surface wettability has been found to have the direct link with the osseo-integration process[180]. Surface wettability is measured by the formation of contact angle by a liquid at an interface. However, it is quite difficult to determine the specific contribution of wettability as the solid surface of wettability is directly linked with other features such as surface free energy, surface roughness, surface chemistry, surface geometrical structures[181]. Fig. 4.5.1 (a) and 4.5.1(b) showed the contact angle measurement of the implants for 5 to 90 degrees SLM plate for both upper and lower surface. The figure demonstrates irregularities of SLM plates for both upper and lower surface. Without some exceptions in most of the inclined SLM parts shows hydrophobic surface. The surface wettability of titanium implants fabricated by SLM has previously been reported to have a more hydrophilic contact angle of < 90 degrees[119]. In this case, the contact angle measurements reported for the 5 degrees and 90 degrees of upper SLM parts completely differ from each other due to the geometrical dissimilarity of the surface for the upper surface of SLM plates. In the case of the 90 degrees inclination, a larger number of partially melted particles induces hydrophobicity on the implant surface resulting in an average contact angle of 122^0 whereas 10 degrees case the value of contact angle is 85.66^0. Highest contact angle value 130.150^0 is found in 75 degrees inclination and lowest contact angle value 80.81^0 is found in 10 degrees inclination for upper surface. In case of lower surface, the contact angle value observed for all inclined SLM plates > 90 degrees which means the lower surface of SLM plates reveal the hydrophobic surface. The highest hydrophobicity value 126.15^0 for lower SLM plates is found in 65 degrees inclination angle and lowest hydrophobicity value 101.96^0 is found in 40 degrees inclination angle.

(a)

Angle	Upward Surface	Downward Surface	Angle	Upward Surface	Downward Surface
5^0	91.3 ± 1.78	106.1 ± 0.28	50^0	112.63±1.09455	123.93 ±0.18
10^0	85.66±1.46	122.29 ±1.35	55^0	108.71±0.90	114.30 ± 1.30
15^0	102.45±1.02	105.00±2.20	60^0	118.1 ± 1.42	108.2 ± 0.37
20^0	94.50±1.01	123.36 ±0.85	65^0	116.53±0.90	126.15 ±2.59
25^0	101.0±1.05	109.4±2.41	70^0	120.69±1.20	124.8737 ±0.39
30^0	109.65±0.75	115.58±8.98	75^0	130.15±1.22	116.63 ±1.39
35^0	80.81±1.045	120.43 ±2.52	80^0	122.96±1.09	120.16 ±1.71
40^0	104.70±3.29	101.9681.63	85^0	124.86±0.97	121.4394 ±0.69
45^0	118.86±1.09	119.26 ±2.82	90^0	122.18±0.97	120.33 ±0.43

(b)

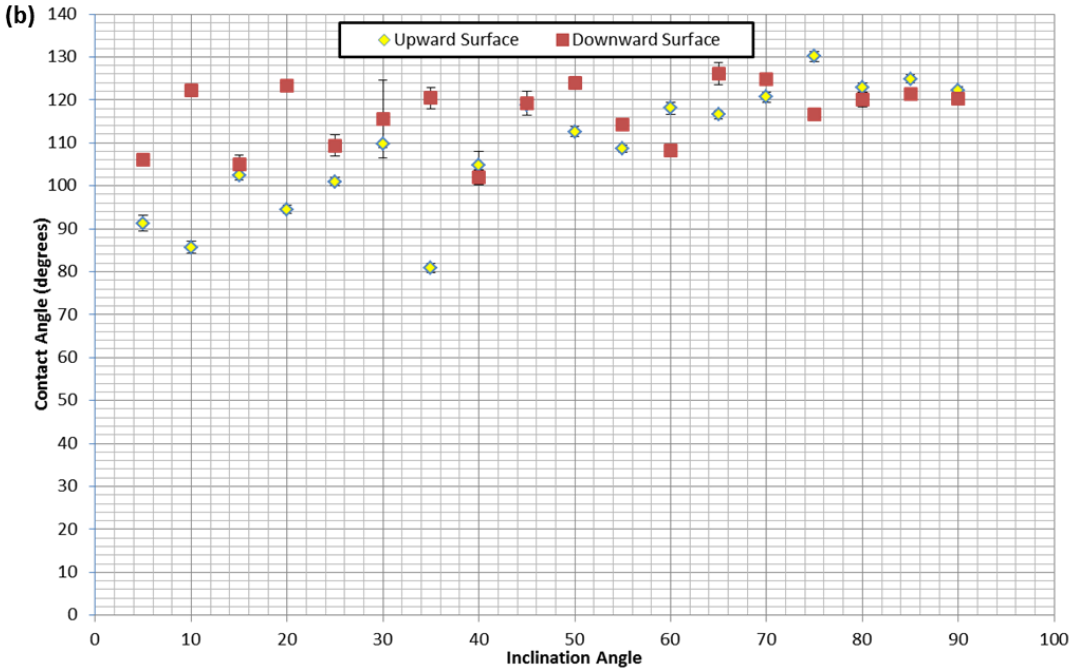

Figure 4.5.1: Surface wettability of 5 to 90 degrees inclination of SLM plated for both upper and lower surface by the contact angle measurement

4.6. Conclusions

1. There is much more percentage of correlation of arithmetic average of roughness (Ra) value for 5 average data points is found on lower surface on the linear, exponential and logarithmic regression line than the upper surface of SLM plates in the change of inclination angle.

2. In case of lower surface of SLM plates from the plots for 5 average data points, the highest R_a value is found for 15 degrees (R_a=12.34μm) inclination angle whereas highest R_a value is found for 10 degrees (R_a=10.32μm) for the upward surface. Lowest R_a value exists (5 degrees) for upward (R_a=4.906μm) and 70 degrees (R_a=7.79μm) for downward surface.

3. In case of lower surface of SLM plates from the plots for 5 average data points, the highest R_q value is found for 15 degrees (R_q=14.66 μm) inclination angle whereas highest R_q value is found for 10 degrees (R_q=12.7μm) for the upward surface. Lowest R_q value exists in 5 degrees inclination angle of upward (R_q=6.93 μm) and 70 degrees of downward (R_q=9.49μm) surface.

4. It is clearly observed from the surface morphology that there is a corresponding increase in the number of partially melted particles on the upward SLM support-free part from 5 to 90 degrees and there is no regular trend was observed in terms of partially melted particles on downward surface.

5. Partially melted particles are in agglomerate fashion from 5 degrees to 35 degrees on downward surface where 5 to 15 degrees are particularly highly agglomerated. From 40 to 90 degrees it can be observed that the partially melted particles located densely on SLM plates but there is not so much agglomeration of partially melted particles.

6. The step edge borders look clearly visible from 5 to 20 degrees and dimmed from 25 to 45 degrees on the upward surface of SLM plates whereas there is no existence of step edge border on any of the inclined downward surface from 5 degrees to 90 degrees.

7. Highest contact angle value 130.150^0 is found in 75 degrees inclination and lowest contact angle value 80.81^0 is found in 35 degrees inclination for upper surface.

8. In case of lower surface, the contact angle value observed for all inclined SLM plates > 90 degrees which means the lower surface of SLM plates reveal the hydrophobic surface. The highest hydrophobicity value 126.15^0 for lower SLM plates is found in 65 degrees inclination angle and lowest hydrophobicity value 101.96^0 is found in 40 degrees inclination angle.

Chapter-Five: Angle defines attachment: Switching the biological response to titanium interfaces by modifying the inclination angle during selective laser melting

5.1. Chapter overview

In the previous chapter, the comprehensive analysis of different surface properties of Ti6Al4V SLM implants with the change of the inclination angle from 5 degrees to 90 degrees for both upward and downward surface has been reported.

As selective laser melted (SLM) metallic additive manufactured implants become common, a key, but overlooked design parameter influencing the surface properties and implant biocompatibility is its inclination angle. In this study, we have fabricated Ti6Al4V implants at three different inclination angles (0 degree, 45 degrees, and 90 degrees) reporting the relationship between cell attachment, surface topography and surface chemistry at each inclination angle. During the SLM process, we show that as the inclination angles increase, there is a corresponding increase in the number of partially melted particles adhering to the surface, greatly affecting the surface topography, morphology, roughness, chemistry, and wettability of the implant. In order to validate the approach, the effect of the surface properties on cell fate was determined. In each case, the overall viability of Chinese hamster ovarian cells (CHO) was found to be statistically indistinguishable; however, the number of spindle cells and their dimension were found to increase significantly at higher inclination angles by applying matlab based program. [1]

*The part of these research findings has been published in ***Materials & Design.***
A. Sarker, N. Tran, A. Rifai, J. Elambasseril, M. Brandt, R. Williams, M. Leary, K. Fox, "***Angle defines attachment: Switching the biological response to titanium interfaces by modifying the inclination angle during selective laser melting"***, Materials & Design 154 (2018) 326-339.

5.2. Introduction

Metals and metal-alloys have a long history of application as bone, cardiovascular implants [73, 85, 86, 182, 183]. Metal and metal alloys including magnesium, iron, titanium, tantalum, titanium-nickel, stainless steels, cobalt (Co) based alloys (CoCrMo) have been applied as potential bone graft, cardiovascular stents [87-90, 184, 185]. Among a wide variety of different metals used for biomedical implants, titanium and its alloy has been used as an effective implant material due to its excellent biocompatibility, strength to weight ratio, corrosion resistance, toughness, and bio-inert oxide surface [91, 186-189]. The titanium alloy presented this paper Ti6Al4V covers about 50% industrial applications of all titanium [190].

Rapid prototyping or additive manufacturing (AM) makes possible the fabrication of biomedical implants with hitherto unprecedented structural complexity and prescribed microstructure and macrostructure [21, 67, 82, 95]. Additive manufacturing offers numerous commercial technologies for the fabrication of robust components via a layer-by-layer design associated with a computer model [37, 44, 191]. This control over the shape, size and mechanical properties enables the investigation of individual implant parameters such as porosity, pore size, shape and permeability [31]. Metal based AM is being widely used for tissue engineering applications for manufacturing patient-specific orthopaedic, cardiac implants, [73, 192-198] and the biological performance of synthetic bone grafts [31].

Selective laser melting (SLM) is a Metallic AM (MAM) process that creates parts by scanning powdered materials using the thermal energy supplied by a focused and computer-controlled laser beam based on a digital representation of the intended implant geometry. SLM is a layer-by-layer material addition technique that allows the generation of complex 3D parts by selectively melting successive layers of metal powder [37]. With reference to commercial MAM technologies, SLM is characterized by medium productivity, good repeatability and

medium to high surface quality [21]. The SLM process was reported to be capable of fabricating implants of several pure titanium and titanium based alloys for implants such as Ti6Al7Nb [45], Ti-24Nb-4Zr-8Sn [44],Ni-Ti [46], Ti-13Nb-13Zr [47] other β titanium alloys [48] and most importantly Ti6Al4V [49, 50]. Recently, it was reported that SLM has the ability to fabricate porous bio-inert Ti6Al4V structures with high control and reproducibility in terms of their morphological and mechanical properties [51] and showed excellent biocompatibility [52].

Significant research on the design of cellular lattice structures has shown potential for controlling dimensional accuracy, mechanical properties and associated biocompatibility [44, 173, 199, 200]. The final surface topography, morphology, chemistry, and wettability of the implants can be altered to adjust the interaction between the implant and the host tissue [148-151, 201]. These properties are dependent on the associated SLM process parameters [202-205]. Laser power, scanning speed, scanning pattern, hatch spacing, layer thickness, powder bed temperature and working atmosphere are the most critical processing parameters for the SLM process, and several groups focused their research on optimizing these parameters for the final desired parts [145-147, 206].

Cellular lattice structures fabricated by SLM process are the combination of numerous strut elements, each with specific inclination angle to the SLM platen. Here, for the first time, we report the relationship of the inclination angle of the implant of 0, 45 and 90 degrees with their surface morphology, surface wettability, and surface chemistry; and, demonstrate that these parameters have a direct relationship with biocompatibility, cell attachment and cell morphology. This work will have significant impact on the design and fabrication of these materials for biomedical applications and the fabrication of the next generation of just-in-time, patient specific implants.

5.3. Experimental Section

The samples were fabricated according to chapter-3.3 – Materials and Methods section outlined in 3.2, characterized according to section 3.4, mammalian cell culture and cell morphology analysis according to section 3.5.

5.4. Results and Discussion

5.4.1. Design and Fabrication of SLM Ti6Al4V Alloy with Different Inclination Angles

Figure 5.1(a) shows the SLM laser *scanning* strategy for a single layer of the 10×10 mm cross-section specimen. The scanning strategy consists of a perimeter laser scan which is then in-filled using a raster scan. Fig. 5.1(b) shows the stairstep effect inherent to SLM process due to the effect of layer-wise manufacture and the associated inclination to the build plate, α. Where a reduction in α tends to increase the associated step size. Particle size distribution of the Ti6Al4V powder used to fabricate test specimens, Fig. 5.1(c), has parameters: D_{10}=35.1, D_{50}=48.9, D_{90}=69.7 µm; and displays a surface morphology that is spherical in shape with some irregularities, Figure 5.1(d), as is typical for gas atomized powders. SLM Ti6Al4V implant specimens were fabricated with inclination angle α of 0, 45, and 90 degrees, and are supported by frangible support structures shown in Fig. 5.1(e). SLM process parameters are defined in the materials and method section. SLM manufacture results in specific geometric defects, including raised edge features associated with perimeter laser scan, and partially fused powder shown in Fig. 5.1(f) by CT scanning.

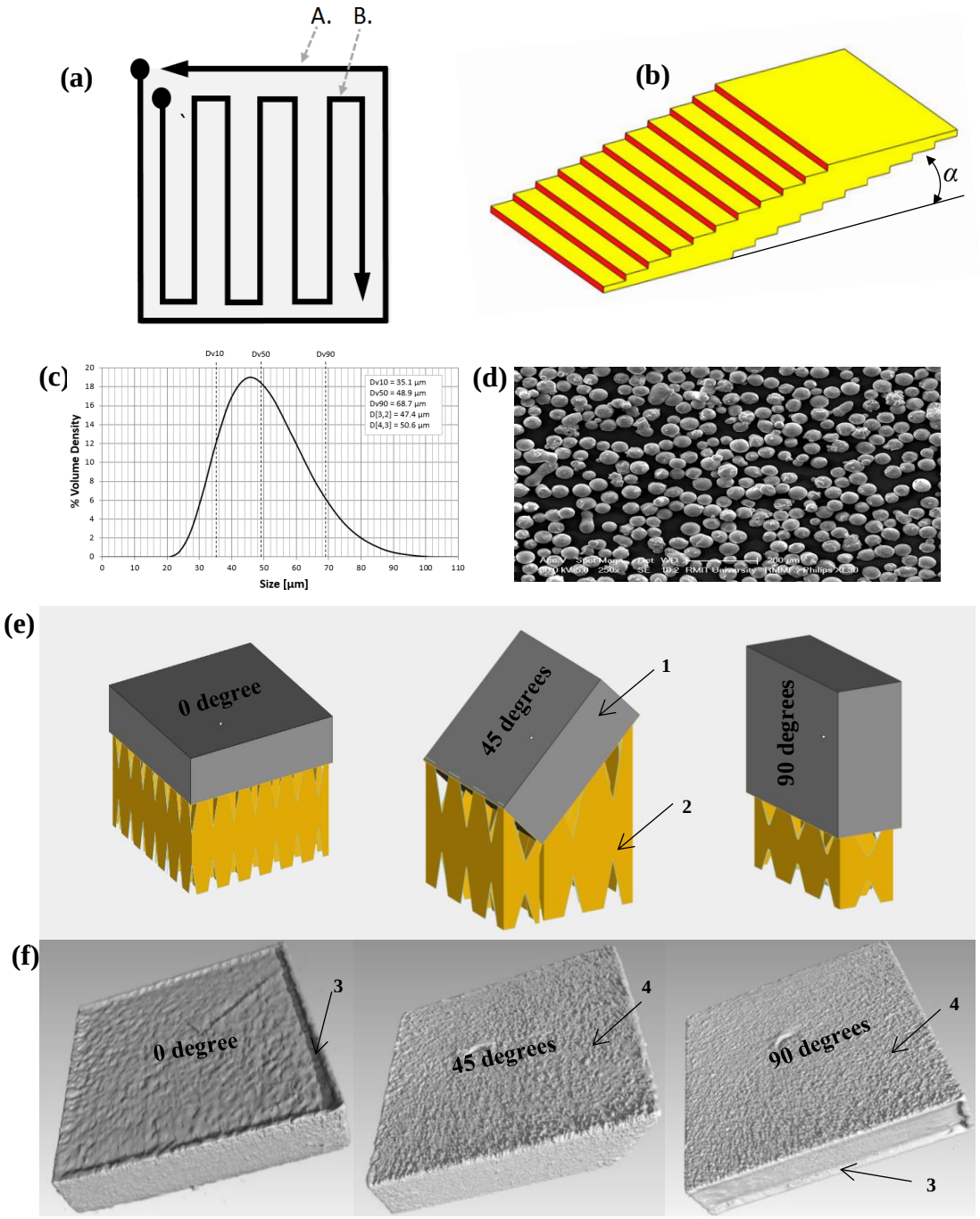

Figure 5.1: (a) Perimeter laser scan (solid line). Raster (fill) laser scan (broken line), circle indicates laser path initiation. Arrow head indicates laser trajectory, (b) stair-step effect on inclination angle, (c) Size distribution of Ti6Al4V raw powder, (d) SEM micrograph shows the surface morphology of raw Ti6Al4V powder, (e) Design of SLM printed Ti6Al4V Alloy of 0, 45 and 90 degrees inclination showing the part and its support structure, (f) CT-scanned images of 0, 45 and 90 degrees inclined part. Legend: 1). Fabricated component, 2). Supporting structure, 3). Geometric defect associated with perimeter laser scan, 4). Adhered powder particles.

5.4.2. Surface Topography and Surface Wettability of Selective Laser Melted Ti6Al4V of Different Inclinations

The 2D and 3D surface texture of Ti6Al4V implants of 0, 45, and 90 inclination angles are shown in Fig.5.2(a). It is clearly observed that the number of partially melted titanium particles increases with the increase of the inclination angle(α) on the implant surface. In case of 0 degree, the rippling effect is found from the surface texture during the selective laser melting process. The bullet-shaped like appearance is also noticed on the surface of 0-degree inclination which is marked by white arrow in Fig.5.2(a). In case of 45 degrees inclination, we can observe very dim step edge border due to the stair-step effect and no step edge is observed in 90 degrees as there is no effect of stair-step [156].

It is clearly observed that in the case of 0degree inclination angle only few partially melted titanium particles are adhered on the sample. With the increase of inclination angle, considerably more partially melted particles are visible on the surface of the implants. The 90 degrees inclination angle part reveals the dense population of partially melted particles on the implant surface.

Surface profile properties such as maximum peak height (R_p), maximum valley depth (R_v), arithmetic average of roughness profile (R_a), root mean square deviation of the roughness profile (R_q), skewness of the roughness profile (R_{sk}), kurtosis of the roughness profile (R_{ku}) are obtained using a profilometer which are shown in Figure 5.2(b) based on Figure 5.3.1, 5.3.2 & 5.3.3. For the 0degree inclination, it is found that the average peak height (R_p) is 10.48 μm and average depth of the valley (R_v) is 7.70 μm. For 45, and 90 degrees inclination, the average peak heights are 20.3 μm, 24.8 μm respectively and the average depth of the valley is 18.28 μm and 26.18 μm respectively. The increase of the average peak height and valley depth with the increase of the inclination angle can be explained by the increasing number of partially melted particles on the implant surface.

The surface arithmetic average of roughness profile (R_a), root mean square deviation of the roughness profile (R_q) for the 0, 45, and 90 degrees inclination angles are shown in Fig. 5.2(b). Both R_a and R_q values increase with increasing inclination angle(α). The highest arithmetic average of roughness (7.25 μm) and root mean square deviation of the roughness profile (8.83 μm) have been found for 90 degrees inclination. The trend of increasing roughness with the inclination may be explained by the increasing concentration of partially melted particles and stair-step effect[156]. In case of the 0degree inclination, few partially melted particles adhered on the surface; consequently, the surface morphology and roughness, R_a value for the 0degree inclination is 2.53 μm, remains largely uninfluenced by these few particles. In the case of 90 degrees, R_a value is 7.25 μm which is higher than observed at 45 degrees (R_a=5.96) and 0 degree (2.53 μm), respectively, because of no stairstep effect and higher amount of partially melted particles on the surface of the implant which is shown by white arrow in Fig. 5.2(a). Skewness of the roughness profile describes the asymmetry of the profile relative to the mean plane. From the Fig. 5.2(b), it is observed that the skewness of the roughness profile (R_{sk}) is greater than 0 for all inclination angles, indicating that peaks predominate over the valleys on surface. Finally, kurtosis of the roughness profile has been used to describe the sharpness of the surface, i.e. sharpness of the peaks and valleys [207, 208]. When the kurtosis is higher than 3, the surface is defined as

spiky, meaning that the peaks and valleys are very high and if the kurtosis is lower than 3 that means the surface is bumpy [209]. In this case, the 0, and 45 degrees inclination angle are associated with a spiky surface as R_{ku} value is 3.33 and 3.26 respectively, whereas the surface of 90 degrees inclination angle is bumpy, as R_{ku} is 2.43. The bumpy surface for 90 degrees inclination angle implant is associated with the densely located partially melted titanium particles.

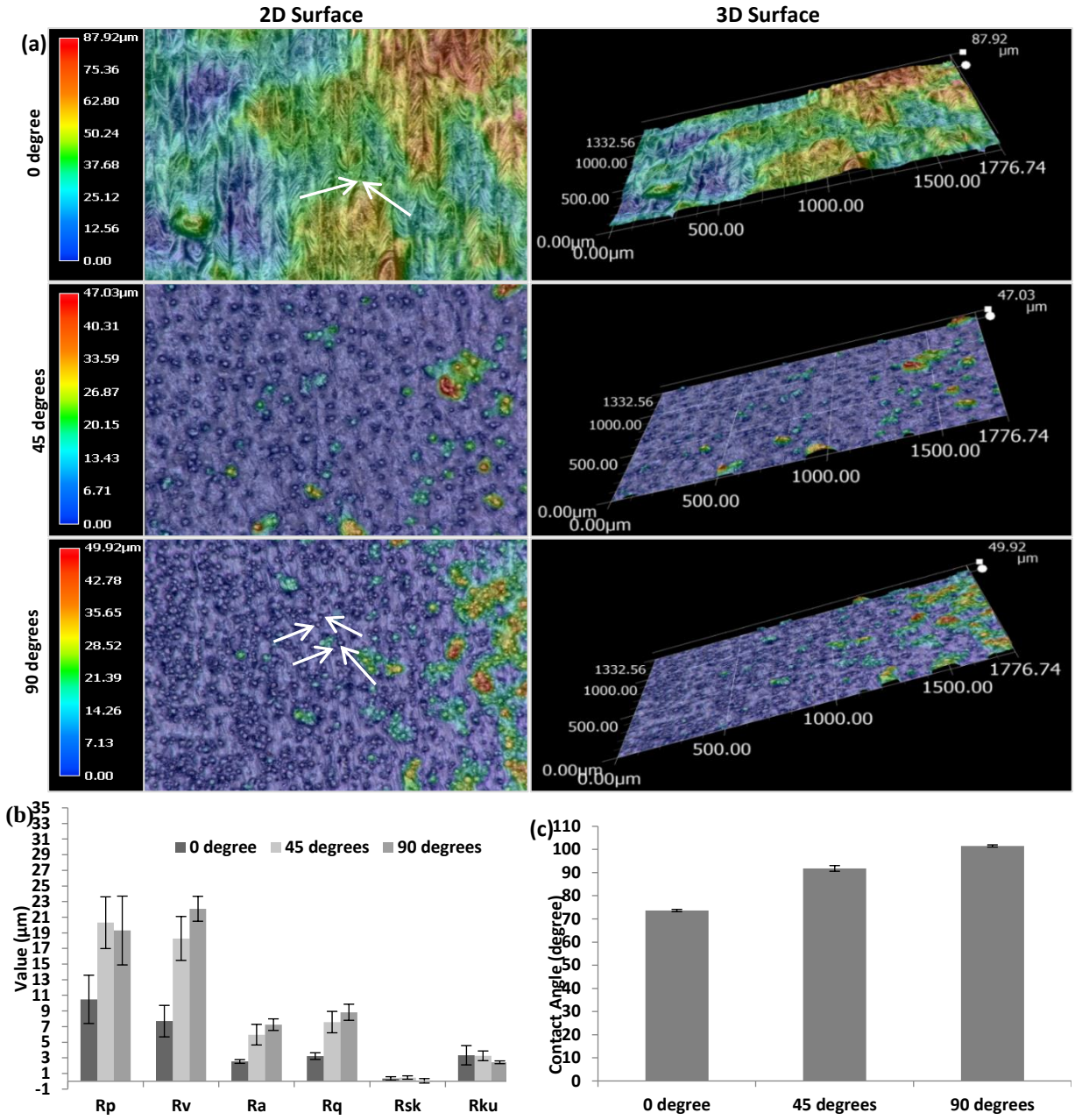

Figure 5.2: (a) 2D surface profile and 3D surface profile of 0, 45 and 90 degrees inclined implant obtained by the digital microscope showing topographical changes as the angle increases, (b) Surface profile properties such as surface maximum peak height (R_p), maximum valley depth (R_v), arithmetic average of roughness profile (R_a), root mean square deviation of the roughness profile (R_q), skewness of the roughness profile (R_{sk}), kurtosis of the roughness profile (R_{ku}) obtained by profilometer, (c) Surface wettability of 0, 45 and 90 degrees inclination by the contact angle measurement suggesting that the samples become more hydrophobic as the inclination angle increases.

Figure 5.3.1: Surface profile properties for 0 degree inclination such as maximum peak height (R_p), maximum valley depth (R_v), arithmetic average of roughness profile (R_a), root mean square deviation of the roughness profile (R_q), skewness of the roughness profile (R_{sk}), kurtosis of the roughness profile (R_{ku}) obtained by profilometer for 5 consecutive scans

Figure 5.3.2: Surface profile properties for 45 degrees inclination such as maximum peak height (R_p), maximum valley depth (R_v), arithmetic average of roughness profile (R_a), root mean square deviation of the roughness profile (R_q), skewness of the roughness profile (R_{sk}), kurtosis of the roughness profile (R_{ku}) obtained by profilometer for 5 consecutive scans.

Figure 5.3.3: Surface profile properties for 90 degrees inclination such as maximum peak height (R_p), maximum valley depth (R_v), arithmetic average of roughness profile (R_a), root mean square deviation of the roughness profile (R_q), skewness of the roughness profile (R_{sk}), kurtosis of the roughness profile (R_{ku}) obtained by profilometer for 5 consecutive scans.

Surface wettability has been reported to play a crucial role in terms of biological interaction between implant surface and surrounding host tissue including blood [179]. For example, surface wettability has been found to have the direct link with the osseo-integration process. [180] Surface wettability is measured by the formation of contact angle by a liquid at an interface. However, it is quite difficult to determine the specific contribution of wettability as the solid surface of wettability is directly linked with other features such as surface free energy, surface roughness, surface chemistry, surface geometrical structures [181]. Fig. 5.2(c) showed the contact angle measurement of the implants for 0, 45, and 90 degrees inclination. The

0degree inclination specimen demonstrates an average contact angle of 74 degrees, with the 45 degree and 90 degrees parts progressively more hydrophobic with average contact angles of 92 and 102 degrees, respectively. The surface wettability of titanium implants fabricated by SLM has previously been reported to have a more hydrophilic contact angle of < 90 degrees [119]. In this case, the contact angle measurements reported for the 0, 45, and 90 degrees inclined implants differ from each other due to the geometrical dissimilarity of the surface. In the case of the 90 degrees inclination, a larger number of partially melted particles induces hydrophobicity on the implant surface resulting in an average contact angle of 102 degrees.

Fig. 5.4.1(a) shows obtained surface morphologies of the implants of various inclination angles (0, 45, and 90 degrees). It is clearly observed that with the increase of inclination angle(α) there is an increase in the number of partially melted particles adhered to the implant surface. The quantification of partially melted particles number is shown in Fig. 5.4.1(c) based on the same depth of field SEM image of 500X magnifications. A custom Matlab script was applied based on Fig. 5.4.1(a) to quantify the numbers of partially melted particles. For the 0, 45, and 90 degrees inclination angles, the number of partially melted particles is 5, 52 and 71, respectively; and the associated average size of partially melted particles is 27.76, 35.79, 38.40 μm, respectively. The surface areas of 0, 45, and 90 degrees inclined implants are shown in Fig.5.4.1(d) based on the same depth of field SEM image of 500X magnification from Fig. 5.4.1(a). It was observed that with the increase of the inclination, there is a corresponding increase in the number of partially melted particles. For 0degree inclination, bullet shaped appearance is observed presumably due to slower cooling in the centre of each track which can be confirmed from SEM image of high magnification (500X) which is shown by white arrow. From the 45 degrees inclined surface morphology, we can observe the step edge due to stairstep effect which is shown by white arrow. However, in the case of the implant surface for the 90 degrees inclination angle, we can see the surface is almost covered with partially melted

particles having no step edge border as there is no effect of stair-step. From the high magnification images, we can see the sizes and shape of the partially melted particle are not in uniform for all inclination angles (0, 45, and 90 degrees).

The phenomena of partially melted particles occurs by three mechanisms: (1) thermal diffusion occurs due to the significant temperature difference between loose powder and solidified material, leading to local fusion of powder to the edge of the scan track of the implant surface; [171, 172] (2) balling phenomenon in SLM process which is responsible for forming particles on the laser melted surface; [144] (3) the stair-stepping effect of the implant of varying inclination angles are partially built on the loose powder; and thus some metal particles below each layer will be totally or partially melted and then bonded on the bottom of the layer [173]. Fig. 5.4.1(b) shows the EDX spectrum of Ti6Al4V of 0, 45, and 90 degrees inclination angle. The EDX spectrum confirms the presence of metal titanium, aluminium, vanadium on the surface of Ti6Al4V implants for all inclinations which has also been shown in the Fig. 5.5.1, Fig.5.5.2, Fig. 5.5.3 by EDX mapping.

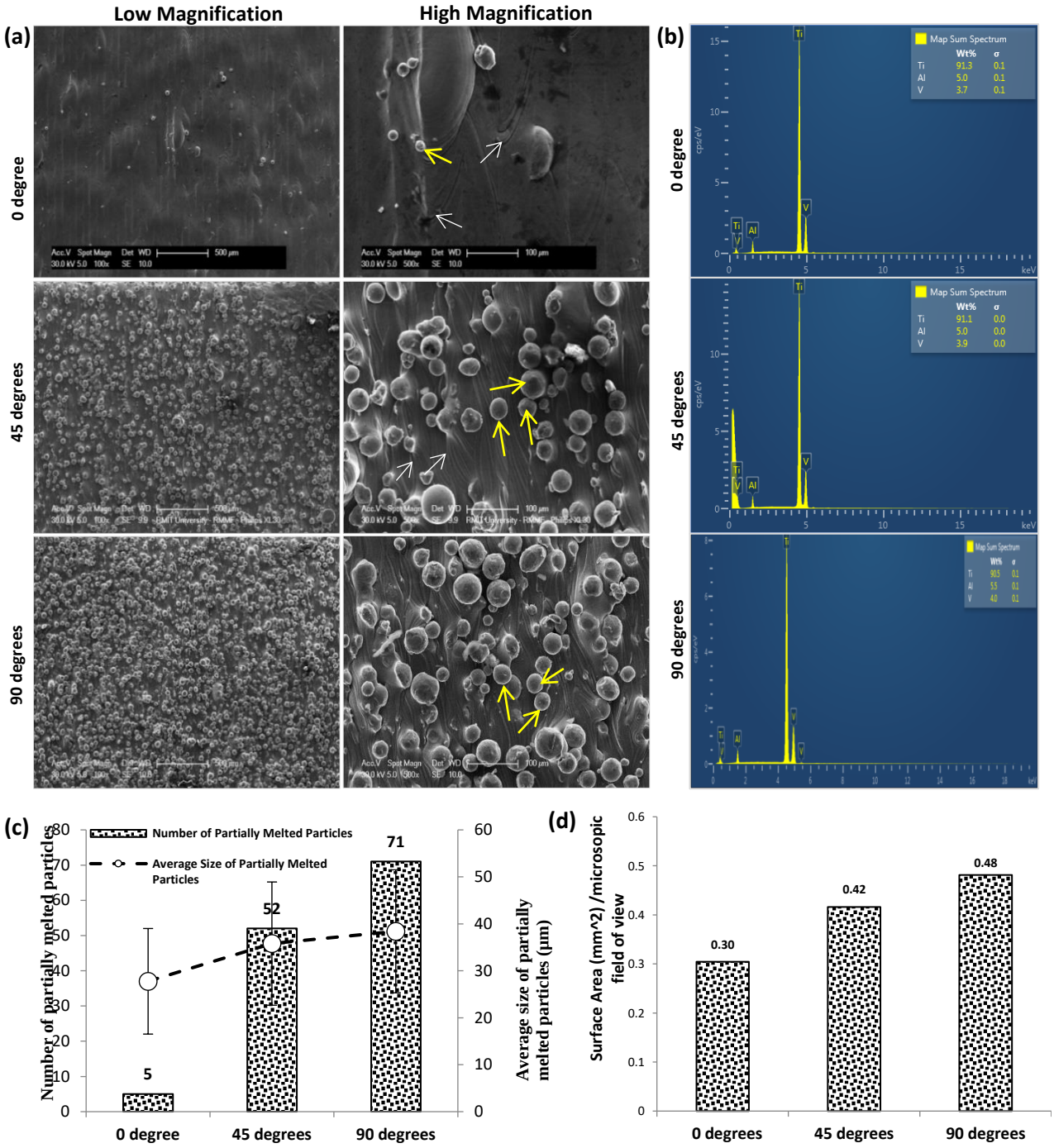

Figure 5.4.1: (a) SEM micrograph shows the surface morphology of 0, 45 and 90 degrees inclination angle upward surface for both low (100X) and high magnitude (500X) magnification, partially melted titanium particles are indicated by an arrow on the high magnification (500X) image, (b) EDX spectra for 0, 45, and 90 degrees inclination confirms the presence of Ti, Al and V on the surface, (c) Quantification and average size measurement of partially melted particles by image analysis of high magnification SEM images for same field of view (Figure 5.4.2), (d) Surface area measurement of 0, 45 and 90 degrees inclination for the high magnification SEM image.

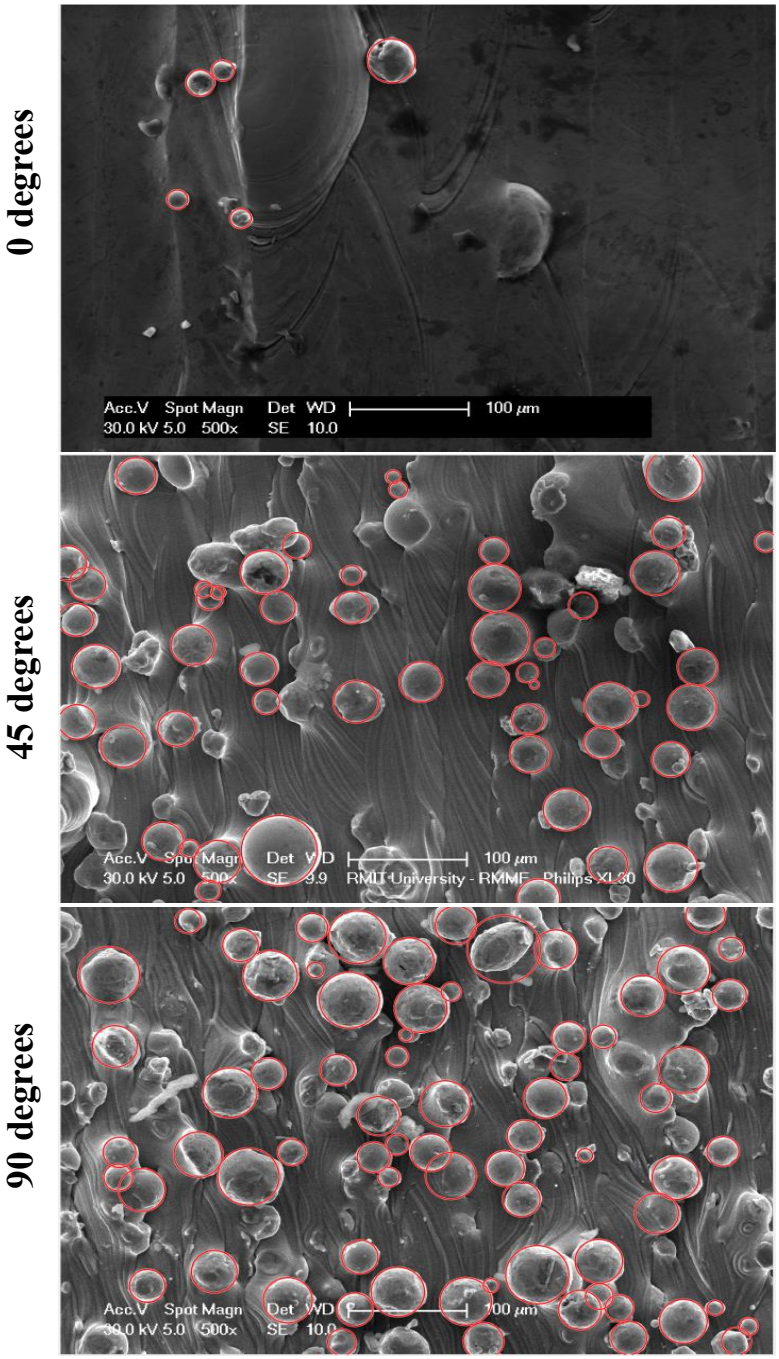

Figure 5.4.2 : Quantification and average size measurement of partially melted particles for 0, 45, and 90 degrees inclination inclinations by Matlab programming

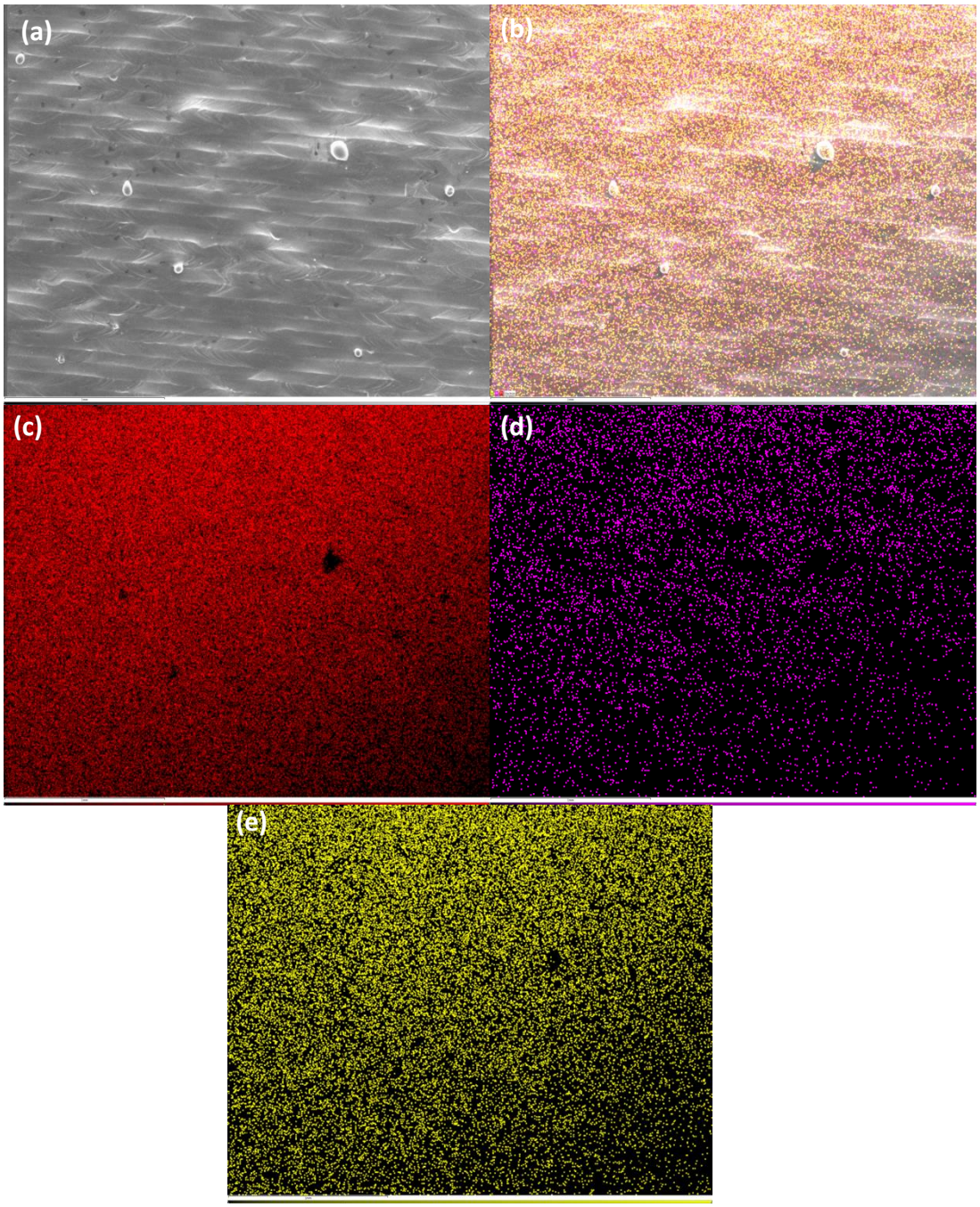

Figure 5.5.1: EDX Mapping for 0degree inclined part showing SEM image (a), superimposed image (b), Titanium colour map(c), Aluminium colour map (d), Vanadium colour map(e).

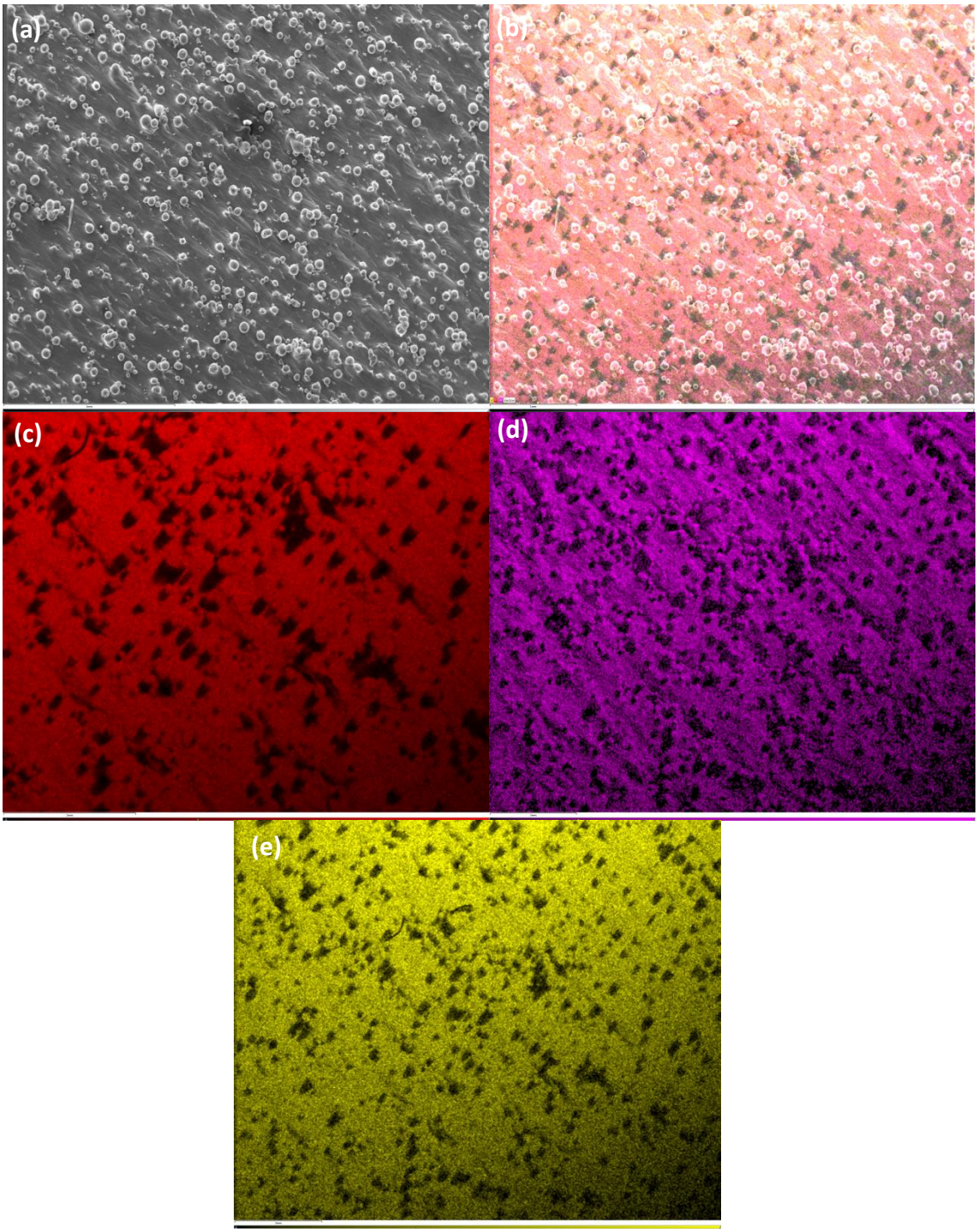

Figure 5.5.2: EDX Mapping for 45 degrees inclined part showing SEM image (a), superimposed image (b), Titanium colour map(c), Aluminium colour map (d), Vanadium colour map(e).

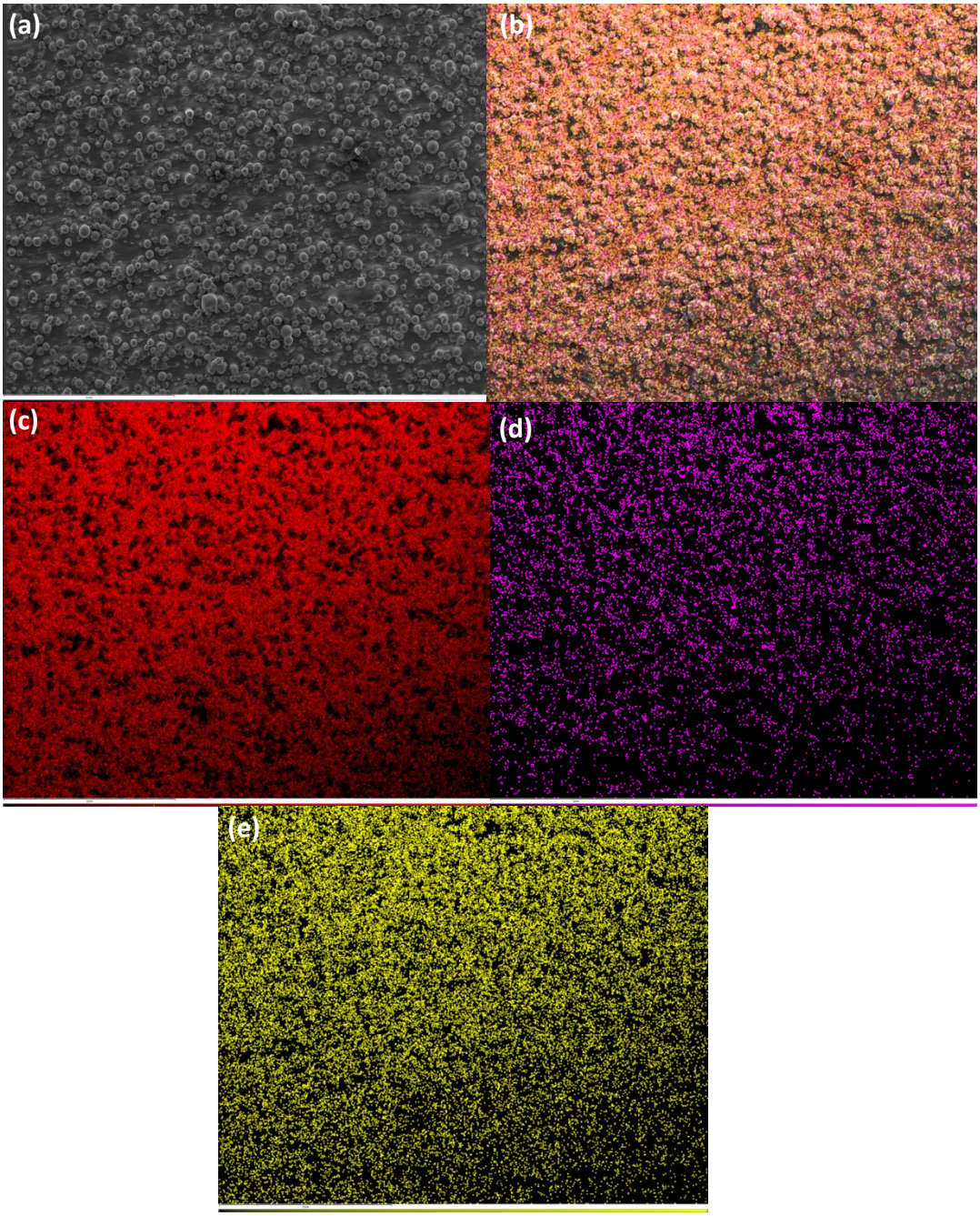

Figure 5.5.3: EDX Mapping for 90 degrees inclined part showing SEM image (a), superimposed image (b), Titanium colour map(c), Aluminium colour map(d), Vanadium colour map(e).

5.4.3. Surface Chemistry Analysis of Inclination angles of SLM Ti6Al4V Implants

Fig. 5.6.1(a) shows the XPS survey spectra of the detected elements for 0, 45, and 90 degrees inclined implants which confirmed the presence of carbon, nitrogen, oxygen and metals (titanium and aluminium). Vanadium was not detected on any surface which might be explained with the rough nature of implant surface which retarded the signal by reducing the electron counts reaching the detector during XPS characterisation. Fig. 5.6.1(b) shows the average relative atomic percentage of the detected elements from the high-resolution spectra for five different spots on 0, 45, and 90 degrees inclination samples. The extensive percentage of carbon element is detected which is related to the environment maintained at SLM machine and the collection process of sample from the machine. The samples exhibited the dominant signals from Ti, O and C with the weak contribution from Al, V and N. The ratios of Ti/O for 0, 45, and 90 degrees inclination are 0.2071, 0.2100 and 0.6598 respectively. The higher magnitude of Ti/O ratio for 90 degrees could be explained with the increasing amount of partially melted particles on the sample. The ratio for Al/O is 0.1440, 0.0982, and 0.1519 for 0, 45, and 90 degrees inclined samples. Fig. 5.6.1(c) shows the high-resolution spectra of Titanium (Ti2p) for all three implants (0, 45 and 90 degrees). The spectra can be fitted with sets of binding energies that confirm the presence of several oxidation states of Ti2p. These are TiO_2, TiO, Ti_2O_3 and Ti metallic state with TiO_2 being the most dominant. The binding energies (E) values are listed into the Table 5.1.

Ti2p State	Binding Energy(eV) for 0 degree	Binding Energy(eV) for 45 degrees	Binding Energy(eV) for 90 degrees
$TiO_2(Ti^{4+})$	458.31, 464.07	458.19, 464.05	458.22, 464.18
$TiO(Ti^{2+})$	455.11, 461.26	455.09, 461.57	455.64, 462.15
Ti_2O_3 $((Ti^{3+})$	456.35, 462.64	456.59, 462.48	456.73, 462.79
Ti metallic state	453.73, 458.61	453.64, 459.64	453.87, 459.87

Table 5.1: Binding Energy of Ti2p for different inclination inclined implants

Fig. 5.6.2 depicts the depth profile for titanium and oxygen, respectively. Fig. 5.6.1(d) shows the average relative atomic percentage of different oxides (TiO_2, TiO and Ti_2O_3) and Ti metallic state. It is clearly found that TiO_2 is the most dominating among different titanium oxides for all samples. The relative atomic percentage of TiO_2 for 0, 45, and 90 degrees inclinations are 67.80%, 73.00% and 72.57% respectively. The relative atomic percentage of TiO for 0, 45, and 90 degrees inclinations are 7.23%, 11.45%, 5.77%. Higher amount of Ti_2O_3 have been found for 0degree (8.52%) than 45 degrees (5.11%) and 90 degrees (6.23%) inclination inclinations. The relative atomic percentage of Ti metallic state for 0, 45, and 90 degrees inclination inclinations are 16.44%, 10.44% and 15.43% respectively. Figure 5.6.1(e) shows the graph for TiO_2 layer thickness. The thickness of the TiO_2 oxide film on the 0, 45 and 90 degrees inclinations is calculated using the Strohmeier equation: [210]

$$do(nm) = \lambda oxide \sin\theta \ln \left[\left(\frac{\mathrm{Ioxide} * \lambda \mathrm{metal} * \mathrm{Nm}}{\mathrm{Imetal} * \lambda \mathrm{oxide} * \mathrm{N0}} \right) + 1 \right]$$

where *do* is TiO2 layer thickness; θ is the photoelectron output angle; λ_{oxide} (1.73nm) and λ_{metal} (3.08) are the mean free paths of photoelectrons in the substrate and the oxide layer, I_{metal} and I_{oxide} are the intensities of the titanium components in the metallic state and as Ti from the Ti2p peak, Nm and No are the volume densities of titanium atoms in metal and oxide. [211] The thickness of TiO_2 layer is found to be 3.92 nm, 6.08 nm and 5.26 nm, respectively, for 0, 45, and 90 degrees inclined part.

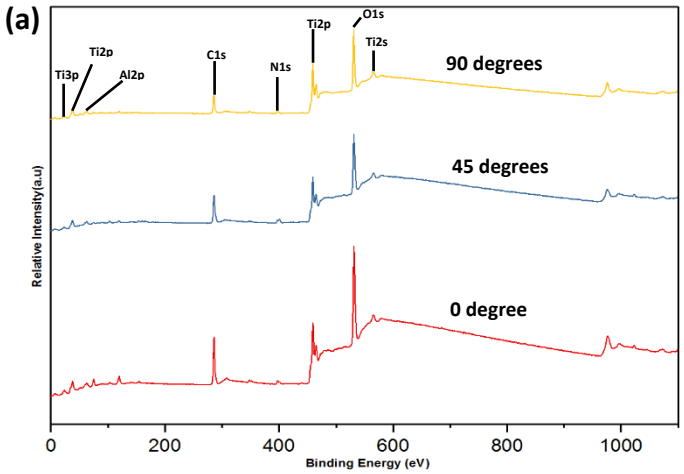
(a)
Ti3p
Ti2p
Al2p
C1s
N1s
Ti2p
O1s
Ti2s
90 degrees
45 degrees
0 degree
Relative Intensity(a.u)
0
200
400
600
800
1000
Binding Energy (eV)

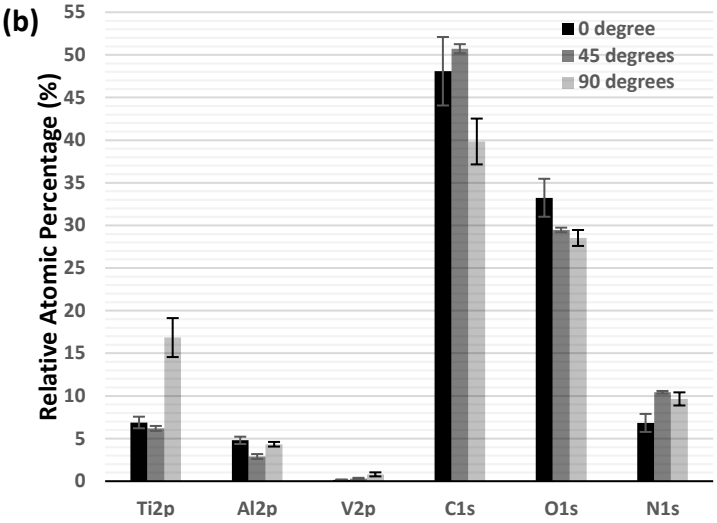
(b)
0 degree
45 degrees
90 degrees
Relative Atomic Percentage (%)
Ti2p
Al2p
V2p
C1s
O1s
N1s

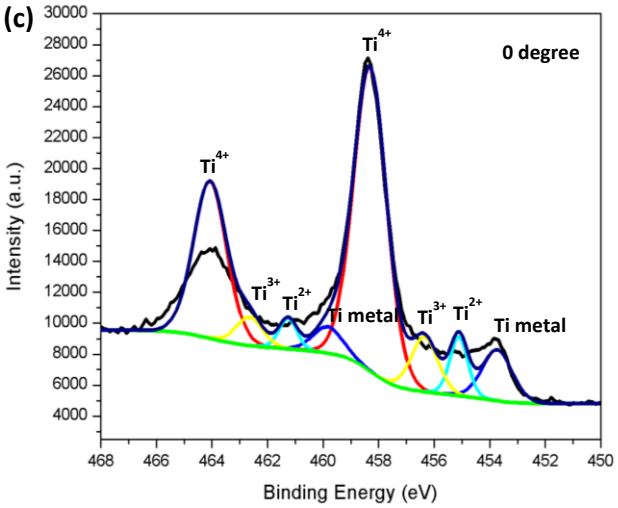
(c)
0 degree
Ti4+
Ti3+
Ti2+
Ti metal
Intensity (a.u.)
Binding Energy (eV)

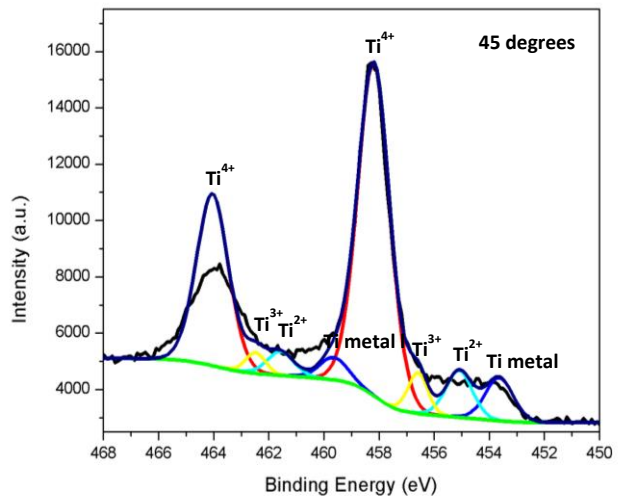
45 degrees
Ti4+
Ti3+
Ti2+
Ti metal
Intensity (a.u.)
Binding Energy (eV)

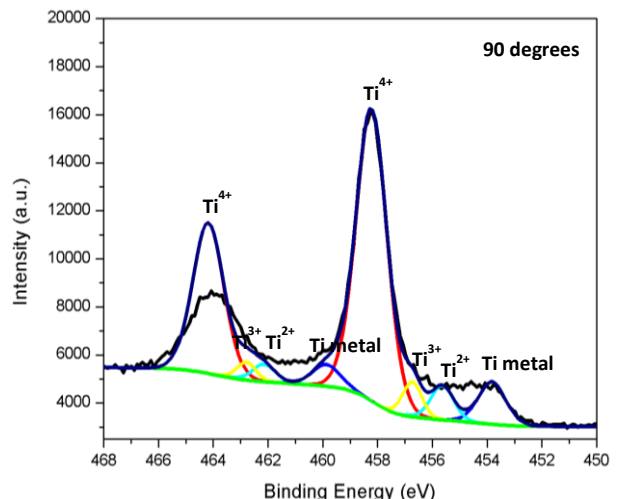
90 degrees
Ti4+
Ti3+
Ti2+
Ti metal
Intensity (a.u.)
Binding Energy (eV)

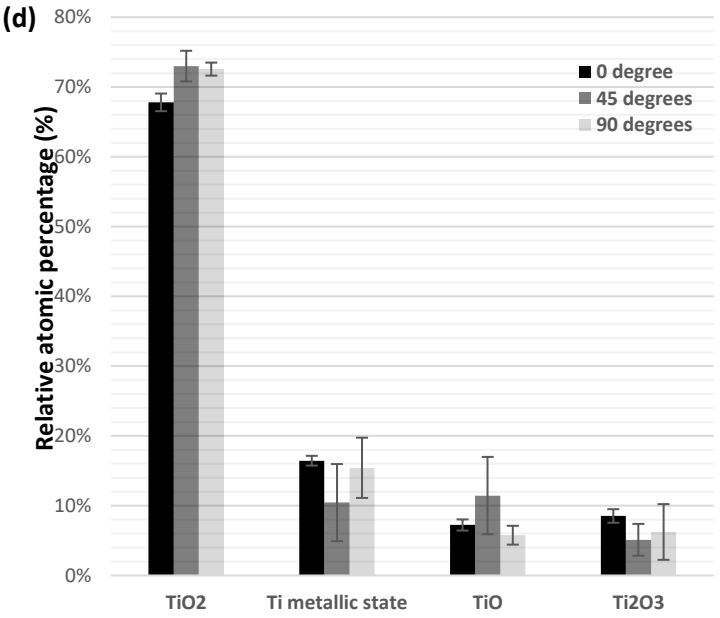
(d)
0 degree
45 degrees
90 degrees
Relative atomic percentage (%)
TiO2
Ti metallic state
TiO
Ti2O3

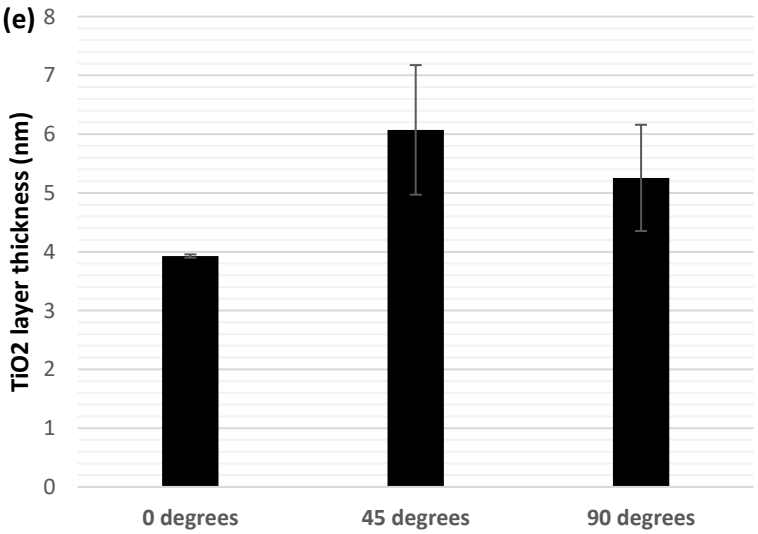
(e)
TiO2 layer thickness (nm)
0 degrees
45 degrees
90 degrees

Figure 5.6.1: (a) Survey spectra of 0, 45 and 90 degree inclinations of Ti6Al4V implants showing Ti, Al, C, N and O, (b) Relative atomic percentage of elements detected using XPS for 0, 45 and 90 degrees inclination for five different spots, (c) High resolution spectra of Ti2p region for each representative spot of 0, 45 and 90 degrees inclination inclinations,(d) Relative atomic percentage of different titanium oxides(TiO_2,TiO, Ti_2O_3) and Ti metallic state detected using XPS for 0, 45 and 90 degrees inclinations, (e) Average TiO_2 layer thickness measurement from the high resolution spectra of Ti2p.

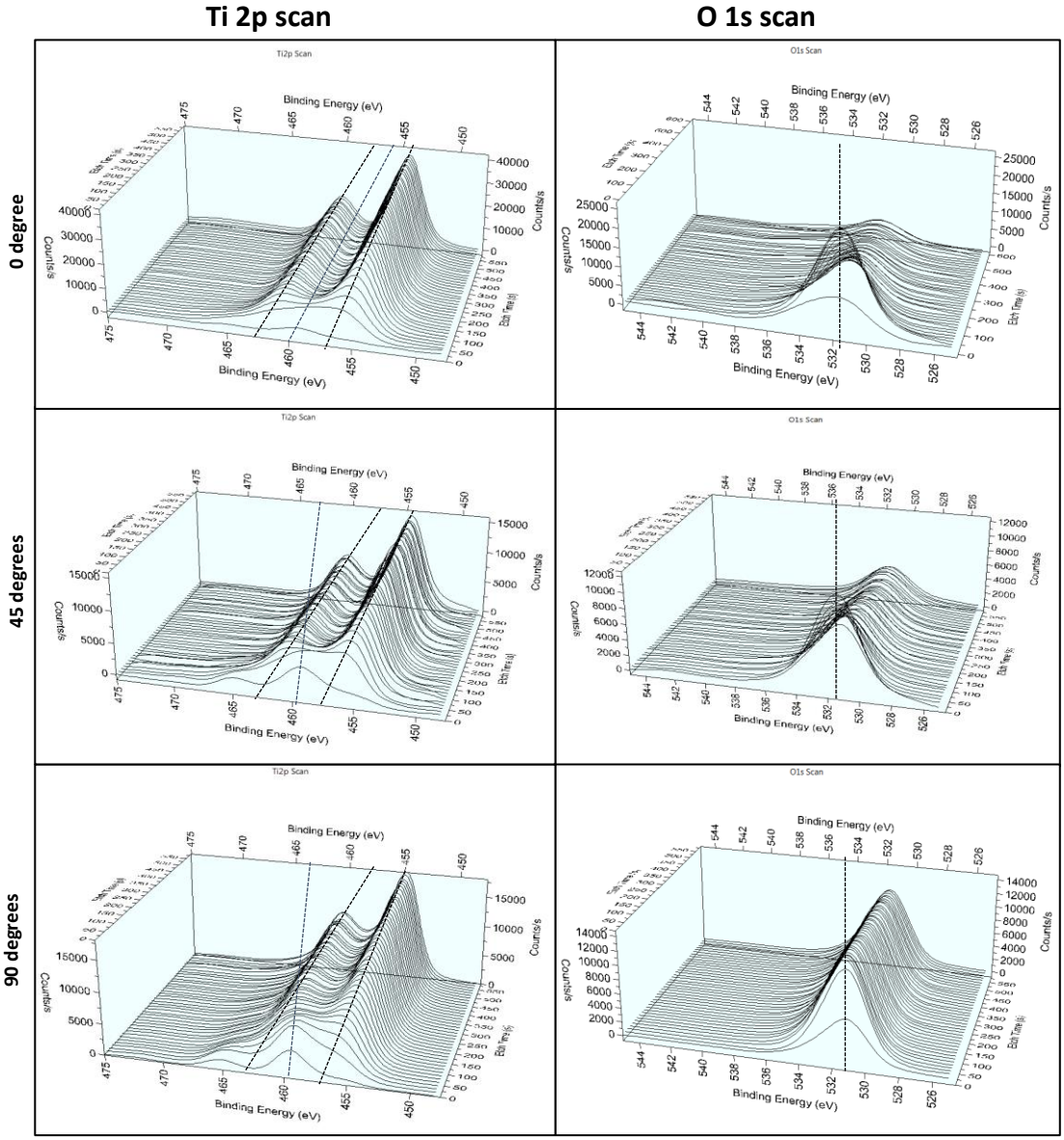

Figure 5.6.2 **:** Depth Profiles of Ti2p and O1s regions for 0, 45, and 90 degrees inclination inclinations, depth profiling was performed at every 15.031 seconds from 0 to 586.73s.A clear transformation of oxide to pure metal can be observed for all inclination inclinations.

5.4.4. Cellular Viability and Attachment Behaviour with Inclined Ti6Al4V Implants

Fig. 5.7.1(a) demonstrates the cell viability of 0, 45, and 90 degrees inclination of Ti6Al4V implants after 24 hours, 72 hours and 96 hours of incubation using the MTS assay. CHO cells were selected because they were a cell line that is regular used to test material cytotoxicity[212]. CHO cells were seeded on three inclinations at a density of $4*10^4 cell/cm^2$ and was noted that after 24 hours, the number of cells had exceeded the number in the initial stage in all three inclinations. There was no statistical significance found in terms of the cell viability for 0, 45, and 90 degrees inclinations than control after 24 hours. The number of viable cells present on 0, 45, and 90 degrees implants are not statistically significant different than the control after 72 hours and 96 hours of incubation. This indicates that the substrates, regardless of the inclination angle pose no adverse effect on cell viability.

Fig. 5.7.1(b) shows the SEM images of the cell attachment on the surface of 0, 45, and 90 degrees inclination after 24 hours. Cells have been found to be well adhered for all inclinations. CHO cells, as shown in Fig. 5.7.1(b) displayed almost rounded shape which can be confirmed from both 2000X and 4000X magnification of SEM micrographs in the case of the 0degree sample. For the 45 degrees and 90 degrees inclined implants, the cells appeared elongated and exhibited a spindle shaped appearance especially across the partially melted particles. Fig. 5.7.1(c) shows the confocal images of the morphology of CHO cells on the surface of 0, 45, and 90 degrees inclinations after 72 hours of incubation. The CHO cells on 0-degree inclined surface exhibited spherical morphology. On the 45, and 90 degrees inclined parts, there appeared to be more filopodia, indicating better spreading on these samples. Several groups have reported that SLM manufactured Ti6Al4V implants are biocompatible and exhibited well in-vitro cell attachment and cell proliferation behaviour. [52, 168, 213] The increased surface roughness and amount of spherical shaped partially melted particles on the surface of the

implants with the increase of inclination may have influenced the cells morphology and responsible for spindled like appearance. [119, 184, 214-217]

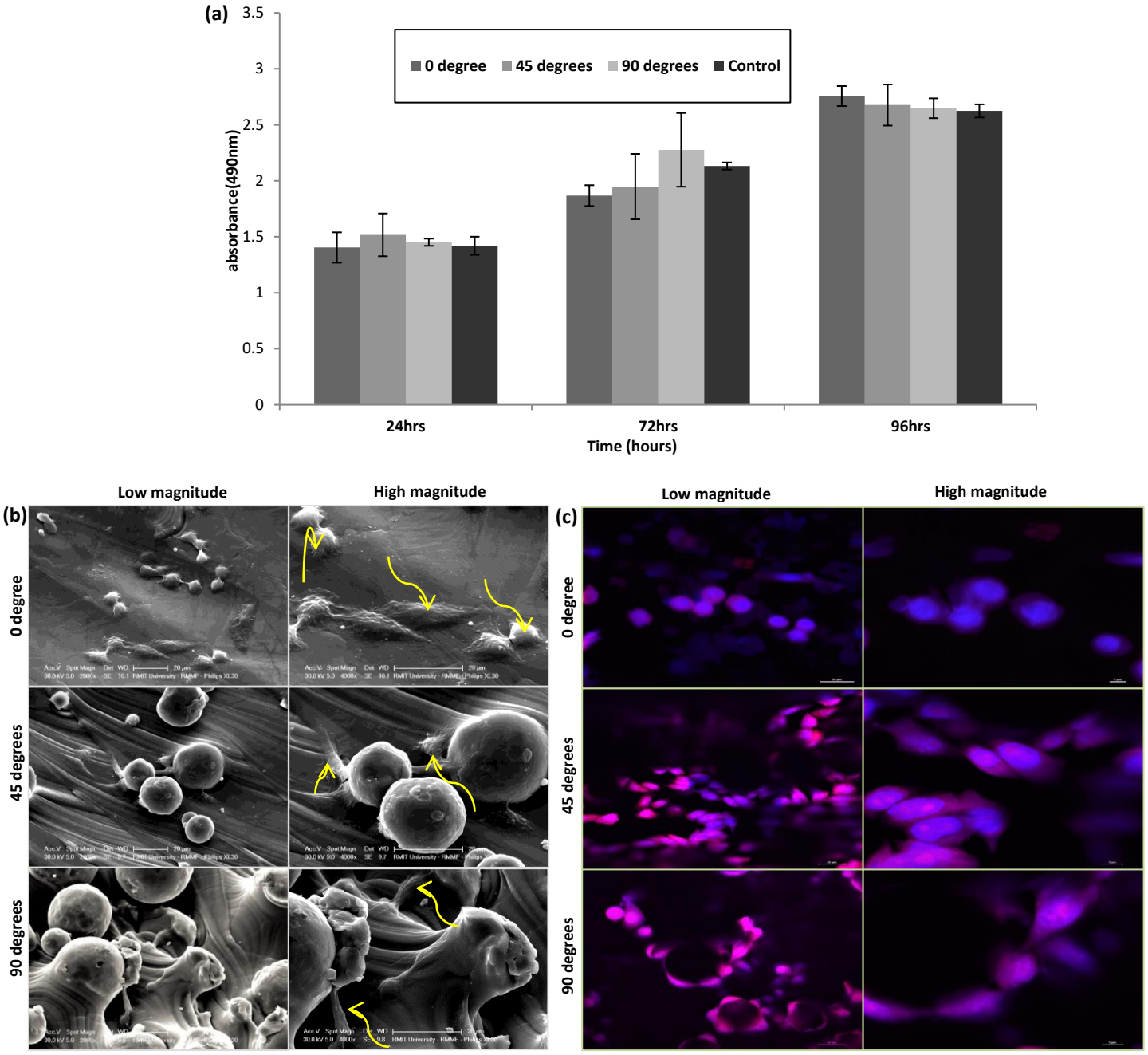

Figure 5.7.1: (a) CHO cell viability after 24hrs, 72hrs and 96 hrs of incubation on 0, 45 and 90 degrees inclined implants as measured by MTS assays, (b) SEM micrographs of (both 2000X and 4000X magnification) CHO cells attachments shown by yellow arrow on 0, 45 and 90 degrees inclined implant after 24 hrs of incubation, (c) Confocal laser scanning micrographs of CHO cells after 72 hours of incubation. Actin and nucleus were stained with Rhodamine and DAPI respectively.

5.4.5. Cell Proliferation and Morphology Analysis on Inclination Angles of SLM Implants

Fig. 5.8.1(a) and (b) shows the morphology of CHO cells by confocal microscopy cultured on the struts for 0, 45, and 90 degrees inclinations after 24 hours and 72 hours of incubation respectively. The cell proliferation behaviour for all inclination angles after 24 hours of incubation is similar as observed in Fig. 5.8.1(a) from both lower and higher magnification. The cells strongly adhered to all inclinations after 24 hours. It is clearly visible with increase of incubation time, there is an increasing trend of cell proliferation behaviour for all inclinations. After 72 hours of incubation CHO cells appeared to fully cover all types of surfaces shown in Fig. 5.8.1(b). In the case of 0-degree inclined implant, the cells are uniformly distributed, but mostly present rounded morphologies, indicating the cells are sitting on the surface, rather than attached and spreading. However, in the case of 45, and 90 degrees inclination, the cells are appeared as mostly spindle-like morphology, suggesting better spreading. From the higher magnification confocal image in Figure 5.8.1(b), we can also observe that the spindle shape cells are significantly elongated on 90 degrees inclination as compared to the 45 degrees implant.

For calculating the percentage of spherical and spindle shaped cells, the same field of view image has been used as for Fig. 5.8.1(b), with results shown in the (Fig. 5.8.2(a)-(c)), where red plus mark was used for spherical cells and blue line mark for spindle cells. It was revealed clearly from Fig. 5.8.1(c) that with the increase of the inclination angle, the percentage of spherical cells decreases and spindle like cells increases. For 0degree inclination, 58.09% cells are found to be spherical in shape whereas only 41.9 % cells are spindle shaped. On the surface of 45 degrees and 90 degrees inclined implants; the percentage of spindle cells increases, with 82.29% and 91.92% cells being spindle shaped, respectively. That means only 17.7% and 8.08% cells are spherical in shape for 45, and 90 degrees inclination which are significantly less than 0degree inclination. The mean spindle cells dimension has also been reported in Fig.

5.8.1(c). With the increase of the inclination angle, spindle like CHO cells appear in a more elongated fashion. There is a clear increasing trend of spindle CHO cells from 0 degree to 90 degrees inclination where the mean spindle dimension for 0, 45 and 90 degrees are 13.0 μm, 14.8 μm, 21.1 μm respectively even though the standard deviation of spindle dimension is pretty high for each case.

The higher percentage of spindle cells compared to spherical cells on the surface of 45, and 90 degrees implants than 0-degree implant may be explained by the increasing surface roughness due to the increasing number of partially melted particles. Mean roughness R_a was 2.532 μm, 5.962 μm, 7.246 μm respectively for 0, 45, and 90 degrees implant. Extensive studies have been carried out so far to understand the relationship between roughness and cell attachment, proliferation and differentiation. [119] Generally, rough surfaces have been reported as beneficial for bone integration [117, 118] but the literature lacks agreement on optimal roughness for cell attachment. For example, some studies suggest higher roughness values (Ra=3-5μm); while others favour more smooth surfaces (Ra<1 μm); [119, 120] and, other studies suggest that surfaces with nano roughness or a hierarchical nano/submicron roughness are more favourable for cell growth and fraction. Increased roughness can simultaneously increase the surface area of the implant, improve cell migration and attachment to the implant. [152] The surface topography has also been identified as a crucial factor for cell attachment and cell proliferation on implants. [218-221] It has been found from Fig. 5.8.1(c) that with the increase of the inclination, the number of partially melted particles increased on the implant surface. In case of 90 degree inclination angle implant, it was found that the implant surface is almost completely covered with the partially melted particles that create a porous surface structure which may influence the spindled CHO cells to be more elongated by the infiltration and enhancement of cells attachment, than for the 45 degree inclination specimens, where the partially melted particles are not located densely. [222] Spherical shaped particles on the

surface of the implant have been reported to enhance cell migration and extracellular matrix growth. [8, 223] In case of 0degree inclined implant, only few partially melted particles exist on the surface, resulting in fewer spindle-like cells and with lower average length than for 45 degrees and 90 degrees.

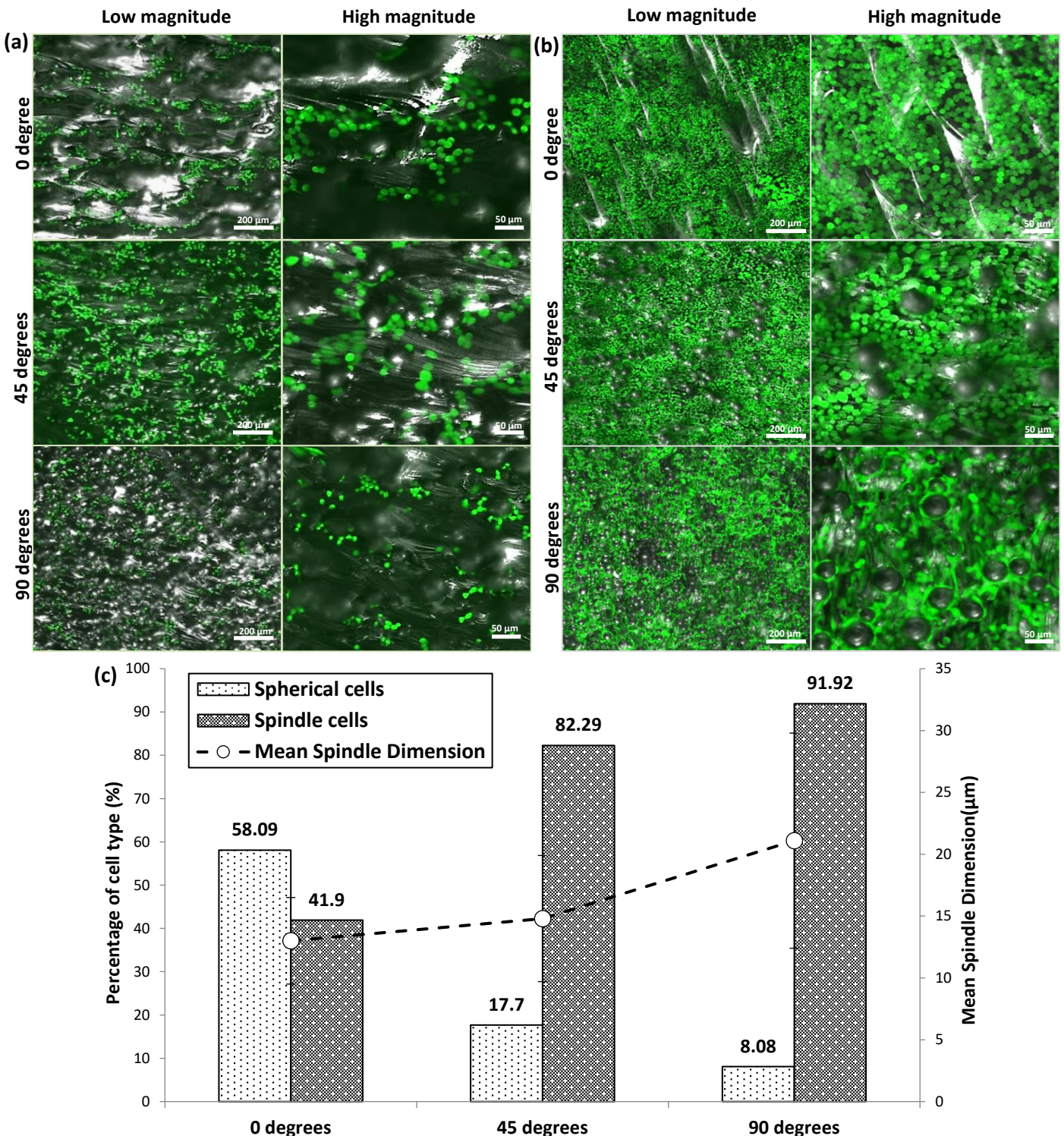

Figure 5.8.1 : Confocal images of CHO cells after 24 hrs(a) and 72 hrs(b) of incubation on 0, 45, and 90 degrees inclinations, (c) percentage of cell type and mean spindle dimension measurement on 0, 45 and 90 degrees inclined implants using same field of view high magnitude image based on matlab programming.

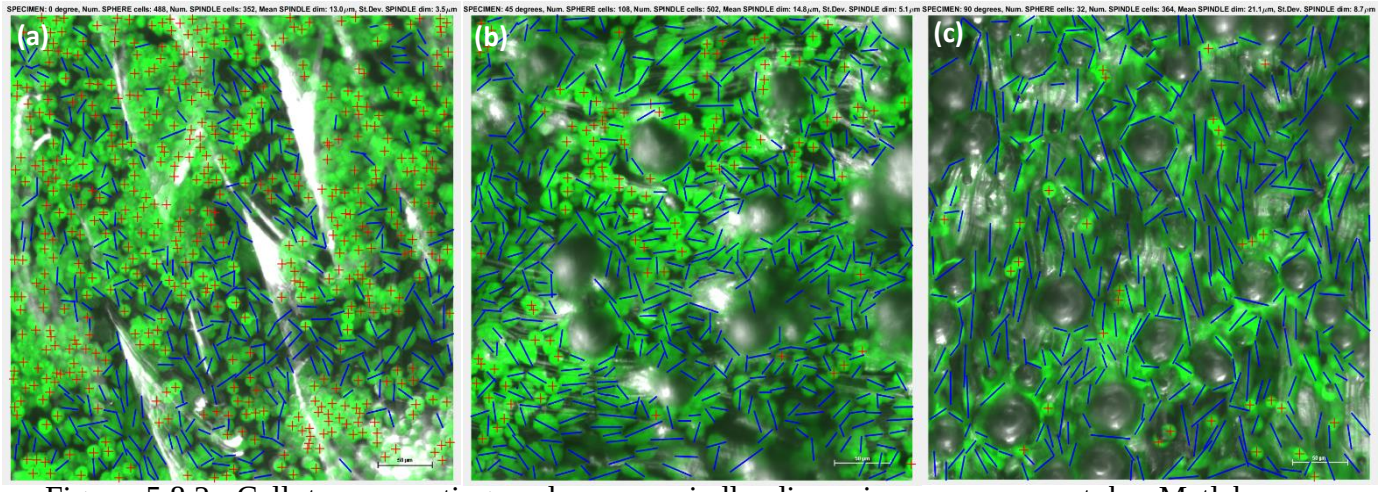

Figure 5.8.2 :Cell type counting and mean spindle dimension measurement by Matlab simulation for (a) 0 degree; (b) 45 degrees; and (c) 90 degrees inclined implant (spherical cells are marked by red plus sign and spindle like cells are marked by blue straight line) Scale bar 50 µm

5.5. Conclusion

Previously, it was suggested by other research groups that the surface modification of SLM manufactured implants by polishing or chemical etching can improve the biological interaction of the implant. Here, we demonstrate that minimal surface treatment is required if the inclination angle is used to functionalise the surface. From the surface morphology of each inclination, it was observed that a larger number of partially melted particles were observed to be adhered to the surface of 90 degrees inclined implants than for the 45 degrees and 0degree case, there are only few partially melted particles existed. Thus, the roughness from 0 degree to 90 degrees are increased. From the surface chemistry analysis, it has been revealed that TiO_2 is the most predominating oxide among different titanium oxides for each inclined implant. Although the overall cell viability was found to be same on implants with inclination angles of 0, 45 and 90 degrees, the morphology and spreading were observed to change significantly. On the 45, and 90 degrees inclination angle implants, a higher percentage of spindle like shape cells was found in a more elongated fashion than for the 0degree inclined implant. From an implant design perspective, implants with higher inclinations could be useful for improving

cell attachment, whereas low inclination angles may induce low adherent surface. The 90 degrees inclination angle implants could also be an appropriate choice as a higher corrosion resistant implant because of their ability to diffuse higher amount of oxygen on the metal surface which has been confirmed by the depth profile analysis of XPS. We suggest the finding reported here will be beneficial for rapidly fabricating, functionalising and implanting personalised, just-in-time biomedical devices in a single process, without the need for post-processing treatments. The findings of this study also established a missing link between additively manufactured relatively high rough surface part and attached cells behaviour and gives us new insights in the field of biomaterial-aided tissue regeneration.

Chapter Six: Engineering the Bio-interface: Rational Design of Additively Manufactured Ti6Al4V Implants to Control *Staphylococcus aureus* Biofilm Formation

6.1. Chapter Overview:

In the previous chapter, the author of this thesis has shown that how the alteration of inclination angle of SLM Ti6Al4V implants can change different surface properties, and how these surface properties are directly corelated with mammalian cell attachment behaviour. In this current chapter how the rational design of build inclination angle of implant surface by additive manufacturing process can successfully inhibit biofilm formation on implant surface has been discussed.

Here, we for the first time, we report on how the SLM build inclination angle can be utilised to modify the surface topography of metallic implants for directed *Staphylococcus aureus* biofilm formation. From an initial build inclination angle of 90°, lowering the angle gave metallic surfaces with lower roughness, lower hydrophobicity, higher surface energy, and fewer partially melted metal particles without altering the bulk surface chemistry. This directly correlated with significantly lower biofilm coverage and an associated reduction in biomass without compromising mammalian cell attachment. This work provides a facile single step method at the manufacturing stage for the development of additively manufactured metallic implants with superior, inherent protection against implant associated infection.[2]

*The part of these research findings has been published in ***Materialia***.
A. Sarker, N. Tran, A. Rifai, M. Brandt, P.A. Tran, M. Leary, K. Fox, R. Williams, "***Rational design of additively manufactured Ti6Al4V implants to control Staphylococcus aureus biofilm formation"***, Materialia 5 (2019) 100250.

6.2. Introduction

Metal and metal alloys including titanium, tantalum, titanium-nickel, stainless steels, cobalt (Co) based alloys (CoCrMo) have been extensively utilised to fabricate bone implants because of their favorable mechanical properties and associated biocompatibility [87-90]. However, implants made from these metallic materials usually exhibit higher modulus of elasticity than the host bone which can lead to a stress shielding effect [224]. This effect leads to a reduction in bone density and is the primary reason for bone resorption and eventual failure of such implants [5]. Cortical bone (compact bone) has elastic moduli ranging from 3 to 30 GPa, while trabecular or cancellous bone has significantly lower elastic moduli of 0.02 to 5 GPa [70, 225]. Titanium alloys, particularly Ti-6Al-4V, are widely used as orthopaedic and dental implants because of their excellent biocompatibility, corrosion resistance, high strength to weight ratio, and modulus of elasticity relatively lower modulus of elasticity than cobalt (Co) based alloy(CoCrMo) and stainless steel [91-94].

With the advent of additive techniques such as electron beam melting (EBM), selective laser sintering (SLS), selective laser melting (SLM), laser engineered net shaping (LENS), direct metal laser sintering (DMLS) and laser aided additive manufacturing (LAAM), the direct replication of biological structures has become increasingly feasible. Moreover, the desired mechanical properties of local bone can be easily achieved using additive manufacturing process by different ways such as manipulating the volume fraction and size distribution of the pore structures [224]. SLM and EBM utilize laser-beam and electron beam, respectively, to fuse powder particles on a layer-by-layer basis. SLM uses a laser beam with a tunable wavelength and EBM an electron beam. The main advantage of SLM process over EBM is that SLM can process polymers, ceramics and metal whereas EBM can process only conductive metals and minimum feature size[37, 70]. Selective laser melting (SLM) is an emerging metallic additive manufacturing process, which can create complex three-dimensional (3D)

parts by selectively melting successive layers of Ti6Al4V powder. The SLM process provides a unique approach to manufacture new generations of orthopaedic implants allowing highly customizable, patient specific designs, such as hitherto unavailable lattice structures offering controlled mechanical properties, and precise dimensional accuracy[44, 226, 227]. The SLM process is capable of fabricating implants of pure titanium and titanium based alloys such as Ti6Al7Nb[45], Ti-24Nb-4Zr-8Sn[44],Ni-Ti[46], Ti-13Nb-13Zr[47] other β titanium alloys[48] and most importantly Ti6Al4V[49, 50]. Recently, SLM has been used to fabricate porous, bio-inert Ti6Al4V structures with complex and reproducible morphological and mechanical properties [51, 99] yet retained their excellent biocompatibility [52].

However, despite these advances, implant failure due to bacterial infection during implantation is still one of the greatest concerns for SLM produced implants; indeed bacterial infection may be of greater concern for complex printed structures due to the large surface area compared to traditional metallic implants[17, 123, 228, 229]. Another thing is that often it is very challenging to clean properly of additively manufactured implants. Common implant infections are associated with pathogens such as *Staphylococcus aureus* (*S. aureus*); these bacteria are able to form polysaccharide based biofilms on implant surfaces, making control with conventional antibiotics extremely difficult [121, 122]. Implant associated infections are associated with loosening; usually require revision surgery, resulting in longer hospital stays, significant cost to the patients and higher mortality rates[123].

Much research effort has therefore been focused on developing anti-biofilm implant surfaces, which are typically achieved by adding an antimicrobial agent, such as silver compounds, to the surfaces through secondary processes such as coating, immobilising, or grafting[124-129]. Although some of these techniques are suitable for both traditionally manufactured and 3D printed implants, there are concerns regarding their risk; such as delamination of the functional layers, off target effects arising from the toxicity or carcinogenicity of the antimicrobial

agents[130, 131], associated high cost, and often slow and cumbersome processing [132]. In addition, the concern for bacterial resistance against traditional antibacterial agents is rising globally which poses a great medical threat.

Motivated by the need for a simple approach, we report for the first time a method to limit biofilm growth on titanium surfaces without the use of antibacterial agents or expensive surface modification processes. Instead, the surface topographies of selective laser melted Ti6Al4V parts were controlled by adjusting the build inclination angle which is the design parameter of SLM where no other process parameter was altered. It has been shown that both chemical and surface topographical modification can inhibit biofilm formation [133, 134]. However, changing only the surface topography for controlling biofilm formation without the need for an additional chemical agent or process is receiving increasing interest [135, 136] due to its low cost and less risk of cytotoxicity. Mechanisms of manipulating the surface topography have been achieved; both nature inspired[136], bio-inspired[132, 137] or by introducing both micro and nano-scale surface features [138]. Here, we report the methodology where Ti6Al4V parts produced from a single step, in-situ SLM manufacturing process retain the desirable surface chemistry and mechanical strength without affecting mammalian cell viability and attachment. Further analysis however, revealed the inclination angle allowed markedly significant control over the surface topography, area, roughness, wettability, and surface energy; these differences enable significant control over the level of *Staphylococcus aureus* (*S.aureus*) biofilm formation.

6.3. Experimental Section

The samples were fabricated according to chapter-3.3 – Materials and Methods section outlined in 3.2, characterized according to section 3.4, *Staphylococcus aureus* bacterial culture according to section 3.6.

6.4. Results and discussion

6.4.1. Fabrication and surface topography of different inclined (10, 45, and 90 degrees) SLM samples

Ti6Al4V specimens were manufactured by an SLM process with build inclination angle α (the most acute measurable angle to platen) of 10, 45, and 90 degrees with respect to the building plane as shown in Figure 6.1. The size of the Ti6Al4V powders was ~ 30µm. Briefly, the laser scanning strategy used here consisted of a perimetric scan then subsequently filled with a raster scan. The parameters of the SLM process are provided in the supporting information. Fig. 6.1(a) shows the CAD design part of 10, 45 and 90 degrees build inclined part with frangible support structure. Fig. 6.1(b) reveals the micro-CT reconstructed design part of 10, 45, and 90 degrees build inclined part with frangible support structure where the laser scanning track edges are clearly visible for 10 degrees whereas there is no visible scanning track edge is found for 45 degrees and 90 degrees. Fig. 6.1(c) shows the sliced top section of micro-CT generated image processed by Magics software taking consideration of 4.28 mm diameter of circle area out of 5*5 mm2 samples surface. Fig. 6.1(d) shows the

bar diagram of effective measured surface area from sliced section of reconstructed micro-CT image. The measured effective surface area of 10, 45, and 90 degrees build inclination surface is 20.72, 19.24, 19.61 mm^2. respectively. The higher surface area has been found at lower inclinations (10 degrees) than at 45 degrees and 90 degrees because of its unique topographical feature with fewer partially melted particles along with the scanning track edge bumpy border. This phenomenon is only applicable for 10 degrees and not for 45 degrees or for 90 degrees as it has been found that the 90 degrees surface area is higher due to the greater amount of partially melted particles present on the surface. There is no observation of a scanning track edge border on either the 45 degrees or 90 degrees sample.

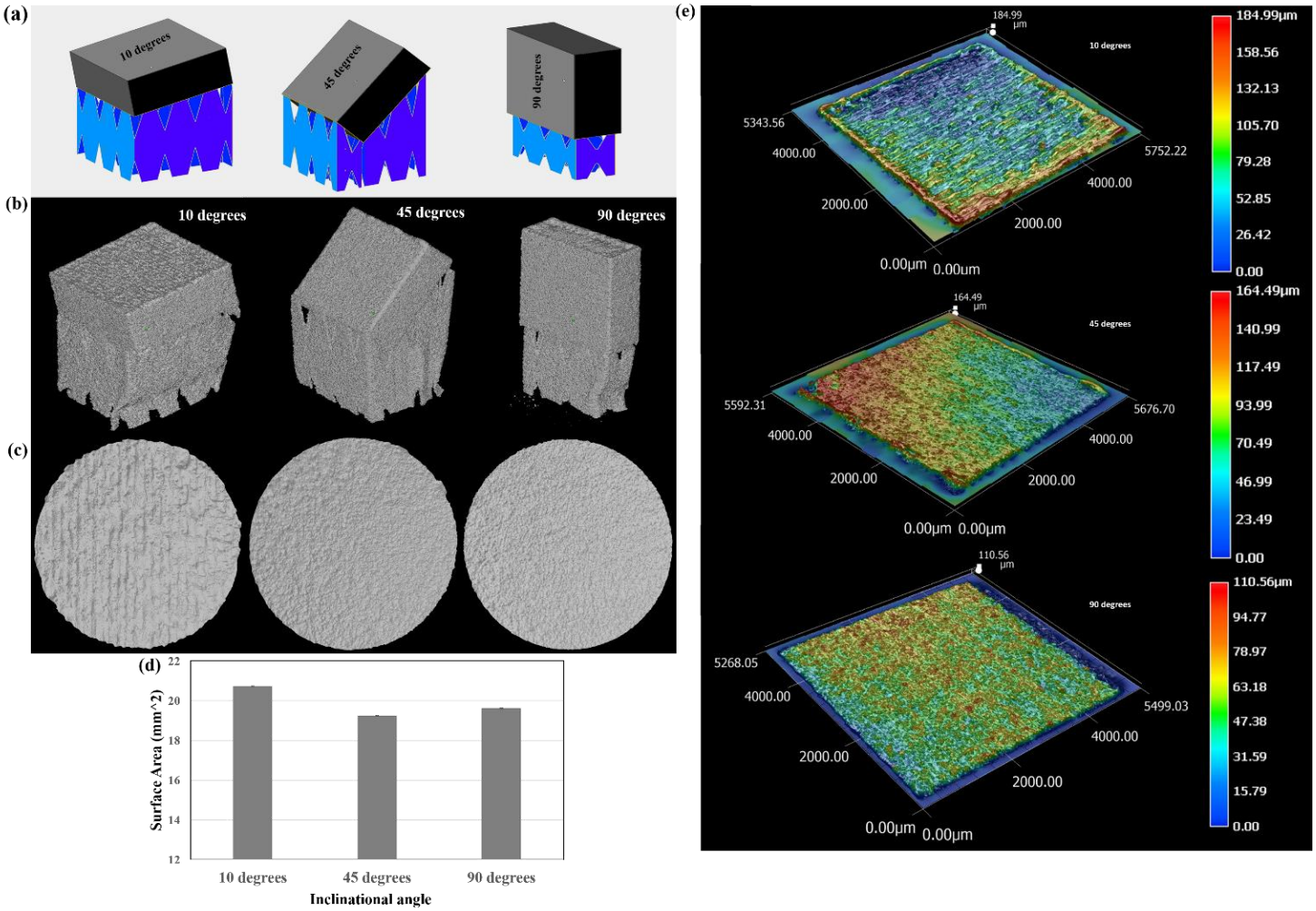

Figure 6.1: (a) Illustration of SLM printed Ti6Al4V implants with build inclination angle of 10, 45 and 90 degrees from CAD design with support structure, (b) Illustration of SLM printed Ti6Al4V implants with build inclination angle of 10, 45 and 90 degrees from reconstructed micro-CT image with support structure, (c) Upper sliced surface of 10, 45, and 90 degrees inclined surface from micro-CT generated .STL file, (d) Surface area measurement of 10, 45 and 90 degrees build inclination from upper sliced SLM part of micro-CT reconstructed image, (e) Optical images of 10, 45, and 90 degrees inclined implant obtained by the optical digital microscope showing the topographical changes as the inclination angle change.

Fig. 6.1.(e) shows surface topography of Ti6Al4V implants of 10, 45 and 90 inclination angles. It is clearly observed that the number of partially melted titanium particles increases with the increase of the inclination angle(α) on the implant surface. In the case of 10 degrees, the laser scanning track edge border is clearly visible with fewer partially melted particles. In case of 45 degrees inclination, we can observe very dim step edge border with relatively higher partially melted particles than 10 degrees due to the stair-step effect and no step edge is observed with 90 degrees with high densely located partially melted particles due to having no effect of stair-step[26].

Fig. 6.3(a) shows the surface morphology of SLM printed Ti6Al4V samples obtained by a scanning electron microscope (SEM). As is typical of an SLM produced part, partially melted Ti6Al4V particles are clearly observed on all specimens. Lower magnification SEM micrographs show that with the increasing inclination angle there is an increased number of partially melted particles. However, from the high magnification SEM images, it can be observed that the partially melted particles are not uniform in shape and size; the particles are distributed between spherical and semi-spherical morphologies. The phenomena of partially melted particles occurs via two main mechanisms: (1) thermal diffusion occurs due to the significant temperature difference between the loose powder and the solidified material leading to local fusion of powder to the edge of the scan track of the implant surface; (2) the stair-stepping effect of the implant of varying inclination angles are partially built on the loose

powder. Through one or a combination of these mechanisms, some metal particles below each layer will be totally or partially melted and then bonded on the bottom of the layer[26]. It is also observed from low magnification SEM micrographs (Fig. 6.3) that the step-edge borders

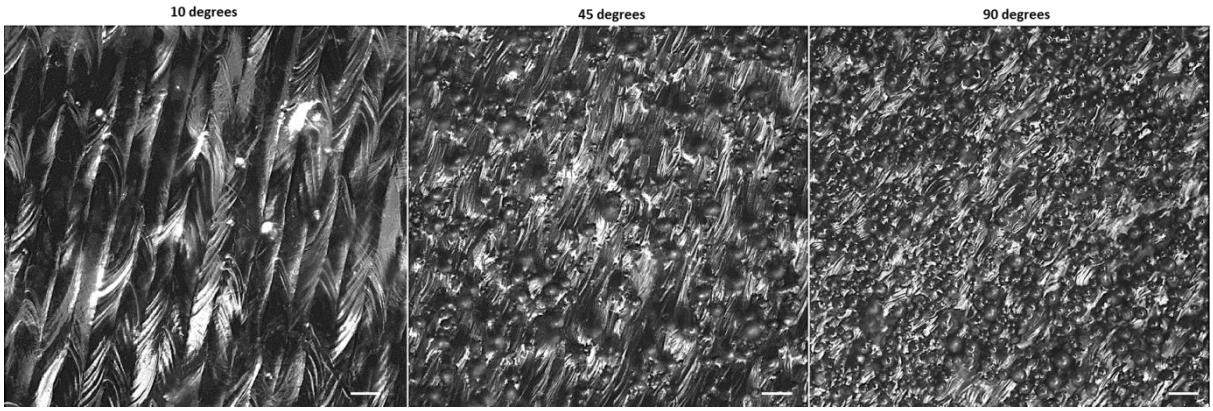

clearly visible (refer to the yellow line).

Figure 6.2: Confocal microscope shows the topology of 10, 45, and 90 degrees inclined surface, scale bar = 200 μm

Fig. 6.2. shows the confocal images of different build inclination angles revealing the same topography shown by both optical and SEM images. Fig. 6.3(b) shows the graph for quantifying the number of partially melted particles and measuring the average diameter of partially melted particles for 10, 45 and 90 degrees build inclination surface. A custom Matlab script was developed to measure the average diameter and number of partially melted particles from the lower magnification(250X) SEM images shown in Fig.6.4. The average diameter of partially melted particles is 42.97, 34.03, 38.40 μm for 10, 45, and 90 degrees inclinations respectively with higher standard deviation (15.24, 16.01, 15.30). The chart also shows that there is an increasing trend of partially melted particles from 10 degrees to 90 degrees. The number of partially melted particles with the field of view increased significantly, with 61, 218 and 383 counted for 10, 45 and 90 degrees respectively.

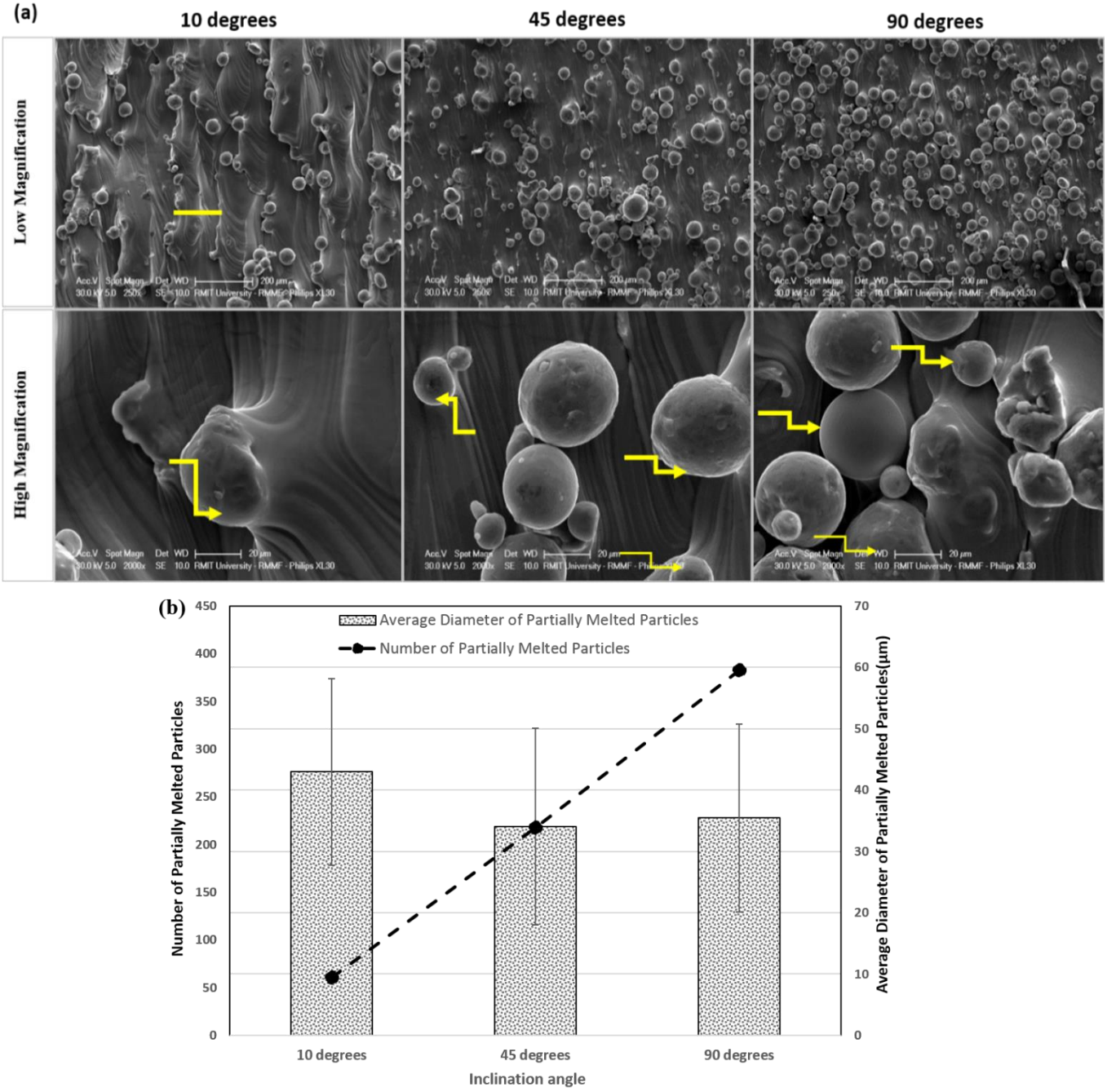

Figure 6.3: (a) SEM micrographs showing the surface morphology of SLM prepared samples (10, 45, and 90 degrees inclined) at low (250X) magnification and high (2000X) magnification, scale bar (20µm). Selected partially melted particles are indicated by arrows, (b) Quantification and average diameter measurement of partially melted particles by semi-automated matlab script (shown in Figure 6.4) from low magnification(250X) SEM images for 10, 45, and 90 degrees inclined samples, N=1.

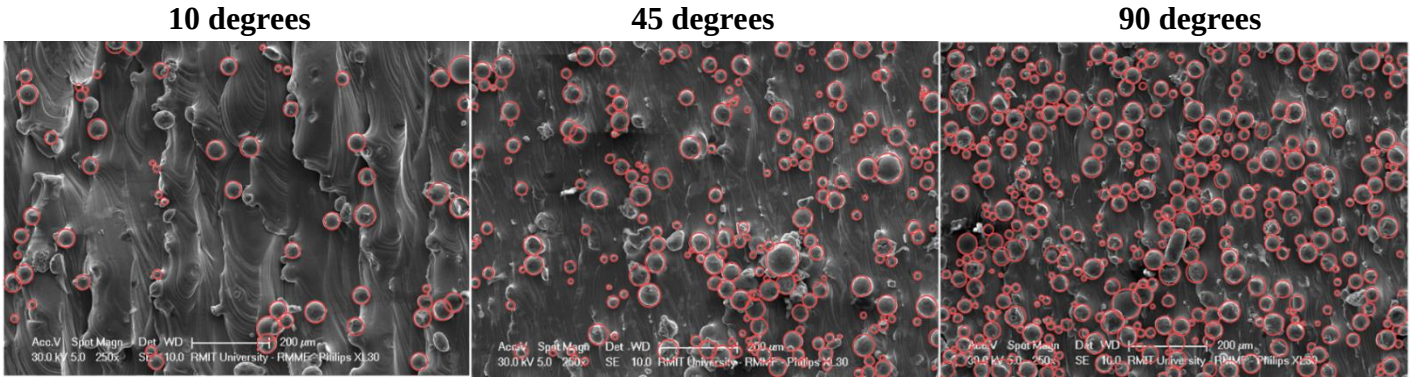

Figure 6.4 **:** Quantification and average diameter measurement of partially melted particles by semi-automated Matlab script from low magnification (250X) SEM images for 10, 45, and 90 degrees inclined samples.

6.4.2. Surface wettability, surface roughness, surface energy of different inclined SLM samples

Surface wettability and surface roughness are crucial in governing implant-bacteria interactions [179, 230]. Fig. 6.5(a) shows the water contact angles of samples printed at 10, 45 and 90 degrees build inclination angles. All samples were found to be hydrophobic, with the contact angles of 10, 45, and 90 degrees inclined samples found to be 95.3^{o}, 108.5^{o} and 114.5^{o} respectively. The increase in hydrophobicity with inclination angle is most likely due to the increasing number of partially melted particles on the specimens. The increase in hydrophobicity with inclination angle is most likely due to the presence of air pockets created by the increasing number of partially melted particles, as suggested by the Cassie Baxter model for composite surfaces[231, 232]. Fig. 6.5(b) shows the profilometry measurements of the arithmetic mean deviation (R_a), root mean square deviation (R_q) for SLM printed samples with different inclination angles. It is found that with an increase of inclination angle, both R_a and R_q values also increase. The highest R_a and R_q values were 8.17 μm and 9.84 μm respectively, which were measured on the 90 degrees inclined sample. We suggest the increase in roughness is due to the increasing concentration of partially melted particles and the stair-step effect[156]. Fig. 6.5(c) demonstrates the surface topographical features of different inclined implant surfaces. Here, it is evident that the partially melted particles are most densely located on the

90 degrees surface. Fig. 6.5(c) also shows the colour mapping of SLM substrates of the different inclinations (10, 45 and 90 degrees). It should be noted that the SLM process with different build angles only affect the surface roughness, topography, and wettability.

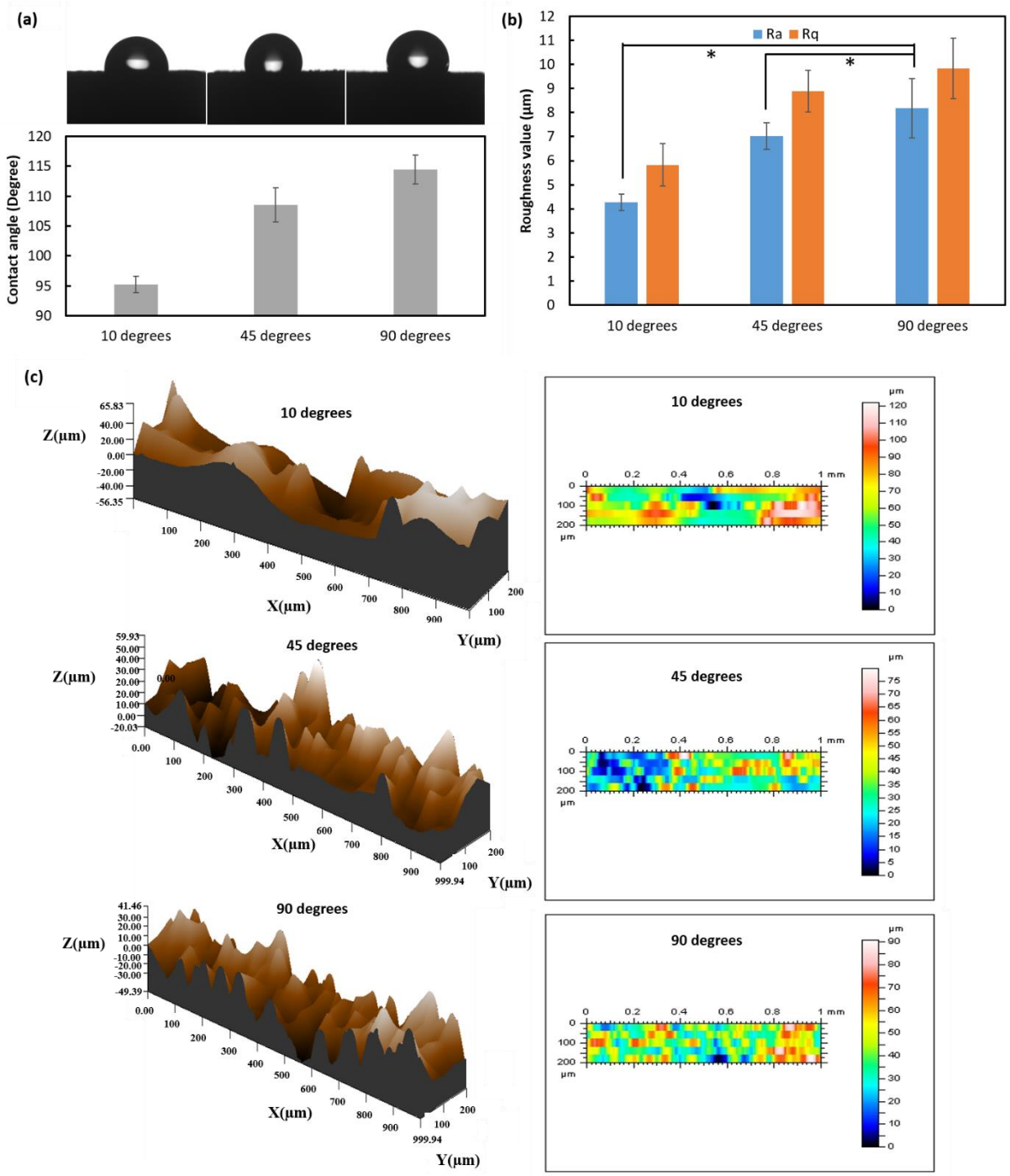

Figure 6.5 **:** (a) Water contact angle measurements of SLM printed substrates with different build inclination angles suggest that the surfaces become more hydrophobic as the inclination

angle increases. The contact angles for substrates printed with 10, 45, and 90 degrees inclination are 95.3, 108.5, and 114.5 respectively. Data = Mean ± SD from measurements performed in triplicate. (b, c) Surface roughness measurements and surface topography of SLM printed samples as measured by a profilometer. Arithmetic mean deviation (R_a) and root mean square deviation (R_q) were measured and averaged from at least four different locations, Data = Mean ± SD. * $p < 0.05$.

Fig. 6.6 shows the measured surface energy for 10, 45 and 90 degrees build inclination for three different solvents (water, ethelyene glycol and glycerol) from the contact angle measurement applying both the Owens-Wandt-Kaelble and equation of state methods[139, 140, 233]. From 10 degrees to 90 degrees a decreasing trend was observed in surface energy by both methods, for all solvents. The measured surface energy for 10 ,45 and 90 degrees are 13.81, 9.13 and 7.76 mJ/m^2 respectively for water (Owens-Wandt-Kaelble). The highest surface energy for 10 degrees could be explained by the lowest wettability for 10 degrees which correlates to fewer partially melted particles on the surface. The measured surface energy for 10 ,45 and 90 degrees are 26.45, 23.44 and 22.79 mJ/m^2 for water by Equation of State method shown in figure 7.6. The same trend was found for other two solvents (ethelyene glycol and glycerol).

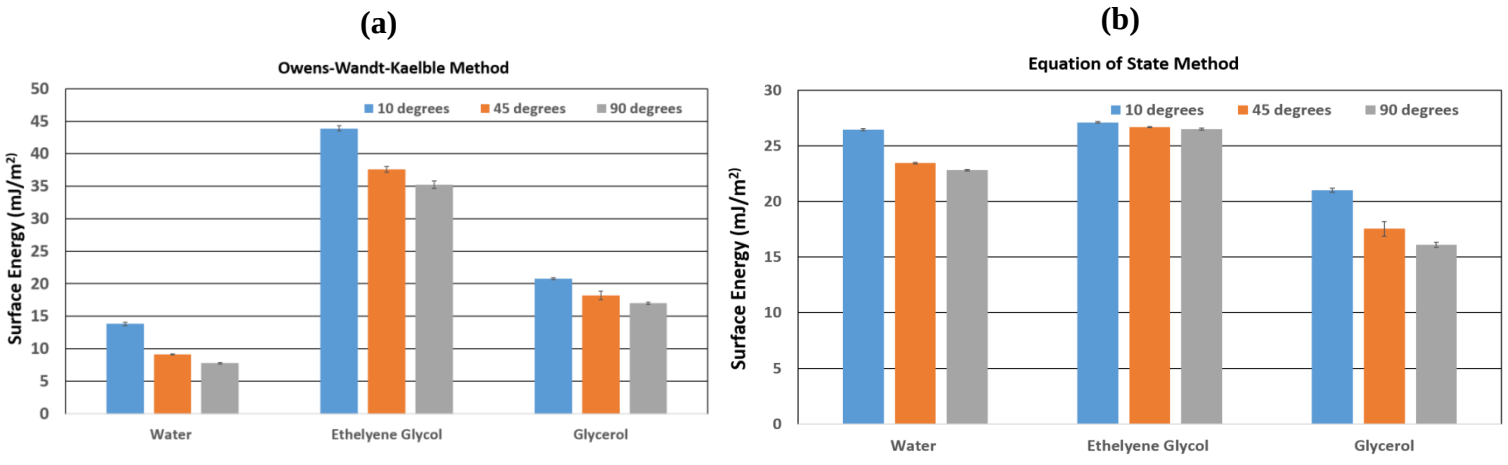

Figure 6.6 : **(a)** Surface Energy measurement of SLM-manufactured Ti–6Al–4V samples of 10, 45 and 90degrees inclination angle from contact angle measurement for three different solvents (water, ethelyene glycol and glycerol) by Owens-Wandt-Kaelble method, **(b)** Surface

Energy measurement of SLM-manufactured Ti–6Al–4V samples of 10, 45, and 90 degrees inclination angle from contact angle measurement for three different solvents (water, ethelyene glycol and glycerol) by equation of method.

6.4.3. XRD and XPS analysis of different inclined (10, 45, and 90 degrees) SLM samples

Fig.6.7 shows the XRD patterns of different inclined Ti64 SLM specimens and the spectra obtained from the middle cross section (6 mm high) of each cube. All inclination angles reveal the same microstructure, consisting of complete martensite α′ (100), α′ (002), α′ (101), α′ (102), α′ (110) position on 35.08^0, 38.39^0, 40.16^0, 52.98^0, 62.94^0 respectively. There are several reports that show that SLM Ti64 results in a complete martensite phase formation[234, 235] when no post-heat treatment is applied.

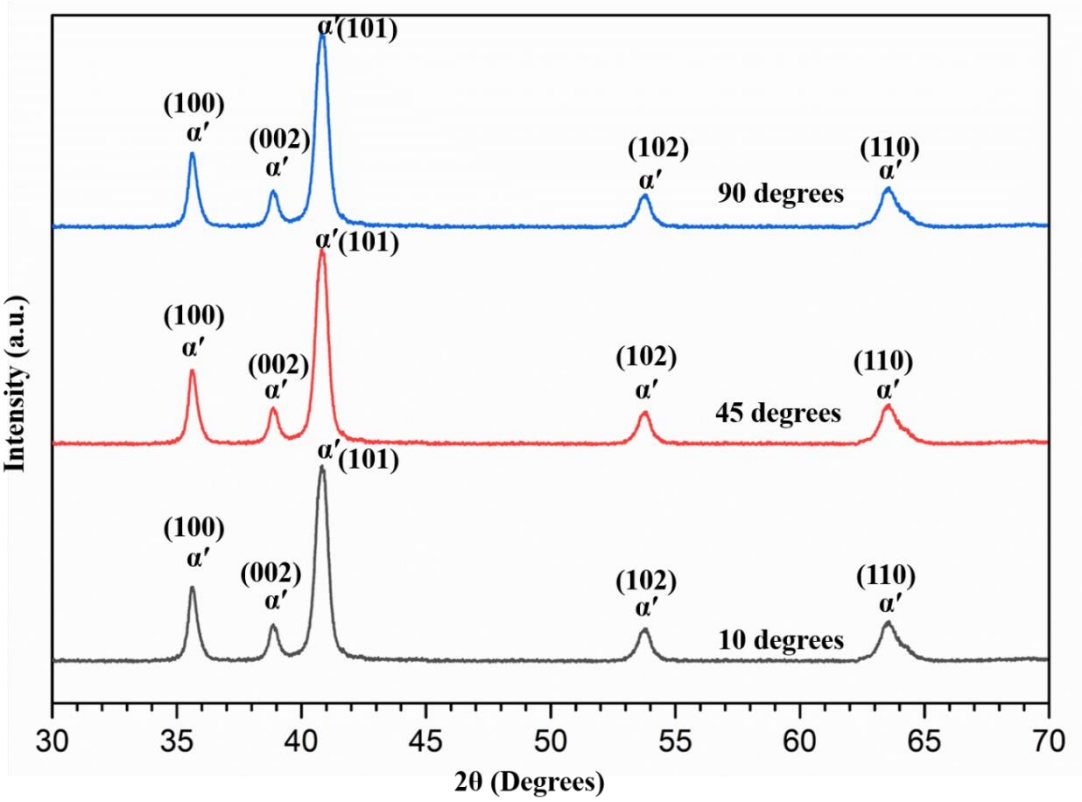

Figure 6.7 **:**XRD patterns of SLM-manufactured Ti–6Al–4V samples of 10, 45, and 90 degrees inclination angle showing martensite phase formation.

Fig. 6.8(a) represents the presence of carbon, nitrogen, oxygen and metals (titanium, aluminium, vanadium) for the 10, 45, and 90 degrees inclined SLM samples. A very weak signal was detected for vanadium, possibly due to the rough implant surface reducing the electron counts reaching the detector. There is no difference in the elemental presence by XPS survey spectra of 10, 45, and 90 degrees inclination. Fig. 6.8(b) shows the fitted high- resolution spectra for titanium (Ti2p) for different inclination angle (10, 45, and 90 degrees). The peak fitting was performed based on the existing literature[236]. From Fig. 6.8(b), it is observed that Ti2p consisted of different oxides $TiO_2(Ti^{4+})$, $TiO(Ti^{2+})$, $Ti_2O_3(Ti^{3+})$ and the pure metallic state which always appears in a doublet fashion. Table 1 shows the binding energy(eV) position for $TiO_2(Ti^{4+})$, $TiO(Ti^{2+})$, $Ti_2O_3(Ti^{3+})$, and pure metallic state of Ti2p3/2 and Ti2p1/2. The binding energy gap(Δ) between Ti2p3/2 and Ti2p1/2 for $TiO_2(Ti^{4+})$, $TiO(Ti^{2+})$, $Ti_2O_3(Ti^{3+})$, and the pure metallic state is 5.72 eV, 5.7 eV, 5.6 eV, and 6.10 eV respectively for each of the inclination angles (10 ,45 and 90 degrees). The binding energies found for Ti2p3/2 and Ti2p1/2 and $TiO_2(Ti^{4+})$ are 458.38 and 464.1 for 10 degrees; 458.1 and 463.82 for 45 degrees; and 458.18and 463.9 for 90 degrees. It is clearly visible from Table 6.1 that all the titanium Ti2p oxides level and pure metallic state of Ti64 SLM samples have located into same binding energy which reveals that the surface chemistry of different inclined SLM samples almost same[236].

Table 6.2 represents the relative atomic percentage of $TiO_2(Ti^{4+})$, $TiO(Ti^{2+})$, $Ti_2O_3(Ti^{3+})$, and pure metallic state. It is clear from Table 2 that $TiO_2(Ti^{4+})$ is the most predominating oxides among other oxides for all inclination angles (10, 45 and 90 degrees) and values are 73.49 ± 2.30%, 79.48 ± 4.35%, 74.68 ± 3.24% respectively for 10, 45, and 90 degrees inclination angle. The lowest atomic percentage was found for pure metallic state and it is 1.63 ± 1.12%, 1.62 ± 1.45%, 5.54 ± 2.24%. The ratio between TiO_2 to pure Ti metal state for 10, 45 and 90 degrees build inclination are 45.08, 49.06 and 13.48 respectively.

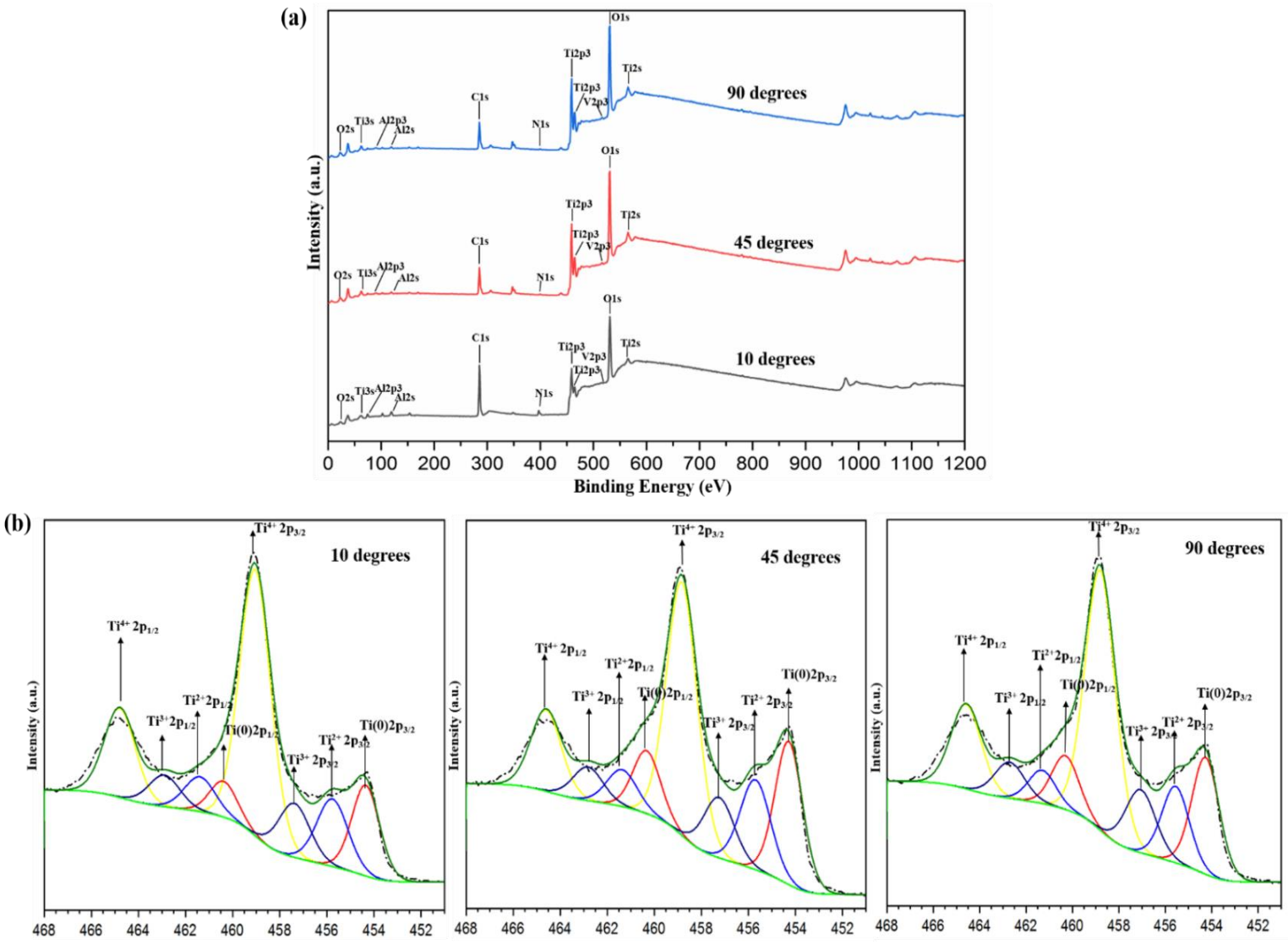

Figure 6.8:(a) XPS survey spectra showing the presence of elements of different build inclinations, (b) High resolution spectra of Ti2p region for each representative spot of 10, 45, and 90 degrees inclinations.

Inclination Angle	Binding Energy position Ti2p3/2 & Ti2p1/2 for $TiO_2(Ti^{4+})$ eV	Binding Energy position Ti2p3/2 & Ti2p1/2 for $TiO(Ti^{2+})$ eV	Binding Energy position Ti2p3/2 & Ti2p1/2 for $Ti2O3(Ti^{3+})$ eV	Binding Energy position Ti2p3/2 & Ti2p1/2 for Ti pure metallic state eV
10 degrees	458.38, 464.1	455.31, 461.01	457.37, 463.33	453.58, 459.68
45 degrees	458.1, 463.82	455.51,461.21	457.3,462.9	453.26, 459.36
90 degrees	458.18, 463.9	455.4, 461.1	457.27, 462.87	453.6, 459.7

Table 6.1: Binding energy position of different oxide levels of titanium and pure metal for 10, 45, and 90 degrees build inclination angle.

Inclination Angle	Relative Atomic Percentage (%) for $TiO_2(Ti^{4+})$	Relative Atomic Percentage (%) for $TiO(Ti^{2+})$	Relative Atomic Percentage (%) for $Ti_2O_3(Ti^{3+})$	Relative Atomic Percentage (%) for Ti pure metal
10 degrees	73.49 ± 2.30	10.51 ± 1.36	14.37 ± 4.34	1.63 ± 1.12
45 degrees	79.48 ± 4.35	10.00 ± 2.21	8.90 ± 2.56	1.62 ± 1.45
90 degrees	74.68 ± 3.24	11.19 ± 2.56	8.58 ± 1.24	5.54 ± 2.24

Table 6.2: Relative atomic percentage of different oxide levels of titanium and pure metal for 10, 45, and 90 degrees build inclination angle

6.4.4. Biofilm growth on different inclined (10, 45, and 90 degrees) SLM samples

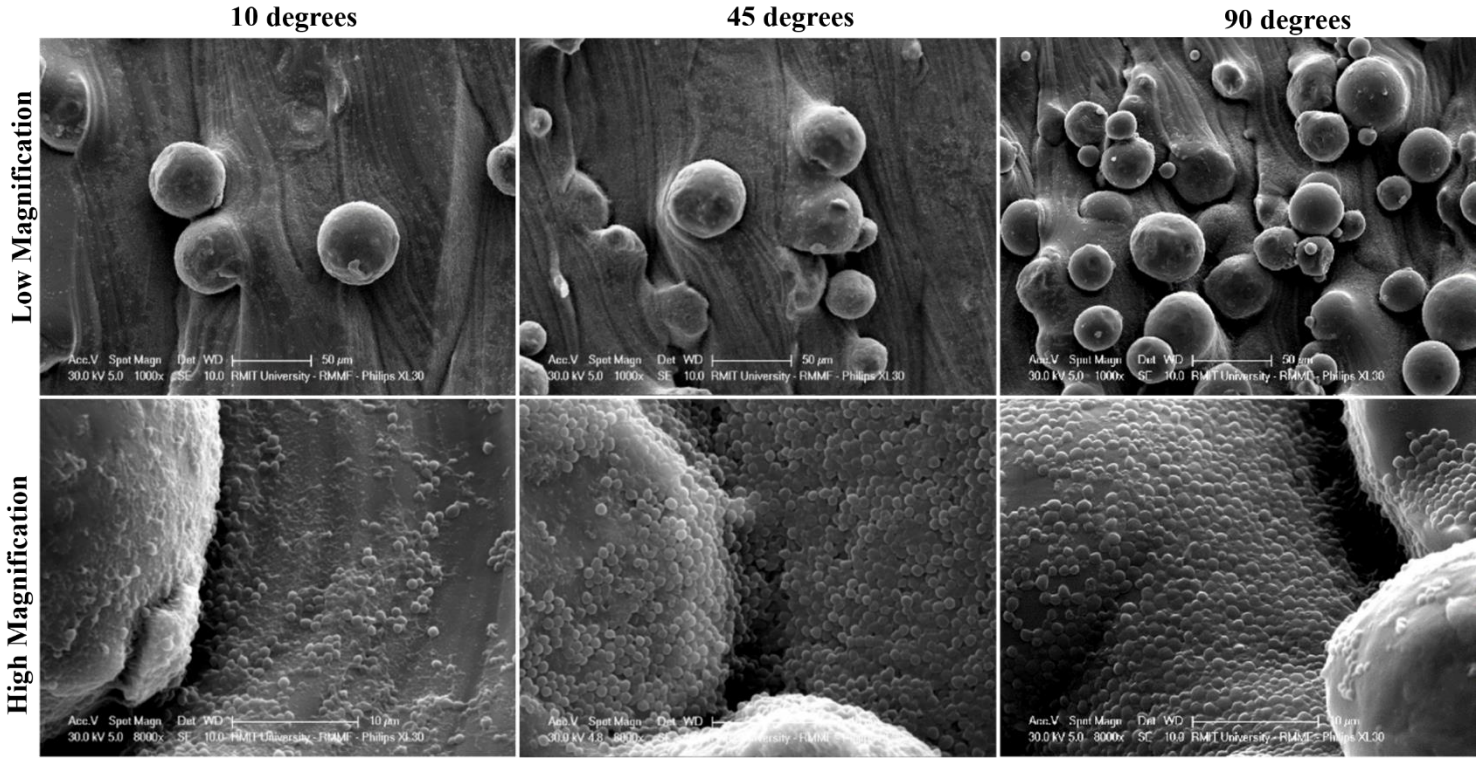

Figure 6.9 : Representative SEM images at lower(1000x) and higher(8000x) magnification of 10, 45, and 90 degrees SLM printed samples after 48 hrs incubation with *S. aureus* showing an increase of biofilm as the inclination angle is increased.

Fig. 6.9 and Fig. 6.10 show the formation of *S. aureus* biofilm on these SLM printed samples after 48 hours of incubation as observed by SEM (Figure 6.9) and confocal fluorescent microscopy (Figure 6.10), respectively. It is clearly visible from the SEM images that the higher the sample inclination angle, the more *S. aureus* are attached to the samples' surfaces. On the sample printed at 90 degrees, we observe that the surface is almost entirely covered with *S. aureus*, whereas only sporadic colonies of bacteria are found on the 10 degrees sample. In the confocal fluorescent microscopy images, individual *S. aureus* were stained with DAPI dye and appear blue (Figure 6.10). A similar trend is observed in these fluorescent images; more extensive biofilm coverage was found on 90 degrees printed substrates as compared to the 10, and 45 degrees samples. Notably, most bacteria are observed to grow around, rather than upon, the partially melted particles. We confirm that the large number of partially melted

particles in the 90 degrees sample correlates to the highest number of bacterial colonies formed. Image analyses were performed to quantify the surface coverage of biofilm on each of the SLM printed substrates. From this, surface coverage of biofilm from the low magnification images on 10 and 45 degrees samples was measured as 11.5% and 13.6% respectively, which is significantly less than that observed on the 90 degrees sample (20.3%).Even though 10 degrees sample case, the number of partially melted particles is fewer than 45 degrees but the biofilm formation percentage is close to 45 degrees because of the unique bumpy topographical feature of sample which comes from the scanning track edge border which also contributed biofilm formation along with fewer partially melted particles on surface.

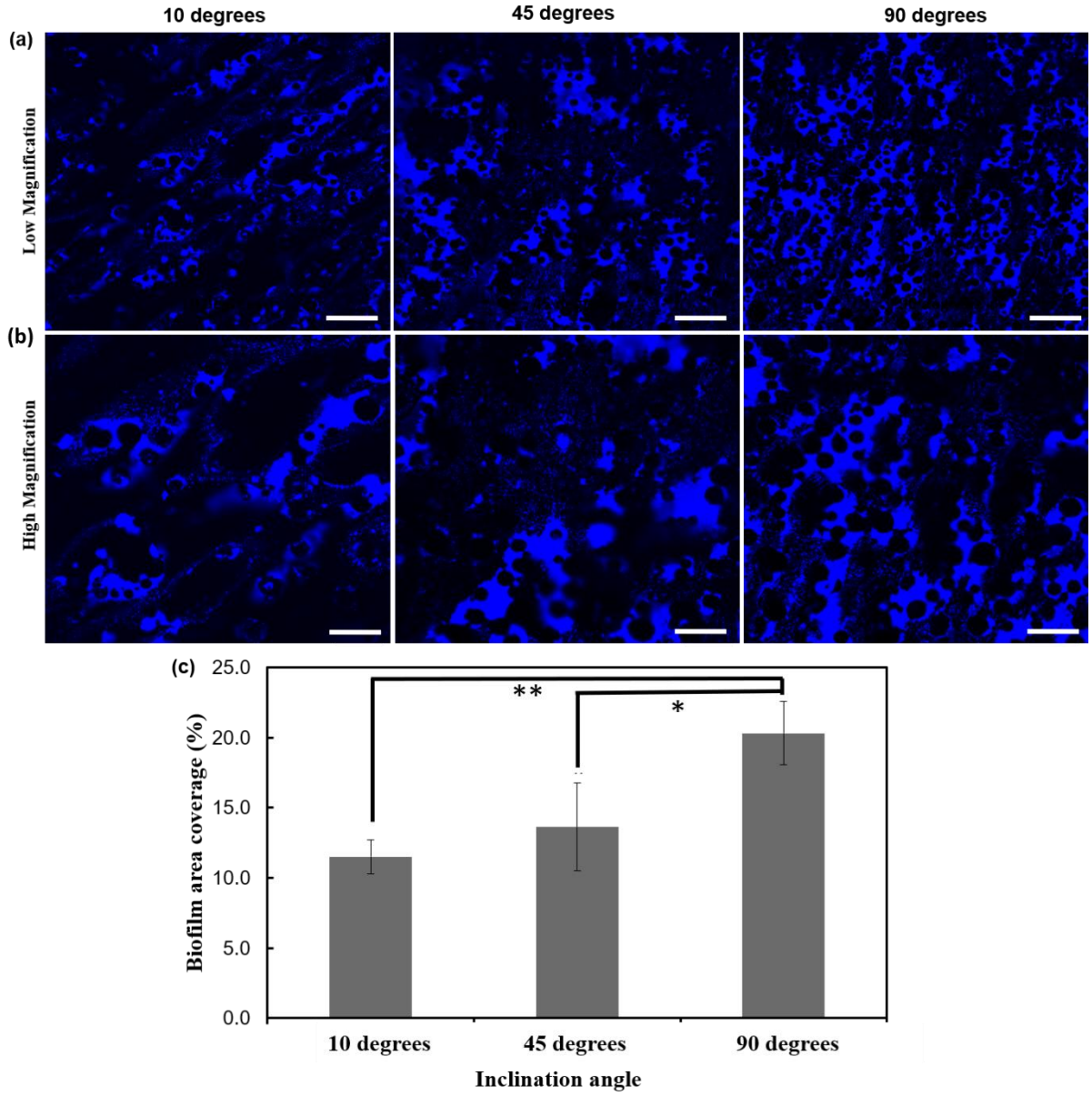

Figure 6.10 : Representative fluorescent images of *S. aureus* biofilm on SLM samples after incubation period of 48 hrs. *S. aureus* were stained with Hoechst 33258 (Blue) for both low magnification(a), Scale bar 100µm and high magnification(b), scale bar 200µm, (c) Surface coverage of biofilm obtained from fluorescent images via analysis using ImageJ (NIH). The biofilm coverage was calculated from at least three random locations on three separated samples, Data = Mean ± SD, $n \geq 4$, * $p<0.05$, ** $p<0.01$.

Fig. 6.11. shows the quantitative crystal violet staining of different inclined substrates. Quantitative crystal violet staining was performed to compare the relative biomass of the biofilms on the substrates with different build inclination angles. The substrates were

challenged with *S. aureus* and the biofilms were allowed to grow for 48 hours at 37°C. Figure 6.11(a) and Figure 6.11(b) show the crystal violet stained substrates, and the absorbance value (OD550) of the dissolved crystal violet from these substrates which directly correlates to biomass. The crystal violet assay result shows significantly lower biomass on samples with lower build inclination angles. These results further confirm the SEM and fluorescent imaging observations that the reduction in build inclination angle directly reduces the formation of a *S. aureus* biofilm.

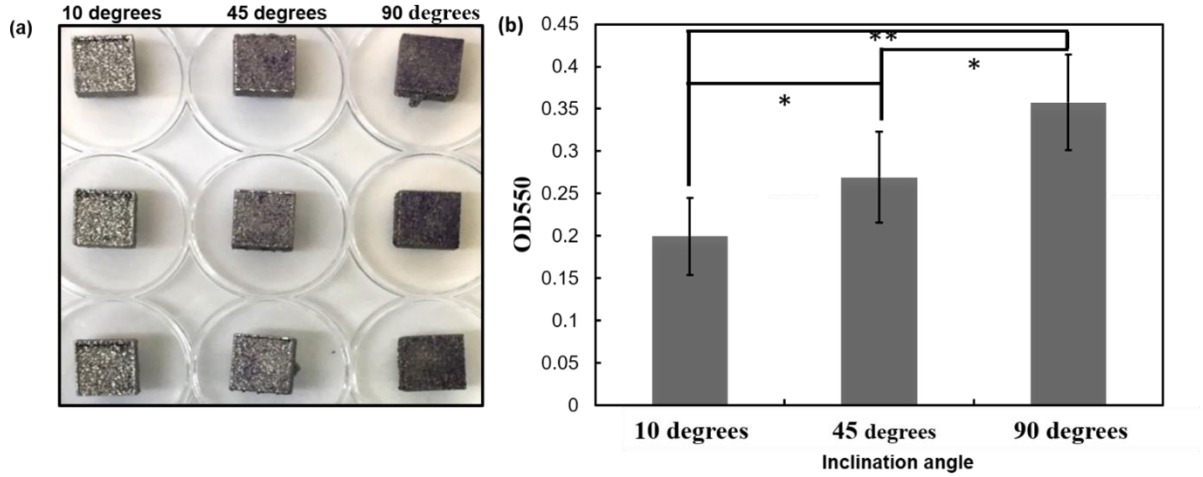

Figure 6. 11 **:** (a) Images of SLM printed substrates with *S. aureus* biofilms stained with crystal violet. Higher crystal violet stain was observed on 90 degrees build angle samples compared to 10, and 45 degrees samples. (b) Absorbance of crystal violet stain read at 550 nm shows higher biomass of biofilm grown on substrates with higher build inclination angle, Data = Mean ± SD, $n \geq 5$, * $p<0.05$, ** $p<0.01$.

The surface chemistry has not been altered in any of the inclined SLM samples, so the surface topography played the entire role in terms of bacterial attachment and subsequent biofilm formation. There is likely more than one factor that contributes to the increase in *S. aureus* biofilm formation on SLM substrates manufactured with increased inclination angles.

We suggest that these factors involve (1) the amount of partially melted particles on surface; (2) the surface wettability[237]; (3) the surface roughness[132, 230, 238] ; (4) surface free

energy[239], (5) surface area[239]. There are substantially more partially melted particles (383) found on 90 degrees samples shown in figure 6.3(b) than 45 degrees (218) and 10 degrees (61) samples. The large number of these particles contributes the higher surface roughness for 90 degrees surface than 45 degrees and 10 degrees, triggering the bacteria to form a biofilm. The higher surface roughness found in samples built at higher inclination angles correlates to more extensive *S. aureus* biofilm colonisation. Previous studies have demonstrated that a rougher surface with more peaks and valleys tend to promote bacterial growth. *S. aureus*, a species of bacteria with relatively low motility, have the tendency to grow in valleys[240].

Regarding the surface wettability, the Derjaguin-Landau-verwey-overbeek theory supports the mechanism of increased bacterial adhesion on rough titanium substrates; the initial attachment of bacteria on substrates is due to a combination of forces such as van der Waals (vdW) and electrostatic repulsive[241]. In the case of the 45 degrees and the 90 degrees specimens, the surfaces are more hydrophobic than 10 degrees. The increase in hydrophobicity with inclination angle is most likely due to the presence of air pockets created by the increasing number of partially melted particles, as suggested by the Cassie Baxter model for composite surfaces[231, 232].

Since *S. aureus* biofilms have been reported to be hydrophobic[242], the more hydrophobic a surface is, the stronger *S. aureus* will adhere to it, leading to more extensive and stable biofilm formation. It has been shown by a thermodynamic model that hydrophobic bacteria tend to grow more colonies on materials which show hydrophobic properties and vice versa[243, 244]. It has been also reported that hydrophobic titanium surfaces have a greater tendency to form colonies than hydrophilic equivalents[237]. It has been shown that the surface free energy can play also provide a contribution (albeit to a lesser extent than roughness and wettability) [135, 245]. Surface energy is directly correlated with surface wettability. We show that with the increase of the inclination angle, there is a reduction in the surface free energy. Therefore, the

lowest inclination (10 degrees) has the highest surface free energy; providing fewer hydrophobic interactions limiting the biofilm formation. In the high inclination case (90 degrees), the lowest surface free energy was observed, enabling significantly more hydrophobic interactions and a corresponding increase in the biofilm formation[246, 247].

Surface area of different inclination angle perhaps has also played role in terms of biofilm formation[239] even though there is no correlation found between surface area and build inclination angle. The higher surface area has been found in case of lower inclination (10 degrees) than 45 degrees and 90 degrees because of its unique topographical feature with fewer partially melted particles along with scanning track edge bumpy border which might exhibit recalcitrance towards *S.aureus* biofilm formation[247]. But this phenomenon is only applicable for 10 degrees not for 45 degrees and 90 degrees as it has been found that 90 degrees' surface area is higher than 45 degrees because of its greater amount of partially melted particles presence on surface where the effect of scanning track edge border has not observed for both 45 degrees and 90 degrees.

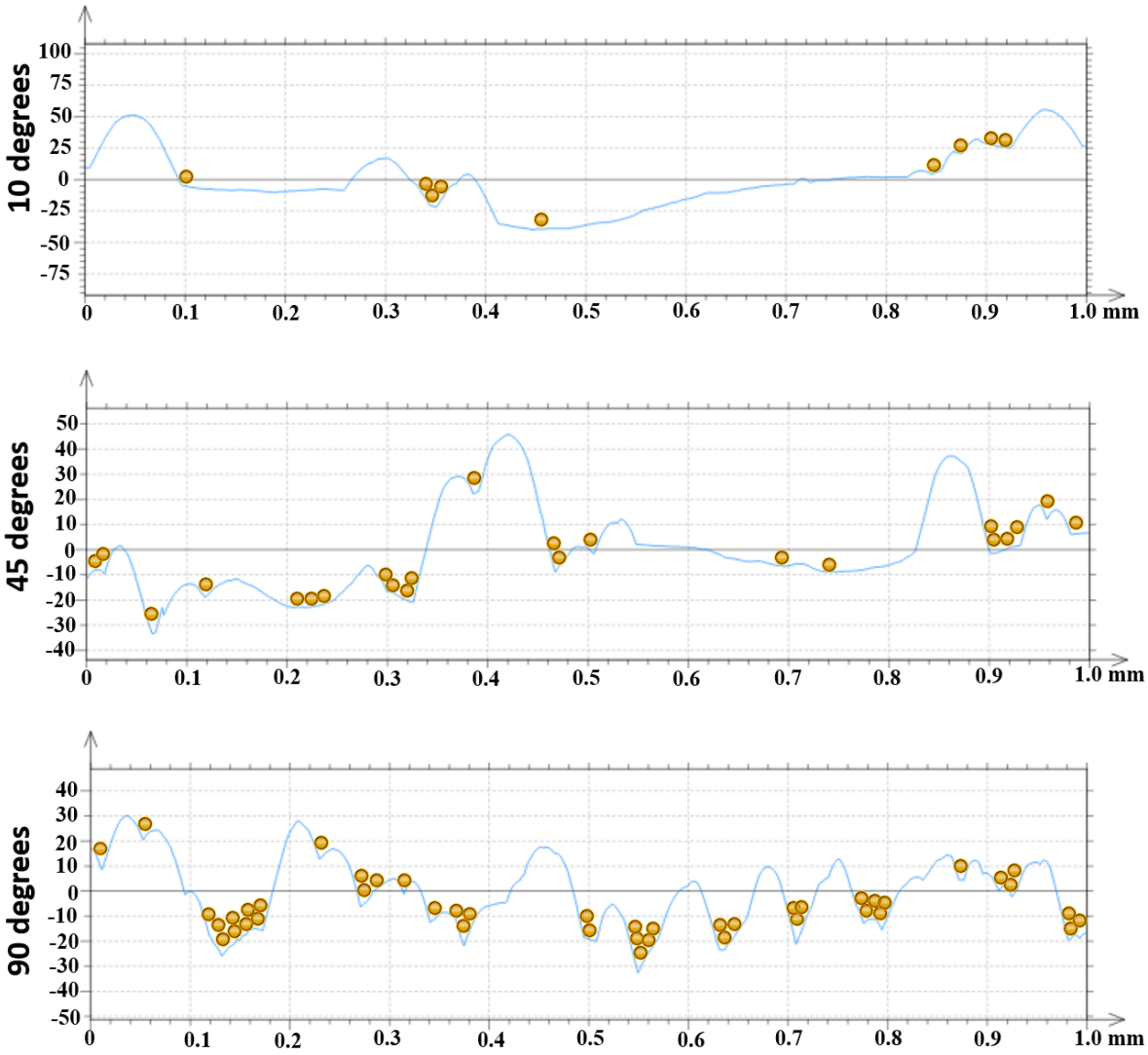

Figure 6.12: A proposed mechanism for *S. aureus* biofilm formation on SLM surfaces. *S. aureus* (orange circles) are overlaid on the surface roughness profiles of SLM substrates printed with 10, 45, and 90 degrees inclination angle. 90 degrees sample, being the roughest with more peaks and valleys among the three samples, promotes the attachment of *S. aureus* and the formation of the largest biofilm.

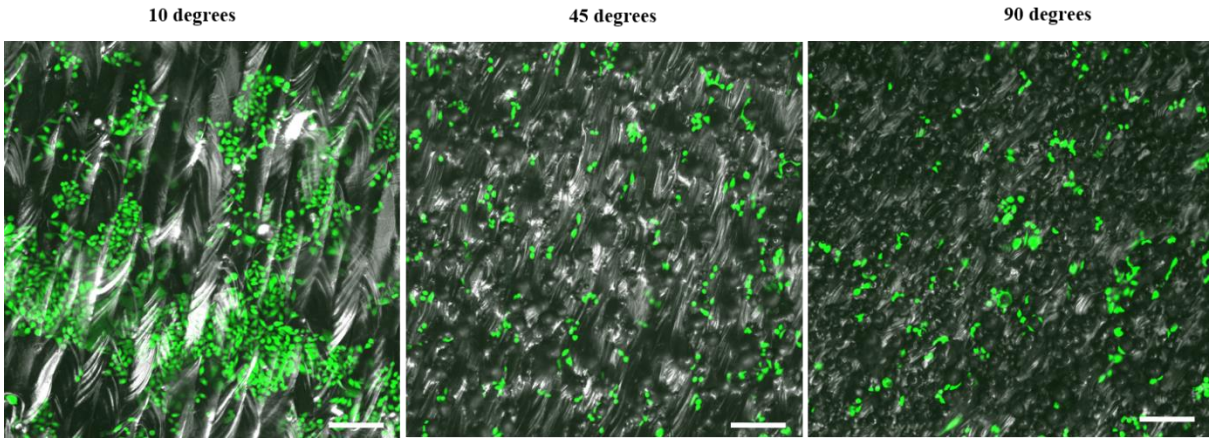

Figure 6.13: Confocal fluorescent images of Chinese hamster ovarian (CHO) cells grown on different inclined (10, 45, and 90 degrees) surfaces after 24 hrs of incubation, scale bars= 200μm.

However, in order to form an effective substrate for integration into the surrounding tissue, a substrate must encourage growth of the surrounding host cells. In order to test the change in angle of fabrication on the overall biocompatibility of the surfaces, we cultured an attachment dependant mammalian cell line on the surfaces[26]. Here, Chinese hamster ovarian (CHO) cells were seeded on SLM substrates and incubated for 24 hr before analysed using a fluorescent confocal microscope. The result shows that CHO cells adhered well to all SLM substrates in Fig. 6.13. Interestingly, despite having significantly different biofilm support, these SLM substrates appear to support mammalian cell growth equally across all three inclination angles.

6.5. Conclusion

In conclusion, we report that SLM printed substrates' topography, roughness, and wettability were highly dependent on the build inclination angle. It was found that for the lowest build inclination angle (10 degrees), only few partially melted particles were observed, whereas the surface printed at a higher inclination angle (90 degrees) was densely covered with partially melted particles. As a result, the substrates printed at 90 degrees were both rougher and more hydrophobic than the samples printed at 10 and 45 degrees. The build angle, however, did not

alter the bulk surface chemistry. More importantly, we found that the substrate printed with the lowest inclination angle (10 degrees) exhibited the least amount of biofilm formation, which was evident from both SEM and fluorescent imaging observations and a crystal violet biomass assay. Importantly, this capacity for reduced biofilm formation did not come at the expense of biocompatibility, as confirmed by mammalian cell viability. We, therefore, suggest the implementation of a low build angle to future SLM printed implants is a facile yet effective mechanism to minimise the colonisation of *S. aureus*, one of the most common pathogens associated with the majority of implant related infections.

Chapter-Seven: Bone Cell Response on Additively Manufactured Single Struts with Different Inclination Angle, Diameter in Lattice Implant

7.1. Chapter Overview

In the previous chapter, the author of this thesis has shown how the rational design of additively manufactured surface can control biofilm formation and prevent against implant associated infection. In this chapter, the manufacture and design of single cylindrical strut with the alteration of both inclination angle and strut diameter have been described. In addition, the behaviour of primary bone cell attachment on individual cylindrical strut with different inclination angle and strut diameter has been observed.

In this study, we have manufactured Ti6Al4V cylindrical single struts by selective laser melting process at three different inclination angles (30 degrees, 60 degrees and 90 degrees) with 0.2 mm, 0.6 mm, 1.0 mm diameter as a proof of concept of orthopaedic lattice implants. For 30° and 90° specimens, stress concentration reduced with increasing strut diameter. For 90° specimens, the stress concentration factor was the greatest for 0.6 mm diameter, whereas they were very similar for 0.2 mm and 1.0 mm diameters. It has been found from the roughness profile for 30 deg inclination angle that the profile angle is varied significantly. The roughness has been maximum for the downward facing surface and the thinner struts (0.2mm, 0.6mm) show their minimum at the upward facing surface. The 1mm strut has minimums at the sides with an increased roughness at the upward facing surface. For the 60 deg and 90 deg cases the roughness shows less variation around the strut.

The effect of the surface property such as surface roughness for cylindrical strut on cell fate was determined. In each case, rat primary osteoblasts (r-POB) was found to be well adhered; however, primary osteoblasts appeared to be more filopodia, indicating better spreading on 60

degrees samples with 0.2, 0.6, and 1.0 mm strut diameter as the neighbouring two partially melted particles. This work gives us a novel insight in terms of developing additively manufactured cylindrical strut with different inclination angle with strut diameter for the next generation orthopaedic lattice implant.

7.2. Introduction

Musculoskeletal disorders are one of the biggest health related concerns across the world with over in excess of 1 million patients per year undergoing joint replacement surgery in the United States of America[248] with 310,800 hip replacements were performed in US alone in patients above the age of 45[249]. Due to an active lifestyle, the age of recipients is decreasing with an increased incidence of patients under 40 years receiving hip implants. As a result, implant lifetime often means that patients are undertaking revision surgery as they outlive their total joint replacement and replacement is becoming the norm [112, 250]. There are several factors which are directly responsible for limiting life of load-bearing implants such as poor osseointegration, stress shielding, or implant loosening. Metallic implants are widely used to address different musculoskeletal disorders because of their high mechanical properties, high corrosion resistance, toughness, high durability, and superior biocompatibility [251-254].

Around 70-80% of medical implants are made from metallic biomaterials [255] for different purposes in orthopaedic field such as bone repair, fracture fixation, load-bearing [256, 257]. Metal and metal alloys including stainless steels, tantalum, titanium, cobalt based alloys (CoCrMo), titanium–nickel, have been extensively utilised in metallic implants [258] [90] [259] [260]. Among different metallic alloy used as biomedical implants, titanium and its alloy has been used as a proven implant material due to its excellent biocompatibility, corrosion resistance, toughness, strength to weight ratio, and bio-inert oxide surface [261]. Rapid prototyping or additive manufacturing (AM) enables to make patient specific orthopaedic implants with the greatest precision and complex architecture with prescribed microstructure

and macrostructure [262].Additive manufacturing introduces several commercial technologies for the fabrication of robust component using layer-by-layer depositing material based on a computer model. Metallic additive manufacturing is being used widely for different tissue engineering application such as bone grafts, cardiovascular implants, cartilage regeneration [263, 264].

Selective laser melting (SLM) is a Metallic AM (MAM) process where a layer- by-layer material addition technique is applied to create complex 3D parts by selectively melting successive layers of metal powder [19]. In comparison with other metallic additive manufacturing technique, SLM is characterized by good repeatability, medium productivity, and medium to high surface quality [26]. The SLM process was reported to be capable of fabricating implants of several pure titanium and titanium-based alloys for implants such as Ti-24Nb-4Zr-8Sn, Ni-Ti, Ti6Al7Nb, Ti-13Nb-13Zr and other β titanium alloys and most importantly Ti6Al4V [44]. Recently, different literatures show that SLM has the capability to make any complex Ti6Al4V structure with great reproducibility with excellent mechanical properties and biocompatibility[73]. These properties are highly dependent on the associated SLM process parameters such as laser power, scanning pattern, scanning speed, layer thickness, hatch spacing, powder bed temperature and working atmosphere [44].

Cellular lattice structures fabricated by SLM process are the combination of numerous strut elements, each with specific inclination angle to the SLM platen. It has been shown previously that the mechanical properties of SLM manufactured Ti-6Al-4V lattice can be manipulated by the alteration of the strut build inclination angle, strut diameter [19, 265]. Different groups have also shown how the surface topography and surface roughness of Ti6Al4V implants manufactured by SLM played role on cellular attachment and growth[266, 267].Previously we have shown that how the build inclination angle during SLM manufacturing process can influence the surface properties and associated biological response of Ti6Al4V implant[8]. But

there has been limited research carried out showing how the both design parameter of cylindrical strut such as strut inclination angle and strut diameter can influence the surface properties of Ti6Al4V implants and how primary bone cell respond on individual strut. In order to validate the approach different cylindrical implants with inclination angle 30, 45, and 90 degrees with 0.2, 0.6, and 1.0 mm strut diameter were successfully manufactured and their surface morphology, surface roughness were investigated; and, demonstrate that these parameters have a direct relationship with biocompatibility, bone cell attachment and morphology. This work will have significant impact on the design and fabrication of future AM lattice implants with desirable strut geometry for successful orthopaedic applications.

7.3. Experimental Section

The samples were fabricated according to chapter-3.3 – Materials and Methods section outlined in 3.2, characterized according to section 3.4, rat calvariae cell culture and cell morphology analysis according to section 3.5.6.

7.4. Results & Discussion

7.4.1. Fabrication and surface topography of different inclined (30, 45, and 90 degrees) Cylindrical Specimen with 0.2, 0.6, & 1.0 mm strut diameter

Fig.7.1 (a) represents the graphical representation of (Ti6Al4V) lattice implants manufactured by SLM implanted into bone defect model(femur) as a proof of concept. Ti6Al4V single cylindrical struts were fabricated using SLM process with build inclination angle α of 30, 45, and 90 degrees with 0.2, 0.6 and, 1.0 mm strut diameter with respect to the building plane as shown in Fig.7.1 (b). It has been previously shown that porous Ti6Al4V cage with computer designed macro- and micro-architecture was reproduced by selective laser melting (SLM)[267]. They have shown that dense Ti6Al4V discs with six different angles were fabricated to investigate the effects of additive angle (inevitable in SLM manufacturing) on

surface properties and biocompatibility. It has also been reported that functionally graded Ti6Al4V Porous Scaffolds manufactured by additive manufacturing can be an effective apporach to enhance cell penetration and proliferation[268]. However there has been limited research carried out to understand how the individual cylindrical struts are manufactured and what is their associated biological response for orthopaedic application. From the optical image of Fig 7.1 (b), all the cylindrical struts with 30, 60 and 90 degrees build inclination with 0.2,0.6, and 1.0 mm strut diameter were manufactured robustly without any failure and deformation. The size of the Ti6Al4V powders was ~ 30µm. Briefly, the laser scanning strategy used here consisted of a perimetric scan then subsequently filled with a raster scan.

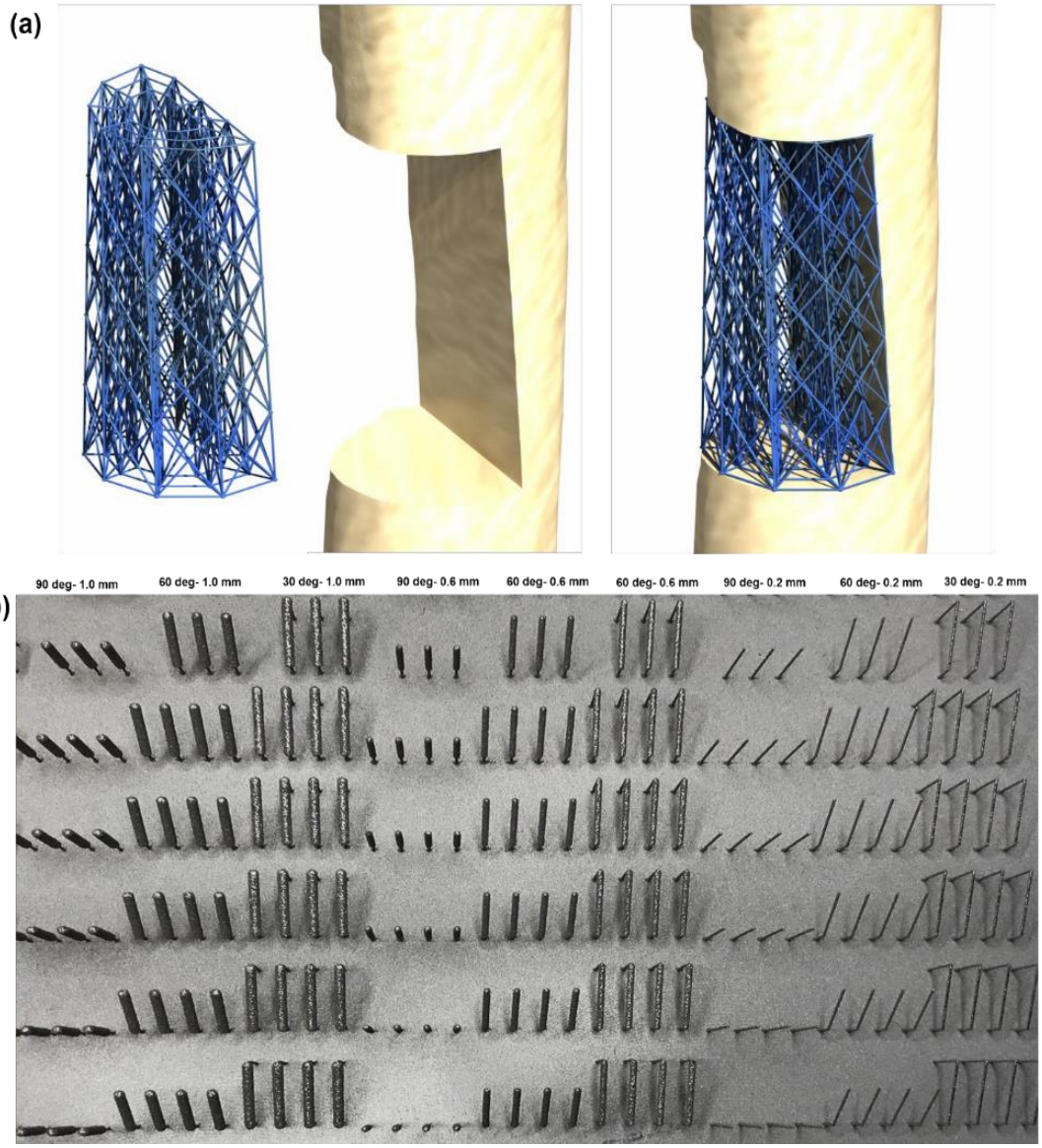

Figure 7.1: (a) Demonstration of (Ti6Al4V) lattice implants manufactured by SLM implanted into bone defect model(femur) as a proof of concept, (b) Optical view of titanium (Ti6Al4V) implants manufactured by SLM by 90, 60, and 30 degrees build inclination angle with 1.0, 0.6, and 0.2 mm diameter with respect to the build plane.

7.4.2. Micro-Computed Tomography results of different inclined (30, 45, and 90 degrees) Cylindrical Specimen with 0.2, 0.6, & 1.0 mm strut diameter

Number of pores and porosity distribution (%) for each strut diameter at build orientation angles are presented in Fig. 7.2. Further investigation of pore sizes and pore orientations are presented in Fig.7.3 and 7.4.

Initial μCT results are reported for the number of pores and porosity (%) extracted within each strut specimens at different inclination angles. Presence of pores are not observed from strut specimens with diameter of 0.2 mm, therefore are not included for further analysis:

1. Minimal porosity percentage and number of pores were observed for the 1 mm strut specimen inclined at 60-degree angle when compared to strut specimens of 1mm diameter inclined at 30 and 90-degree angles. Minimal changes were also observed when comparing 0.6 mm strut diameters at 30,60 and 90-degree inclined angles.
2. The highest porosity percentage and number of pores were observed from the 1 mm strut specimen inclined at 90-degree angle, followed by strut specimen of 1 mm diameter inclined at 30-degree angle. High distribution of these pores is illustrated in Figure 7.2 (b).

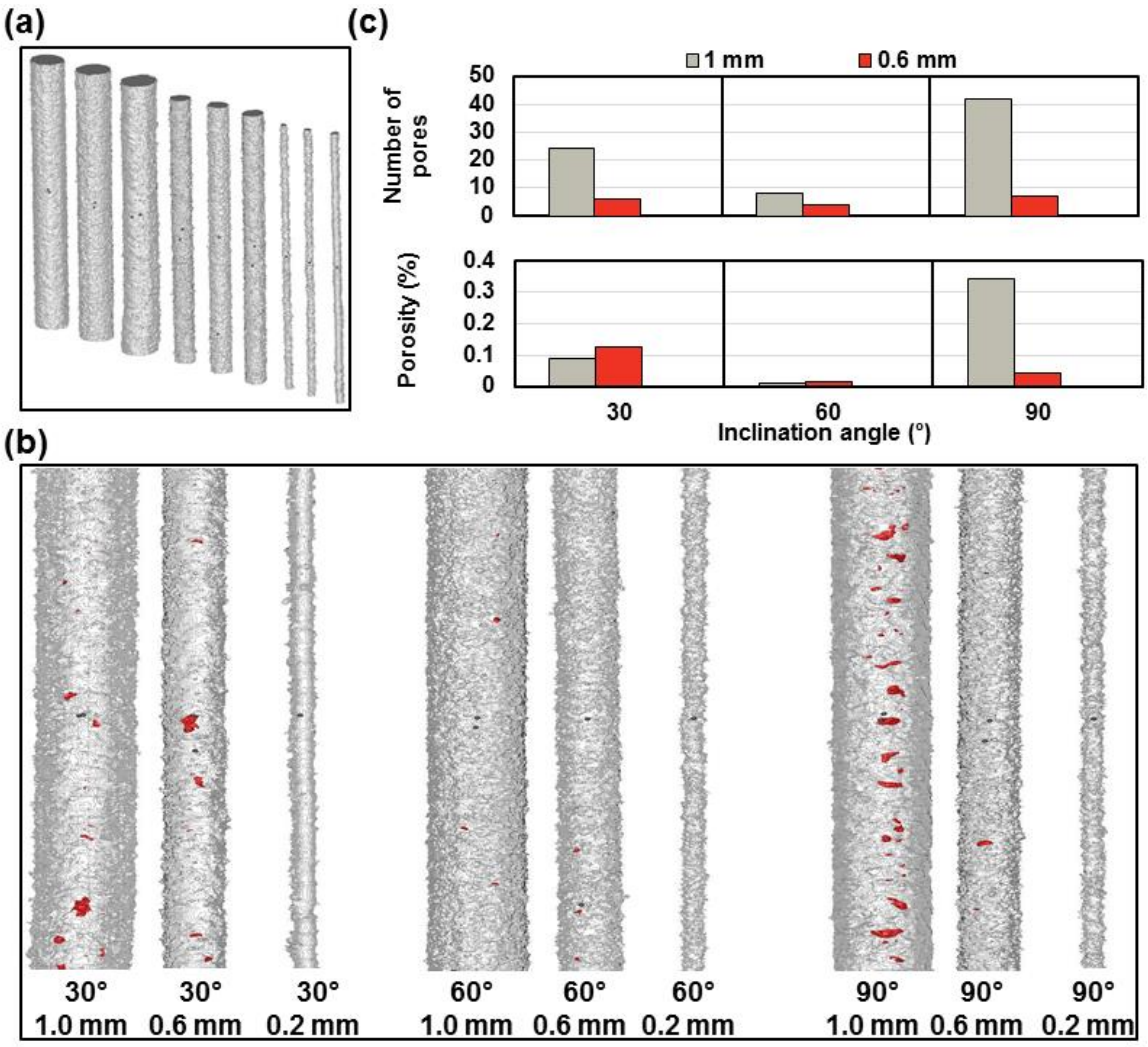

Figure 7. 2: (a) Micro-CT results: reconstructed 3D models iso-view, (b) reconstructed 3D models and their associated pores (red), and (c) Number of pores and porosity, sample size N=1.

The strut specimen's pore sizes (mm^3) shown in Fig.7.3(a) and pore orientations (theta) shown in Fig.7.3(b) were also investigated to further investigate manufacturability:

1. Regarding the pore size distributions along each SLM strut specimens, there exists no linear correlation between pore sizes and specimen height.
2. From linear regression line, pore orientations tend to stay within the range of 30 to 100-degree angle (along the scan direction). Only three strut specimens were observed to produce pore orientations lower than 30 degrees, 1 and 0.6mm for 30-degree strut specimen

and the 1 mm strut specimen inclined at 90-degree angle. No valid relationship can be observed with both pore orientations and specimen height.

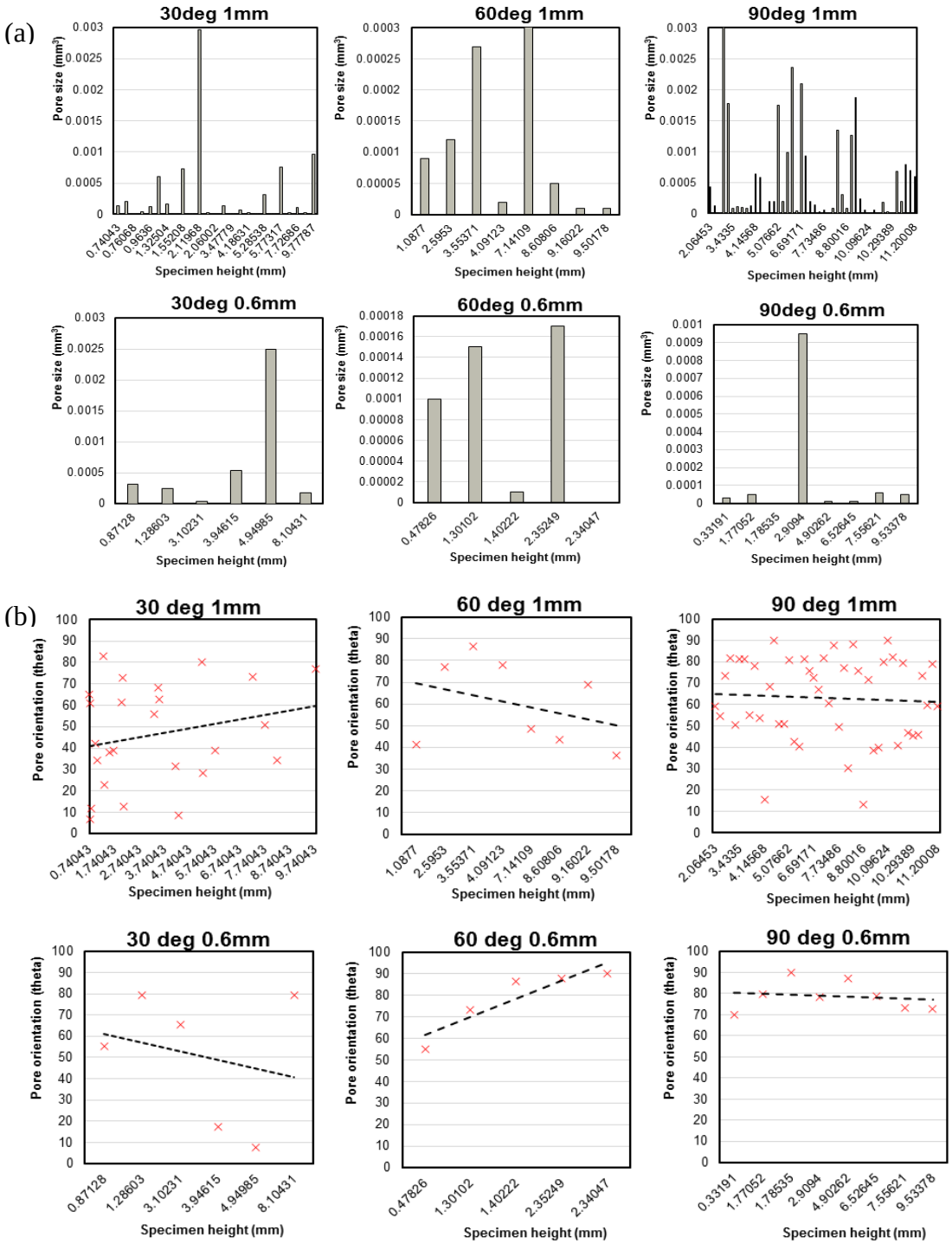

Figure 7. 3: (a) Distribution of pore size of different inclined cylindrical strut with different strut diameter along build height, (b) Distribution of pore orientation of different inclined cylindrical strut with different strut diameter along build height.

7.4.3. Surface morphology of different inclined (30, 45, and 90 degrees) Cylindrical Specimen with 0.2, 0.6, & 1.0 mm strut diameter

Fig.7.4 and Fig.7.5 show the surface morphology of 30, 60, and 90 degrees inclined cylindrical strut with 0.2, 0.6, 1.0 mm diameter for lower magnification((150x) and higher magnification (1200x) by scanning electron microscopy. It has been found from the lower magnification image that strut diameter is not varied across the length of strut in case of 0.6 and 1.0 mm dimeter of 30, 60 and 90 degrees build inclination but the strut diameter is changed around the length of strut for 0.2 mm diameter of 30, 60 and 90 degrees.

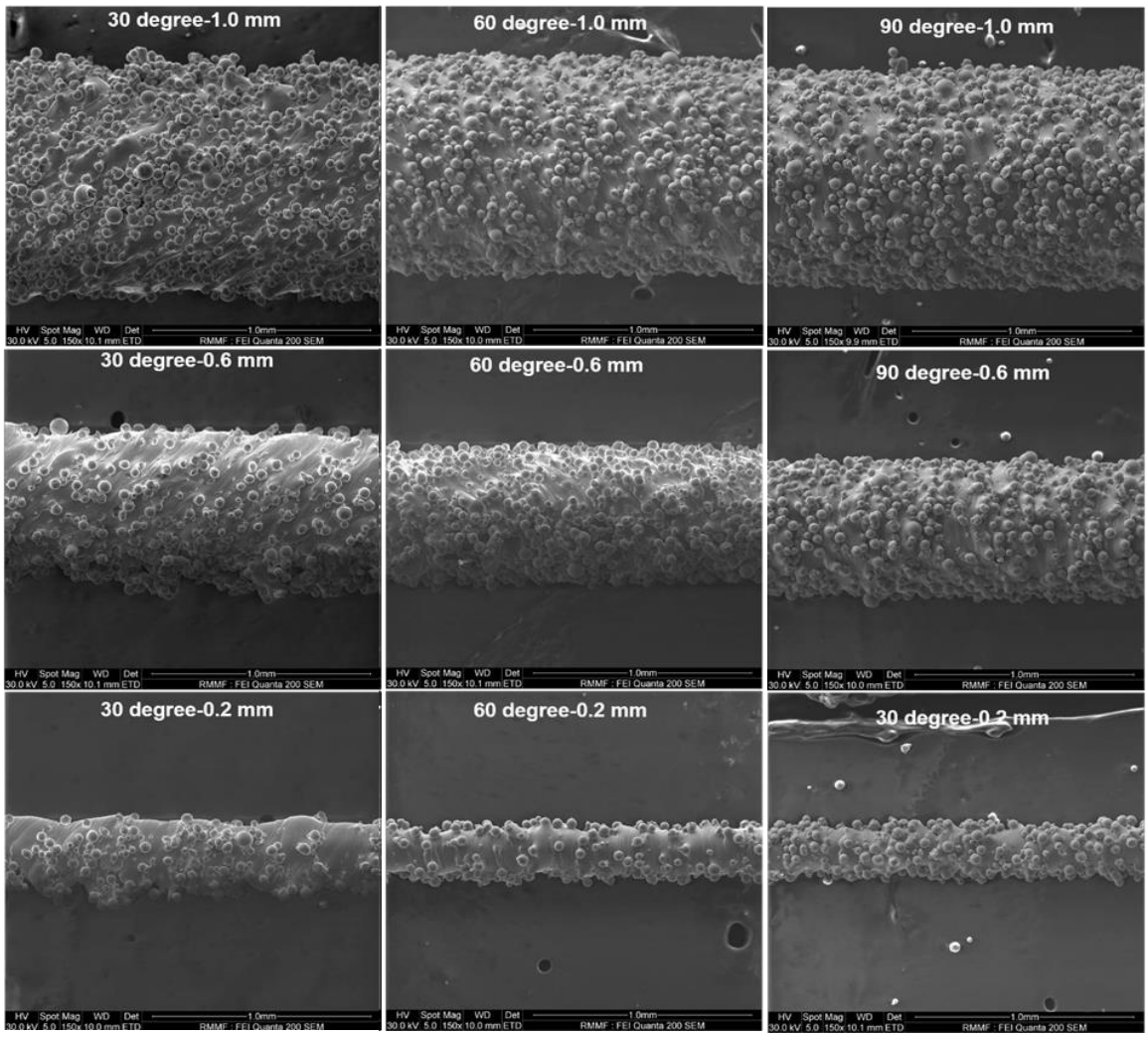

Figure 7.4: (a) SEM micrograph shows the surface morphology of 30, 60, and 90 degrees inclination angle with 0.2, 0.6, & 1.0 mm strut dimeter of low (150X) magnification.

Fig.7.5 shows that each inclined cylindrical strut surface with 0.2, 0.6, and 1.0 mm diameter is covered with randomly fashioned partially melted particles. It has also been observed that partially melted are in different size and spherical in shape.

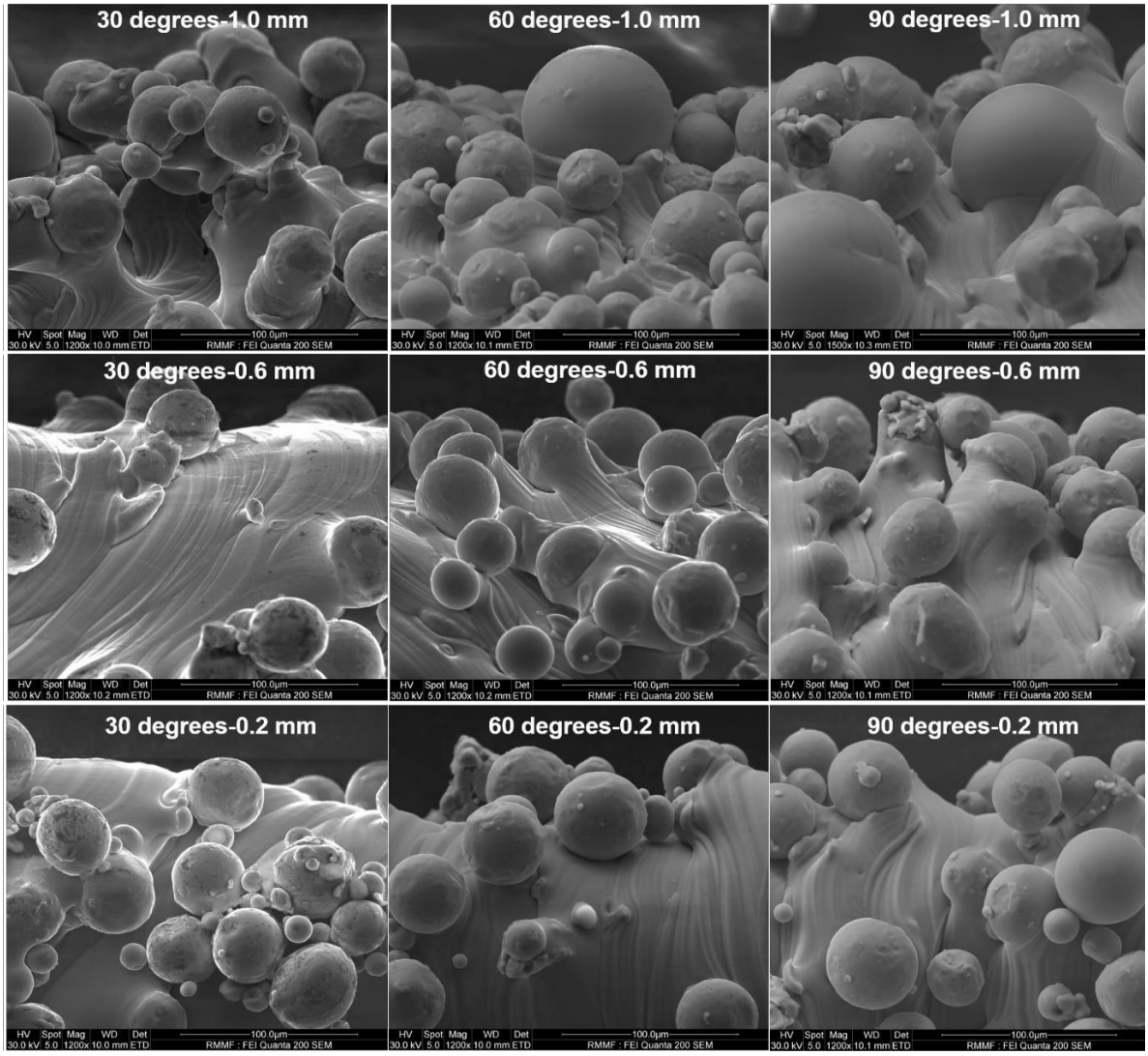

Figure 7.5: (a) SEM micrograph shows the surface morphology of 30, 60, and 90 degrees inclination angle with 0.2, 0.6, & 1.0 mm strut diameter of high (1200X) magnification.

7.4.4. Surface roughness analysis of different inclined (30, 45, and 90 degrees) Cylindrical Specimen with 0.2, 0.6, & 1.0 mm strut diameter

Fig.7.6 shows the roughness (Ra) along the strut with profiles taken at different angles around the strut axis. The alignment of the struts is based on determining the principal axes of inertia, and an assumption is made that the minimum principal axes resolves into the strut axis while another will align with the direction of the upward/downward facing surface. This appears to work reasonably well for the 30deg strut but is less reliable at 60deg. To confirm/improve the angle alignment it would be ideal to have the support strut visible within the image stack.

We are seeing significant difference in roughness with profile angle for the struts fabricated with 30deg inclination angle. The roughness maximum for the downward facing surface. The thinner struts (0.2mm, 0.6mm) show their minimum at the upward facing surface. The 1mm strut has minimums at the sides with an increased roughness at the upward facing surface. For the 60deg and 90deg cases the roughness shows less variation around the strut. For the 60deg struts the support is only visible in the 1mm case, and the angle has been shifted to match. For the other diameters we are uncertain of the angle for the downward facing surface and relying on the determination of principle axes and a best guess as to which axis might be aligned with the downward surface.

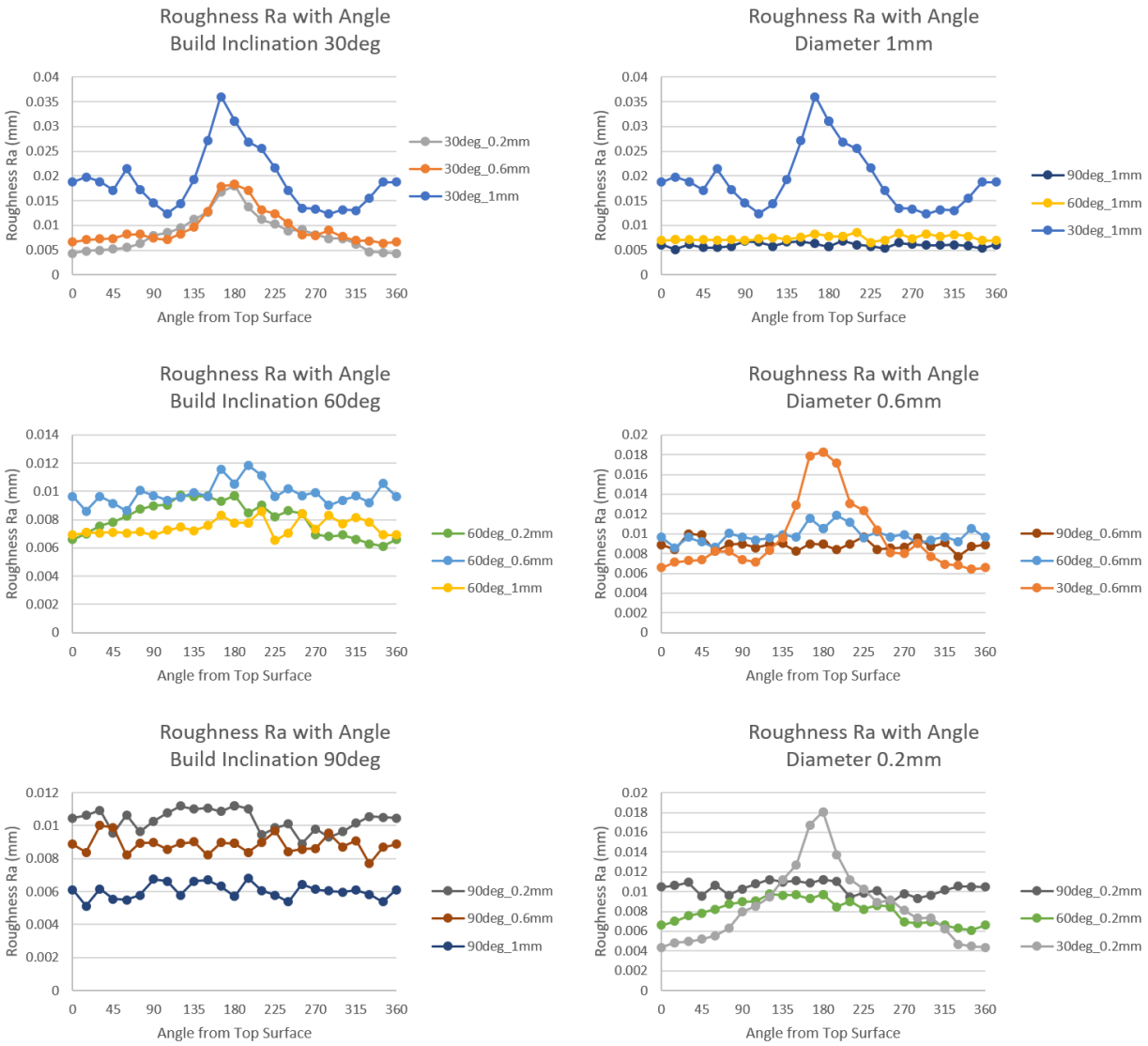

Figure 7.6: Roughness (Ra) along the strut with profiles taken at different angles with different strut diameter around the strut axis.

7.4.5. Finite Element (FE) Stress analysis of different inclined (30, 45, and 90 degrees) Cylindrical Specimen with 0.2, 0.6, & 1.0 mm strut diameter

It has been found from Figure 7.7 that the effect of build orientation angle on the maximum stress is most significant for the 0.2 mm struts. This is clear from the difference in maximum stress between the different build orientation angles, with 30° struts having the largest stress, and 90° having the least. As diameter increases this effect reduces, with only minor discrepancies between the maximum stress within the 1 mm struts. Low build orientation

angles lead to distortion of struts due to manufacturability limitations of the SLM process [20]. This effect is more pronounced for smaller strut diameters as there is less material to offset these effects.

The minimum manufacturable build orientation angle for SLM struts is related to material properties and processing parameters, but is usually approximated as 45° [269]. As a result, it would be expected that the 60° and 90° struts would behave more similarly than the 30° struts as they are above this threshold. However, the maximum stress was more similar between the 30° and 60° struts most prominently for 0.2 mm diameter specimens. This phenomenon may be related to geometries of these cylindrical specimens, and analysis of a larger population of specimens is required for greater confidence in the characterisation of this behaviour.

The distribution of stress across the models shown in Fig.7.8 differed depending on build angle and strut diameter. For the 30° and 60° 0.2 mm diameter struts there are large blue areas, which would suggest the stress is concentrated in a certain region of the struts. Conversely, the 60° 1 mm strut is mostly green, meaning stress is evenly distributed within it. The 90°, 1 mm strut is mostly blue, suggesting a region of high stress, though the end of this strut where the boundary condition was applied was tapered, leading to stress concentration.

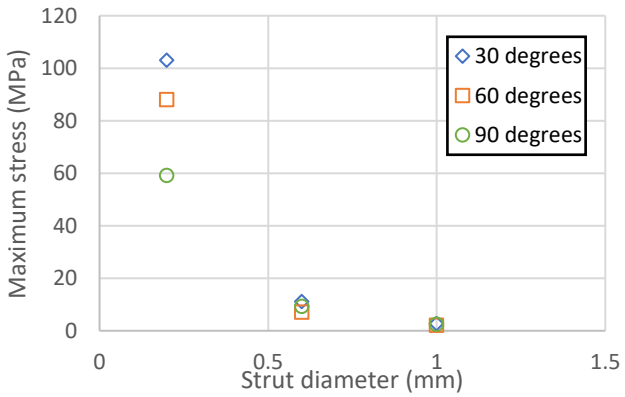

Figure 7. 7: Maximum stress for each build orientation angle and strut diameter.

	D = 0.2mm	D = 0.6mm	D = 1mm
Build angle = 30°	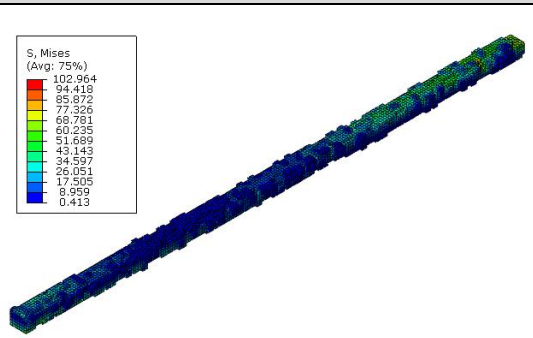	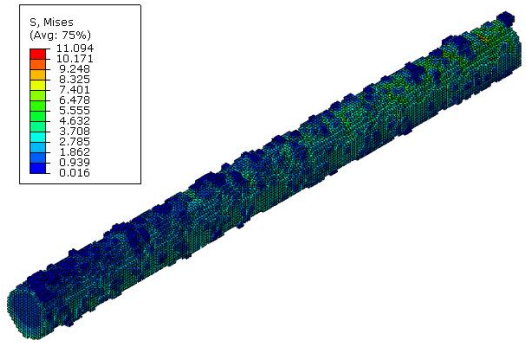	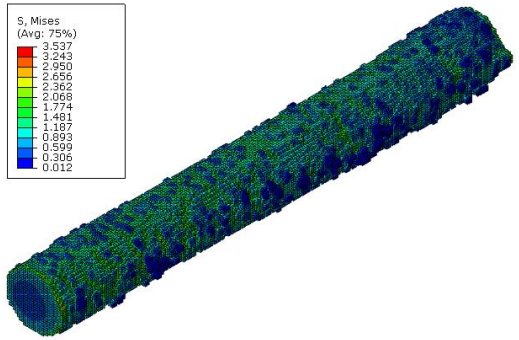
Build angle = 60°	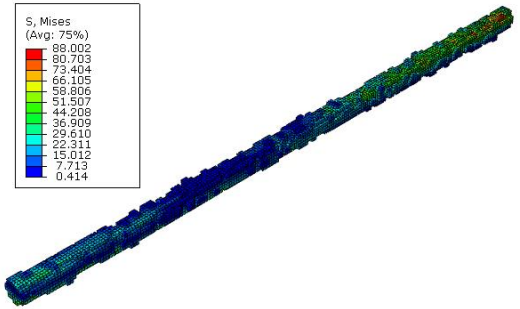	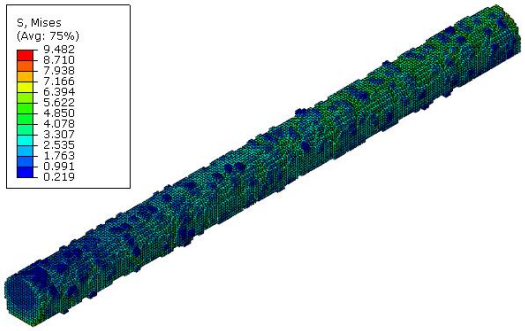	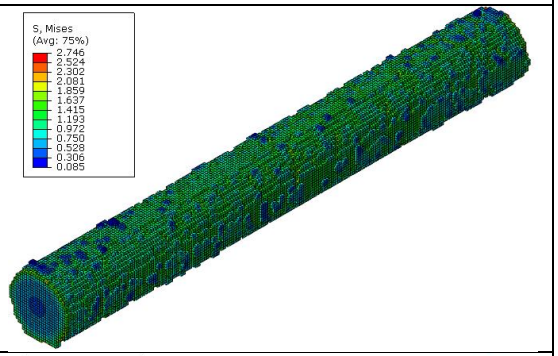
Build angle = 90°	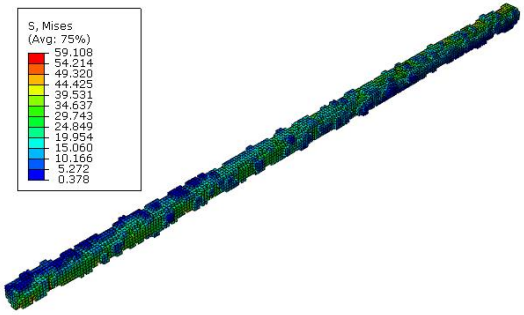	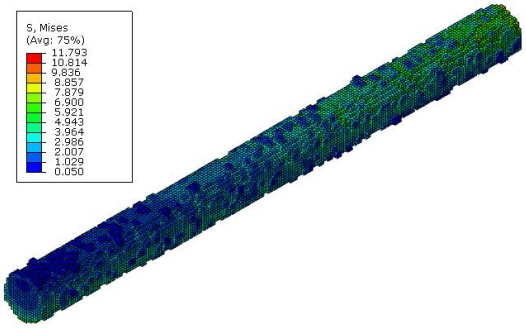	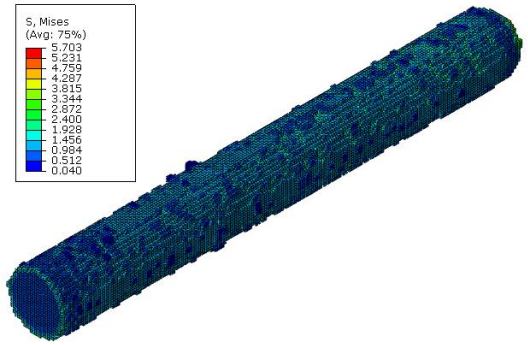

Figure 7. 8: Stress (MPa) contours for different strut diameters and build orientations.

7.4.6. Rat Primary Osteoblast (r-POB) Cell attachment of Different Inclined (30, 45, and 90 degrees) Cylindrical Specimen with 0.2, 0.6, & 1.0 mm Strut Diameter

Fig.7.9 (a), (b), & (c) respectively shows the SEM images (5000x magnification) of the primary osteoblast cell attachment on the surface of 30, 45, and 90 degrees inclination with 0.2, 0.6, and 1.0 mm strut diameter after 3 days and 7 days of incubation. It has been found that primary bone cells have been well adhered for all cylindrical struts irrespective of its build inclination angle and strut diameter. It is also visible that the bone cell is well connected from one partially melted particle to another partially melted particle in case of all cylindrical struts. The primary bone cells appeared elongated and exhibited a more spindled appearance after 7 days of incubation on all cylindrical struts than after 3 days of incubation. There have been several literatures show that SLM manufactured Ti6Al4V implants are highly biocompatible and exhibited well in-vitro cell attachment and cell proliferation behaviour [52, 168, 213]. It has been observed that rather than the surface roughness the bone cell attachment behaviour is mostly influenced by the surface topography of all single cylindrical strut which has been confirmed from all SEM images of Fig.7.9 (a), (b) & (c). The location of partially melted particles on single cylindrical strut influences directly the morphology of bone cell. It has been found from Fig. 7.9 (a) and 7.9 (c) that 30 degrees and 90 degrees inclined cylindrical strut surface with 0.2, 0.6, and 1.0 mm strut diameter that the cells appeared not to be elongated enough after 3 days of incubation due to the small distance between two partially melted particles. Primary osteoblasts appeared to be more filopodia, indicating better spreading on 60 degrees samples shown in Fig. 7.9 (b) with 0.2, 0.6, and 1.0 mm strut diameter as the neighbouring two partially melted particles have higher distance from each other which indicates that osteoblast get enough space to be stretched with elongated morphology.

(a)

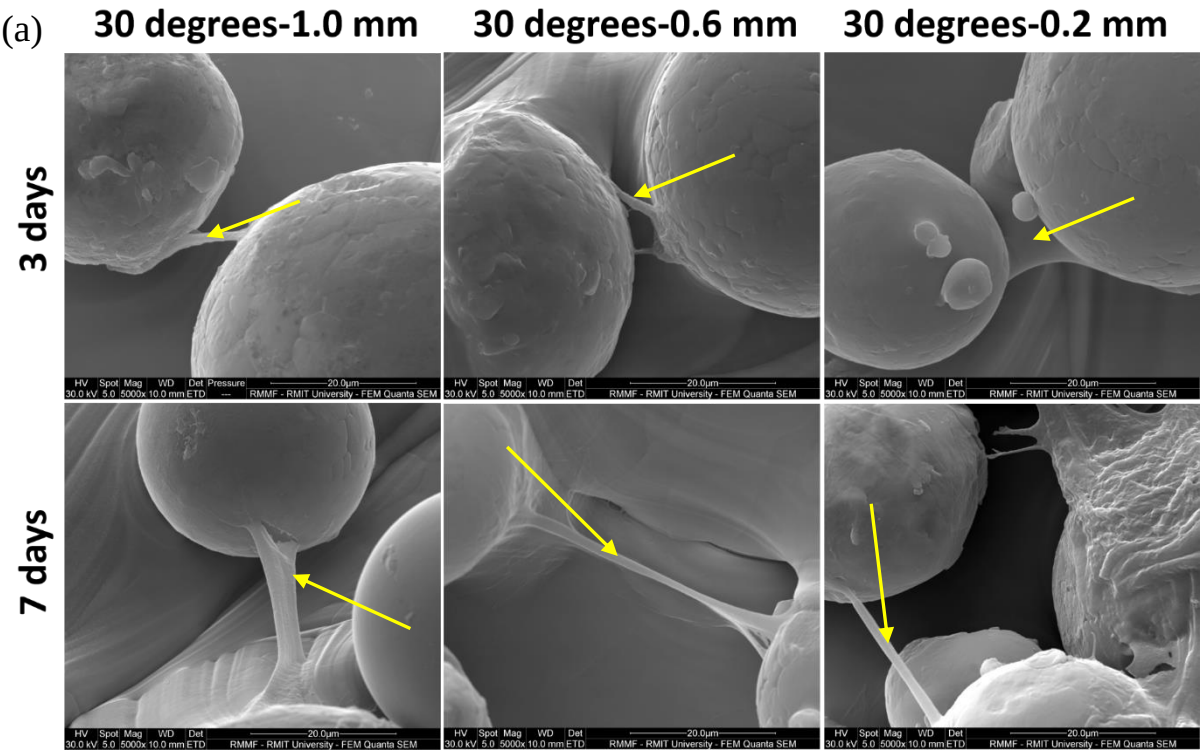
30 degrees-1.0 mm
30 degrees-0.6 mm
30 degrees-0.2 mm
3 days
7 days

(b)

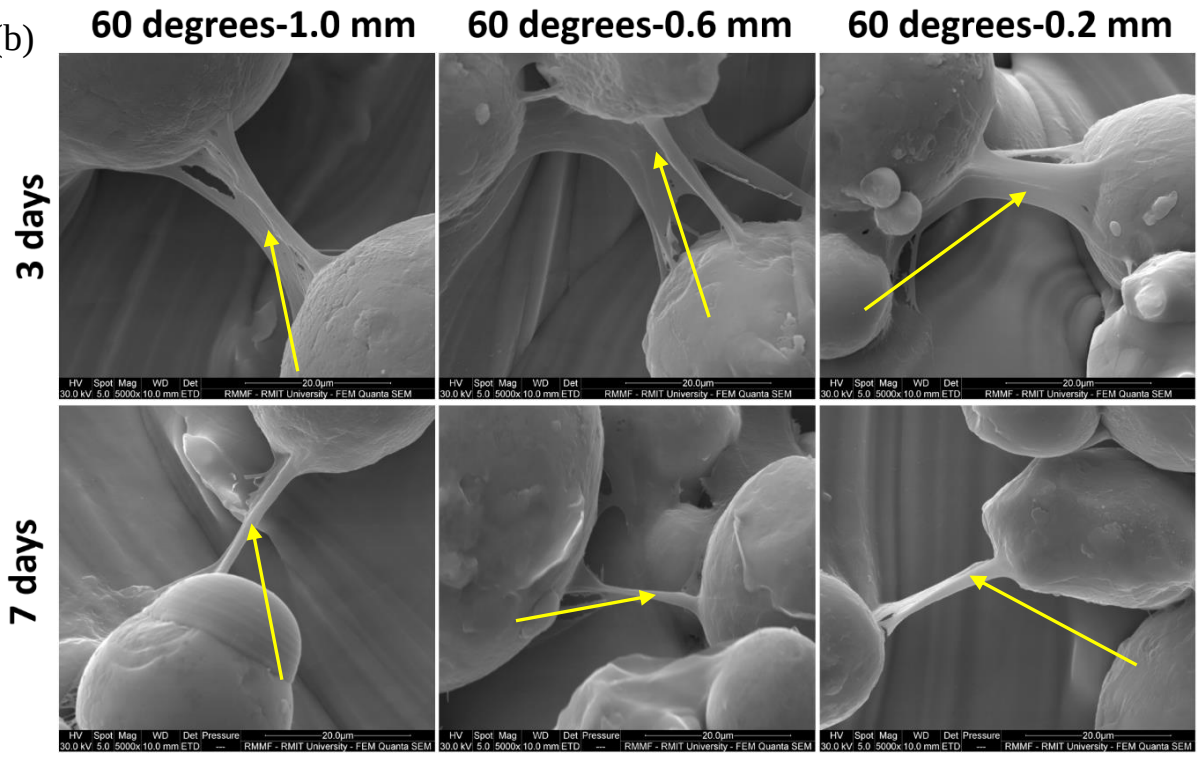
60 degrees-1.0 mm
60 degrees-0.6 mm
60 degrees-0.2 mm
3 days
7 days

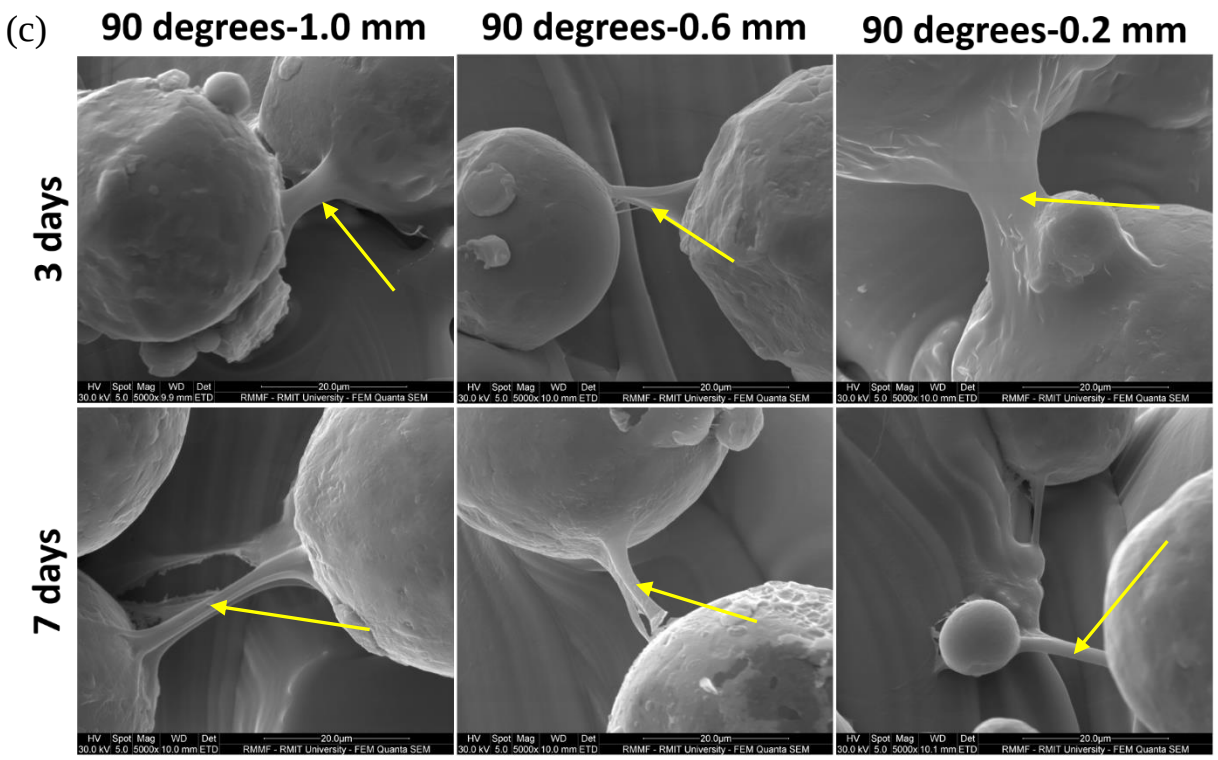

Figure 7.9: (a) SEM micrographs of rat primary cell (r-POB) attachments shown by yellow arrow on 30 degrees cylindrical inclined with 0.2, 0.6, and 1.0 mm strut diameter after 3 days and 7 days of incubation, scale bar=20 µm (b) SEM micrographs of rat primary cell (r-POB) attachments shown by yellow arrow on 60 degrees cylindrical inclined with 0.2, 0.6, and 1.0 mm strut diameter after 3 days and 7 days of incubation, scale bar=20 µm (c) SEM micrographs of rat primary cell (r-POB) attachments shown by yellow arrow on 90 degrees cylindrical inclined with 0.2, 0.6, and 1.0 mm strut diameter after 3 days and 7 days of incubation, scale bar=20 µm.

7.5. Conclusion

In this study, Ti6Al4V cylindrical single strut of different inclination angles (30 degrees, 60 degrees, and 90 degrees) with 0.2 mm, 0.6 mm, 1.0 mm diameter was manufactured successfully by SLM process as a proof of concept for applying as orthopaedic lattice implant. Micro-CT results show us that the highest porosity percentage and number of pores has been observed from the 1 mm strut specimen inclined at 90-degrees angle, followed by strut specimen of 1 mm diameter inclined at 30-degrees angle. It has been found that for 90° specimens, the stress concentration factor was the greatest for 0.6 mm diameter, whereas they

were very similar for 0.2 mm and 1.0 mm diameters. The surface profile property (surface roughness) results show us that the roughness has been maximum for the downward facing surface and the thinner struts (0.2mm, 0.6mm) show their minimum at the upward facing surface. From the in-vitro result, it has been found that rat primary osteoblasts (r-POB) was found to be well adhered irrespective of strut build inclination angle and strut diameter ; however, primary osteoblasts appeared to be more filopodia, indicating better spreading on 60 degrees samples with 0.2, 0.6, and 1.0 mm strut diameter as the neighbouring two partially melted particles are located far from each other. This work provides us a novel insight in terms of developing next- generation additively manufactured cylindrical strut with required design geometry.

Chapter Eight: Conclusions and Future Study

8.1. Conclusion

Metallic patient-specific orthopaedic implant manufactured by additive manufacturing has shown its incredible potentiality for matching desired mechanical properties with host bone, structural efficacy, dimensional accuracy, and osseointegration. For the successful clinical outcome of orthopaedic implants for patients, it is quite essential to integrate the knowledge between materials science, manufacturing with bone biology. The precision, personalisation and superior functionality of additive manufacturing techniques, such as selective laser melting (SLM), enables the fabrication of metallic implants with patient specific customisation.

The following conclusions have been made from this thesis:

1. At the initial stage of this research, Ti6Al4V SLM implants with support-free structure with different build inclinations from 5 degrees to 90 degrees were manufactured with 5 degrees interval and after that the detailed surface profile properties such as surface roughness, surface morphology and surface wettability were investigated. It has been found from the roughness study that with the change of the inclination angle higher percentage of correlation with R_a is found on lower surface of SLM plates on the linear, exponential and logarithmic regression line than the upper surface of SLM plates.
2. It is also found from the surface morphology that with the increase of the build inclination that there is a corresponding increase in the number of partially melted particles on the upward SLM support-free part from 5 to 90 degrees and there is no regular trend was observed in terms of partially melted particles on downward surface. It has been found from the surface wettability that the highest and lowest contact angle value for upward surface is 130.150^0 and 80.81^0 respectively for 75 and 35 degrees build inclined SLM samples. In case of lower surface all different inclined SLM plates reveal the hydrophobic surface.

3. After getting through investigation of 5 to 90 degrees inclined surface, we have chosen three different inclination angles (0, 45, & 90 degrees) to grow mammalian cell (Chinese hamster ovarian). It has been found from 0 to 90 degrees that the surface roughness is increased due to the increasing amount of partially melted particles. The surface chemistry (TiO_2) of all different inclination angle has not been altered. In spite of having similar cell viability on all inclined SLM samples, the attachment behaviour of mammalian cells is quite different. Higher amount of spindle like cells have been found in 45 degrees and 90 degrees with less spherical type cells than 0 degrees. In addition, mammalian cells were found to be more elongated shape on 45, and 90 degrees than 0degree inclined implant.
4. It is quite evident from implant's design perspective that implants manufactured in higher inclination angle could be more useful than lower inclination angle because of improved cell adhesion behaviour. The finding of this study will help to design additively manufactured implants with appropriate inclination angle for improved bio-interface without the need for any post-processing treatment from a single manufacturing stage. In the next stage of study, we tried to understand if the additively manufactured implants can prevent biofilm formation if the design angle of inclination is rationally chosen as bacterial attachment and subsequent biofilm formation on medical implants is a serious infection risk. An unexpected outcome of this process, however, is a hitherto unachievable fine control over the bio-interface in a single manufacturing step. It was found that the lowest printing angle (10 degrees) implant surface has only few partially melted particles, whereas the surface printed at a higher inclination angle (90 degrees) was densely covered with partially melted particles. So that the implant surface printed at 90 degrees exhibit rougher and hydrophobic than 10 and 45 degrees.
5. The bulk surface chemistry of implant surface with different inclination angle remain unchanged. After 48 hours of incubation with *Staphylococcus aureus* bacteria, it has been

found that the lowest build inclination angle(10 degrees) inducing the surface which can significantly inhibit biofilm formation than 45 degrees and 90 degrees which has been confirmed from both SEM and fluorescent imaging observations and a crystal violet biomass assay. Herein, we suggest that the implementation of a low inclination angle to future SLM printed implants is a facile yet effective mechanism to minimise the colonisation of *S. aureus*, one of the most common pathogens associated with the majority of implant related infections.

6. In the final stage of our research we have manufactured single cylindrical struts with 30, 60, and 90 degrees with 0.2, 0.6, 1.0 mm strut diameter as a proof of concept in lattice implants. Micro-CT results show us that the highest porosity percentage and number of pores has been observed from the 1 mm strut specimen inclined at 90-degrees angle, followed by strut specimen of 1 mm diameter inclined at 30-degrees angle. It has been found that for 90° specimens, the stress concentration factor was the greatest for 0.6 mm diameter, whereas they were very similar for 0.2 mm and 1.0 mm diameters. The surface roughness has been measured for all cylindrical struts around the strut diameter from the micro-CT reconstructed image. It has been found from the roughness study that the roughness has been maximum for the downward facing surface and the thinner struts (0.2mm, 0.6mm) show their minimum at the upward facing surface.
7. Rat primary osteoblast cells were grown over 3 days and 7 days on all single struts to understand the adhesion behaviour of bone cells on individual strut. From in-vitro result it has been found that rat primary osteoblasts (r-POB) was found to be well adhered irrespective of strut build inclination angle and strut diameter ; however, primary osteoblasts appeared to be more filopodia, indicating better spreading on 60 degrees samples with 0.2, 0.6, and 1.0 mm strut diameter as the neighbouring two partially melted particles are located far from each other. This study has given us a huge insight to develop

and design next-generation patient-specific lattice implant choosing the appropriate strut design (inclination angle and diameter) proving better osseo-integration for successful clinical outcome.

8.2. Recommendations for future work

Further studies are required to address some advanced level of experimental design to develop next generation customized orthopaedic implants with improved bio-interface by powder-bed metallic additive manufacturing process. These include:

• As manufactured additively manufactured implants surface exhibits higher surface roughness adhering groove patterned partially melted particles. It is important to know how the surface properties of as-manufactured implant triggers the osteogenic differentiation and mineralization. Therefore, further studies can be carried out running RT-PCR and western blot to see the gene expression of osteogenic marker such as ALP, OPN, OCN and collagen-II. It is also important to observe if there is any upregulation of RANKL gene expression which can trigger the osteoclastogenisis over osteogenesis.

• As additively manufactured implant surface exhibit partially melted particles on its surface. Some of these particles are loosely adhered on implant surface due to weak Van der Wales force which needs to be properly cleaned prior to any clinical trial as loosely adhered particles can cause osteolysis which is one of the reasons for implant failures due to aseptic loosening. Therefore, it is very essential to develop proper cleaning protocol particularly for complex geometric lattice topology prior to clinical trial making sure no loosely adhered particles remain on implant surface.

• Further studies are required to evaluate the performance of additively manufactured titanium with different build inclination angle running *in-vivo*. Therefore, it is important to observe the new bone growth into animal defect model after implanting different inclined additively manufactured titanium implants after certain period of time. In-vivo bone tissue regeneration

evaluation by immunohistochemistry (H & E Staining Analysis, Masson's Trichrome Staining) and 3D Micro-CT reconstructed model can provide us the detailed information about the percentage of new bone formation by implanting different inclined additively manufactured titanium implant into animal defect model.

• Surface modification of additively manufactured titanium implant can improve the osseo-integration and prevent against biofilm formation than as manufactured surface. Therefore, creating nano-surface topography by surface modification on additively manufactured implant surface could be a great approach altering different surface properties to improve the interface between host bone and implant to ensure better osseo-integration and faster bone healing.

References

[1] Z.J. Balogh, M.K. Reumann, R.L. Gruen, P. Mayer-Kuckuk, M.A. Schuetz, I.A. Harris, B.J. Gabbe, M. Bhandari, Advances and future directions for management of trauma patients with musculoskeletal injuries, The Lancet 380(9847) (2012) 1109-1119.
[2] R. Burge, B. Dawson-Hughes, D.H. Solomon, J.B. Wong, A. King, A. Tosteson, Incidence and economic burden of osteoporosis-related fractures in the United States, 2005–2025, Journal of bone and mineral research 22(3) (2007) 465-475.
[3] K. Strømsøe, Fracture fixation problems in osteoporosis, Injury 35(2) (2004) 107-113.
[4] Medical Technology: Key facts and figures 2013.
[5] L. Dyrda, 10 Predictions for the Global Orthopedic Device Market, (2014).
[6] M. Kaur, K. Singh, Review on titanium and titanium based alloys as biomaterials for orthopaedic applications, Materials Science and Engineering: C 102 (2019) 844-862.
[7] S. Kurtz, K. Ong, E. Lau, F. Mowat, M. Halpern, Projections of primary and revision hip and knee arthroplasty in the United States from 2005 to 2030, Jbjs 89(4) (2007) 780-785.
[8] A. Sarker, J. Amirian, Y.K. Min, B.T. Lee, HAp granules encapsulated oxidized alginate–gelatin–biphasic calcium phosphate hydrogel for bone regeneration, International Journal of Biological Macromolecules 81 (2015) 898-911.
[9] J. Parthasarathy, 3D modeling, custom implants and its future perspectives in craniofacial surgery, Annals of maxillofacial surgery 4(1) (2014) 9.
[10] Australia's first 3D printed spine implant, (2015).
[11] D. Shidid, M. Leary, M. Brandt, P. Choong, A method for producing a customised orthopaedic implant, Google Patents, 2017.
[12] M.B. Berger, T.W. Jacobs, B.D. Boyan, Z. Schwartz, Hot isostatic pressure treatment of 3D printed Ti6Al4V alters surface modifications and cellular response, Journal of Biomedical Materials Research Part B: Applied Biomaterials (2019).
[13] A. Bandyopadhyay, I. Mitra, A. Shivaram, N. Dasgupta, S. Bose, Direct comparison of additively manufactured porous titanium and tantalum implants towards in vivo osseointegration, Additive Manufacturing 28 (2019) 259-266.
[14] S. Amin Yavari, Y.C. Chai, A.J. Böttger, R. Wauthle, J. Schrooten, H. Weinans, A.A. Zadpoor, Effects of anodizing parameters and heat treatment on nanotopographical features, bioactivity, and cell culture response of additively manufactured porous titanium, Materials Science and Engineering: C 51 (2015) 132-138.
[15] A. Rifai, N. Tran, P. Reineck, A. Elbourne, E.L.H. Mayes, A. Sarker, C. Dekiwadia, E.P. Ivanova, R.J. Crawford, T. Ohshima, Engineering the Interface: Nanodiamond Coating on 3D-Printed Titanium Promotes Mammalian Cell Growth and Inhibits Staphylococcus aureus Colonization, ACS applied materials & interfaces (2019).
[16] S. Ghosh, S. Abanteriba, S. Wong, R. Brkljača, S. Houshyar, Optimisation of grafted phosphorylcholine-based polymer on additively manufactured titanium substrate for hip arthroplasty, Materials Science and Engineering: C 101 (2019) 696-706.
[17] I.A.J. van Hengel, M. Riool, L.E. Fratila-Apachitei, J. Witte-Bouma, E. Farrell, A.A. Zadpoor, S.A.J. Zaat, I. Apachitei, Selective laser melting porous metallic implants with immobilized silver nanoparticles kill and prevent biofilm formation by methicillin-resistant Staphylococcus aureus, Biomaterials 140 (2017) 1-15.
[18] M.C. Melican, M.C. Zimmerman, M.S. Dhillon, A.R. Ponnambalam, A. Curodeau, J.R. Parsons, Three-dimensional printing and porous metallic surfaces: A new orthopedic application, Journal of Biomedical Materials Research: An Official Journal of The Society for Biomaterials, The Japanese Society for Biomaterials, and The Australian Society for Biomaterials and the Korean Society for Biomaterials 55(2) (2001) 194-202.

[19] B. Lozanovski, M. Leary, P. Tran, D. Shidid, M. Qian, P. Choong, M. Brandt, Computational modelling of strut defects in SLM manufactured lattice structures, Materials & Design 171 (2019) 107671.
[20] M. Leary, M. Mazur, H. Williams, E. Yang, A. Alghamdi, B. Lozanovski, X. Zhang, D. Shidid, L. Farahbod-Sternahl, G. Witt, I. Kelbassa, P. Choong, M. Qian, M. Brandt, Inconel 625 lattice structures manufactured by selective laser melting (SLM): Mechanical properties, deformation and failure modes, Materials & Design 157 (2018) 179-199.
[21] W.E. Frazier, Metal additive manufacturing: a review, Journal of Materials Engineering and Performance 23(6) (2014) 1917-1928.
[22] M. Tomlin, J. Meyer, Topology optimization of an additive layer manufactured (ALM) aerospace part, Proceeding of the 7th Altair CAE technology conference, 2011, pp. 1-9.
[23] I. Gibson, D. Rosen, B. Stucker, Directed energy deposition processes, Additive Manufacturing Technologies, Springer2015, pp. 245-268.
[24] V. Seyda, N. Kaufmann, C. Emmelmann, Investigation of Aging Processes of Ti-6Al-4 V Powder Material in Laser Melting, Physics Procedia 39 (2012) 425-431.
[25] A. Gebhardt, Understanding Additive Manufacturing, in: A. Gebhardt (Ed.), Understanding Additive Manufacturing, Hanser2011, pp. I-IX.
[26] A. Sarker, N. Tran, A. Rifai, J. Elambasseril, M. Brandt, R. Williams, M. Leary, K. Fox, Angle defines attachment: Switching the biological response to titanium interfaces by modifying the inclination angle during selective laser melting, Materials & Design 154 (2018) 326-339.
[27] M.P. Chhaya, P.S.P. Poh, E.R. Balmayor, M. van Griensven, J.-T. Schantz, D.W. Hutmacher, Additive manufacturing in biomedical sciences and the need for definitions and norms, Expert Review of Medical Devices 12(5) (2015) 537-543.
[28] W.M. Mihalko, Chapter 5 - Additive Manufacturing of Arthroplasty Implants, in: M. Dipaola, F.M. Wodajo (Eds.), 3D Printing in Orthopaedic Surgery, Elsevier2019, pp. 49-53.
[29] G. Reinhart, S. Teufelhart, Load-Adapted Design of Generative Manufactured Lattice Structures, Physics Procedia 12 (2011) 385-392.
[30] F. Cucinotta, E. Guglielmino, G. Longo, G. Risitano, D. Santonocito, F. Sfravara, Topology Optimization Additive Manufacturing-Oriented for a Biomedical Application, Springer International Publishing, Cham, 2019, pp. 184-193.
[31] S.T. Becker, H. Bolte, O. Krapf, H. Seitz, T. Douglas, S. Sivananthan, J. Wiltfang, E. Sherry, P.H. Warnke, Endocultivation: 3D printed customized porous scaffolds for heterotopic bone induction, Oral oncology 45(11) (2009) e181-e188.
[32] I. Gibson, D. Rosen, B. Stucker, Additive manufacturing technologies: 3D printing, rapid prototyping, and direct digital manufacturing, Springer2014.
[33] R.M. Mahamood, Laser metal deposition process of metals, alloys, and composite materials, Springer2018.
[34] M. Leary, L. Merli, F. Torti, M. Mazur, M. Brandt, Optimal topology for additive manufacture: A method for enabling additive manufacture of support-free optimal structures, Materials & Design 63 (2014) 678-690.
[35] O. Sigmund, Topology optimization: a tool for the tailoring of structures and materials, Philosophical Transactions of the Royal Society of London. Series A: Mathematical, Physical and Engineering Sciences 358(1765) (2000) 211-227.
[36] T. Zegard, G.H. Paulino, Bridging topology optimization and additive manufacturing, Structural and Multidisciplinary Optimization 53(1) (2016) 175-192.
[37] T.G. Spears, S.A. Gold, In-process sensing in selective laser melting (SLM) additive manufacturing, Integrating Materials and Manufacturing Innovation 5(1) (2016) 2.
[38] O. Rehme, C. Emmelmann, Rapid manufacturing of lattice structures with selective laser melting, Laser-based Micropackaging, International Society for Optics and Photonics, 2006, p. 61070K.

[39] J.-P. Kruth, P. Mercelis, J. Van Vaerenbergh, T. Craeghs, Feedback control of selective laser melting, Proceedings of the 3rd international conference on advanced research in virtual and rapid prototyping, Taylor & Francis Ltd, 2007, pp. 521-527.
[40] M. McMillan, M. Leary, M. Brandt, Computationally efficient finite difference method for metal additive manufacturing: A reduced-order DFAM tool applied to SLM, Materials & Design 132 (2017) 226-243.
[41] T. Craeghs, S. Clijsters, J.-P. Kruth, F. Bechmann, M.-C. Ebert, Detection of process failures in layerwise laser melting with optical process monitoring, Physics Procedia 39 (2012) 753-759.
[42] A. Gusarov, T. Laoui, L. Froyen, V. Titov, Contact thermal conductivity of a powder bed in selective laser sintering, International Journal of Heat and Mass Transfer 46(6) (2003) 1103-1109.
[43] K. Kempen, L. Thijs, E. Yasa, M. Badrossamay, W. Verheecke, J. Kruth, Process optimization and microstructural analysis for selective laser melting of AlSi10Mg, Solid Freeform Fabrication Symposium, 2011, pp. 484-495.
[44] S.L. Sing, J. An, W.Y. Yeong, F.E. Wiria, Laser and electron-beam powder-bed additive manufacturing of metallic implants: A review on processes, materials and designs, Journal of Orthopaedic Research 34(3) (2016) 369-385.
[45] E. Chlebus, B. Kuźnicka, T. Kurzynowski, B. Dybała, Microstructure and mechanical behaviour of Ti—6Al—7Nb alloy produced by selective laser melting, Materials Characterization 62(5) (2011) 488-495.
[46] T. Bormann, R. Schumacher, B. Müller, M. Mertmann, M. de Wild, Tailoring Selective Laser Melting Process Parameters for NiTi Implants, Journal of Materials Engineering and Performance 21(12) (2012) 2519-2524.
[47] M. Speirs, J.V. Humbeeck, J. Schrooten, J. Luyten, J.P. Kruth, The Effect of Pore Geometry on the Mechanical Properties of Selective Laser Melted Ti-13Nb-13Zr Scaffolds, Procedia CIRP 5 (2013) 79-82.
[48] B. Vrancken, L. Thijs, J.P. Kruth, J. Van Humbeeck, Microstructure and mechanical properties of a novel β titanium metallic composite by selective laser melting, Acta Materialia 68 (2014) 150-158.
[49] C.-Y. Lin, T. Wirtz, F. LaMarca, S.J. Hollister, Structural and mechanical evaluations of a topology optimized titanium interbody fusion cage fabricated by selective laser melting process, Journal of Biomedical Materials Research Part A 83A(2) (2007) 272-279.
[50] L.E. Murr, S.A. Quinones, S.M. Gaytan, M.I. Lopez, A. Rodela, E.Y. Martinez, D.H. Hernandez, E. Martinez, F. Medina, R.B. Wicker, Microstructure and mechanical behavior of Ti–6Al–4V produced by rapid-layer manufacturing, for biomedical applications, Journal of the Mechanical Behavior of Biomedical Materials 2(1) (2009) 20-32.
[51] T.B. Kim, S. Yue, Z. Zhang, E. Jones, J.R. Jones, P.D. Lee, Additive manufactured porous titanium structures: Through-process quantification of pore and strut networks, Journal of Materials Processing Technology 214(11) (2014) 2706-2715.
[52] P.H. Warnke, T. Douglas, P. Wollny, E. Sherry, M. Steiner, S. Galonska, S.T. Becker, I.N. Springer, J. Wiltfang, S. Sivananthan, Rapid prototyping: porous titanium alloy scaffolds produced by selective laser melting for bone tissue engineering, Tissue engineering part c: Methods 15(2) (2008) 115-124.
[53] D.K. Pattanayak, A. Fukuda, T. Matsushita, M. Takemoto, S. Fujibayashi, K. Sasaki, N. Nishida, T. Nakamura, T. Kokubo, Bioactive Ti metal analogous to human cancellous bone: fabrication by selective laser melting and chemical treatments, Acta Biomaterialia 7(3) (2011) 1398-1406.
[54] K.V. Wong, A. Hernandez, A review of additive manufacturing, ISRN Mechanical Engineering 2012 (2012).
[55] N. Guo, M.C. Leu, Additive manufacturing: technology, applications and research needs, Frontiers of Mechanical Engineering 8(3) (2013) 215-243.
[56] P.P. Mehta, R.R. Otten, E.B. Cooper Jr, Method and apparatus for repairing metal in an article, Google Patents, 1988.

[57] I.Y. Smurov, A. Yakovlev, Laser-assisted direct manufacturing of functionally graded 3D objects by coaxial powder injection, Laser-Assisted Micro-and Nanotechnologies 2003, International Society for Optics and Photonics, 2004, pp. 27-38.
[58] A. Ramakrishnan, G.P. Dinda, Direct laser metal deposition of Inconel 738, Materials Science and Engineering: A 740-741 (2019) 1-13.
[59] K. Zhang, S. Wang, W. Liu, X. Shang, Characterization of stainless steel parts by laser metal deposition shaping, Materials & Design 55 (2014) 104-119.
[60] A. Yadollahi, N. Shamsaei, S.M. Thompson, D.W. Seely, Effects of process time interval and heat treatment on the mechanical and microstructural properties of direct laser deposited 316L stainless steel, Materials Science and Engineering: A 644 (2015) 171-183.
[61] P. Guo, B. Zou, C. Huang, H. Gao, Study on microstructure, mechanical properties and machinability of efficiently additive manufactured AISI 316L stainless steel by high-power direct laser deposition, Journal of Materials Processing Technology 240 (2017) 12-22.
[62] W.J. Sames, F. List, S. Pannala, R.R. Dehoff, S.S. Babu, The metallurgy and processing science of metal additive manufacturing, International Materials Reviews 61(5) (2016) 315-360.
[63] H. Dobbelstein, E.L. Gurevich, E.P. George, A. Ostendorf, G. Laplanche, Laser metal deposition of compositionally graded TiZrNbTa refractory high-entropy alloys using elemental powder blends, Additive Manufacturing 25 (2019) 252-262.
[64] M.N. Ahsan, C.P. Paul, L.M. Kukreja, A.J. Pinkerton, Porous structures fabrication by continuous and pulsed laser metal deposition for biomedical applications; modelling and experimental investigation, Journal of Materials Processing Technology 211(4) (2011) 602-609.
[65] R. Mines, Additive Manufacturing Processes and Materials for Metallic Microlattice Structures Using Selective Laser Melting, Electron Beam Melting and Binder Jetting, Metallic Microlattice Structures: Manufacture, Materials and Application, Springer International Publishing, Cham, 2019, pp. 17-31.
[66] G. Epasto, G. Palomba, D.D. Andrea, S. Di Bella, R. Mineo, E. Guglielmino, F. Traina, Experimental investigation of rhombic dodecahedron micro-lattice structures manufactured by Electron Beam Melting, Materials Today: Proceedings 7 (2019) 578-585.
[67] L.E. Murr, S.M. Gaytan, D.A. Ramirez, E. Martinez, J. Hernandez, K.N. Amato, P.W. Shindo, F.R. Medina, R.B. Wicker, Metal Fabrication by Additive Manufacturing Using Laser and Electron Beam Melting Technologies, Journal of Materials Science & Technology 28(1) (2012) 1-14.
[68] G.L. Knapp, N. Raghavan, A. Plotkowski, T. DebRoy, Experiments and simulations on solidification microstructure for Inconel 718 in powder bed fusion electron beam additive manufacturing, Additive Manufacturing 25 (2019) 511-521.
[69] S. Li, Q. Xu, Z. Wang, W. Hou, Y. Hao, R. Yang, L. Murr, Influence of cell shape on mechanical properties of Ti–6Al–4V meshes fabricated by electron beam melting method, Acta biomaterialia 10(10) (2014) 4537-4547.
[70] X.Z. Zhang, M. Leary, H.P. Tang, T. Song, M. Qian, Selective electron beam manufactured Ti-6Al-4V lattice structures for orthopedic implant applications: Current status and outstanding challenges, Current Opinion in Solid State and Materials Science 22(3) (2018) 75-99.
[71] A.L. Jardini, M.A. Larosa, C.A. de Carvalho Zavaglia, L.F. Bernardes, C.S. Lambert, P. Kharmandayan, D. Calderoni, R. Maciel Filho, Customised titanium implant fabricated in additive manufacturing for craniomaxillofacial surgery: This paper discusses the design and fabrication of a metallic implant for the reconstruction of a large cranial defect, Virtual and physical prototyping 9(2) (2014) 115-125.
[72] S. Biamino, A. Penna, U. Ackelid, S. Sabbadini, O. Tassa, P. Fino, M. Pavese, P. Gennaro, C. Badini, Electron beam melting of Ti–48Al–2Cr–2Nb alloy: Microstructure and mechanical properties investigation, Intermetallics 19(6) (2011) 776-781.
[73] X. Wang, S. Xu, S. Zhou, W. Xu, M. Leary, P. Choong, M. Qian, M. Brandt, Y.M. Xie, Topological design and additive manufacturing of porous metals for bone scaffolds and orthopaedic implants: A review, Biomaterials 83 (2016) 127-141.

[74] L.E. Murr, S. Gaytan, F. Medina, H. Lopez, E. Martinez, B. Machado, D. Hernandez, L. Martinez, M. Lopez, R. Wicker, Next-generation biomedical implants using additive manufacturing of complex, cellular and functional mesh arrays, Philosophical Transactions of the Royal Society A: Mathematical, Physical and Engineering Sciences 368(1917) (2010) 1999-2032.
[75] J.A. Sanz-Herrera, J.M. García-Aznar, M. Doblaré, On scaffold designing for bone regeneration: A computational multiscale approach, Acta Biomaterialia 5(1) (2009) 219-229.
[76] B.G. Sengers, M. Taylor, C.P. Please, R.O.C. Oreffo, Computational modelling of cell spreading and tissue regeneration in porous scaffolds, Biomaterials 28(10) (2007) 1926-1940.
[77] J.D. Boerckel, Y.M. Kolambkar, H.Y. Stevens, A.S.P. Lin, K.M. Dupont, R.E. Guldberg, Effects of in vivo mechanical loading on large bone defect regeneration, Journal of Orthopaedic Research 30(7) (2012) 1067-1075.
[78] S. Bose, M. Roy, A. Bandyopadhyay, Recent advances in bone tissue engineering scaffolds, Trends in biotechnology 30(10) (2012) 546-554.
[79] J.P. Vacanti, R. Langer, Tissue engineering: the design and fabrication of living replacement devices for surgical reconstruction and transplantation, The Lancet 354 S32-S34.
[80] Q.L. Loh, C. Choong, Three-Dimensional Scaffolds for Tissue Engineering Applications: Role of Porosity and Pore Size, Tissue Engineering. Part B, Reviews 19(6) (2013) 485-502.
[81] J. Rouwkema, N.C. Rivron, C.A. van Blitterswijk, Vascularization in tissue engineering, Trends in Biotechnology 26(8) (2008) 434-441.
[82] J.P. Li, J.R. de Wijn, C.A. Van Blitterswijk, K. de Groot, Porous Ti6Al4V scaffold directly fabricating by rapid prototyping: Preparation and in vitro experiment, Biomaterials 27(8) (2006) 1223-1235.
[83] R. Zhang, P.X. Ma, Poly(alpha-hydroxyl acids)/hydroxyapatite porous composites for bone-tissue engineering. I. Preparation and morphology, J Biomed Mater Res 44(4) (1999) 446-55.
[84] G. Li, L. Wang, W. Pan, F. Yang, W. Jiang, X. Wu, X. Kong, K. Dai, Y. Hao, In vitro and in vivo study of additive manufactured porous Ti6Al4V scaffolds for repairing bone defects, Scientific reports 6 (2016) 34072.
[85] M. Long, H.J. Rack, Titanium alloys in total joint replacement—a materials science perspective, Biomaterials 19(18) (1998) 1621-1639.
[86] X. Liu, P.K. Chu, C. Ding, Surface modification of titanium, titanium alloys, and related materials for biomedical applications, Materials Science and Engineering: R: Reports 47(3–4) (2004) 49-121.
[87] H. Hahn, W. Palich, Preliminary evaluation of porous metal surfaced titanium for orthopedic implants, Journal of Biomedical Materials Research 4(4) (1970) 571-577.
[88] R.A. Lueck, J. Galante, W. Rostoker, R.D. Ray, Development of an open pore metallic implant to permit attachment to bone, Surgical forum 20 (1969) 456-7.
[89] R.P. WELSH, R.M. PILLIAR, I. MACNAB, Surgical Implants, THE ROLE OF SURFACE POROSITY IN FIXATION TO BONE AND ACRYLIC 53(5) (1971) 963-977.
[90] G.S. Leventhal, Titanium, a metal for surgery, J Bone Joint Surg Am 33(2) (1951) 473-474.
[91] Y. Li, C. Yang, H. Zhao, S. Qu, X. Li, Y. Li, New Developments of Ti-Based Alloys for Biomedical Applications, Materials 7(3) (2014) 1709.
[92] W.E. Roberts, R.K. Smith, Y. Zilberman, P.G. Mozsary, R.S. Smith, Osseous adaptation to continuous loading of rigid endosseous implants, American Journal of Orthodontics 86(2) (1984) 95-111.
[93] A. Cheng, D.J. Cohen, A. Kahn, R.M. Clohessy, K. Sahingur, J.B. Newton, S.L. Hyzy, B.D. Boyan, Z. Schwartz, Laser Sintered Porous Ti–6Al–4V Implants Stimulate Vertical Bone Growth, Annals of Biomedical Engineering 45(8) (2017) 2025-2035.
[94] P. Xiu, Z. Jia, J. Lv, C. Yin, Y. Cheng, K. Zhang, C. Song, H. Leng, Y. Zheng, H. Cai, Z. Liu, Tailored Surface Treatment of 3D Printed Porous Ti6Al4V by Microarc Oxidation for Enhanced Osseointegration via Optimized Bone In-Growth Patterns and Interlocked Bone/Implant Interface, ACS Applied Materials & Interfaces 8(28) (2016) 17964-17975.
[95] G.E. Ryan, A.S. Pandit, D.P. Apatsidis, Porous titanium scaffolds fabricated using a rapid prototyping and powder metallurgy technique, Biomaterials 29(27) (2008) 3625-3635.

[96] R. Goodall, Porous metals: Foams and sponges, Advances in Powder Metallurgy: Properties, Processing and Applications (2013) 273.
[97] J. Li, Porous titanium for biomedical applications: development, characterization and biological evaluation, University of Twente2007.
[98] M. Tamaddon, S. Samizadeh, L. Wang, G. Blunn, C. Liu, Intrinsic osteoinductivity of porous titanium scaffold for bone tissue engineering, International journal of biomaterials 2017 (2017).
[99] A. Fukuda, M. Takemoto, T. Saito, S. Fujibayashi, M. Neo, D.K. Pattanayak, T. Matsushita, K. Sasaki, N. Nishida, T. Kokubo, T. Nakamura, Osteoinduction of porous Ti implants with a channel structure fabricated by selective laser melting, Acta Biomaterialia 7(5) (2011) 2327-2336.
[100] X. Tan, Y. Tan, C. Chow, S. Tor, W. Yeong, Metallic powder-bed based 3D printing of cellular scaffolds for orthopaedic implants: A state-of-the-art review on manufacturing, topological design, mechanical properties and biocompatibility, Materials Science and Engineering: C 76 (2017) 1328-1343.
[101] S. Van Bael, Y.C. Chai, S. Truscello, M. Moesen, G. Kerckhofs, H. Van Oosterwyck, J.-P. Kruth, J. Schrooten, The effect of pore geometry on the in vitro biological behavior of human periosteum-derived cells seeded on selective laser-melted Ti6Al4V bone scaffolds, Acta biomaterialia 8(7) (2012) 2824-2834.
[102] Y.C. Chai, G. Kerckhofs, S.J. Roberts, S. Van Bael, E. Schepers, J. Vleugels, F.P. Luyten, J. Schrooten, Ectopic bone formation by 3D porous calcium phosphate-Ti6Al4V hybrids produced by perfusion electrodeposition, Biomaterials 33(16) (2012) 4044-4058.
[103] A. Bandyopadhyay, F. Espana, V.K. Balla, S. Bose, Y. Ohgami, N.M. Davies, Influence of porosity on mechanical properties and in vivo response of Ti6Al4V implants, Acta biomaterialia 6(4) (2010) 1640-1648.
[104] THE

4WEB

DIFFERENCE.
[105] K2M Enhances 3D-Printed Spine Portfolio Following FDA Clearance of Two CASCADIA™ Interbody Systems Featuring Lamellar 3D Titanium Technology, (2016, June 01).
[106] S.N. Williams, M.L. Wolford, A. Bercovitz, Hospitalization for Total Knee Replacement Among Inpatients Aged 45 and Over: United States, 2000-2010, NCHS data brief (210) (2015) 1-8.
[107] A. Chug, S. Shukla, L. Mahesh, S. Jadwani, Osseointegration—Molecular events at the bone–implant interface: A review, Journal of Oral and Maxillofacial Surgery, Medicine, and Pathology 25(1) (2013) 1-4.
[108] G.A. Rodan, T.J. Martin, Role of osteoblasts in hormonal control of bone resorption—a hypothesis, Calcified Tissue International 33(1) (1981) 349-351.
[109] D. Lacey, E. Timms, H.-L. Tan, M. Kelley, C. Dunstan, T. Burgess, R. Elliott, A. Colombero, G. Elliott, S. Scully, Osteoprotegerin ligand is a cytokine that regulates osteoclast differentiation and activation, cell 93(2) (1998) 165-176.
[110] N. Sykaras, A.M. Iacopino, V.A. Marker, R.G. Triplett, R.D. Woody, Implant materials, designs, and surface topographies: their effect on osseointegration. A literature review, International Journal of Oral & Maxillofacial Implants 15(5) (2000).
[111] L. Le Guéhennec, A. Soueidan, P. Layrolle, Y. Amouriq, Surface treatments of titanium dental implants for rapid osseointegration, Dental Materials 23(7) (2007) 844-854.
[112] J. Raphel, M. Holodniy, S.B. Goodman, S.C. Heilshorn, Multifunctional coatings to simultaneously promote osseointegration and prevent infection of orthopaedic implants, Biomaterials 84 (2016) 301-314.
[113] A.B. Novaes Jr, S.L.S.d. Souza, R.R.M.d. Barros, K.K.Y. Pereira, G. Iezzi, A. Piattelli, Influence of implant surfaces on osseointegration, Brazilian dental journal 21(6) (2010) 471-481.
[114] A. Barfeie, J. Wilson, J. Rees, Implant surface characteristics and their effect on osseointegration, British dental journal 218(5) (2015) E9.

[115] L. Tang, P. Thevenot, W. Hu, Surface chemistry influences implant biocompatibility, Current topics in medicinal chemistry 8(4) (2008) 270-280.
[116] H. Rafi, N. Karthik, H. Gong, T.L. Starr, B.E. Stucker, Microstructures and mechanical properties of Ti6Al4V parts fabricated by selective laser melting and electron beam melting, Journal of materials engineering and performance 22(12) (2013) 3872-3883.
[117] A. Wennerberg, T. Albrektsson, Effects of titanium surface topography on bone integration: a systematic review, Clinical Oral Implants Research 20 (2009) 172-184.
[118] H.J. Kim, S.H. Kim, M.S. Kim, E.J. Lee, H.G. Oh, W.M. Oh, S.W. Park, W.J. Kim, G.J. Lee, N.G. Choi, J.T. Koh, D.B. Dinh, R.R. Hardin, K. Johnson, V.L. Sylvia, J.P. Schmitz, D.D. Dean, Varying Ti-6Al-4V surface roughness induces different early morphologic and molecular responses in MG63 osteoblast-like cells, Journal of Biomedical Materials Research Part A 74A(3) (2005) 366-373.
[119] A. Shaoki, J.-y. Xu, H. Sun, X.-s. Chen, J. Ouyang, X.-m. Zhuang, F.-l. Deng, Osseointegration of three-dimensional designed titanium implants manufactured by selective laser melting, Biofabrication 8(4) (2016) 045014.
[120] R.A. Gittens, R. Olivares-Navarrete, A. Cheng, D.M. Anderson, T. McLachlan, I. Stephan, J. Geis-Gerstorfer, K.H. Sandhage, A.G. Fedorov, F. Rupp, B.D. Boyan, R. Tannenbaum, Z. Schwartz, The Roles of Titanium Surface Micro/Nanotopography and Wettability on the Differential Response of Human Osteoblast Lineage Cells, Acta biomaterialia 9(4) (2013) 6268-6277.
[121] M. Stolzoff, J.E. Burns, A. Aslani, E.J. Tobin, C. Nguyen, N. De La Torre, N.H. Golshan, K.S. Ziemer, T.J. Webster, Decreased bacterial growth on titanium nanoscale topographies created by ion beam assisted evaporation, International Journal of Nanomedicine 12 (2017) 1161-1169.
[122] F. Zhang, Z. Zhang, X. Zhu, E.-T. Kang, K.-G. Neoh, Silk-functionalized titanium surfaces for enhancing osteoblast functions and reducing bacterial adhesion, Biomaterials 29(36) (2008) 4751-4759.
[123] N. Tran, P.A. Tran, Nanomaterial-based treatments for medical device-associated infections, ChemPhysChem 13(10) (2012) 2481-2494.
[124] N. Masurier, J.-B. Tissot, D. Boukhriss, S. Jebors, C. Pinese, P. Verdié, M. Amblard, A. Mehdi, J. Martinez, V. Humblot, Site-specific grafting on titanium surfaces with hybrid temporin antibacterial peptides, Journal of Materials Chemistry B 6(12) (2018) 1782-1790.
[125] A. Rifai, N. Tran, D.W. Lau, A. Elbourne, H. Zhan, A.D. Stacey, E.L.H. Mayes, A. Sarker, E.P. Ivanova, R.J. Crawford, P.A. Tran, B.C. Gibson, A.D. Greentree, E. Pirogova, K. Fox, Polycrystalline Diamond Coating of Additively Manufactured Titanium for Biomedical Applications, ACS Applied Materials & Interfaces 10(10) (2018) 8474-8484.
[126] L. Zhao, P.K. Chu, Y. Zhang, Z. Wu, Antibacterial coatings on titanium implants, Journal of Biomedical Materials Research Part B: Applied Biomaterials 91(1) (2009) 470-480.
[127] B.e. Nie, H. Ao, T. Long, J. Zhou, T. Tang, B. Yue, Immobilizing bacitracin on titanium for prophylaxis of infections and for improving osteoinductivity: An in vivo study, Colloids and Surfaces B: Biointerfaces 150 (2017) 183-191.
[128] M. Gabriel, K. Nazmi, E.C. Veerman, A.V. Nieuw Amerongen, A. Zentner, Preparation of LL-37-Grafted Titanium Surfaces with Bactericidal Activity, Bioconjugate Chemistry 17(2) (2006) 548-550.
[129] N. Tran, M.N. Kelley, P.A. Tran, D.R. Garcia, J.D. Jarrell, R.A. Hayda, C.T. Born, Silver doped titanium oxide–PDMS hybrid coating inhibits Staphylococcus aureus and Staphylococcus epidermidis growth on PEEK, Materials Science and Engineering: C 49 (2015) 201-209.
[130] P. AshaRani, G. Low Kah Mun, M.P. Hande, S. Valiyaveettil, Cytotoxicity and genotoxicity of silver nanoparticles in human cells, ACS nano 3(2) (2008) 279-290.
[131] W.H. De Jong, L.T. Van Der Ven, A. Sleijffers, M.V. Park, E.H. Jansen, H. Van Loveren, R.J. Vandebriel, Systemic and immunotoxicity of silver nanoparticles in an intravenous 28 days repeated dose toxicity study in rats, Biomaterials 34(33) (2013) 8333-8343.
[132] J. Hasan, S. Jain, R. Padmarajan, S. Purighalla, V.K. Sambandamurthy, K. Chatterjee, Multi-scale surface topography to minimize adherence and viability of nosocomial drug-resistant bacteria, Materials & Design 140 (2018) 332-344.

[133] A. Gao, R. Hang, X. Huang, L. Zhao, X. Zhang, L. Wang, B. Tang, S. Ma, P.K. Chu, The effects of titania nanotubes with embedded silver oxide nanoparticles on bacteria and osteoblasts, Biomaterials 35(13) (2014) 4223-4235.
[134] E.T. Rochford, G. Subbiahdoss, T.F. Moriarty, A.H. Poulsson, H.C. van der Mei, H.J. Busscher, R.G. Richards, An in vitro investigation of bacteria-osteoblast competition on oxygen plasma-modified PEEK, Journal of Biomedical Materials Research Part A 102(12) (2014) 4427-4434.
[135] V.K. Truong, R. Lapovok, Y.S. Estrin, S. Rundell, J.Y. Wang, C.J. Fluke, R.J. Crawford, E.P. Ivanova, The influence of nano-scale surface roughness on bacterial adhesion to ultrafine-grained titanium, Biomaterials 31(13) (2010) 3674-3683.
[136] J. Hasan, R.J. Crawford, E.P. Ivanova, Antibacterial surfaces: the quest for a new generation of biomaterials, Trends in Biotechnology 31(5) (2013) 295-304.
[137] K. Glinel, P. Thebault, V. Humblot, C.M. Pradier, T. Jouenne, Antibacterial surfaces developed from bio-inspired approaches, Acta Biomaterialia 8(5) (2012) 1670-1684.
[138] J. Hasan, K. Chatterjee, Recent advances in engineering topography mediated antibacterial surfaces, Nanoscale 7(38) (2015) 15568-15575.
[139] Z. Yao, D. Wu, J.Y.Y. Heng, W. Wu, H. Zhao, J. Liu, J. Tang, Solids surface characterization using computational algorithms: A case study for talc fillers, Applied Clay Science 141 (2017) 212-218.
[140] Z. Yao, D. Wu, J.Y.Y. Heng, H. Zhao, W. Wu, J. Tang, Surface characterization of bio-fillers from typical mollusk shell using computational algorithms, International Journal of Adhesion and Adhesives 84 (2018) 48-53.
[141] G.A. O'Toole, Microtiter dish biofilm formation assay, Journal of visualized experiments: JoVE (47) (2011).
[142] A. Hussein, L. Hao, C. Yan, R. Everson, Finite element simulation of the temperature and stress fields in single layers built without-support in selective laser melting, Materials & Design (1980-2015) 52 (2013) 638-647.
[143] M. Mazur, M. Leary, M. McMillan, S. Sun, D. Shidid, M. Brandt, Mechanical properties of Ti6Al4V and AlSi12Mg lattice structures manufactured by selective laser melting (SLM), Laser Additive Manufacturing: Materials, Design, Technologies, and Applications (2016) 119.
[144] C. Yan, L. Hao, A. Hussein, D. Raymont, Evaluations of cellular lattice structures manufactured using selective laser melting, International Journal of Machine Tools and Manufacture 62 (2012) 32-38.
[145] T. Kurzynowski, E. Chlebus, B. Kuźnicka, J. Reiner, Parameters in selective laser melting for processing metallic powders, 2012, pp. 823914-823914-6.
[146] I. Yadroitsev, P. Bertrand, I. Smurov, Parametric analysis of the selective laser melting process, Applied Surface Science 253(19) (2007) 8064-8069.
[147] M. Van Elsen, Complexity of Selective Laser Melting: a new optimisation approach, Citeseer, 2007.
[148] A. Barfeie, J. Wilson, J. Rees, Implant surface characteristics and their effect on osseointegration, Br Dent J 218(5) (2015) E9-E9.
[149] T. Ma, X. Ge, Y. Zhang, Y. Lin, Effect of Titanium Surface Modifications of Dental Implants on Rapid Osseointegration, in: K. Sasaki, O. Suzuki, N. Takahashi (Eds.), Interface Oral Health Science 2016: Innovative Research on Biosis–Abiosis Intelligent Interface, Springer Singapore, Singapore, 2017, pp. 247-256.
[150] P. Thevenot, W. Hu, L. Tang, SURFACE CHEMISTRY INFLUENCE IMPLANT BIOCOMPATIBILITY, Current topics in medicinal chemistry 8(4) (2008) 270-280.
[151] A.B. Novaes Jr, S.L.S.d. Souza, R.R.M.d. Barros, K.K.Y. Pereira, G. Iezzi, A. Piattelli, Influence of implant surfaces on osseointegration, Brazilian Dental Journal 21 (2010) 471-481.
[152] A. Jemat, M.J. Ghazali, M. Razali, Y. Otsuka, Surface Modifications and Their Effects on Titanium Dental Implants, BioMed Research International 2015 (2015) 11.

[153] A. Sarker, N. Tran, A. Rifai, M. Brandt, P.A. Tran, M. Leary, K. Fox, R. Williams, Rational Design of Additively Manufactured Ti6Al4V Implants to Control Staphylococcus aureus Biofilm Formation, Materialia (2019) 100250.
[154] M. Mazur, M. Leary, S. Sun, M. Vcelka, D. Shidid, M. Brandt, Deformation and failure behaviour of Ti-6Al-4V lattice structures manufactured by selective laser melting (SLM), The International Journal of Advanced Manufacturing Technology 84(5-8) (2016) 1391-1411.
[155] M. Leary, M. Mazur, J. Elambasseril, M. McMillan, T. Chirent, Y. Sun, M. Qian, M. Easton, M. Brandt, Selective laser melting (SLM) of AlSi12Mg lattice structures, Materials & Design 98 (2016) 344-357.
[156] G. Strano, L. Hao, R.M. Everson, K.E. Evans, Surface roughness analysis, modelling and prediction in selective laser melting, Journal of Materials Processing Technology 213(4) (2013) 589-597.
[157] J. Lincks, B.D. Boyan, C.R. Blanchard, C.H. Lohmann, Y. Liu, D.L. Cochran, D.D. Dean, Z. Schwartz, Response of MG63 osteoblast-like cells to titanium and titanium alloy is dependent on surface roughness and composition, Biomaterials 19(23) (1998) 2219-2232.
[158] K. Suzuki, K. Aoki, K. Ohya, Effects of surface roughness of titanium implants on bone remodeling activity of femur in rabbits, Bone 21(6) (1997) 507-514.
[159] M.M. Shalabi, A. Gortemaker, M.A.V.t. Hof, J.A. Jansen, N.H.J. Creugers, Implant Surface Roughness and Bone Healing: a Systematic Review, Journal of Dental Research 85(6) (2006) 496-500.
[160] E.S. Gadelmawla, M.M. Koura, T.M.A. Maksoud, I.M. Elewa, H.H. Soliman, Roughness parameters, Journal of Materials Processing Technology 123(1) (2002) 133-145.
[161] J. Dobes, J.E.S. Leal, J. Profeta, M.M. de Sousa, F.P.L. Neto, A. Piratelli-Filho, R.V. Arencibia, Effect of mechanical vibration on Ra, Rq, Rz, and Rt roughness parameters, The International Journal of Advanced Manufacturing Technology 92(1) (2017) 393-406.
[162] T.P. Kunzler, T. Drobek, M. Schuler, N.D. Spencer, Systematic study of osteoblast and fibroblast response to roughness by means of surface-morphology gradients, Biomaterials 28(13) (2007) 2175-2182.
[163] O. Zinger, K. Anselme, A. Denzer, P. Habersetzer, M. Wieland, J. Jeanfils, P. Hardouin, D. Landolt, Time-dependent morphology and adhesion of osteoblastic cells on titanium model surfaces featuring scale-resolved topography, Biomaterials 25(14) (2004) 2695-2711.
[164] L. Le Guehennec, M.-A. Lopez-Heredia, B. Enkel, P. Weiss, Y. Amouriq, P. Layrolle, Osteoblastic cell behaviour on different titanium implant surfaces, Acta Biomaterialia 4(3) (2008) 535-543.
[165] Y. Germanier, S. Tosatti, N. Broggini, M. Textor, D. Buser, Enhanced bone apposition around biofunctionalized sandblasted and acid-etched titanium implant surfaces, Clinical Oral Implants Research 17(3) (2006) 251-257.
[166] G. Zhao, A.L. Raines, M. Wieland, Z. Schwartz, B.D. Boyan, Requirement for both micron- and submicron scale structure for synergistic responses of osteoblasts to substrate surface energy and topography, Biomaterials 28(18) (2007) 2821-2829.
[167] P.T. de Oliveira, S.F. Zalzal, M.M. Beloti, A.L. Rosa, A. Nanci, Enhancement of in vitro osteogenesis on titanium by chemically produced nanotopography, Journal of Biomedical Materials Research Part A 80A(3) (2007) 554-564.
[168] S. Van Bael, Y.C. Chai, S. Truscello, M. Moesen, G. Kerckhofs, H. Van Oosterwyck, J.P. Kruth, J. Schrooten, The effect of pore geometry on the in vitro biological behavior of human periosteum-derived cells seeded on selective laser-melted Ti6Al4V bone scaffolds, Acta Biomaterialia 8(7) (2012) 2824-2834.
[169] G. Pyka, G. Kerckhofs, I. Papantoniou, M. Speirs, J. Schrooten, M. Wevers, Surface Roughness and Morphology Customization of Additive Manufactured Open Porous Ti6Al4V Structures, Materials 6(10) (2013) 4737.
[170] G. Pyka, A. Burakowski, G. Kerckhofs, M. Moesen, S. Van Bael, J. Schrooten, M. Wevers, Surface Modification of Ti6Al4V Open Porous Structures Produced by Additive Manufacturing, Advanced Engineering Materials 14(6) (2012) 363-370.

[171] L. Mullen, R.C. Stamp, P. Fox, E. Jones, C. Ngo, C.J. Sutcliffe, Selective laser melting: A unit cell approach for the manufacture of porous, titanium, bone in-growth constructs, suitable for orthopedic applications. II. Randomized structures, Journal of Biomedical Materials Research Part B: Applied Biomaterials 92B(1) (2010) 178-188.
[172] S. Van Bael, G. Kerckhofs, M. Moesen, G. Pyka, J. Schrooten, J.-P. Kruth, Micro-CT-based improvement of geometrical and mechanical controllability of selective laser melted Ti6Al4V porous structures, Materials Science and Engineering: A 528(24) (2011) 7423-7431.
[173] C. Yan, L. Hao, A. Hussein, P. Young, D. Raymont, Advanced lightweight 316L stainless steel cellular lattice structures fabricated via selective laser melting, Materials & Design 55 (2014) 533-541.
[174] K. Mumtaz, N. Hopkinson, Selective laser melting of Inconel 625 using pulse shaping, Rapid Prototyping Journal 16(4) (2010) 248-257.
[175] M. Rombouts, J.-P. Kruth, L. Froyen, P. Mercelis, Fundamentals of selective laser melting of alloyed steel powders, CIRP Annals-Manufacturing Technology 55(1) (2006) 187-192.
[176] J. Fuh, Y. Choo, A. Nee, L. Lu, K. Lee, Improvement of the UV curing process for the laser lithography technique, Materials & Design 16(1) (1995) 23-32.
[177] R. Morgan, C. Sutcliffe, W. O'neill, Density analysis of direct metal laser re-melted 316L stainless steel cubic primitives, Journal of materials science 39(4) (2004) 1195-1205.
[178] J.-P. Kruth, L. Froyen, J. Van Vaerenbergh, P. Mercelis, M. Rombouts, B. Lauwers, Selective laser melting of iron-based powder, Journal of materials processing technology 149(1-3) (2004) 616-622.
[179] R.A. Gittens, L. Scheideler, F. Rupp, S.L. Hyzy, J. Geis-Gerstorfer, Z. Schwartz, B.D. Boyan, A Review on the Wettability of Dental Implant Surfaces II: Biological and Clinical Aspects, Acta biomaterialia 10(7) (2014) 2907-2918.
[180] Z. Deng, B. Yin, W. Li, J. Liu, J. Yang, T. Zheng, D. Zhang, H. Yu, X. Liu, J. Ma, Surface characteristics of and in vitro behavior of osteoblast-like cells on titanium with nanotopography prepared by high-energy shot peening, International Journal of Nanomedicine 9 (2014) 5565-5573.
[181] K. Liu, L. Jiang, Metallic surfaces with special wettability, Nanoscale 3(3) (2011) 825-838.
[182] M. Moravej, D. Mantovani, Biodegradable Metals for Cardiovascular Stent Application: Interests and New Opportunities, International Journal of Molecular Sciences 12(7) (2011) 4250.
[183] F. Witte, Reprint of: The history of biodegradable magnesium implants: A review, Acta biomaterialia 23 (2015) S28-S40.
[184] H. Hermawan, D. Dubé, D. Mantovani, Developments in metallic biodegradable stents, Acta Biomaterialia 6(5) (2010) 1693-1697.
[185] M. Schinhammer, A.C. Hänzi, J.F. Löffler, P.J. Uggowitzer, Design strategy for biodegradable Fe-based alloys for medical applications, Acta biomaterialia 6(5) (2010) 1705-1713.
[186] R. Bothe, L. Beaton, H. Davenport, Reaction of bone to multiple metallic implants, Surg Gynecol Obstet 71(6) (1940) 598-602.
[187] B. Zhao, H. Wang, N. Qiao, C. Wang, M. Hu, Corrosion resistance characteristics of a Ti-6Al-4V alloy scaffold that is fabricated by electron beam melting and selective laser melting for implantation in vivo, Materials Science and Engineering: C 70 (2017) 832-841.
[188] E. Eisenbarth, D. Velten, M. Müller, R. Thull, J. Breme, Biocompatibility of β-stabilizing elements of titanium alloys, Biomaterials 25(26) (2004) 5705-5713.
[189] F. Abe, E.C. Santos, Y. Kitamura, K. Osakada, M. Shiomi, Influence of forming conditions on the titanium model in rapid prototyping with the selective laser melting process, Proceedings of the Institution of Mechanical Engineers, Part C: Journal of Mechanical Engineering Science 217(1) (2003) 119-126.
[190] G.D. Revankar, R. Shetty, S.S. Rao, V.N. Gaitonde, Wear resistance enhancement of titanium alloy (Ti–6Al–4V) by ball burnishing process, Journal of Materials Research and Technology 6(1) (2017) 13-32.
[191] G.N. Levy, R. Schindel, J.-P. Kruth, Rapid manufacturing and rapid tooling with layer manufacturing (LM) technologies, state of the art and future perspectives, CIRP Annals-Manufacturing Technology 52(2) (2003) 589-609.

[192] W.-Y. Yeong, C.-K. Chua, K.-F. Leong, M. Chandrasekaran, Rapid prototyping in tissue engineering: challenges and potential, Trends in Biotechnology 22(12) (2004) 643-652.
[193] A.L. Jardini, M.A. Larosa, C.A. de Carvalho Zavaglia, L.F. Bernardes, C.S. Lambert, P. Kharmandayan, D. Calderoni, R. Maciel Filho, Customised titanium implant fabricated in additive manufacturing for craniomaxillofacial surgery, Virtual and Physical Prototyping 9(2) (2014) 115-125.
[194] C. Mertens, H. Löwenheim, J. Hoffmann, Image data based reconstruction of the midface using a patient-specific implant in combination with a vascularized osteomyocutaneous scapular flap, Journal of Cranio-Maxillofacial Surgery 41(3) (2013) 219-225.
[195] F.P.W. Melchels, M.A.N. Domingos, T.J. Klein, J. Malda, P.J. Bartolo, D.W. Hutmacher, Additive manufacturing of tissues and organs, Progress in Polymer Science 37(8) (2012) 1079-1104.
[196] D. Tang, R.S. Tare, L.-Y. Yang, D.F. Williams, K.-L. Ou, R.O.C. Oreffo, Biofabrication of bone tissue: approaches, challenges and translation for bone regeneration, Biomaterials 83(Supplement C) (2016) 363-382.
[197] I.A.J. van Hengel, M. Riool, L.E. Fratila-Apachitei, J. Witte-Bouma, E. Farrell, A.A. Zadpoor, S.A.J. Zaat, I. Apachitei, Selective laser melting porous metallic implants with immobilized silver nanoparticles kill and prevent biofilm formation by methicillin-resistant Staphylococcus aureus, Biomaterials 140(Supplement C) (2017) 1-15.
[198] A.K. Capulli, M.Y. Emmert, F.S. Pasqualini, D. Kehl, E. Caliskan, J.U. Lind, S.P. Sheehy, S.J. Park, S. Ahn, B. Weber, J.A. Goss, S.P. Hoerstrup, K.K. Parker, JetValve: Rapid manufacturing of biohybrid scaffolds for biomimetic heart valve replacement, Biomaterials 133(Supplement C) (2017) 229-241.
[199] N.W. Hrabe, P. Heinl, R.K. Bordia, C. Körner, R.J. Fernandes, Maintenance of a bone collagen phenotype by osteoblast-like cells in 3D periodic porous titanium (Ti-6Al-4 V) structures fabricated by selective electron beam melting, Connective tissue research 54(6) (2013) 10.3109/03008207.2013.822864.
[200] A. Jonitz-Heincke, J. Wieding, C. Schulze, D. Hansmann, R. Bader, Comparative Analysis of the Oxygen Supply and Viability of Human Osteoblasts in Three-Dimensional Titanium Scaffolds Produced by Laser-Beam or Electron-Beam Melting, Materials 6(11) (2013) 5398.
[201] S.C. Cox, P. Jamshidi, N.M. Eisenstein, M.A. Webber, H. Burton, R.J.A. Moakes, O. Addison, M. Attallah, D.E.T. Shepherd, L.M. Grover, Surface Finish has a Critical Influence on Biofilm Formation and Mammalian Cell Attachment to Additively Manufactured Prosthetics, ACS Biomaterials Science & Engineering 3(8) (2017) 1616-1626.
[202] Y.P. Kathuria, Microstructuring by selective laser sintering of metallic powder, Surface and Coatings Technology 116–119 (1999) 643-647.
[203] A. Simchi, H. Pohl, Effects of laser sintering processing parameters on the microstructure and densification of iron powder, Materials Science and Engineering: A 359(1–2) (2003) 119-128.
[204] H.K. Rafi, N.V. Karthik, H. Gong, T.L. Starr, B.E. Stucker, Microstructures and Mechanical Properties of Ti6Al4V Parts Fabricated by Selective Laser Melting and Electron Beam Melting, Journal of Materials Engineering and Performance 22(12) (2013) 3872-3883.
[205] L. Thijs, F. Verhaeghe, T. Craeghs, J.V. Humbeeck, J.-P. Kruth, A study of the microstructural evolution during selective laser melting of Ti–6Al–4V, Acta Materialia 58(9) (2010) 3303-3312.
[206] M. Agarwala, D. Bourell, J. Beaman, H. Marcus, J. Barlow, Direct selective laser sintering of metals, Rapid Prototyping Journal 1(1) (1995) 26-36.
[207] M. Niemczewska-Wójcik, W. Piekoszewski, The surface texture and its influence on the tribological characteristics of a friction pair: metal–polymer, Archives of Civil and Mechanical Engineering 17(2) (2017) 344-353.
[208] A. Townsend, N. Senin, L. Blunt, R.K. Leach, J.S. Taylor, Surface texture metrology for metal additive manufacturing: a review, Precision Engineering 46 (2016) 34-47.
[209] G.P. Petropoulos, C.N. Pandazaras, J.P. Davim, Surface Texture Characterization and Evaluation Related to Machining, in: J.P. Davim (Ed.), Surface Integrity in Machining, Springer London, London, 2010, pp. 37-66.

[210] B.R. Strohmeier, An ESCA method for determining the oxide thickness on aluminum alloys, Surface and Interface Analysis 15(1) (1990) 51-56.
[211] M.P. Chávez-Díaz, M.L. Escudero-Rincón, E.M. Arce-Estrada, R. Cabrera-Sierra, Osteoblast Cell Response on the Ti6Al4V Alloy Heat-Treated, Materials 10(4) (2017) 445.
[212] B. Ekwall, V. Silano, A. Paganuzzi-Stammati, F. Zucco, Toxicity tests with mammalian cell cultures, Short-term toxicity tests for non-genotoxic effects 41 (1990) 75-82.
[213] D.A. Hollander, M. von Walter, T. Wirtz, R. Sellei, B. Schmidt-Rohlfing, O. Paar, H.-J. Erli, Structural, mechanical and in vitro characterization of individually structured Ti–6Al–4V produced by direct laser forming, Biomaterials 27(7) (2006) 955-963.
[214] J. Shim, H. Nakamura, T. Ogawa, V. Gupta, An Understanding of the Mechanism That Promotes Adhesion Between Roughened Titanium Implants and Mineralized Tissue, Journal of Biomechanical Engineering 131(5) (2009) 054503-054503-9.
[215] C.M. Haslauer, J.C. Springer, O.L.A. Harrysson, E.G. Loboa, N.A. Monteiro-Riviere, D.J. Marcellin-Little, In vitro biocompatibility of titanium alloy discs made using direct metal fabrication, Medical Engineering & Physics 32(6) (2010) 645-652.
[216] Y.-F. Chou, W. Huang, J.C.Y. Dunn, T.A. Miller, B.M. Wu, The effect of biomimetic apatite structure on osteoblast viability, proliferation, and gene expression, Biomaterials 26(3) (2005) 285-295.
[217] M.G. Diniz, G.A. Soares, M.J. Coelho, M.H. Fernandes, Surface topography modulates the osteogenesis in human bone marrow cell cultures grown on titanium samples prepared by a combination of mechanical and acid treatments, Journal of Materials Science: Materials in Medicine 13(4) (2002) 421-432.
[218] R. Singhvi, G. Stephanopoulos, D.I. Wang, Effects of substratum morphology on cell physiology, Biotechnology and Bioengineering 43(8) (1994) 764-771.
[219] Y. Wan, Y. Wang, Z. Liu, X. Qu, B. Han, J. Bei, S. Wang, Adhesion and proliferation of OCT-1 osteoblast-like cells on micro- and nano-scale topography structured poly(l-lactide), Biomaterials 26(21) (2005) 4453-4459.
[220] N. Gui, W. Xu, D.E. Myers, R. Shukla, H.P. Tang, M. Qian, The effect of ordered and partially ordered surface topography on bone cell responses: a review, Biomaterials Science 6(2) (2018) 250-264.
[221] K.S. Brammer, S. Oh, C.J. Cobb, L.M. Bjursten, H.v.d. Heyde, S. Jin, Improved bone-forming functionality on diameter-controlled TiO2 nanotube surface, Acta Biomaterialia 5(8) (2009) 3215-3223.
[222] T. Douglas, P. Warnke, B. Temel, P. Wollny, S. Becker, I. Springer, J. Wiltfang, S. Sivananthan, Rapid Prototyping: Porous Titanium Alloy Scaffolds Produced by Selective Laser Melting (SLM) for Bone Tissue Engineering, TISSUE ENGINEERING PART A, MARY ANN LIEBERT INC 140 HUGUENOT STREET, 3RD FL, NEW ROCHELLE, NY 10801 USA, 2009, pp. O7-O8.
[223] C.C. Ribeiro, C.C. Barrias, M.A. Barbosa, Preparation and characterisation of calcium-phosphate porous microspheres with a uniform size for biomedical applications, Journal of Materials Science: Materials in Medicine 17(5) (2006) 455-463.
[224] A.T. Sidambe, Biocompatibility of Advanced Manufactured Titanium Implants—A Review, Materials 7(12) (2014) 8168-8188.
[225] E. Alabort, D. Barba, A. De Diego, M.V. Aguirre-Cebrian, R.C. Reed, A Novel Titanium Alloy for Additively Manufactured Orthopaedic Implants, TMS 2020 149th Annual Meeting & Exhibition Supplemental Proceedings, Springer, 2020, pp. 267-276.
[226] A. Jonitz-Heincke, J. Wieding, C. Schulze, D. Hansmann, R. Bader, Comparative analysis of the oxygen supply and viability of human osteoblasts in three-dimensional titanium scaffolds produced by laser-beam or electron-beam melting, Materials 6(11) (2013) 5398-5409.
[227] N.W. Hrabe, P. Heinl, R.K. Bordia, C. Körner, R.J. Fernandes, Maintenance of a bone collagen phenotype by osteoblast-like cells in 3D periodic porous titanium (Ti-6Al-4 V) structures fabricated by selective electron beam melting, Connective tissue research 54(6) (2013) 351-360.

[228] K.G. Neoh, X. Hu, D. Zheng, E.T. Kang, Balancing osteoblast functions and bacterial adhesion on functionalized titanium surfaces, Biomaterials 33(10) (2012) 2813-2822.
[229] A. Sarker, N. Tran, A. Rifai, J. Elambasseril, M. Brandt, R. Williams, M. Leary, K. Fox, Angle defines attachment: Switching the biological response to titanium interfaces by modifying the inclination angle during selective laser melting, Materials & Design (2018).
[230] A. Al-Ahmad, M. Wiedmann-Al-Ahmad, A. Fackler, M. Follo, E. Hellwig, M. Bächle, C. Hannig, J.S. Han, M. Wolkewitz, R. Kohal, In vivo study of the initial bacterial adhesion on different implant materials, Archives of Oral Biology 58(9) (2013) 1139-1147.
[231] A. Cassie, S. Baxter, Wettability of porous surfaces, Transactions of the Faraday society 40 (1944) 546-551.
[232] P.A. Tran, T.J. Webster, Understanding the wetting properties of nanostructured selenium coatings: the role of nanostructured surface roughness and air-pocket formation, International journal of nanomedicine 8 (2013) 2001.
[233] A.W. Neumann, R.J. Good, C.J. Hope, M. Sejpal, An equation-of-state approach to determine surface tensions of low-energy solids from contact angles, Journal of Colloid and Interface Science 49(2) (1974) 291-304.
[234] M. Yoshinari, Y. Oda, T. Kato, K. Okuda, Influence of surface modifications to titanium on antibacterial activity in vitro, Biomaterials 22(14) (2001) 2043-2048.
[235] J. Yang, H. Yu, J. Yin, M. Gao, Z. Wang, X. Zeng, Formation and control of martensite in Ti-6Al-4V alloy produced by selective laser melting, Materials & Design 108 (2016) 308-318.
[236] M.C. Biesinger, L.W.M. Lau, A.R. Gerson, R.S.C. Smart, Resolving surface chemical states in XPS analysis of first row transition metals, oxides and hydroxides: Sc, Ti, V, Cu and Zn, Applied Surface Science 257(3) (2010) 887-898.
[237] D.R. Drake, J. Paul, J.C. Keller, Primary bacterial colonization of implant surfaces, International Journal of Oral and Maxillofacial Implants 14(2) (1999) 226-232.
[238] J. Won-Seok, K. Jae-Sung, L. Jung-Hwan, U. Soo-Hyuk, C. Eun Ha, K. Kwang-Mahn, Bacterial attachment on titanium surfaces is dependent on topography and chemical changes induced by nonthermal atmospheric pressure plasma, Biomedical Materials 12(4) (2017) 045015.
[239] G. Feng, Y. Cheng, S.-Y. Wang, D.A. Borca-Tasciuc, R.W. Worobo, C.I. Moraru, Bacterial attachment and biofilm formation on surfaces are reduced by small-diameter nanoscale pores: how small is small enough?, Npj Biofilms And Microbiomes 1 (2015) 15022.
[240] D.H. Nguyen, V.T. Pham, V.K. Truong, I. Sbarski, J. Wang, A. Balčytis, S. Juodkazis, D.E. Mainwaring, R.J. Crawford, E.P. Ivanova, Role of topological scale in the differential fouling of Pseudomonas aeruginosa and Staphylococcus aureus bacterial cells on wrinkled gold-coated polystyrene surfaces, Nanoscale 10(11) (2018) 5089-5096.
[241] S. Torkzaban, S.S. Tazehkand, S.L. Walker, S.A. Bradford, Transport and fate of bacteria in porous media: Coupled effects of chemical conditions and pore space geometry, Water Resources Research 44(4) (2008).
[242] P. Johsson, T. Wadström, High surface hydrophobicity ofStaphylococcus aureus as revealed by hydrophobic interaction chromatography, Current Microbiology 8(6) (1983) 347-353.
[243] M. Grivet, J.J. Morrier, G. Benay, O. Barsotti, Effect of hydrophobicity on in vitro streptococcal adhesion to dental alloys, Journal of Materials Science: Materials in Medicine 11(10) (2000) 637-642.
[244] A.H. Weerkamp, H.M. Uyen, H.J. Busscher, Effect of Zeta Potential and Surface Energy on Bacterial Adhesion to Uncoated and Saliva-coated Human Enamel and Dentin, Journal of Dental Research 67(12) (1988) 1483-1487.
[245] R. Bürgers, T. Gerlach, S. Hahnel, F. Schwarz, G. Handel, M. Gosau, In vivo and in vitro biofilm formation on two different titanium implant surfaces, Clinical Oral Implants Research 21(2) (2010) 156-164.
[246] C. Liu, Q. Zhao, The CQ ratio of surface energy components influences adhesion and removal of fouling bacteria, Biofouling 27(3) (2011) 275-285.

[247] Y. Yuan, M.P. Hays, P.R. Hardwidge, J. Kim, Surface characteristics influencing bacterial adhesion to polymeric substrates, RSC Advances 7(23) (2017) 14254-14261.
[248] H.M. Kremers, D.R. Larson, C.S. Crowson, W.K. Kremers, R.E. Washington, C.A. Steiner, W.A. Jiranek, D.J. Berry, Prevalence of total hip and knee replacement in the United States, The Journal of bone and joint surgery. American volume 97(17) (2015) 1386.
[249] N.C.f.H. Statistics, Hospitalization for Total Knee Replacement Among Inpatients Aged 45 and over: United States, 2000–2010, (2015).
[250] S.M. Kurtz, E. Lau, K. Ong, K. Zhao, M. Kelly, K.J. Bozic, Future young patient demand for primary and revision joint replacement: national projections from 2010 to 2030, Clinical Orthopaedics and Related Research® 467(10) (2009) 2606-2612.
[251] F.M. Michael, M. Khalid, R. Walvekar, C.T. Ratnam, S. Ramarad, H. Siddiqui, M.E. Hoque, Effect of nanofillers on the physico-mechanical properties of load bearing bone implants, Materials Science and Engineering: C 67 (2016) 792-806.
[252] B. Van Hooreweder, Y. Apers, K. Lietaert, J.-P. Kruth, Improving the fatigue performance of porous metallic biomaterials produced by Selective Laser Melting, Acta biomaterialia 47 (2017) 193-202.
[253] X. Ye, L. Wang, T. Zion, G. Tang, G. Song, RETRACTED: Effects of high-energy electro-pulsing treatment on microstructure, mechanical properties and corrosion behavior of Ti–6Al–4V alloy, Elsevier, 2015.
[254] J.-X. Liu, D.-Z. Yang, F. Shi, Y.-J. Cai, Sol–gel deposited TiO2 film on NiTi surgical alloy for biocompatibility improvement, Thin Solid Films 429(1-2) (2003) 225-230.
[255] W. Harun, R. Asri, J. Alias, F. Zulkifli, K. Kadirgama, S. Ghani, J. Shariffuddin, A comprehensive review of hydroxyapatite-based coatings adhesion on metallic biomaterials, Ceramics International 44(2) (2018) 1250-1268.
[256] M. Niinomi, Mechanical properties of biomedical titanium alloys, Materials Science and Engineering: A 243(1-2) (1998) 231-236.
[257] M. Niinomi, Recent metallic materials for biomedical applications, Metallurgical and materials transactions A 33(3) (2002) 477.
[258] R.P. WELSH, R.M. PILLIAR, I. Macnab, Surgical implants: the role of surface porosity in fixation to bone and acrylic, JBJS 53(5) (1971) 963-977.
[259] R.A. Lueck, J. Galante, W. Rostoker, R. Ray, Development of an open pore metallic implant to permit attachment to bone, Surgical forum, 1969, p. 456.
[260] A. Sarker, N. Tran, A. Rifai, M. Brandt, P.A. Tran, M. Leary, K. Fox, R. Williams, Rational design of additively manufactured Ti6Al4V implants to control Staphylococcus aureus biofilm formation, Materialia 5 (2019) 100250.
[261] M. Saini, Y. Singh, P. Arora, V. Arora, K. Jain, Implant biomaterials: A comprehensive review, World J Clin Cases 3(1) (2015) 52-57.
[262] K. Wong, A. Hernandez, A Review of Additive Manufacturing. ISRN Mechanical Engineering, 2012, Article ID: 208760, 2012.
[263] C. Mota, D. Puppi, F. Chiellini, E. Chiellini, Additive manufacturing techniques for the production of tissue engineering constructs, Journal of tissue engineering and regenerative medicine 9(3) (2015) 174-190.
[264] A.A. Zadpoor, J. Malda, Additive manufacturing of biomaterials, tissues, and organs, Springer, 2017.
[265] M. Mazur, M. Leary, M. McMillan, S. Sun, D. Shidid, M. Brandt, Mechanical properties of Ti6Al4V and AlSi12Mg lattice structures manufactured by Selective Laser Melting (SLM), Laser Additive Manufacturing, Elsevier2017, pp. 119-161.
[266] A. Lerebours, P. Vigneron, S. Bouvier, A. Rassineux, M. Bigerelle, C. Egles, Additive manufacturing process creates local surface roughness modifications leading to variation in cell adhesion on multifaceted TiAl6V4 samples, Bioprinting 16 (2019) e00054.

[267] C. Chen, Y. Hao, X. Bai, J. Ni, S.-M. Chung, F. Liu, I.-S. Lee, 3D printed porous Ti6Al4V cage: Effects of additive angle on surface properties and biocompatibility; bone ingrowth in Beagle tibia model, Materials & Design 175 (2019) 107824.
[268] E. Onal, J.E. Frith, M. Jurg, X. Wu, A. Molotnikov, Mechanical Properties and In Vitro Behavior of Additively Manufactured and Functionally Graded Ti6Al4V Porous Scaffolds, Metals 8(4) (2018) 200.
[269] B. Vandenbroucke, J.-P. Kruth, Selective laser melting of biocompatible metals for rapid manufacturing of medical parts, Rapid Prototyping Journal 13(4) (2007) 196-203.